Application of Cellulose Nanomaterials in Water Treatment Processes

By

Nathan Grishkewich

A thesis
presented to the University of Waterloo
in fulfillment of the
thesis requirement for the degree of
Doctor of Philosophy
in
Chemical Engineering

Waterloo, Ontario, Canada, 2019

Examining Committee Membership

The following served on the Examining Committee for this thesis. The decision of the Examining Committee is by majority vote.

External Examiner	NAME: Jose Moran-Mirabal Title: Associate Professor
Supervisor	NAME: Michael K. C. Tam Title: Full Professor
Internal Member	NAME: Mark Pritzker Title: Full Professor
Internal Member	NAME: Xianshe Feng Title: Full Professor
Internal-external Member	NAME: Neil Thomson Title: Full Professor

Author's Declaration

This thesis consists of material all of which I authored or co-authored: see Statement of Contributions included in the thesis. This is a true copy of the thesis, including any required final revisions, as accepted by my examiners.

I understand that my thesis may be made electronically available to the public.

Statement of Contributions

Chapter 3 of this thesis consists of a manuscript that was co-authored by myself, my supervisor, Dr. Michael Tam, a former Ph. D student, Dr. Yingzhan Li, and an Undergraduate researcher, Kimberly Liu. I wrote the entire manuscript, and planned and executed experiments, Dr. Li provided expertise and assistance regarding CNF-organosilica aerogel synthesis, and Kimberly assisted in the execution of some experiments.

Chapter 4 of this thesis consists of a manuscript that was co-authored by myself, my supervisor, Dr. Michael Tam, and three Undergraduate students, Mackenzie Strong, Kimberly Liu, and Eli Bulger. I wrote the entire manuscript, and planned and executed the experiments, Mackenzie planned and executed some of the experiments, Kimberly assisted in the execution of some experiments, and Eli conducted initial research and conducted preliminary experiments.

Chapter 5 consists of a manuscript that was co-authored by myself, my supervisor, Dr. Michael Tam, and an Undergraduate student, Kathryn Toffolo. I wrote the entire manuscript, and planned and executed experiments, and Kathryn assisted in the execution of some experiments.

Chapter 6 of this thesis consists of a manuscript that was co-authored by myself, my supervisor, Dr. Michael Tam, two post-doctoral researchers, Dr. Nishil Mohammed and Dr. Zengqian Shi, a MASc student, Stephen Wei, an Undergraduate researcher, Madhav Vasudev, and an industrial collaborator, Dr. Richard Berry. I wrote the entire manuscript, as well as planned and executed the experiments, Dr. Mohammed planned and executed some experiments, Stephen developed the membrane formation process, Dr. Shi developed the synthesis protocol for melamine formaldehyde cellulose nanocrystals, Madhav assisted in the execution of some experiments, and Dr. Berry provided the cellulose nanocrystals.

Abstract

Many advanced water treatment processes have been designed and implemented to purify water, such as adsorption, photocatalysis, and membrane filtration processes. All these processes have the potential to be enhanced through the use of nanotechnology, although it is paramount that materials that are both functional and sustainable be used. The most abundant resource on the planet, cellulose, fits the above criteria as it is the source of cellulose nanomaterials (CNs). CNs which encompass both cellulose nanocrystals (CNCs) and cellulose nanofibres (CNFs) possess, many excellent properties, such as high specific strength, enormous surface area, high dispersibility in water, and immense potential for modification via the surface hydroxyl groups. Their ease of modification and abundance make them excellent candidates for water treatment applications, both in pristine form and as nanocomposites. They can be easily incorporated into both aerogel and hydrogel structures to adsorb contaminants, coated with semiconducting metal oxides as supports for photocatalysts, and embedding them in membranes to enhance strength and functionality in membrane filtration processes. This thesis will explore (1) the synthesis of new CN nanocomposites tailored for advanced water treatment operations, and (2) the fabrication and evaluation of continuous water treatment processes utilizing CN nanocomposites.

Compressible aerogels consisting of CNFs and 3-mercaptopropyl trimethoxylsilane (MPTMS) were developed and further functionalized with diallydimethylammonium chloride (DADMAC) and N,N'-methylenebis(acrylamide) (MBAA) via thiol-ene click to remove the anionic dye methyl orange (MO) from wastewater. The performance of the aerogel adsorbent was evaluated from batch equilibrium experiments, and shown to have a maximum adsorption capacity for MO dye of 186.7 mg/g based on the Langmuir isotherm analysis. Kinetic adsorption experiments revealed that mass transfer of MO dye into the aerogel could be described by a pore

diffusion model, with a pore diffusion coefficient of $1.8x10^{-9}$ m^2/s. In addition, the effect of altering environmental conditions, such as solution pH, ionic strength and temperature suggested that the process occurs by physisorption driven by electrostatic interactions. Lastly, the regeneration of the aerogel was achieved using 2 M NaCl, and the adsorbent retained 77 % of its adsorption capacity during a second treatment step.

We also investigated the use of CNCs as templates for the preparation of bismuth oxybromide photocatalysts. CNCs were modified with tannic acid to provide a platform for the growth of BiOBr nanocrystals, which was accomplished via the addition of $Bi(NO_3)_3$ to a solution containing stoichiometric amounts of CNC-TA and hydrobromic acid. Transmission and scanning electron microscopy, powder X-ray diffraction and UV-Vis spectrophotometry confirmed the formation of BiOBr on CNCs (CNC-TA-BiOBr). The photocatalytic activity of the CNC-TA-BiOBr was evaluated by degrading rhodamine B (RhB) dye under UV irradiation. Performance improved as the amount of Bi^{3+} in CNC-TA-BiOBr increased. Mechanistic studies revealed that the photocatalyst could degrade the RhB dye via the generation of superoxide (O_2^-) and direct oxidation from photogenerated holes (h^+) when RhB was adsorbed on the photocatalyst surface. In addition, the CNC-TA-BiOBr photocatalyst was shown to effectively degrade RhB dye faster than BiOBr prepared on pure tannic acid. The photocatalyst was immobilized within a calcium alginate hydrogel matrix (ALG) for easy recovery from the treated solution. The amount of ALG used to form the hydrogel had negligible effect on the performance of the photocatalyst to degrade RhB. Not surprisingly, smaller diameter beads possessed larger external surface area and exhibited greater degradation capacity. The results indicated that CNCs are effective templates for preparing the BiOBr nanocatalyst, providing new opportunities for the development of different bismuth oxyhalide structures for enhanced photocatalytic ability.

The use of sodium alginate/cellulose nanocrystal (ALG-CNC) composite hydrogels produced via ionotropic gelation with Ca^{2+} in removing methylene blue (MB) in a fixed bed column was studied. A self-contained wastewater treatment unit capable of producing the ALG-CNC beads in-situ and loading into the fixed bed vessel was also developed. Batch adsorption studies using 0.5 wt% ALG and 2 wt% CNC hydrogels revealed that the beads exhibited a maximum adsorption capacity of 410.5 mg MB/g adsorbent determined from the Langmuir isotherm. Fixed bed column experiments were conducted with various initial dye concentrations, flow rates and adsorbent content (bed height). The models developed from the flow continuity and particle phase continuity equations incorporating axial dispersion, film and pore diffusion, were shown to give good agreement with the experimental data. The effect of residual Ca^{2+} ions during batch and column adsorption studies was studied. These experiments showed that the residual Ca^{2+} in the adsorbent affected the dye adsorption in batch processes more than in continuous flow column processes. An initial shrinkage of the adsorbent in the column was associated with the loss of Ca^{2+} ions. On the other hand, the presence of Ca^{2+} interfered with the initial adsorption resulting in the observed overshoot in MB concentration profiles.

The use of melamine formaldehyde (MF) functionalized CNCs in hardwood pulp (HWP) membranes for the removal of anionic contaminants in water was also examined. MF was first coated onto CNCs using an *in situ* polycondensation reaction and characterized in batch experiments to examine its capability to remove MO dye. The adsorption of MO onto MF-CNCs obeyed the Freundlich isotherm, MF-CNCs could rapidly and effectively adsorb MO at low concentrations, reaching loadings greater than 80 mg/g at 25^{o}C. The MF-CNCs were regenerated via washing with 1 M HCl. MF-CNCs were easily incorporated into HWP membranes via a simple paper making process, with 14 wt% MF-CNC demonstrating the best balance of increased wet strength and dye removal performance. In addition, the inclusion of MF-CNCs decreased the flux

through the membranes due to the reduction of the pore size of HWP membranes. Dead-end filtration tests with 20 MF-CNC HWP membranes in series could handle feed pressures up to 30 psi. MF-CNCs could readily bind MO inside the HWP matrix, making them effective filtration media for potential point-of-use water treatment systems.

In summary, this thesis explores the synthesis of various CN nanocomposites for advanced water treatment applications as well as their application in continuous treatment operations.

Acknowledgments

Five years of graduate studies at the University of Waterloo has had a significant impact on both my personal life and professional life. There are many people I would like to acknowledge for their support and help throughout this journey.

First, I would like to express my sincere gratitude to my supervisor Prof. Michael K. C. Tam for his guidance, support, and patience throughout both my undergraduate and graduate careers. I would also like to thank the members of my doctoral examination committee, Prof. Xianshe Feng, Prof. Mark Pritzker, Prof. Neil Thomson, and Prof. Jose Moran-Mirabal for their feedback and insight regarding my research and thesis.

I would also want to express my sincere thanks to Dr. Nishil Mohammed, whom I collaborated on a number of projects and who provided a great deal of feedback and advice on water related issues. I would also like to thank Dr. Yingzhan Li for providing his insight into compressible cellulose aerogel systems. Thank you Nishil and Yingzhan for your help.

I would also like to thank Prof. Jeuwen Liu, Dr. Neil McManus, Prof. Boxin Zhao, and Prof. Michael Pope for allowing me to use their lab facilities. I would also like to thank Dr. Zhen Zhang, Dr. Zengqian Shi, Dr. Juntao Tang, Dr. Zhaoling Yao, and many other past and current members in the Laboratory of Functional Colloids and Sustainable nanomaterials for their discussions and support throughout my graduate studies.

Last but not least, this could not have been possible without the continual support from friends and family. I am eternally grateful to my parents (Gary and Susan Grishkewich) for their unconditional love and support throughout my academic career. Finally, I am deeply grateful to

my dear wife Luzhu, whose continual support, encouragement, and insightful discussions allowed me to achieve my dreams. Thank you, all of you.

Table of Contents

List of Figures

List of Tables

Chapter 1: Introduction

1.1 Overview

Only one-third of the world's population has access to clean drinking water, while the other two-thirds of the developed and developing world experience a shortage of clean water. This is attributed to residential runoff, illegal dumping and most of all, industrial activities. The textile dyeing and mining industries are two such sectors that rely heavily on water, and produce process wastewaters that are contaminated with vivid coloured dyes. Many techniques for purifying industrial wastewater are currently available such as adsorption, advanced oxidation process, and membrane filtration [1],[2],[3]. Adsorption is widely used to remove specific contaminants from a fluid phase by partitioning them onto solids that possess a high affinity for the target contaminants [4]. Membrane filtration operates similarly by partitioning contaminants into a rejection stream (retentate) while allowing purified water to pass through (permeate). Advanced oxidation processes such as photocatalysis operate by degrading organic contaminants to less harmful forms, with the goal of achieving complete conversion to carbon dioxide and water (mineralization). Through the advent of nanotechnology, materials are being developed that can enhance the effectiveness of these processes for remediating water. This includes using (i) functional nanoparticles with high surface area for adsorption processes [5], (ii) nanoparticles as high surface area templates for semiconductor metal oxide photocatalysts [6], and (iii) nanomaterials to increase the selectivity of membranes in thin film nanocomposite membranes (TFNs) [7].

When evaluating the types of nanomaterial for use in water treatment processes, special care should be taken to the source and end of life disposal of the material. Preference should be given

to systems that are biodegradable and derived from sustainable sources. One class of nanomaterials that satisfies both of these requirements is cellulose [8]. Cellulose nanomaterials (CNs) are inexpensive and biocompatible, and fall into three main types: cellulose nanocrystals (CNCs), cellulose nanofibrils (CNFs) and bacterial cellulose (BC) [9]. Both CNCs and CNFs can be obtained from a wide range of cellulosic sources and possess many desirable properties such as high surface area, high water dispersibility and abundant surface hydroxyl groups that can be easily modified. These materials are well suited to specific applications. For example, CNFs are excellent for hydrogel and aerogel networks due to their high aspect ratio and micrometer lengths, whereas CNCs in their pristine state have high surface area and a highly negative surface that make them excellent adsorbents for cationic contaminants [10].

In addition to modifying their surface, CNs may be incorporated into 1D, 2D and 3D nanocomposite structures to fabricate functional materials (**Figure 1.1**) [11]. Their incorporation into 2D and 3D matrices is also a viable alternative to pure nanoparticle as it eliminates the need for high speed centrifugation or ultrafiltration to separate them from the treated water stream. One example of this includes using CNFs coated with organosilane molecules to form porous aerogels, with surfaces that could be modified for use as effective adsorbents [12],[13]. CNCs can also be templated with semiconductor metal oxides to support photocatalytic nanoparticles, taking advantage of their high aspect ratio and surface area to reduce the amount of metal oxide used [13]. CNCs may also be encapsulated within porous hydrogels prepared using biopolymers to adsorb contaminants, with an added advantage of the nanocomposite hydrogel being contained within a fixed bed vessel to continuously purify a waste stream [14]. In addition, CNCs may be modified to act as both adsorbent and reinforcement material for cellulose membranes, which can then be used in dead-end membrane filtration systems for continuous water purification.

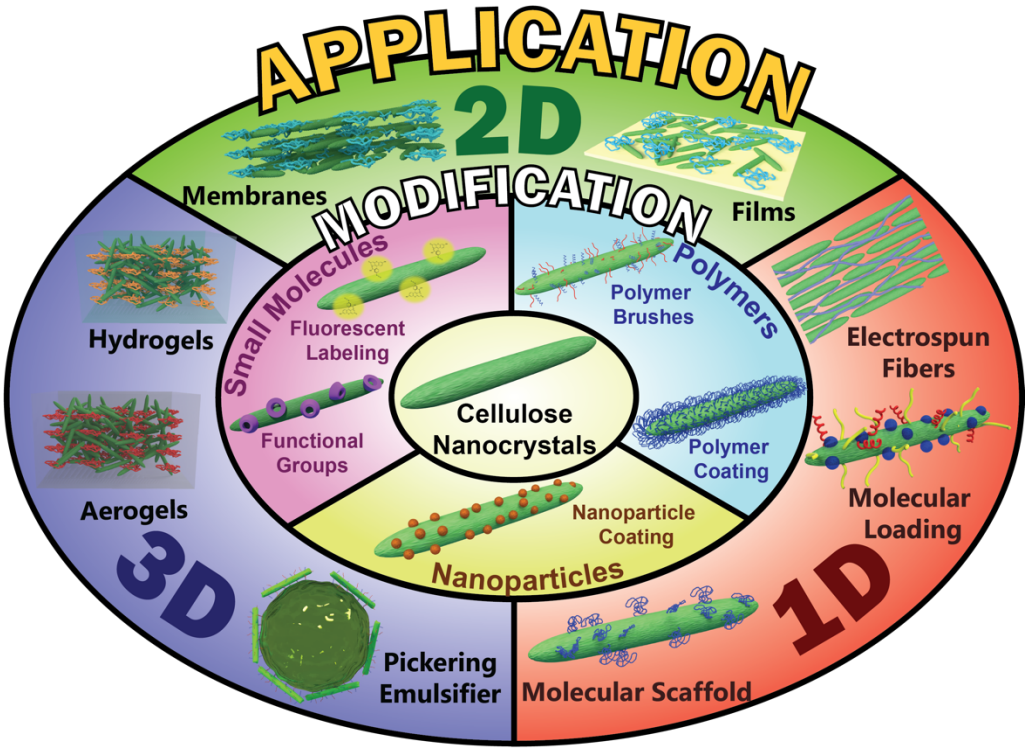

Figure 1.1: Strategies for modifying CNCs and their use in various 1D- 2D- and 3D-structured nanocomposites [11]

The motivation of this research is to develop systems that utilize biorenewable nanomaterials, namely cellulose nanomaterials, for wastewater treatment. The use of CNs can enhance the performance of existing treatment systems while also being a sustainable solution. We will explore and utilize CN nanocomposite systems in both batch adsorption systems to remove cationic dye and in batch photocatalytic processes to degrade organic dyes. The design and operation of a unit that can both produce a CN-based adsorbent and used in a fixed bed column for continuous purification of water will also be investigated. Finally, the synthesis of a modified CN for the simultaneous removal of contaminants and reinforcement of membrane filters for continuous treatment operations will be explored. To summarize, the thesis will describe the design

of CN nanocomposites for water treatment applications, as well as the implementation and evaluation of CN nanocomposites in continuous water treatment processes.

1.2 Research Objectives

Cellulose nanomaterials, with their immense surface area and enormous potential for functionalization, make them ideal candidates for use in a wide range of water remediation technologies. Research into using CNs as adsorbents has been conducted, with many groups focusing on modifying the surface chemistry to enhance their ability to remove specific contaminants. However, many studies stop short of investigating the performance of CNs in continuous water treatment operations and have neglected their use in practical systems. In addition, CNs have the potential to be used in treatment systems other than adsorption, such as photocatalytic and membrane filtration processes. Thus, the objectives of this thesis will be to (1) investigate the synthesis of new CN nanocomposites tailored towards advanced water treatment operations, and (2) evaluate the performance of CN nanocomposites in continuous water treatment operations. CN nanocomposites of interest include CNF-organosilane aerogels, which have been shown to effectively separate oil/water mixtures and emulsions and can also be used as effective adsorbents through surface modification. In addition, CNCs used as metal oxide templates have shown good potential for photocatalytic operations, and will be investigated in the design of new visible light active bismuth oxyhalide compounds. The investigation of a CNC-based adsorbent in a fixed bed column can also be explored, as well as the development of a process to efficiently produce this adsorbent to meet the demands of large-scale treatment systems. In addition, since CNs have the ability to be both active and reinforcing agents in membrane filters, their performance in dead-end filtration process will also be evaluated. Therefore, their use in the following systems will be the focus of this thesis:

1. Synthesis of cellulose nanofibril-organosilane aerogels and their capacity to remove anionic methyl orange dye
2. Synthesis of cellulose nanocrystal tannic acid bismuth oxyhalide photocatalysts for rhodamine B dye degradation
3. Study of cellulose nanocrystal incorporated alginate hydrogel beads (CNC-ALG) in a fixed bed column and their capacity to remove cationic methylene blue dye
4. Synthesis of melamine formaldehyde cellulose nanocrystals and their incorporation in hardwood pulp membranes for removing anionic methyl orange dye

1.3 Thesis Outline

The content of this thesis is organized into 7 chapters. Chapters 3 through 6 include the primary work presented in manuscript format. Chapter 1 briefly goes into industrial wastewaters and the methods used to treat them, as well as using cellulose nanomaterials to address this problem. This chapter also discusses the goals as well as the contents of the thesis. Chapter 2 examines in detail the adsorption, photocatalytic and membrane filtration processes. This chapter also includes a literature review on cellulose nanomaterials, their nanocomposites and applications in various water treatment operations. Chapter 3 investigates the synthesis of a CNF-organosilane aerogel nanocomposite and its use as an adsorbent for methyl orange dye. Chapter 4 explores the use of CNCs as templates for bismuth oxybromide photocatalytic nanoparticles and their ability to degrade rhodamine B dye in pristine nanoparticle form and embedded within alginate (ALG) hydrogels. Chapter 5 describes the design of a self-loading fixed bed vessel utilizing CNC-ALG hydrogels to adsorb methylene blue dye from water, as well the evaluation of the fixed bed vessel performance at various operating parameters. Chapter 6 explores the coating of CNCs with melamine formaldehyde for the purpose of adsorbing methyl orange dye and strengthening hardwood pulp membranes, including evaluating the performance of the membrane for treating

methyl orange dye streams in a dead-end filtration system. Chapter 7 provides a summary of the key conclusions from Chapters 3 – 6 as well as direction for future research related.

Chapter 2: Literature Review

2.1 Introduction

This chapter presents a review of the literature relevant to the understanding of the research contained in this thesis. First, an introduction into different processes used for advanced wastewater treatment will be provided, including adsorption, photocatalysis and membrane filtration. Details regarding the principles of their operation in both batch and continuous treatments modes will be highlighted here. Secondly, an analysis of two main cellulosic nanomaterials, namely cellulose nanocrystals and cellulose nanofibrils will be presented. This will include a discussion on their preparation and unique properties, followed by modification strategies to enhance their performance in wastewater treatment operations. Thirdly, various nanocomposites used in wastewater treatment operations will be reviewed, along with potential areas where cellulosic nanomaterials may be used to enhance their performance. This will include organosilane aerogels, polymeric hydrogels, templates for metal oxide coatings and formation into porous membranes for adsorbent, photocatalytic and membrane filtration processes. These sections will assist the reader in gaining an understanding on the potential CNs in offering sustainable solutions for various wastewater treatment operations.

2.2 Wastewater treatment operations

2.2.1 Water pollution

Generally, wastewater can be a very complex mixture, and is best described by the following terms: total solids (TS) (which includes total suspended solids (TSS) and total dissolved solids (TDS)), chemical oxygen demand (COD), biological oxygen demand (BOD), and other classifications specific to effluents such as the American Dye Manufacturer Institute Color value (ADMI color value) [1]. Three-tiered wastewater treatment processes have been developed to address the broad variety of waste streams, consisting of primary, secondary and tertiary treatments

(**Figure 2.1**) [15]. The goal of primary treatment is to remove suspended and floating particulates using flocculation and sedimentation, filtration and gas flotation. Secondary treatment targets dissolved solids, fine colloidal solids and organic matter via biological oxidation, utilizing processes such as activated sludge, biological contactors and trickling filters. Tertiary treatment uses sophisticated methods for specialized removal of hard-to-remove contaminants using adsorption, chemical oxidation, ozonation and ion exchange. To purify specialized industrial streams, much simpler processes can be applied by adopting only one or two of these in series, such as adsorption of small organic compounds or flocculation/sedimentation of slurries of clay.

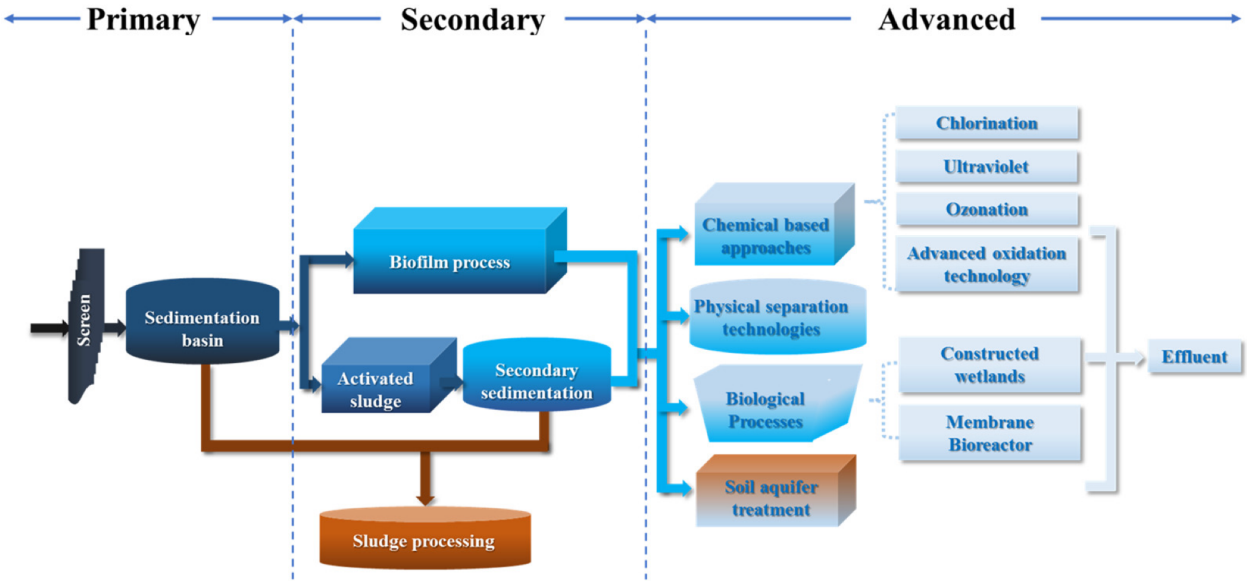

Figure 2.1: Municipal Wastewater treatment stages [16]

Effluents from various industries can differ greatly. For example, textile mill effluents may contain salts, dispersing agents and dyestuffs, whereas effluents from mining operations can contain acids and dissolved heavy metal ions [17],[18]. Wastewater containing various types of dye are primarily generated by the textile, paper, cosmetic, and leather industries [19]. Organic dyes include to a broad range of chemical compounds, such as disperse, direct, reactive, sulphuric, acidic, and basic dye molecules [20]. Dye wastewaters can include salts (40 – 100 g), be highly alkaline (9 – 12 pH)

and have temperatures of 30 – 40°C [1]. In two cases, the discharge conditions for reactive dyes following cotton fabric dyeing can range from 5 to 10 mg/L and 1300 to 1555 mg/L [1]. In Canada, the effects of dye contamination in wastewater are not as pronounced, since these contaminants can be captured by municipal wastewater treatment facilities. However, this is not the case globally [20]. In addition, studies in England concluded that of 18% of 200 dyes belonging to the basic class significantly inhibited the respiration rate of wastewater bacteria [1]. It is therefore essential that dye wastewater is purified to certain standards before it is discharged into the environment, and this can be achieved by implementing specific wastewater treatment operations that are best suited for the particular stream.

Prior to developing a system to treat complex waste streams, researchers focus on developing materials and processes to remove a target contaminant. For example, an organic dye or heavy metal ion can be removed by adsorption, whereas organic compounds can be degraded by advanced oxidation techniques [2] and large colloids or bacteria can be removed by membrane filtration [3]. The simplest experiments that can be performed through bench-scale testing are conducted batchwise and utilize small volumes of contaminants and smaller masses of newly developed treatment materials. Equilibrium and kinetic properties of adsorbents can be assessed to determine their effectiveness at removing contaminants. If the material passes this phase, it can move on to continuous testing, such as adsorbents in a fixed bed or a cross-flow setup for a membrane. Rigorous study is required at this stage before the process can be scaled up to industrial scale. In the case of fixed beds, hydraulic loading levels of 5.15 gal/ft^2*min are common [21]. In this thesis, the performance of the wastewater treatment materials were evaluated on organic dyes, including the azoic dye methyl orange (MO) (anionic), rhodamine B (neutral at pH 7), and methylene blue (MB) (cationic). Their structures are shown in **Figure 2.2**. The concentration of

these model compounds can be readily determined by spectroscopic techniques, such as UV-Vis spectrophotometry.

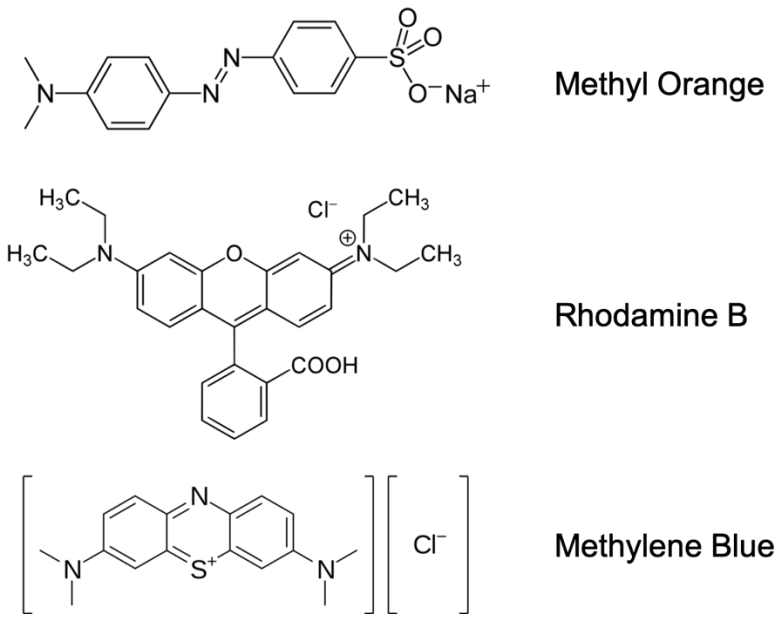

Figure 2.2: Structures of dyes used in these studies

2.2.2 Adsorption

Adsorption is best described as a process where material (adsorbate) accumulates at a gas/solid interface or a liquid/solid interface [22] (**Figure 2.3**). Adsorption plays an essential role in environmental cleanup, whether it is used to remove waterborne contaminants from waterways or capture irritating odors from the air. Adsorption processes can be further divided into two classes: physisorption and chemisorption. Physisorption is the weaker of the two processes, mainly dictated by van der Waals forces or dipole-dipole interactions, rendering it a reversible process. It is an exothermic process, with heats of adsorption ranging from 8 to 65 kJ/mol [23]. Chemisorption is much stronger, with the adsorbate being held at the surface by valence forces that have the same strength of a chemical bond. This is also an exothermic process, with heats of adsorption between

84 - 420 kJ/mol. Whether adsorption is batch or continuous, the adsorbate molecules migrate to the surface of the adsorbent particles. The adsorbate must then find a vacant site for adsorption before it can attach to the solid phase. This process occurs until the concentration of adsorbate in the solid phase is in equilibrium with the concentration of adsorbate in the bulk fluid.

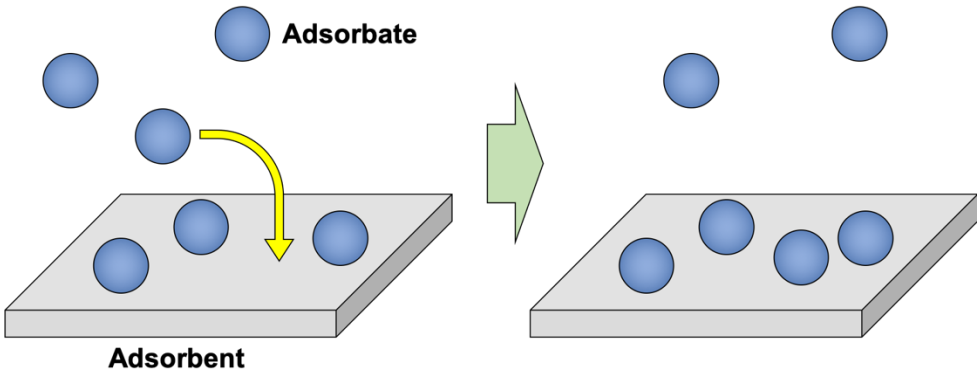

Figure 2.3: Process of adsorption

2.2.3 Batch adsorption

Batch adsorption experiments are crucial to fully study the characteristics of an adsorbent and its efficacy in treating a specific effluent. These experiments are a necessary prerequisite for understanding both the equilibrium properties and the kinetics of the adsorption process. In general, it is straightforward to measure the concentration of adsorbate in the bulk of a solution. A mass balance then allows the concentration of adsorbate on the adsorbent in the batch system to be calculated as follows:

$$q = \frac{(C_0 - C_b) * V}{m} \tag{2.1}$$

where q is the mass of adsorbate adsorbed (mg/g), C_b is the concentration of adsorbate in the bulk solution (mg/L), C_0 is the initial concentration of adsorbate (mg/L), V is the volume of the batch system (L), and m is the mass of adsorbent used (g). The value of q is vital when determining adsorption capacity or adsorption kinetics.

One of the most important characteristics of a particular adsorbate/adsorbent system is the adsorption isotherm, which is determined from batch or equilibrium adsorption experiments. The adsorption isotherm relates the bulk concentration of the adsorbate to the amount of bound adsorbate. The most well-known model is the Langmuir adsorption isotherm [24] which has the following expression:

$$q_e = \frac{q_m K_L C_e}{1+K_L C_e} \tag{2.2}$$

where q_e is the amount of adsorbate in the solid phase at equilibrium per mass of adsorbent (mg/g), q_m is the theoretical maximum amount of adsorbate adsorbed per mass of adsorbent (mg/g), K_L is the adsorption equilibrium constant (L/mg), and C_e is the bulk concentration of adsorbate at equilibrium (mg/L). The Langmuir isotherm is developed based on the following assumptions: (1) monolayer coverage of the adsorbate, (2) all adsorption sites are equally active, (3) and no interaction occurs between adjacent adsorbate molecules [25]. Another commonly used isotherm is the Freundlich isotherm [26], which is an empirical model described by Eq. (2.3):

$$q_e = K_F C_e^{1/n} \tag{2.3}$$

where K_F is a constant related to adsorption capacity and adsorbate/adsorbent affinity, $1/n$ represents a heterogeneity factor of the adsorbent ranging from 0 to 1, and q_e and C_e have the same definitions in Eq. (2.2). Typically, a value of n between 0.1 and 1 denotes that the adsorption process is favorable, whereas a value of n greater than 1 denotes an unfavorable correlation due to limitations of the model at high pressures [27]. This model assumes multilayer coverage on the adsorbent, and that the surface may have heterogeneous adsorption sites [28].

For many systems, especially porous adsorbents, equilibrium is not attained instantaneously [29]. The adsorbate must partition to an adsorption site, whether by advection or diffusion, before it is

adsorbed and removed from the bulk solution. The progression of mass transfer of the adsorbate and adsorption over time is often referred to as adsorption kinetics. For porous adsorbents, the adsorbate must transfer from the bulk solution to the stagnant film boundary layer of the adsorbent, transport through this layer via diffusion, and finally diffuse through the internal pore liquid of the adsorbent before ultimately adsorbing onto a site [29]. **Figure 2.4** provides an illustration of the observed concentration profile of an adsorbate in the bulk solution, the pore liquid, and on the adsorbent surface for a spherical adsorbent.

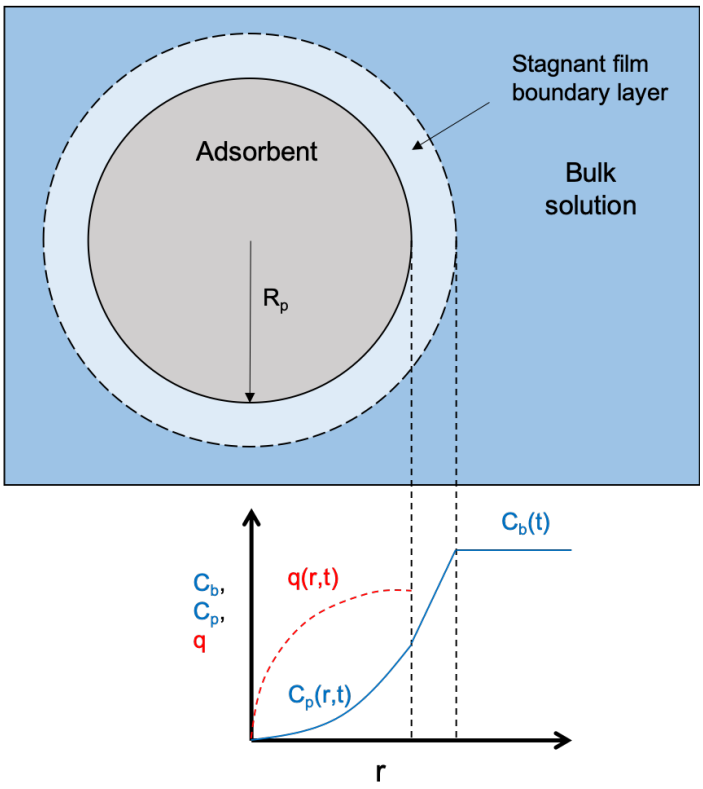

Figure 2.4: Schematic of film diffusion and pore diffusion mass transfer processes inside spherical adsorbent and concentration profiles observed in relation to radial distance from center of adsorbent

Modelling the transport of adsorbate in this manner starts with film diffusion, which is diffusion from the bulk fluid (C_b) into the pore fluid of the adsorbent (C_p) and is given by the following relation [30]:

$$\frac{\partial C_b}{\partial t} = -\frac{3mk_f}{V_L \rho_p R_p}\left[C_b - C_{p,r=R_p}\right] \tag{2.4}$$

This equation has the following initial conditions:

$$C_b = C_b(0) = C_0 \tag{2.5}$$

where m is the mass of adsorbent (kg), k_f is the film diffusion coefficient (m/s), V_L is the volume of water in the batch vessel (L), ρ is the density of the adsorbent (kg/m^3), and R_p is the radius of the adsorbent particle (m) in Eq. (2.4). Coupling transport by diffusion and transfer of the adsorbate from the pore liquid to the adsorbent solid phase can be given by the mass balance in Eq. (2.6) for spherical adsorbents [29]:

$$\rho_p \frac{\partial q}{\partial t} + \varepsilon_p \frac{\partial C_p}{\partial t} = D_p\left[\frac{1}{r^2}\frac{\partial}{\partial r}\left(r^2 \frac{\partial C_p}{\partial r}\right)\right] \tag{2.6}$$

This equation has the following initial and boundary conditions:

$$C_p = C_p(0,r) = 0 \tag{2.7}$$

$$q = q(0,r) = 0 \tag{2.8}$$

$$r = 0,\ t > 0; \qquad \frac{\partial C_p}{\partial r} = 0 \tag{2.9}$$

$$r = R_p,\ t > 0; \qquad \frac{\partial C_p}{\partial r} = \frac{k_f}{D_p}\left(C_b - C_{p,r=R_p}\right) \tag{2.10}$$

where ε_p is the porosity of the adsorbent, and D_p is the pore diffusion coefficient of the adsorbent (m^2/s). The first and second terms on the left-hand side of Eq. 2.6 respectively describe the liquid phase adsorbate and solid phase adsorbate concentrations with time, and the right-hand side portion describes the diffusion of the adsorbate in the liquid phase through the pores of the

adsorbent. Eq. (2.11) describes the differential equilibrium relationship between the adsorbate in the liquid state and with the corresponding pore adsorption sites:

$$\frac{\partial q}{\partial C_p} = \frac{K_L q_m}{(1+K_L C_p)^2} \tag{2.11}$$

where this equation is the derivative of the Langmuir isotherm with respect to C_p. Using Eqs. (2.4 – 2.11), the bulk concentration of adsorbate over time can be modelled and compared to experimental observations with the goal of extracting k_f and D_p.

Since both k_f and D_p are initially unknown, additional methods can be used to estimate these parameters. Eq. (2.12) can be obtained by integrating Eq. (2.4) and assuming $C_p = 0$ at $t = 0$ and used to estimate k_f by using the tangent at $t = 0$ of a $\ln(C_b/C_0)$ vs. time plot of the kinetic data [29]:

$$k_f = -\frac{V_L R_p \rho_p}{3m} \frac{d(\ln(\frac{C}{C_0}))}{dt}_{t=0} \tag{2.12}$$

To confirm the validity of k_f and D_p for describing the mass transfer of the adsorbate, the root mean squared error (RMSE) between the observed bulk concentration and that determined by the model can be calculated:

$$RMSE = \frac{1}{C_0}\sqrt{\frac{1}{N}\sum_{i=1}^{N}\left(C_{b,exp}(t_i) - C_{b,calc}(t_i)\right)^2} \tag{2.13}$$

where $C_{b,exp}$ and $C_{b,calc}$ are the experimental and calculated bulk dye concentrations, respectively.

For systems where mass transfer is not the limiting step for adsorption, the rate of adsorption is controlled by kinetics. In the case of nanoparticle adsorbents, one beneficial advantage is their

large external surface area, so that mass transfer limitations may be negligible in a well-designed system. Two main kinetic models are used to predict the adsorption kinetics in batch systems, the pseudo-first order model [31] and pseudo-second order model [32]. The pseudo-first order model is described by Eq. (2.14):

$$\frac{dq_t}{dt} = k_1(q_e - q_t) \tag{2.14}$$

where q_t is the amount of adsorbate adsorbed at time t, q_e is the amount of adsorbate adsorbed at equilibrium and k_1 is the pseudo-first order rate constant (min^{-1}). The integrated form of this model can be represented by Eq. (2.15) [33]:

$$\frac{q_e - q_t}{q_e} = e^{-k_1 t} \tag{2.15}$$

In this form, q_e and k_1 can be determined by fitting the above equation to experimental data via non-linear regression. The pseudo-second order model is shown in Eq. (2.16):

$$\frac{dq_t}{dt} = k_2(q_e - q_t)^2 \tag{2.16}$$

where q_t and q_e have the same definition as in Eq. (2.14), and k_2 is the pseudo-second order rate constant (g/mg min). The integrated form of this model has the form shown in Eq. (2.17):

$$q_t = \frac{q_e^2 k_2 t}{q_e k_2 t + 1} \tag{2.17}$$

Similar to Eq. (2.15), q_e and k_2 can be determined by fitting the equation to experimental data via non-linear regression.

It should be noted that the kinetic constants obtained from Eqs. (2.14) and (2.16) may only be applied to the adsorbent systems when they are used in batch reactors, whereas D_p estimated from Eq. (2.6) is essential for modelling mass transfer in continuous fixed bed adsorbers. In comparing

the performance between a batch vessel and fixed bed vessel for adsorption, fixed bed vessels will consistently achieve a greater level of adsorption. As shown in **Figure 2.5**, batch systems always show a continual decrease in the bulk concentration of adsorbate as it partitions onto the solid phase of the adsorbent until equilibrium is reached. Meanwhile in a continuous fixed bed operation, the adsorbent reaches equilibrium with the concentration of the incoming stream, C_0, allowing for a higher loading of the adsorbate.

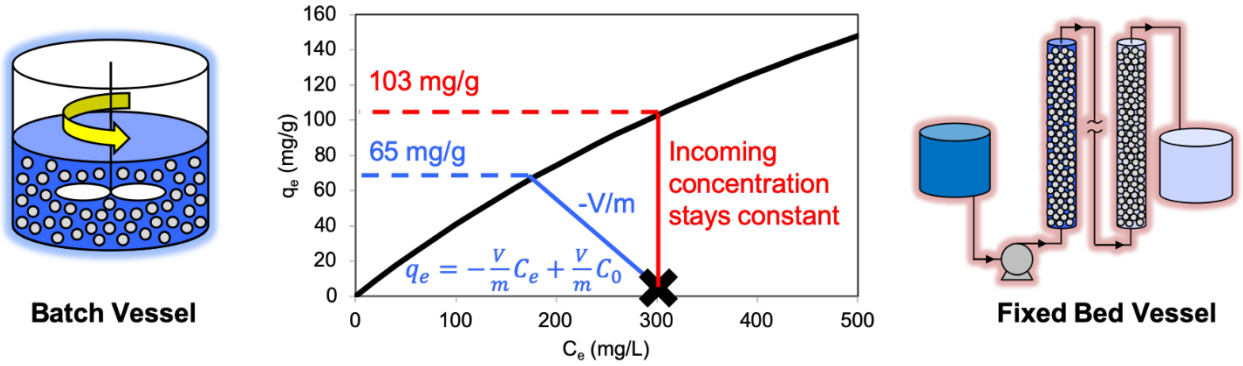

Figure 2.5: Batch vessel adsorption vs. fixed bed adsorption corresponding to adsorbent equilibrium conditions

2.2.4 Column Adsorption

Although batch adsorption vessels are a simple solution for removing waterborne contaminants, they are unable to reach the same equilibrium conditions that can be achieved in continuous treatment systems. Thus, a more efficient solution is to utilize the adsorbent in a continuous treatment system, such as a fixed bed column. Operating a fixed bed column has many advantages, such as the continuous flow of wastewater, and greater loading of contaminant onto the adsorbent [34].

When choosing an adsorbent, one must take into account the size of the adsorbent particles used. A delicate balance must be made between their shape/size and the resulting pressure drop experienced across the fixed bed. Mass transfer effects are reduced when adsorbent particles are very small (larger external surface area), but they will result in a large pressure drop within the column and increase operating costs. During the operation of a fixed bed vessel, a concentration front known as the mass transfer zone (MTZ) forms in the vessel (**Figure 2.6a**). This is the volume inside the vessel where the adsorbent participates in the removal of the adsorbate and the concentration in the liquid phase decreases while the concentration in the solid phase increases. The length and shape of this zone are dependent on the adsorption rate of the adsorbent as well as its equilibrium adsorption properties [35]. The point at which this zone reaches the outlet of the fixed bed is known as breakthrough, where the outlet concentration of the adsorbate is no longer zero. The zone will continue to exit the fixed bed resulting in an increase in effluent concentration until it has fully exited the bed, where the effluent concentration is equal to the inlet concentration, which is denoted as the saturation point. For fixed bed operation, many authors have termed the time at breakthrough (t_b) at the point where the effluent concentration (C) is 10% of C_0, and the saturation time (t_s) when C is 90% of C_0 [36].

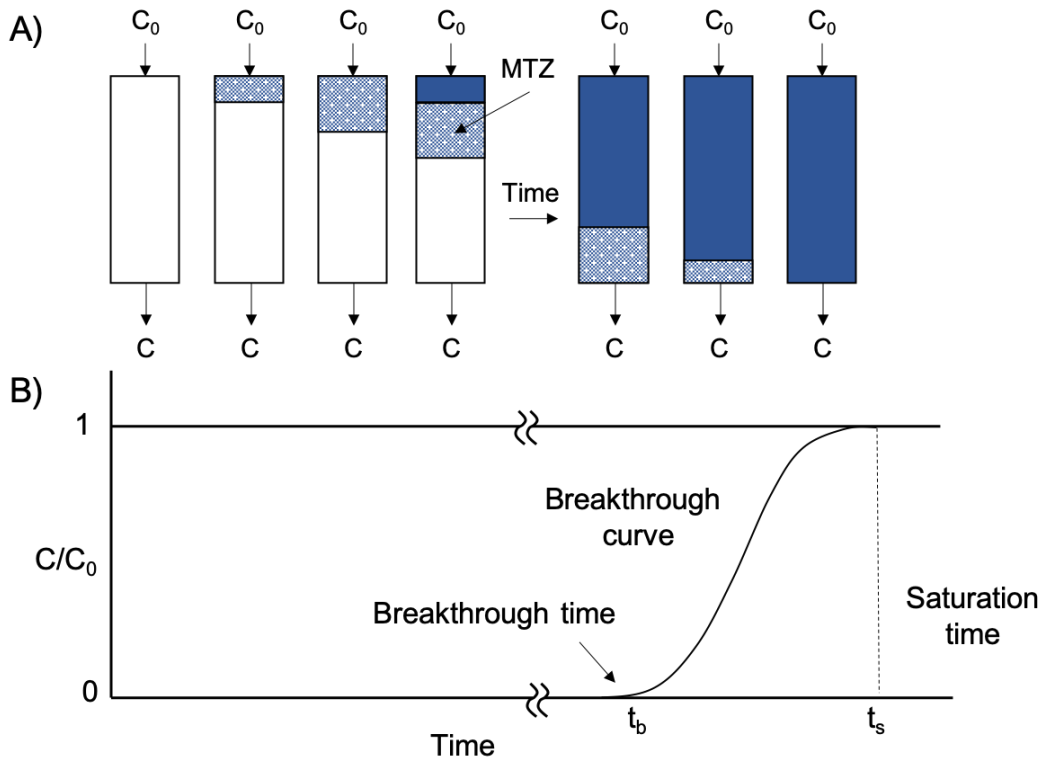

Figure 2.6: a) Operation of fixed bed adsorber with generation and progression of MTZ, and b) normalized concentration of effluent exiting fixed bed vessel showing appearance of MTZ

A plot of the effluent concentration (C) measured versus time (t) (or volume treated) yields the breakthrough curve (**Figure 2.6b**). To determine the total amount of contaminant adsorbed (q) over the course of operation, the following equation can be used:

$$q = Q \int_0^{t=total} C_{ad}(t)\, dt \tag{2.18}$$

where q is the mass of contaminant adsorbed (mg), Q is the volumetric flow rate (L/hr), and t is time (hr). C_{ad} is the concentration of adsorbed contaminant (mg/L), and can be calculated from the following relationship:

$$C_{ad} = C_0 - C \tag{2.19}$$

where C_0 is the concentration of contaminant entering the fixed bed (mg/L) and C is the concentration of contaminant in the effluent (mg/L). To determine the equilibrium adsorption capacity (q_e) of the adsorbent, the following relationship can be used:

$$q_e = \frac{q}{m} \tag{2.20}$$

where q_e is the equilibrium adsorption capacity of the adsorbent (which corresponds to the maximum adsorption capacity of the column at the given initial conditions (mg/g)) at saturation, and m is the mass of adsorbent used in the column (g).

The effectiveness of a fixed bed vessel is governed by the mass transport between the bulk fluid flow and solid adsorbent. The following equations are the material balances of the adsorbate between the bulk fluid and pore fluid in the adsorbent, with Eq. (2.21) describing the bulk flow continuity [21]:

$$\frac{dC_b}{dt} = D_b \frac{\partial^2 C_b}{\partial z^2} - v \frac{\partial C_b}{\partial z} - \frac{3k_f(1-\varepsilon_b)}{R_p \varepsilon_b}[C_b - C_{p,r=R_p}] \tag{2.21}$$

where C_b is the concentration of adsorbate in the bulk solution (kg/m^3), v is the interstitial velocity of the bulk solution (m/s), z is the distance from the inlet of the column (m), t is time (s), ε_b is the bed void fraction, q is the solid phase concentration of adsorbate (kg/m^3) and D_b is the axial dispersion coefficient (m^2/s). The terms of the bulk continuity equation are best described in **Figure 2.7.** From the figure, the term in blue describes the flow of adsorbate through the bed by advection, the term in red describes deviations from plug flow where the adsorbate may diffuse into control volumes ahead or behind itself, and the term in green represents the transfer of adsorbate from the bulk fluid to the adsorbent pore fluid. The terms of k_f and D_b can be determined

via empirical relations depending on the flow regime, with k_f determined by the correlation by Wilson and Geankoplis [37]:

$$k_f = \frac{1.09 D_m}{2\varepsilon_b R_p}\left(\frac{\mu_w}{\rho_w D_m}\right)^{1/3} Re^{1/3} \tag{2.22}$$

The axial dispersion coefficient (D_b) is determined by [38]:

$$D_b = \frac{\mu_w}{\rho_w}\frac{Re}{0.2+0.011Re^{0.48}} \tag{2.23}$$

with Reynolds number (Re) defined as:

$$Re = \frac{2\rho_w v R_p}{\mu_w} \tag{2.24}$$

where D_m is the molecular diffusivity of the adsorbate (m^2/s), ρ_w is the density of water (1000 kg/m^3) and μ_w is the viscosity of water (Pa·s). To model adsorption in the fixed bed, Eq. (2.21) can be coupled with Eq. (2.6) when using spherical adsorbent, and also with Eq. (2.11) if using an adsorbent/adsorbate that obeys the Langmuir isotherm to obtain a breakthrough curve as seen in **Figure 2.6b**.

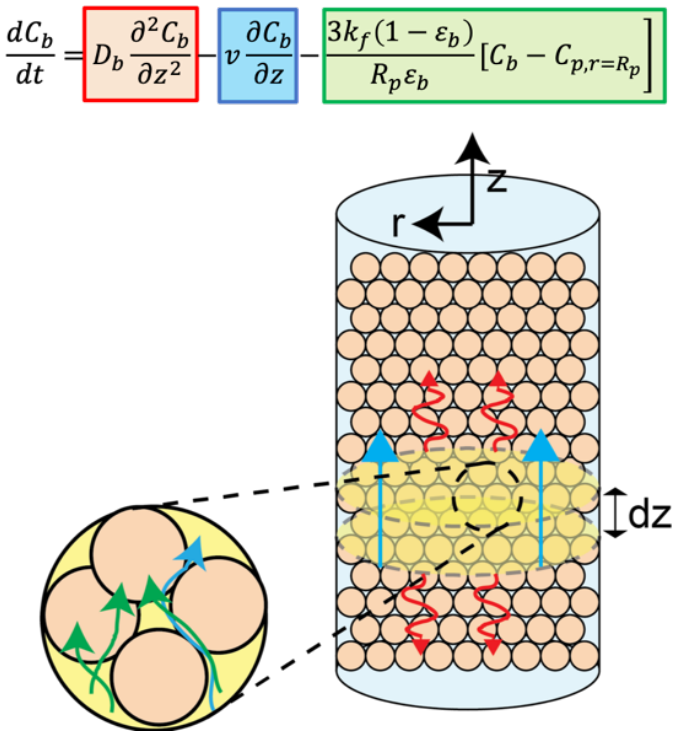

Figure 2.7: Illustration of terms in bulk continuity equation on how they influence mass transport in a fixed bed column

The above relations can be used to predict the adsorbate concentration at any point in the fixed bed vessel, but it is better to validate the breakthrough curve which can be easily obtained. The breakthrough profile produced by the model will be affected by the equilibrium parameters (isotherm parameters), D_p obtained from batch experiments, as well as the ε_b determined from physical observations, and D_b and k_f determined from empirical correlations. It can then be used to ensure that the fixed bed performs well depending on operating conditions, such as initial adsorbate concentration (C_0), flow rate (Q), and mass of adsorbent (or height of packing) (m). Ultimately, the above relations can primarily be used to design a fixed bed vessel to treat a specific wastewater stream. Given the C_0, Q, and desired t_b, the mass of packing can be calculated, which will allow for an appropriately sized column to be designed to achieve an effective treatment.

2.2.5 Photocatalysis

While adsorption is a suitable process for removing contaminants, it usually produces a secondary waste stream that will ultimately require appropriate treatment and disposal [2]. In comparison, advanced oxidation processes (AOPs) aim to treat water by degrading organic contaminants to less harmful forms, with the ultimate goal of converting them to carbon dioxide and water (mineralization). These processes operate by generating reactive oxygen species (ROS), such as hydroxyl radicals (•OH) that effectively break down organic compounds and decolorize dye-containing effluents [39]. AOPs encompass many treatment technologies including ozonation, Fenton oxidation and photocatalysis. The latter process is of great interest as it utilizes light to degrade contaminants without adding chemical reagents [40]. This technique is capable of promoting the degradation of products in both air and water [41],[42]. Metal oxide semiconductors such as titanium dioxide (TiO_2) [43] are good examples of photocatalysts as they can facilitate two simultaneous degradation reactions at their surface when exposed to light: (1) reduction processes from photo-generated electrons (e^-), and (2) oxidation processes from photo-generated holes (h^+) [44]. The generation of an electron/hole pair (exciton) is only possible when these semiconductor metal oxides are excited by a photon with equal or greater energy than its band gap (E_g). This excitation effectively promotes an electron into the conducting band (CB), while leaving a positively charged hole in the valence band (VB) of the semiconductor (**Figure 2.8a**).

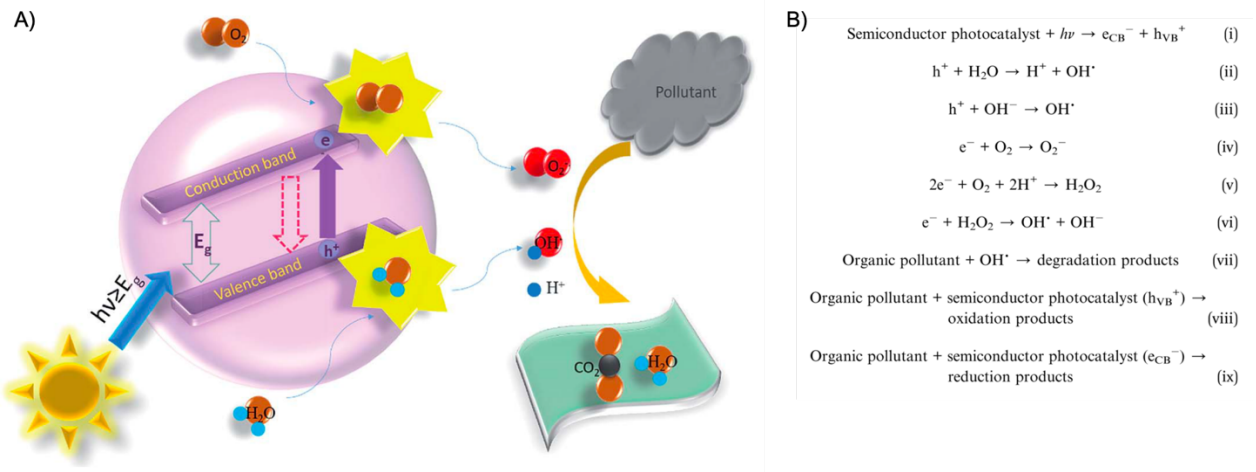

Figure 2.8: a) Electron/hole pair generation via incident light hitting semiconductor surface, generation of reactive oxygen species and degradation of organic pollutants to CO2 and water, and b) Mechanisms of ROS generation and degradation pathways of organic molecules[45]

After the generation of an exciton, a variety of chemical reactions can occur, as illustrated in **Figure 2.8b**. With the positively charged hole on the VB, adsorbed water or moisture can decompose to form •OH (ii), or adsorbed hydroxyl ions can donate an electron to form •OH (iii). The electron promoted to the conducting band can interact with adsorbed O_2 to form superoxide (O_2^-) (iv), or interact with adsorbed oxygen and protons to form hydrogen peroxide (v), and even interact with adsorbed hydrogen peroxide to form additional •OH (vi). The generation of ROS in these previous 5 reactions allow for oxidation processes to occur away from the photocatalyst in the bulk of the treatment media (vii), but through direct adsorption of contaminants onto the photocatalyst surface the oxidation of the pollutant may occur (viii) as well as reduction of the pollutant (ix). The capacity for these reactions to take place depends upon the thermodynamic properties of the semiconductor, namely the band gap and band edge position (**Figure 2.9**). The majority of metal oxide semiconductors being studied as photocatalysts today possess a CB that has the capability of reducing O_2 to superoxide (potential of -0.28 V vs. NHE) and a VB that can oxidize water to •OH (potential of 2.8 V vs. NHE) [46].

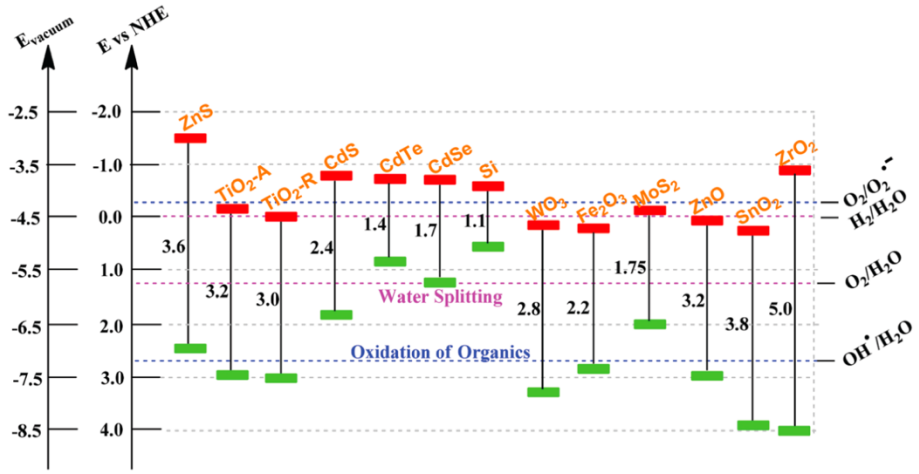

Figure 2.9: CB, VB, and band gap for various metal oxide semiconductors on reference to normal hydrogen electrode (NHE) potential scale[46]

Metal oxide with sufficiently large band gaps, such as TiO_2, will be able to accommodate both these reactions, although the difficulty arises with the photon energy required to promote an electron in this material. Anatase TiO_2 has a band gap energy of 3.2 eV, meaning that light with a wavelength of 387 nm, which lies in the UV range is required to excite it [46]. While the use of high-powered UV lamps to disinfect or perform AOPs in wastewater treatment is common, these lamps require a substantial amount of energy. Thus researchers are investigating semiconductor systems that possess a band gap within the visible light region to alleviate the need for UV lamps.

2.2.6 Photocatalytic processes

Photocatalytic treatment processes may be carried out in both batch and continuous settings. Batch processes are usually conducted in standard vessels, with the inclusion of one or more high-powered UV lamps capable of exciting the photocatalyst. The degradation of organic molecules by this method can be quite complex, with the generation of many intermediate species [47]. Researchers monitor the concentration of the original contaminant during the degradation and use this information to obtain rate expressions, most commonly using the Langmuir-Hinshelwood model [48]:

$$\ln\left(\frac{C_0}{C}\right) = k_{app}t \tag{2.25}$$

where C_0 is the dye concentration at $t = 0$, C is the concentration of dye at time t, and k_{app} is the apparent rate constant. As the decomposition of the target compound may occur both in the bulk of the solution and on the surface of the photocatalyst, the overall rate constant k_{app} is useful to evaluate the photocatalyst capacity to degrade a target contaminant.

To enhance their effectiveness, photocatalysts may be used in the form of nanoparticles, with large surface area to facilitate reactions. However, an additional step is required to remove them from the treated water, whether by centrifugation or membrane filtration [49],[50]. A common method to prepare recyclable photocatalysts that still retain their surface area and accessibility involve anchoring them to magnetic nanoparticles and using a magnetic field to rapidly remove them from the treated media [46],[51]. In continuous photocatalytic processes, anchoring the catalyst on a surface [52] or immobilizing it inside a porous matrix [53],[54] avoids the need for an additional recovery step. However, some lab scale processes have implemented a membrane filtration step with a recurring backwash process to retain the nanosized photocatalysts in continuous operation [50],[55]. (**Figure 2.10**).

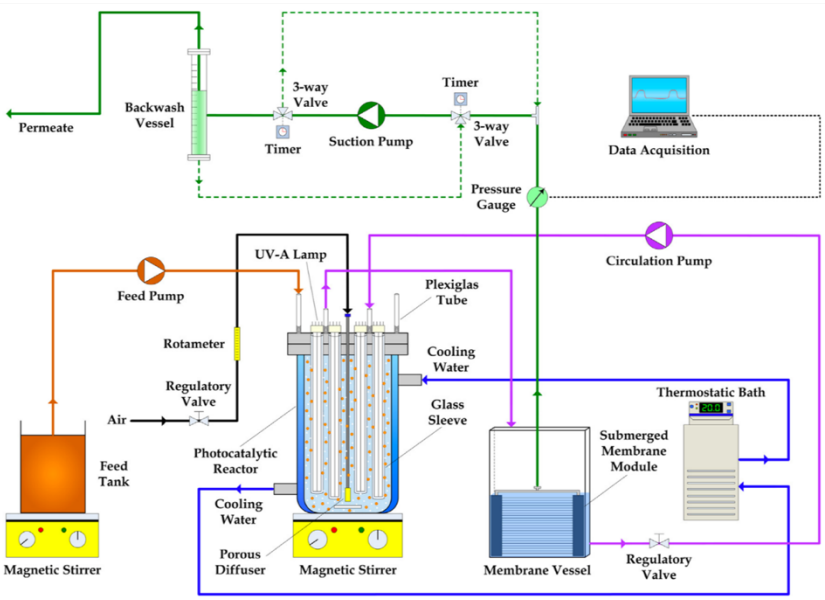

Figure 2.10: Process flow diagram of lab scale continuous photocatalytic reactor incorporating membrane filtration for photocatalyst recovery[50]

2.2.7 Membrane Filtration

Membrane separation processes are another form of physical separation based on size exclusion, where the contaminants are rejected based on their size relative to the pore size of the membrane. In contrast to photocatalysis, membrane filtration processes generate secondary waste stream in addition to their treated stream (permeate), whether it be a rejection stream (retentate) or a fouled/saturated membrane. **Figure 2.11** shows the classification of pressure driven membrane filtration processes based on pore size, starting with microfiltration (with pore sizes ranging from 50 – 500 nm), ultrafiltration (2 – 50 nm), nanofiltration (< 2 nm), and finally reverse osmosis (0.3 – 0.6 nm) [56]. Examples of separations achieved by these membrane are; (a) removal of bacteria and yeast microbes via microfiltration and (b) removal of salt ions via reverse osmosis [3]. Although decreasing the pore size allows for the separation of smaller species, more pressure and energy are required to drive the flow across the membrane. Through the advent of nanotechnology, membranes can be functionalized to carry out the above separations with greater effectiveness by

increasing permeability, fouling resistance and even exhibit self-cleaning abilities by incorporating nanoparticles with catalytic activity [3].

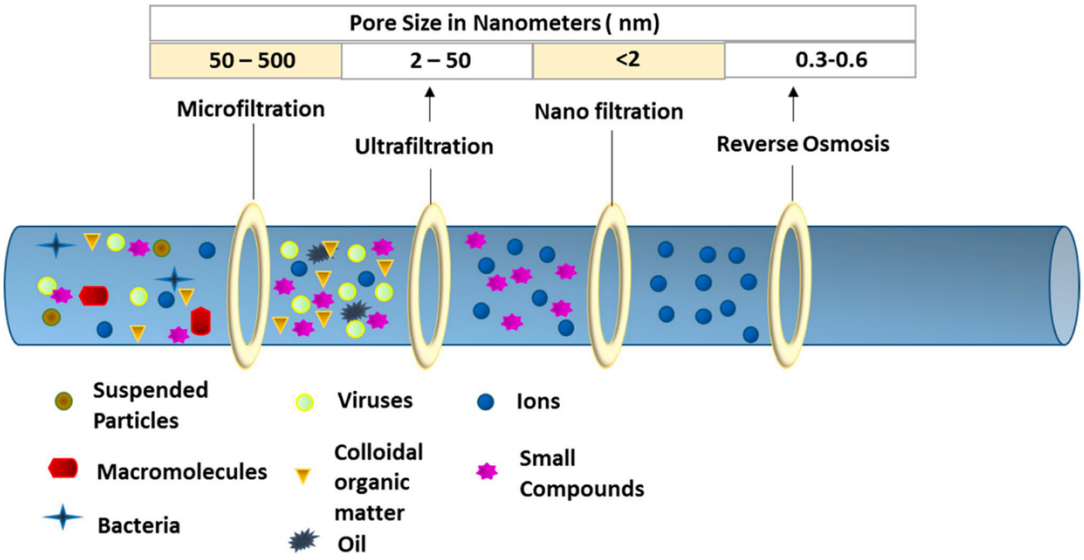

Figure 2.11: Classification of pressure driven membrane separation processes and their pore sizes [56]

Incorporating nanomaterials into membranes serves two main purposes: reinforcement of the membrane structure [57] or barrier layer to enhance the rejection/retention of contaminants [58]. In the latter case, they are best used in thin film nanocomposite membranes (TFN) comprising of a layered structure shown in **Figure 2.12**. The bottom layer consists of a non-woven microfibrous mat that provides mechanical strength to the membrane, while the middle layer serves as another support that is typically a nanofibrous scaffold with relatively high porosity to allow for high flux [58] and the top layer is a very thin, less porous layer that gives the membrane its selectivity either through surface functional groups or nanosized pores. Nanomaterials used for this top layer include carbon nanotubes [59], nanosized alumina [60] and cellulose nanomaterials [58],[61], that promote size exclusion or increase the permeability across the membrane. The selectivity of these membranes can also be tuned based on the type of nanomaterial used. For example, using highly charged nanoparticles can induce repulsion of ions into the retentate stream

[7], or promote adsorption to remove contaminants from the treated stream as they pass through the membrane [62],[63]. In addition to pressure-driven membrane processes, nanoparticles have also been used to aid gravity-driven filtration processes. One example involves the use of silver nanoparticles embedded in filter processes to deactivate bacteria [64],[65]. Such solutions may be applied for point-of-use (POU) water treatment in areas where electricity is not available to support pressure-driven membrane separation processes [66].

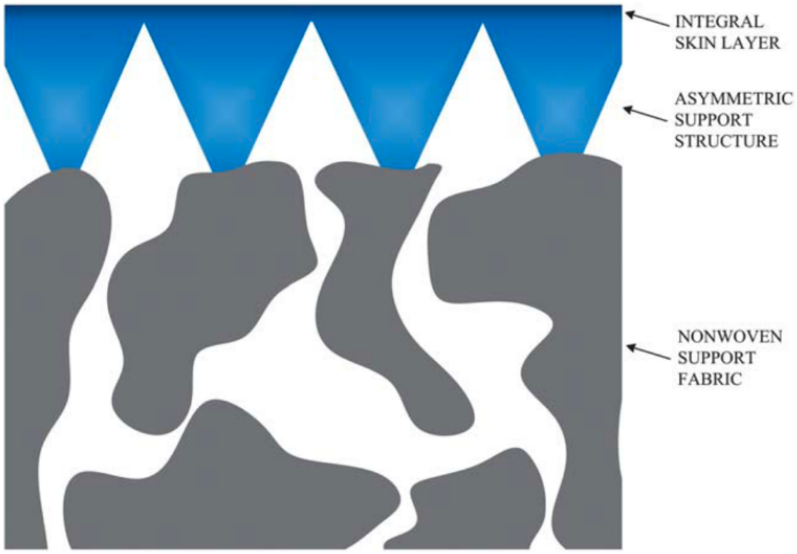

Figure 2.12: Diagram showing layers of thin film nanocomposite membrane [3]

2.2.8 Membrane filtration processes

In essence, membrane filtration processes are continuous with respect to input and discharge streams. The performance of membrane separation processes can be evaluated based on their ability to reject contaminants, given by the rejection ratio [67]:

$$R(\%) = \left(1 - \frac{C_{pm}}{C_0}\right) \times 100\% \tag{2.26}$$

where C_0 is the concentration of the contaminant in the feed (mg/L) and C_{pm} is the concentration of the contaminant in the permeate (mg/L). In addition, the permeate flux J = Q/A is also monitored

during the course of operation to determine if membrane fouling occurs, where Q is the flowrate across the membrane (L/hr) and A is the cross-sectional area of the membrane (m^2).

Membrane filtration processes can be further divided into dead-end filtration and cross-flow filtration (**Figure 2.13**). In dead-end filtration, the incoming feed stream flows perpendicular to the membrane surface (**Figure 2.13a**) to produce only one outlet stream [68]. Depending on the incoming stream, this produces a filter-cake build up on the membrane that decreases the flux, requiring the system to be shut down and the membrane surface cleaned [69]. In cross-flow filtration, the feed travels parallel to the membrane surface (**Figure 2.13b**) and an applied transmembrane pressure forces a portion of the flow through the pores of the membrane to generate a permeate, leaving behind a portion that forms the retentate [70]. Due to the existence of retentate stream, much less accumulation of rejected species on the membrane surface occurs as the shear force from the feed stream aids in slowing the build-up of fouling material [71]. Since membrane fouling may still occur, processes such as backwashing are necessary to help dislodge the fouling compounds from the membrane surface by reversing the transmembrane pressure to flow permeate back through the membrane. Additionally, cleaning agents may be used to degrade the foulant [72]. The simplest POU filtration systems utilize dead-end filtration methods, which may result in the membrane being discarded after it has reached its end of useful life. Therefore, when using nanomaterials for these systems, it is critical to select materials that are both environmentally sustainable and that can also degrade naturally in order to lessen their impact on the environment following disposal.

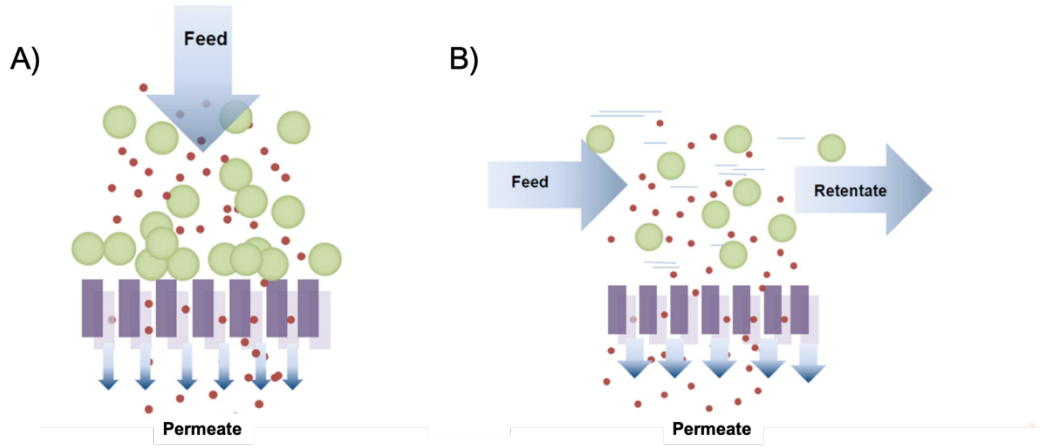

Figure 2.13: A) Dead-end membrane filtration setup and B) Cross-flow membrane filtration setup [69]

2.3 Material selection for wastewater treatment

Many materials can be used in the treatment of wastewater. However, to limit the negative environmental impact of the generation and eventual disposal of wastewater treatment materials, it is important to select materials that are both functional and sustainable. CNs meet both of these criteria as they are produced from renewable cellulosic sources and can undergo a plethora of modifications of their surface hydroxyl groups. This section will provide an overview on the properties and production of cellulose nanomaterials (CNs), including modification strategies that may be employed to enhance their functionality. This will be followed by a discussion of some approaches used to incorporate CNs into nanocomposite systems, such as organosilane/CNF aerogels, metal oxide coated CNs, CN hydrogels, and CN membranes. This section will also include examples of how these nanocomposites have been used in adsorbent, photocatalytic, and membrane filtration processes for treating wastewater.

2.3.1 Cellulose Nanomaterials

Biorenewable materials are gaining traction as replacements for petroleum-based materials due to their abundance and limited negative impact on the environment. These compounds include

cellulose nanomaterials and sodium alginate, among others. Cellulose nanomaterials (CNs) are inexpensive, abundant, biocompatible nanomaterials that have received increasing attention in recent decades. CNs can be classified into three categories: cellulose nanofibrils (CNF), cellulose nanocrystals (CNCs) and bacterial cellulose (BC). CNCs in particular are well known for their useful properties such as large surface area (~250 m^2/g) [73], high dispersibility and high elastic modulus (145 GPa) [74]. CNs can be derived from various sources of cellulose including wood pulp, cotton, tunicates and bacteria [75], [76]. CNCs and CNFs are produced using different processes: CNCs are produced when cellulose pulp fibres are subjected to chemical treatment, whereas CNFs are produced from either a purely mechanical treatment or a combination of mechanical and chemical treatments [77]. During these treatments an intermediary form a cellulose, microcrystalline cellulose (MCC), is formed, which has micro-scale dimensions (10 – 50 μm in diameter) [9]. With prolonged treatment, MCC will degrade into CNC or CNF. The main method for CNC production is acid hydrolysis, a process that disintegrates the amorphous regions of the cellulose fibres to yield nanoparticles with highly crystalline domains. The resulting crystalline nanoparticles (CNCs) are rod-like in shape with high aspect ratio, with lengths of 200 – 1000 nm and diameters of 5 – 15 nm, depending on the cellulose source [78]. The type of acid used in the hydrolysis step plays a crucial role in determining the surface chemistry of the CNCs. For example, sulfuric acid hydrolysis yields negatively charged sulfate half-ester groups on the surface, whereas hydrochloric acid only produces additional hydroxyl groups [79].

CNFs are produced by subjecting pulp fibres to mechanical processes, such as homogenization or grinding, which delaminate plant cell walls and separate out the nanofibrils. The main differences between CNCs and CNFs are their dimensions and crystallinity. CNFs consist of mixtures of amorphous and crystalline cellulose chains (60 – 95% crystalline) with lengths from 0.5 to 5 μm and diameters similar to those of CNCs. Additional chemical treatments

such as 2,2,6,6-tetramethyl-1-piperidinyloxy (TEMPO) oxidation or glycidyltrimethylammonium chloride (GTMAC) treatment may be used to decrease the mechanical energy required when processing the raw fibres to yield CNFs [80]. **Figure 2.14** illustrates the formation of CNCs and CNF from wood pulp fibres, while **Figure 2.15** shows the morphological differences between various CNCs, CNFs and pulp fibres.

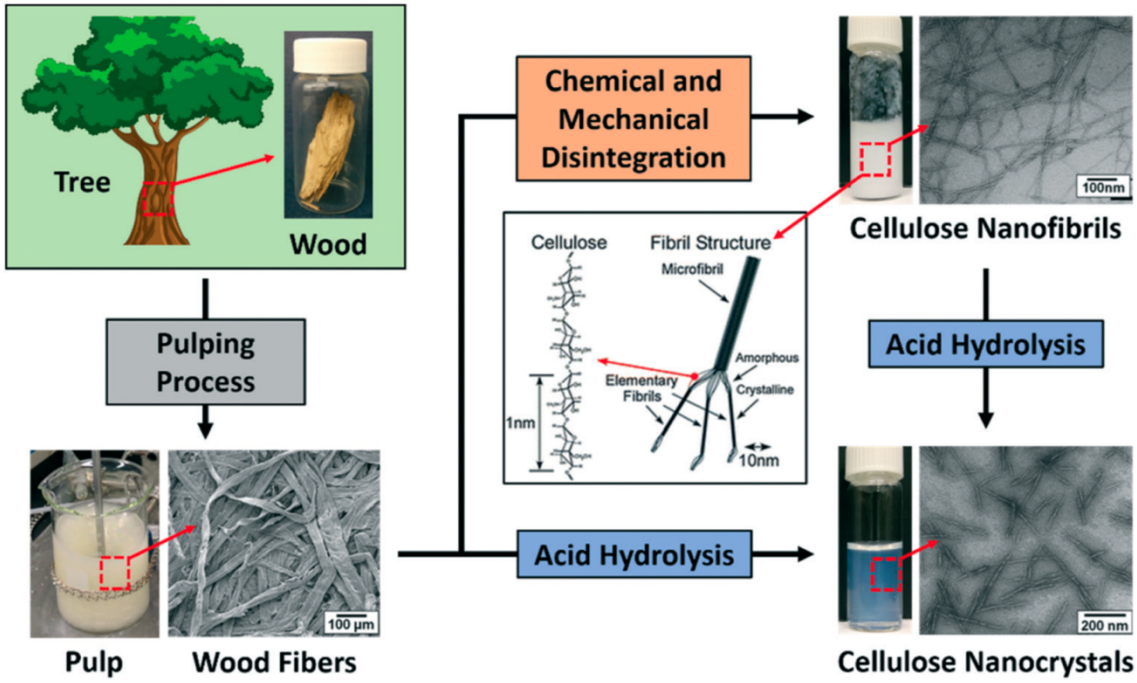

Figure 2.14: Formation of cellulose fibres from wood pulp, and subsequent production of CNFs and CNCs [81]

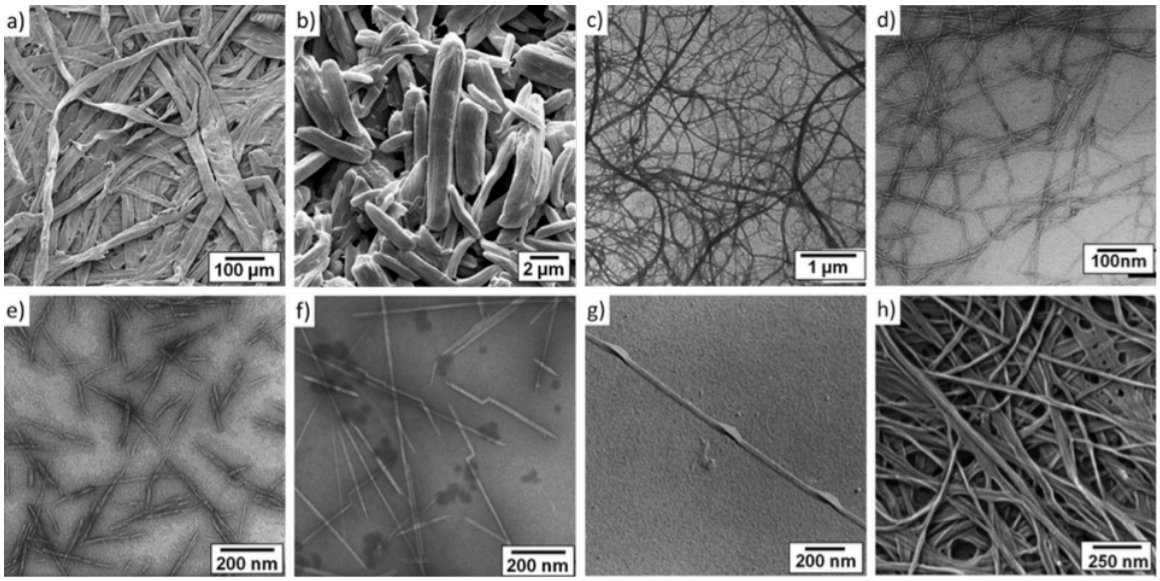

Figure 2.15: Scanning electron microscopy (SEM) and transmission electron microscopy (TEM) images of cellulose nanomaterials: (a) SEM micrograph of wood fibre, (b) SEM micrograph of MCC, (c) TEM micrograph of MCC (d) TEM micrograph of TEMPO-CNFs, (e) TEM micrograph of wood CNCs, (f) TEM micrograph of tunicate-CNCs, (g) TEM micrograph of algae CNCs (h) SEM micrograph of BCs [9]

2.3.2 Modification of Cellulose Nanomaterials

As described earlier, cellulose nanomaterials can be extensively modified due to the large amount of hydroxyl groups present on their surface. Such modifications include grafting small molecules to induce positive charge [82] or enhance negative charge [83] or grafting entire polymers onto the CN surface [84]. **Figure 2.16** illustrates 8 modification reactions that bestow functional groups on CNs through surface hydroxyl group substitution.

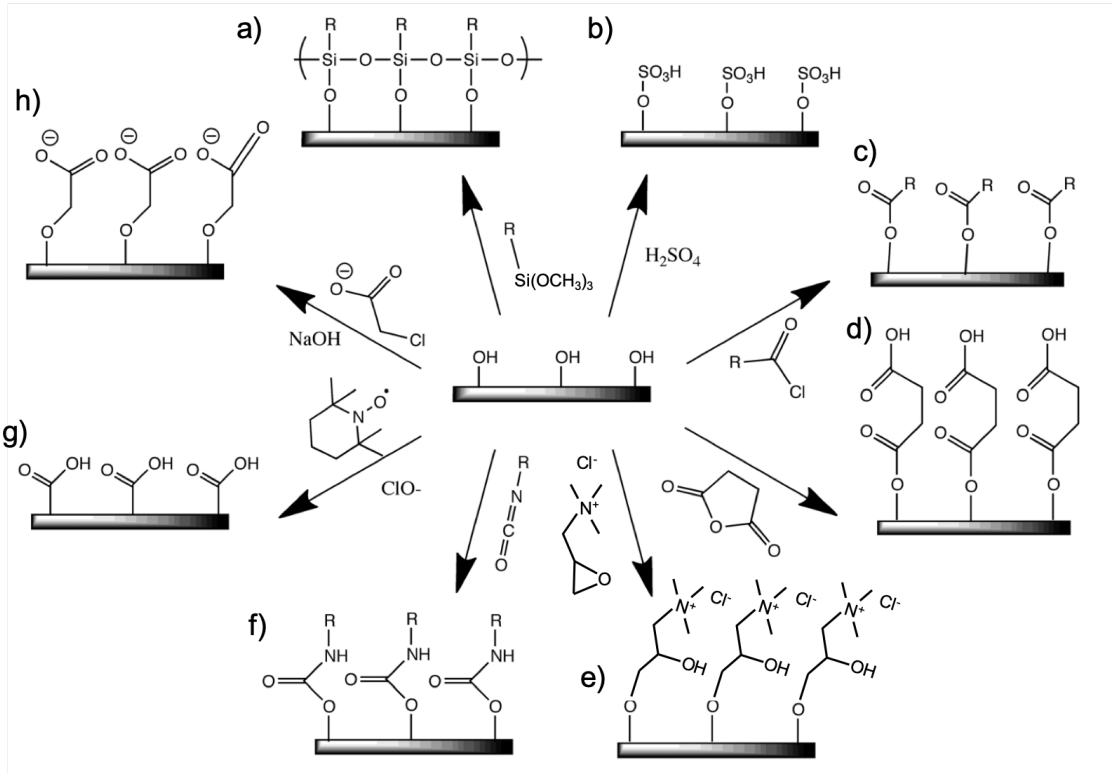

Figure 2.16: Strategies for modifying CNs, a) condensation of organosilane compounds to produce silylated surface, b) sulfuric acid treatment to form sulfate esters, c) using carboxylic acid halides for creating ester linkages, d) using acid anhydrides via ester linkage, e) using epoxide to produce an ether linkage (GTMAC), f) using isocyanates for creating urethane linkages, g) using TEMPO mediated oxidation to transform hydroxyls to carboxylic acids, and h) using halogenated acetic acid for creating carboxylmethyl groups (adapted from [9])

In addition to modification with small molecules, other modification strategies for CNs involve coating with larger compounds. These can include naturally derived compounds such as tannic acid (TA) or synthetic compounds such as melamine formaldehyde (MF). TA is a polyphenolic compound (**Figure 2.17a**) with many hydroxyl groups that can form networked structures through complexation with multivalent ions [85] or chemical cross-linking [86]. Cranston and coworkers reported the polymerization of TA on the surface of CNCs to render them hydrophobic [87]. TA was dispersed in water with CNCs and allowed to oxidize and oligomerize under slightly alkaline conditions, causing the TA to become insoluble and deposit onto the CNC surface. With their phenol groups converted to quinones due to the basic conditions, they could be modified with

decylamine via a Schiff-base reaction, resulting in the grafting of many hydrophobic groups on the CNCs.

MF is a common thermosetting material (**Figure 2.17b**) that has been explored as an adsorbent to remove heavy metal ions [88],[89] and various dye compounds [90] due to its porous structure and abundant amine groups. Shi *et al.* investigated the condensation of MF onto CNCs to produce templated nanoparticles with a high content of amine groups [91]. This was accomplished by mixing melamine and formaldehyde at low pH to form an MF precursor, to which CNCs and sodium hydroxide were added to induce the condensation of MF onto the CNC. This composite was later pyrolyzed to produce nitrogen-doped carbon nanorods for supercapacitors [92], but it also holds promise for use as an adsorbent for anionic compounds.

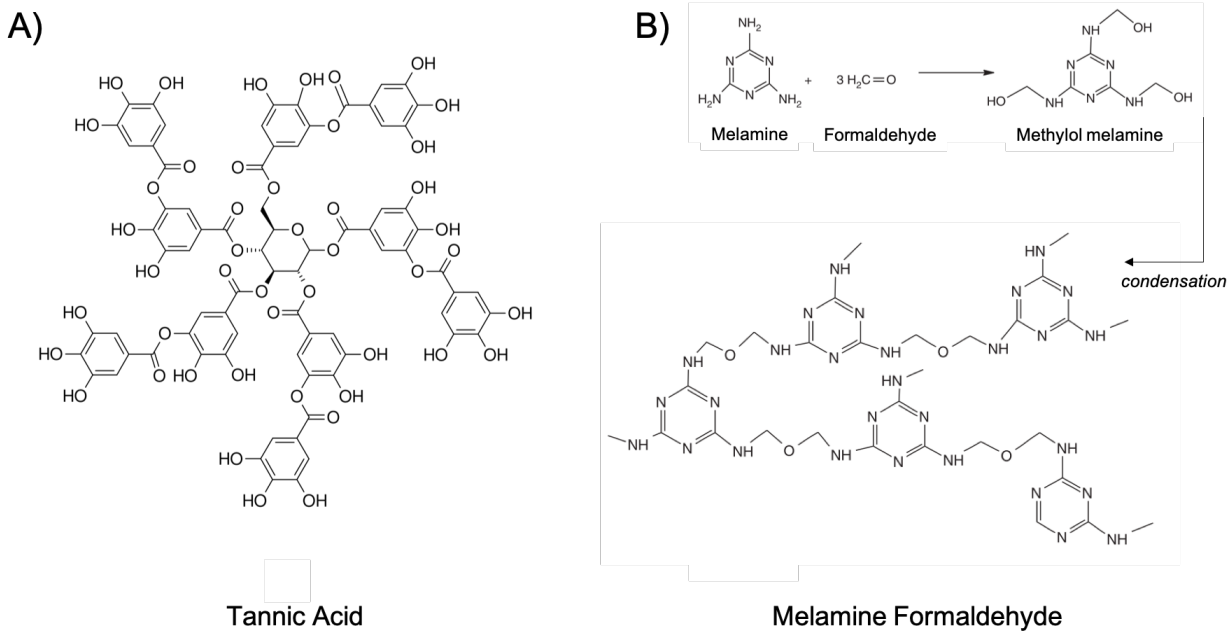

Figure 2.17: A) Chemical structure of tannic acid (TA) and B) formation of melamine formaldehyde (MF) [93]

In summary, CNs possess many desirable properties that make them ideal for wastewater

treatment applications. Their abundance of surface hydroxyl groups enables facile tuning of their surface chemistry. Coupled with their enormous surface area, this gives them enormous potential to be effective adsorbents. Their high aspect ratio, rod-like structure could also prove useful for templating semiconducting metal oxides on their surface, allowing them to act as high surface area photocatalysts. Lastly, with their combined tensile strength and surface functionalization potential, they have the ability to strengthen and improve the performance of membranes to reject various contaminants. The following sections will discuss in detail the preparation of CN nanocomposite materials that are tailored to wastewater treatment processes.

2.3.3 Cellulose nanomaterials for use as adsorbents

CNs can undergo an array of surface modifications that can enhance their effectiveness as adsorbents, allowing them to adsorb textile dyes, metal ions and even hydrophobic drugs. For example, He *et al.* [8] used carboxylated CNCs prepared using ammonium persulfate to adsorb MB dye. The adsorption was shown to follow the Langmuir isotherm, demonstrating a maximum adsorption capacity of 101.16 mg/g of CNC. CNCs have also been modified with maleic anhydride and used to adsorb other cationic dyes such as crystal violet, malachite green and basic fuchsin [94]. The addition of maleic anhydride increased the adsorption capacity of unmodified CNC up to 50% and the maximum adsorption capacity for crystal violet dye to 243.9 mg/g. CNCs have also been used to adsorb anionic dye contaminants, as demonstrated by Eyley & Thielemans [95]. In this work, CNCs were grafted with an imidazolium group to yield a positive surface charge. The positively charged CNCs were then applied to the adsorption of anionic Orange II dye, which exhibited a maximum adsorption capacity of 98.1 mg/g. CNF has demonstrated similar adsorption capabilities to remove both cationic [96] and anionic dyes [82].

CNs have also been widely studied for the capture and removal of heavy metal ions. Yu *et al.* [97] investigated the use of carboxylated CNCs modified by succinic anhydride and $NaHCO_3$

aqueous solution to remove heavy metal ions from water. These modified CNCs could achieve adsorption equilibrium within 5 minutes and maximum adsorption capacities for Pb^{2+} and Cd^{2+} ions of 465.1 and 344.8 mg/g, respectively. Carboxylated CNFs produced via TEMPO oxidation were prepared by Sehaqui *et al.* [98] and used to adsorb copper, zinc, chromium and nickel metal ions. The maximum adsorption capacities for the Cu^{2+}, Ni^{2+}, Zn^{2+}, and Cr^{3+} ions were reported to be 135, 49, 66 and 58 mg/g, respectively. In addition, Liu *et al*. [99] produced phosphorylated CNCs and CNFs via an enzymatic modification, which were able to adsorb Ag^{+}, Cu^{2+} and Fe^{3+} ions.

Although the above studies have demonstrated the effectiveness of CNs in removing contaminants such as organic dyes or heavy metal ions, it can be challenging to remove nanomaterials from the treated solution. Processes such as centrifugation can be used to separate the nanomaterials, but they can be costly and time-consuming. One promising alternative to free-floating CNs is to embed them within a hydrogel or aerogel so that the nanomaterials are immobilized and can easily be removed with a mesh filter.

2.3.4 Organosilane Aerogels

Since their synthesis in the 1930s, silica aerogels have continued to be of great interest due to their enormous specific surface area (500 – 1200 m^2/g), high porosity (up to 80 – 99.8%) and heat insulating abilities [100]. Silica aerogels are formed using organosilane compounds in a 3-step process (**Figure 2.18**): (1) preparation, (2) aging, and (3) drying of the gel [100]. One of the basic building blocks of these aerogels is tetramethoxysilane (TMOS) which contains a silicon atom bonded with 4 methoxy functional groups. The methoxy groups can readily undergo hydrolysis and subsequent condensation under controlled conditions to form networks. The sol-gel process can be described by the following three reactions [101]:

$$\equiv Si - OR + H_2O \leftrightarrow \equiv Si - OH + ROH \qquad (1)$$

$$\equiv Si - OR + HO - Si\equiv \leftrightarrow \equiv Si - O - Si\equiv + ROH \qquad (2)$$

$$\equiv Si - OH + HO - Si\equiv \leftrightarrow \equiv Si - O - Si\equiv + H_2O \qquad (3)$$

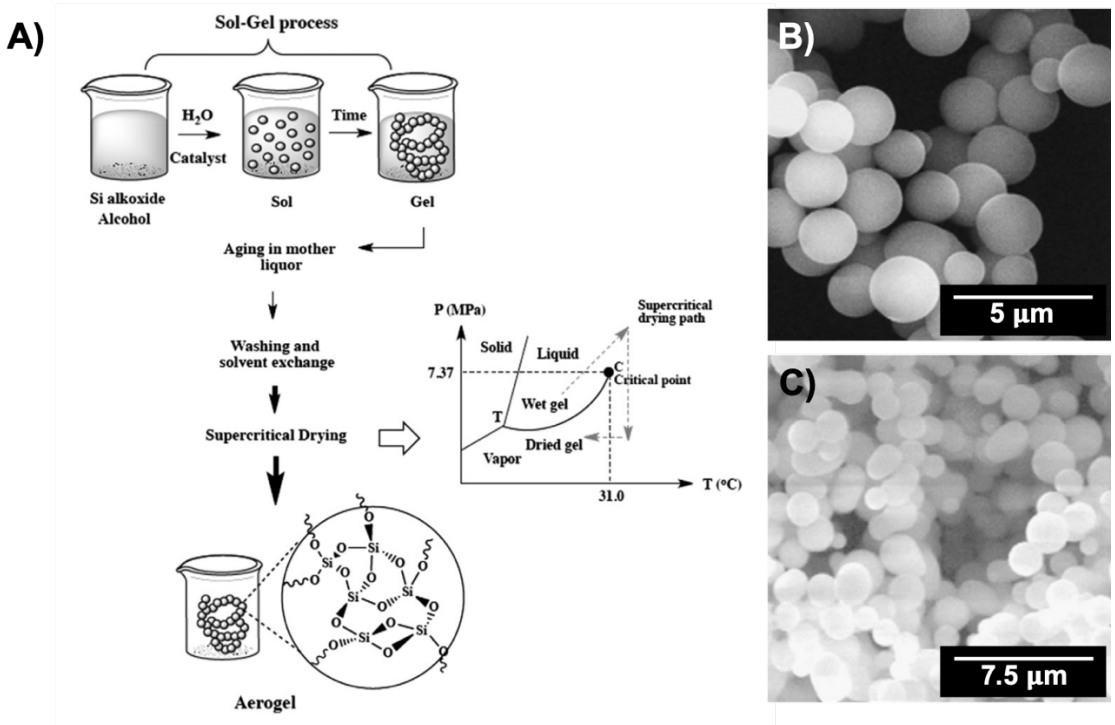

Figure 2.18: A) Steps of organosilica aerogel preparation showing the preparation, growth, aging, drying of the gel via supercritical drying and the final aerogel product [102], B) & C) SEM images of silica aerogel [100]

Although reaction (1) can occur simply in the presence of moisture, the addition of a mineral acid or base catalyst allows it to proceed more quickly. Condensation reactions (2) & (3) occur simultaneously with the first hydrolysis to form siloxane bonds. The rates of these reactions depend on the pH of the gel environment, type of acid or base catalyst used, whether the solution is aqueous- or organic-based and the type of functional groups on the organosilane compounds [101]. From **Fig 2.18a**, gel formation commences with the simultaneous growth of many silica nanoparticles that eventually coalesce to form a network structure (**Figure 2.18b & c).** The

reaction conditions also influences the final structure of the aerogel. Broadly speaking, acid-catalyzed condensation leads to lightly branched structures with many micropores, whereas basic conditions promote more cross-linking that reduces the amount of micropores and in turn generate larger pores [100]. A range of organosilane molecules can be used during the first step to modulate the strength of the gel as well as its functionality [102], as shown in **Figure 2.19**.

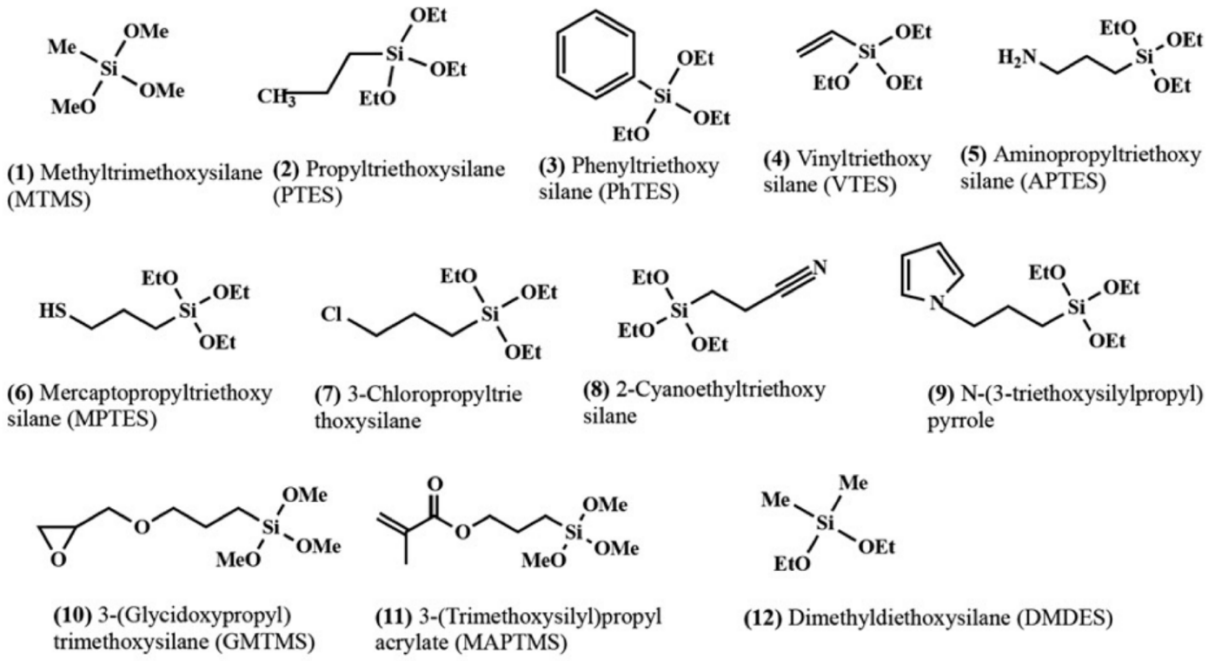

Figure 2.19: Structures of various organosilane monomers [102]

Following gel formation, aging is carried out to increase the strength of the gel through the growth of the silica particles at the expense of microporosity. This step is often conducted in alcohol/water mixtures at slightly basic pH, which can promote the dissolution (depolymerization) of silica. The dissolved silica then reprecipitates onto other colloidal silica particles (necking) or onto larger particles to increase their size (Ostwald ripening) [103]. Following aging, the aerogel is dried. Careful control of this process is critical as evaporation of water from the pores generates immense capillary forces that can crack and break the aerogel structure. The most common method to dry the aerogels is supercritical drying, which involves replacing the pore solvent with another

fluid (such as CO_2) and forcing the system to reach the critical point of the new fluid. Once the critical point is reached, the system is allowed to depressurize to ambient conditions and produce the final dry gel. This method of supercritical drying allows the aerogel to retain a hydrophilic surface containing hydroxyl groups from the initial hydrolysis reactions [100]. Another method of drying is ambient pressure drying, which involves replacing the internal water/alcohol pore fluid with another fluid that does not interact strongly with the aerogel. This minimizes the capillary forces during the evaporation of the solvent and leaves the aerogel intact. This method works best with aerogels with fully condensed silane groups that yield few surface -OH groups that will strongly interact with water [104].

To avoid the brittleness associated with the use of pure TMOS aerogels, modifications can be made to the process, including the use of bridged organosilanes (containing carbon-carbon spacers between functional organosilane ends) [102][105] or by condensing organsilanes onto a porous 3-D scaffold [106]. This second strategy has been used on both cellulose and nanocellulose fibres, which can easily cross-link with organosilanes due to their abundant surface hydroxyl groups.

2.3.5 Cellulose/Nanocellulose Organosilane nanocomposite aerogels

CNF aerogels can be readily formed by freezing CNF suspensions and using freeze drying or supercritical drying to remove the pore fluid [107]. Mixing CNF and organosilanes has opened up new ways to produce CNF aerogels since the incorporation of organosilanes can strengthen the gel and decrease the processing sensitivity of the resulting nanocomposite. Organosilanes can be mixed into a suspension of cellulose or nanocellulose and condensed on the fibre surface, after which the system undergoes freezing and freeze drying to remove the pore fluid [108],[109] without disrupting the aerogel structure. This process is considered advantageous over supercritical drying [100] and has opened up opportunities for the formation of functional

cellulose-silica structures for use in oil/water separation and catalysis. The preparation of cellulose-silica aerogels involves several major steps. First, organosilane molecules are added to a suspension of cellulose or CNF (usually 0.6 – 1.2 wt%), and the pH of the mixture is adjusted to 4 using an acid. This solution is mixed to allow the organosilanes to condense onto the cellulose surface (**Figure 2.20**). This is followed by a freezing step. Often, fast, directional freezing is used, which results in the formation of long ice crystals that will help develop a pore structure along one axis and aggregate the cellulose fibres into sheets that form strong pore walls [107]. Then, the water is usually removed by sublimation and the gel is subsequently cured at high temperature to strengthen the composite. Ambient pressure drying has also been shown to work by exchanging water with a low surface tension solvent such as acetone [107].

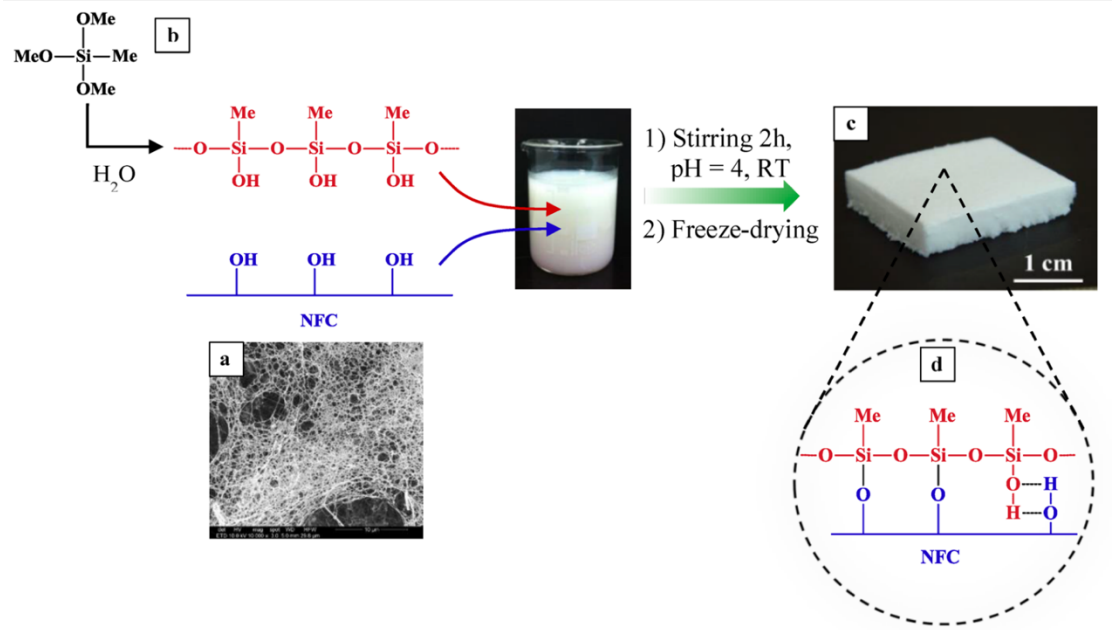

Figure 2.20: Formation of CNF-silica composite aerogel, a) SEM of CNF fibres, b) condensation of MTMS in presence of CNF, c) photograph of dried aerogel, d) chemical structure of MTMS/CNF aerogel. Reprinted (adapted) with permission from [108], Copyright 2014 American Chemical Society.

Exploiting their inherent hydrophobicity, Zhang *et al.* used methyltrimethoxysilane (MTMS)-modified CNF aerogels for oil and organic solvent absorption [108]. These researchers found that cylindrical aerogels of this type with 38 wt% MTMS could recover 96% of their original height following 50% uniaxial compression. They were also able to recover several types of oil and organic solvents from water/oil and water/solvent mixtures, exhibiting an absorption capacity of 102 g solvent/g aerogel when used to absorb chloroform. Wu *et al.* used vinyltrimethoxysilane (VTMOS) CNF aerogels to separate oil/water mixtures [110]. Following formation of the VTMOS-CNF aerogel, 3-mercaptopropionic acid was added in the presence of a radical initiator to conduct a thiol-ene click reaction to enhance the hydrophilicity of the aerogel surface. When used in a filtration system, the aerogel could effectively reject the oil phase in both oil/water mixtures and oil in water emulsions. The oil rejection ratio was as high at 100% for oil/water mixtures even after 10 cycles and as high as 95% for oil-in-water emulsions after 10 cycles. To improve this, Li *et al.* prepared a 3-glycidoxypropyltrimethoxysilane (GPTMS) CNF aerogel grafted with pH-responsive poly 2-(dimethylamino) ethyl methacrylate (DMAEMA) for pH-switchable water/oil separation (**Figure 2.21**) [111]. The gel was strengthened through a combination of GPTMS and polyethyleneimine (PEI) cross-linking (**Figure 2.21c**). Also, the amine groups of PEI were modified with α-bromoisobutyryl bromide for surface-initiated atom transfer radical polymerization of DMAEMA within the pores of the aerogel. The PDMAEMA polymer could be protonated by bubbling CO_2 into the gel for 15 minutes to make its surface more hydrophilic. (**Figure 2.21a)**. By bubbling N_2 through the gel to displace the CO_2, the PDMAEMA polymer deprotonated and collapsed into hydrophobic globules, rendering the aerogel hydrophobic (**Figure 2.21b**). When used as a filter, the stimuli-responsive aerogel allowed the selective passage of either water or oil depending on the protonation state when an oil/water mixture was passed

through the filter (**Figure 2.21d**). The system is capable of treating surfactant stabilized water/oil emulsions, with separation efficiencies of 99.6%.

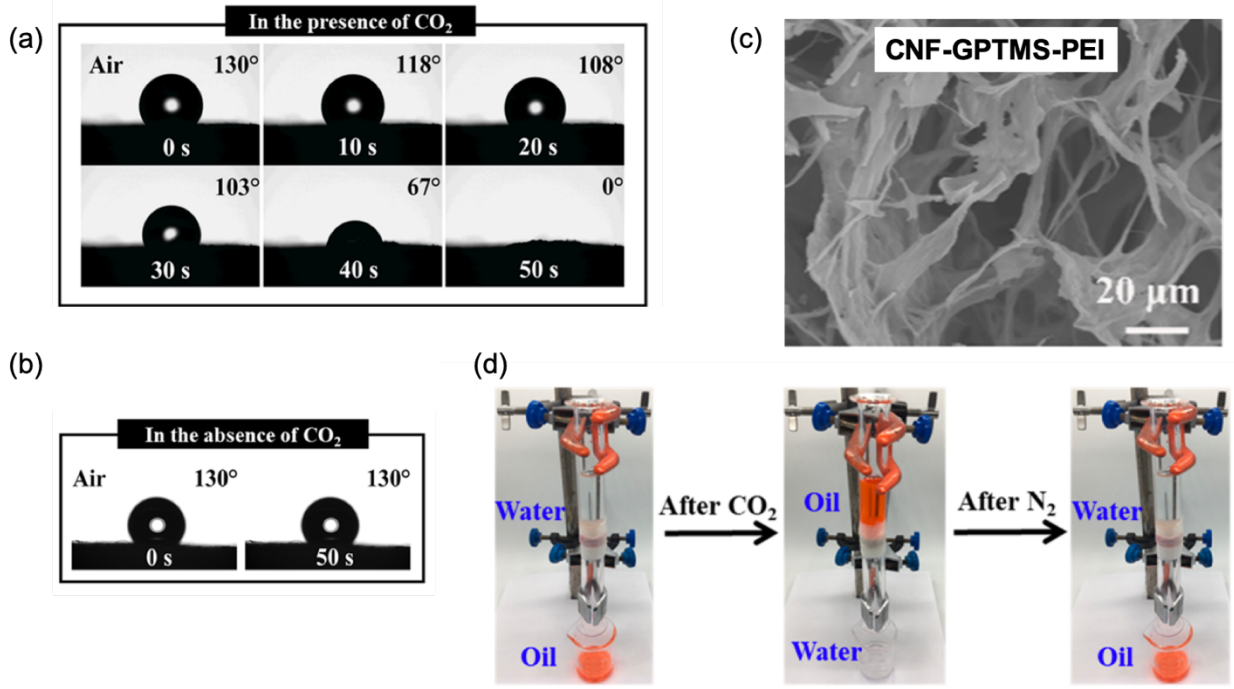

Figure 2.21: Water droplet contact angle measurements of aerogel a) under acidic conditions, b) under basic conditions, and c) photographs of CO_2 responsive aerogel separating oil/water mixtures and oil in water emulsions. Reprinted (adapted) with permission from [111]. Copyright 2019 American Chemical Society.

To produce catalytic cellulose-silane systems, Zhang *et al.* used 3-mercaptopropyltrimethoxysilane (MPTMS) CNF aerogels that could capture copper ions and subsequently carry out regioselective hydroboration of alkyne molecules [12]. Following the formation of the MPTMS-CNF aerogels, the material was contacted with a $CuSO_4$ solution to allow which Cu^{2+} ions to complex with the thiol groups on the aerogel surface and effectively become immobilized. This in turn allowed the aerogel to catalyze the hydroboration of alkynes in ethanol, achieving a 99% conversion rate in the presence of a Cs_2CO_3 base. This CNF-MPTMS aerogel holds great promise for application in wastewater treatment due to its ability to adsorb

heavy metal ions via chelation. The research group also investigated the use of the CNF-MPTMS aerogel in removing Hg^{2+} ions from wastewater [13]. The thiol groups on the aerogel surface showed remarkable selectivity for Hg^{2+} compared to other divalent cations such as Mg^{2+}, Ni^{2+}, Zn^{2+}, and Mn^{2+}. Additionally, batch experiments modeled using the Langmuir isotherm revealed a theoretical maximum adsorption capacity of 700 mg Hg^{2+}/g aerogel.

2.3.6 Polymeric hydrogel adsorbents

In addition to forming aerogels, another strategy for utilizing nanoparticles as adsorbents includes incorporating them into hydrogel beads. By definition, hydrogels are water-swollen polymer networks held together by physical cross-links or covalent bonds [112]. Depending on the polymer, type of cross-linking and degree of cross-linking, hydrogels can be rigid and tough materials or soft and stretchable. Sodium alginate is a water-soluble polysaccharide commonly derived from brown seaweed, consisting of repeating mannuronate (M) and guluronate (G) units [113]. This polymer can easily form a network when a divalent cation such as Ca^{2+} is introduced through ionotropic gelation, by adding alginate dropwise into a bath of Ca^{2+} (**Figure 2.22a**). Divalent cations can coordinate with the repeating G units in the alginate chains and bridge adjacent alginate polymers to form an egg-box structure, resulting in a physically cross-linked system [114]. The degree of cross-linking will depend on the M/G ratio of the alginate chain, yielding more loosely or tightly cross-linked calcium alginate hydrogels (**Figure 2.22b**).

Due to the ease of formation of calcium alginate hydrogels as well as the large abundance of available carboxylate groups, these hydrogels have been investigated as adsorbents for various waterborne contaminants. In one study, Aravindhan *et al.* used calcium alginate beads to remove basic black dye from water [25] and reported a maximum adsorption capacity of 78 mg/g at 30^{o}C. Additional experiments by Papageorgiou *et al.* investigated the capacity of calcium alginate beads to remove Cd^{2+}, Cu^{2+} and Pb^{2+} from aqueous solution [115]. They observed that alginates with

higher M/G ratios had higher capacities to remove the three metal ions. Using a mass transfer model similar to Eqs. (2.4) to (2.10) they determined D_p values ranging from 3.0×10^{-10} m^2/s to 8.3×10^{-10} m^2/s for the ions. By fitting batch adsorption data to the Langmuir isotherm, they determined maximum adsorption capacities for Cd^{2+}, Cu^{2+} and Pb^{2+} of 1.16, 1.40 and 1.81 mmol/g, respectively. The adsorption performance of calcium alginate hydrogels can be further enhanced by mixing various types of nanoparticles with a suspension of alginate before the ionotropic gelation step. In some instances, this step has been shown to improve the mechanical properties as well [27],[14].

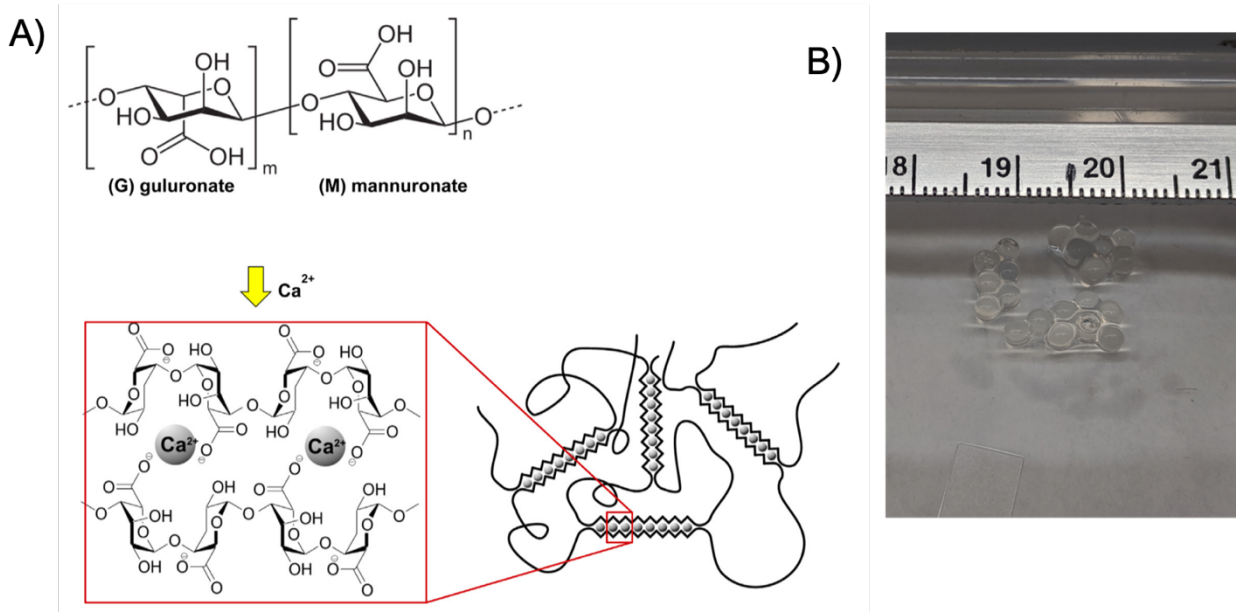

Figure 2.22: A) Formation of alginate hydrogel beads via iontropic gelation [113] B) Photograph of cross-linked calcium alginate hydrogel beads

2.3.7 Cellulose nanomaterial hydrogel nanocomposites

The use of CNs, especially in calcium alginate hydrogels, is a well-established practice to produce easily recoverable adsorbents in wastewater treatment operations [14],[116]. CNCs can be readily incorporated into the hydrogel matrix by physically mixing them with the starting polymer prior to iontropic gelation. This encapsulation of CNCs within hydrogels provides a

simple method to separate the nanoparticles from treated wastewater. One of the first of these nanocomposites used sodium alginate and cellulose nanocrystals to form hydrogel beads to remove methylene blue dye from water [14]. In this study, beads were composed of 0.5 wt% alginate and 1 wt% CNCs, and could adsorb methylene blue dye up to a maximum of 256 mg/g. Adsorption during batch studies was shown to follow pseudo-second order kinetics. The adsorbent could be regenerated using an ethanol-hydrochloric acid mixture and reused up to 5 times while maintaining 95% of its original adsorption capacity. Hu *et al.* utilized carboxylated CNCs incorporated into alginate hydrogels to remove Pb^{2+} ions from water [117]. Carboxylated CNCs were prepared from microcrystalline cellulose through reactions with ammonium persulfate and citric acid. After being formed into alginate beads with ionotropic gelation, the adsorbent was able to remove Pb^{2+} up to a maximum of 339 mg/g.

In addition to alginate, chitosan has been used to fabricate CNC nanocomposites to remove contaminants from water. For example, van de Ven and coworkers developed a porous chitosan-CNC aerogel for removing methylene blue [118]. A carboxymethylated form of chitosan and dialdehyde CNC was able to form a highly cross-linked network through Schiff-base reaction. A porous structure was obtained by ice templating that could remove up to 785 mg MB per gram aerogel. Another approach reported by Zhou *et al.* was to mix CNCs into a partially hydrolyzed polyacrylamide (HPAM) hydrogel (**Figure 2.23**) [119]. Hydrogels were prepared by combining solutions of CNC and HPAM, casting them into a plastic mold and cross-linking the mixture at 80^{o}C to promote esterification between the HPAM matrix and CNCs. The authors demonstrated that CNCs could be incorporated in amounts up to 20 wt% of the hydrogel mass (dry weight) to yield a gel that could achieve maximum adsorption capacities of 326 mg/g MB. Finally, Zhao *et al.* produced a nanocomposite of carboxylated CNCs and polyethyleneimine (PEI) to recover rare earth elements (REEs) from water [120]. They reacted carboxylated CNCs with PEI via peptidic

coupling to produce a highly cross-linked structure that also contained large amounts of NH_2 and NH groups to chelate REEs. Batch adsorption experiments indicated maximum adsorption capacities for La^{3+}, Eu^{3+} and Er^{3+} of 0.611, 0.670 and 0.719 mmol/g, respectively. Ternary batch experiments showed the composite had the greatest selectivity for Er^{3+} and demonstrated that over 95% of the adsorbed ions could be effectively released by regenerating the adsorbent with 0.1 M HNO_3.

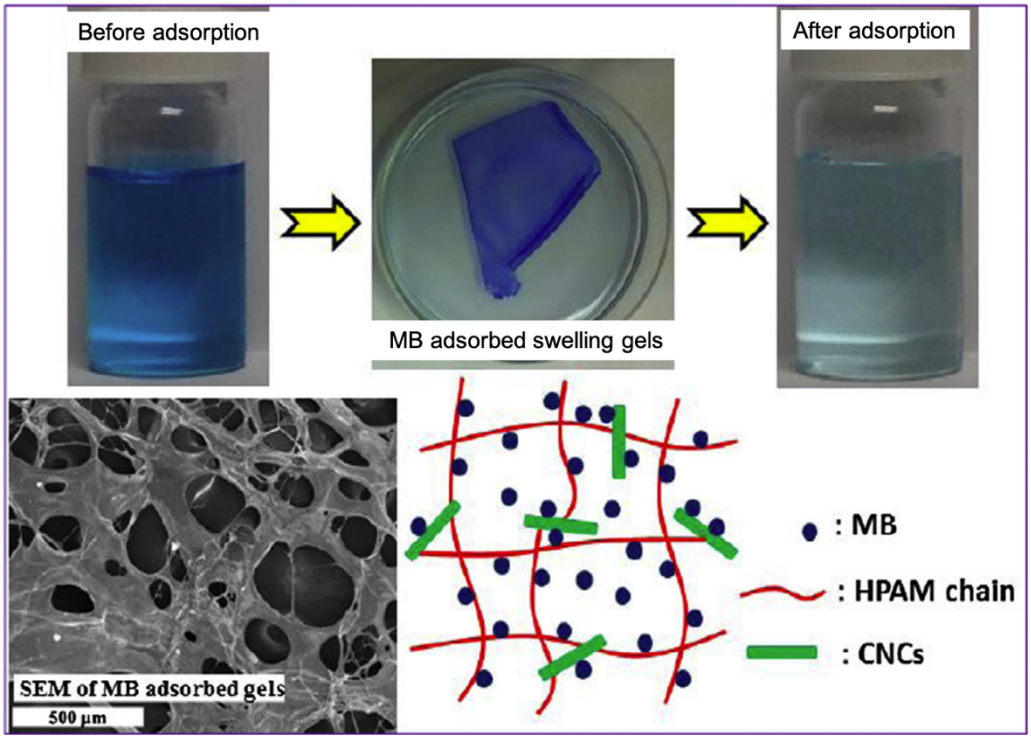

Figure 2.23: HPAM-CNC composite hydrogel for removing MB dye [119]

2.3.8 Metal oxide semiconductor photocatalysts

As mentioned previously, photocatalysis is an excellent method to purify wastewater streams contaminated by organic molecules. When it comes to heterogenous photocatalysts, the most widely characterized systems involve metal oxide semiconductors such as TiO_2 [44]. This material possesses a wide band gap that can adsorb UV light (3.0 – 3.2 eV) and is able both to oxidize water to form •OH and reduce adsorbed oxygen to superoxide. However, TiO_2 is limited

in that it requires a UV source to operate at peak performance. To address this, semiconductor systems based on TiO_2 and ZnO are often enhanced using another material to form a heterojunction that can facilitate more efficient charge separation of photogenerated holes and electrons and ultimately improve light absorption [121]. Wang *et al.* produced a WO_3/TiO_2 heterojunction, which consisted of a WO_3 nanorod with TiO_2 grown on the surface [121]. This photocatalyst demonstrated enhanced rhodamine B degradation under visible light when compared to pure WO_3 or TiO_2 due to more efficient generation of •OH due to better charge separation (**Figure 2.24a**). Another method to excite photocatalysts using visible light involves anchoring metallic nanoparticles to a semiconducting material and exploiting surface plasmon resonance of nanoparticles to achieve charge transfer into the semiconductor [122]. This has been achieved with composites of an Fe electron donor, with AuNP that can inject an electron into the conducting band of TiO_2 following exposure to light. This system was able to reduce oxygen and oxidize both ethanol and methanol (**Figure 2.24b & c)** [123].

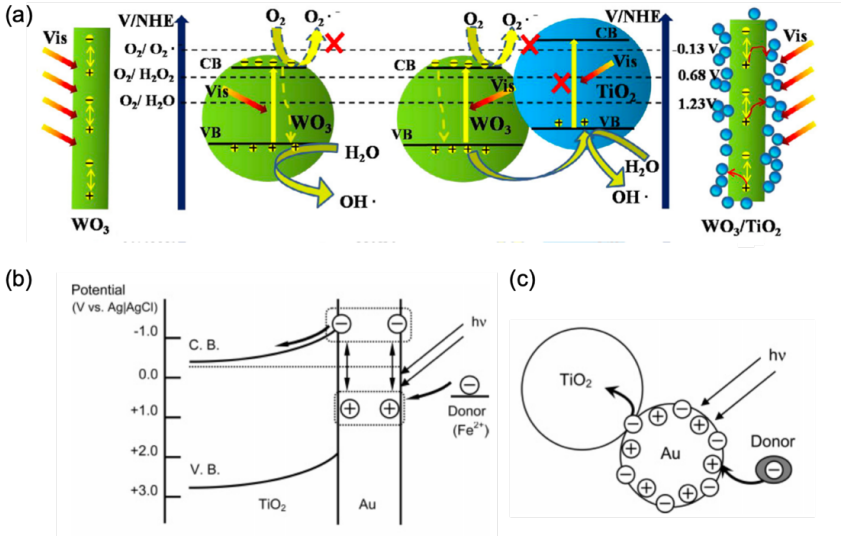

Figure 2.24: a) Band gap diagram of WO_3 and WO_3/TiO_2 heterojunction [121], b) Band diagram showing process of charge transfer from AuNP excited by plasmon resonance to CB of TiO_2, c) Schematic of same charge transfer process. Reprinted (adapted) with permission from [123]. Copyright 2005 American Chemical Society.

In addition to these techniques for improving photocatalytic activity, further studies have been reported on other metal oxide semiconductors with smaller band gaps, such as bismuth oxyhalides. Bismuth oxyhalides are ternary compounds consisting of elements from the V-VI-VII families, which possesses a tetragonal matlockite crystal structure that consists of Bi_2O_2 layers interleaved by double halogen layers (**Figure 2.25a**) [124],[125]. This layered structure of anionic halogens and positive BiO^+ slabs establishes an internal static electric field perpendicular to the layers forms, which facilitates charge separation of electron-hole pairs and ultimately extends their lifetime and allows them to participate in surface reactions [126]. The electronic properties of BiOX compounds can be tweaked by using different halides – for example, the band gaps of BiOCl, BiOBr and BiOI have been determined to be 3.3-3.22, 2.7-2.64 and 1.8-1.77 eV, respectively (**Figure 2.25b**) [127],[128]. These band gap values suggest that both BiOBr and BiOI can be excited by visible light. These compounds have also been used in various heterojunction systems to improve their photocatalytic ability in the visible light range by forming combinations such as BiOBr/BHO [129], Bi/BiOBr [130], BiOCl/BiOBr [131], and BiOI/BiOBr [48]. In addition, these photocatalysts have shown great promise in degrading a variety of water-borne contaminants such as toluene[132], MB dye [131], MO dye [48] and RhB dye [125],[133]. The physical structure of BiOX photocatalysts can also be modulated during synthesis to form nanoparticles, nanoplates, solid microspheres or hollow nanoflowers [125],[134]. An ideal photocatalyst for wastewater treatment would be a superstructure consisting of many nano-sized subunits, which has enormous surface area but are large enough to facilitate easy separation from the treatment media [126]. An effective method to realize this structured material is to form the BiOX on a nanoparticle template, such as CNC. This metal particle templating strategy has already been accomplished with CNCs and other metal oxides [135].

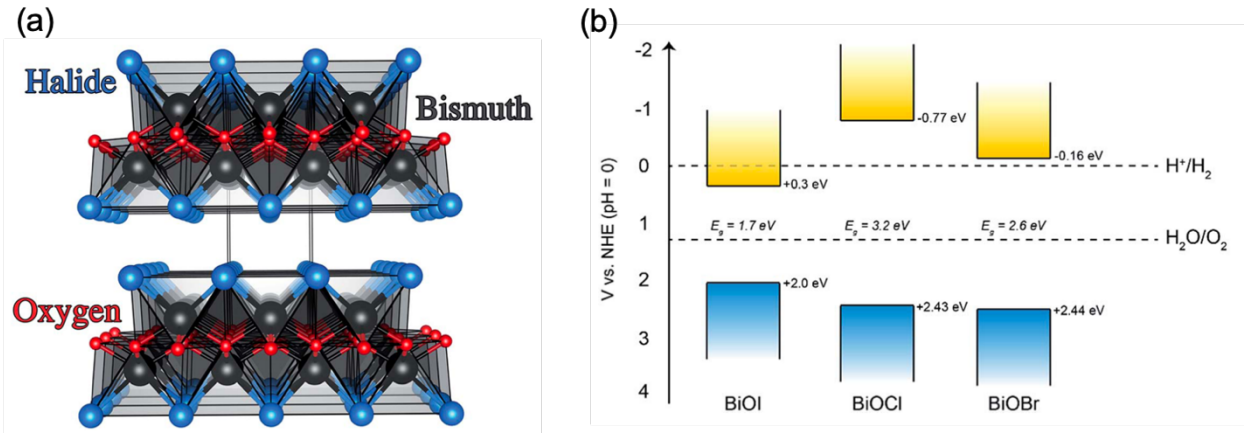

Figure 2.25: a) Layered structure of BiOX metal oxides b) Band structure of BiOI, BiOCl and BiOBr metal oxides [127]. Published by the Royal Society of Chemistry

2.3.9 Cellulose nanomaterial/metal oxide hybrids

CNCs have been used as scaffolds in templating metal oxides for application in conductive systems as well as photocatalysis. Liu *et al.*, for example, coated Fe_3O_4 on CNCs through a coprecipitation method, which could be applied in the production of conductive paper [136]. By mixing $FeCl_2$ and $FeCl_3$ with a suspension of CNC in ammonia at pH 10, the authors obtained Fe_3O_4 nanoparticles coated on CNC, which had better dispersibility in aqueous media when compared to pure Fe_3O_4 nanoparticles. When the metal oxide CNC composite was incorporated into paper at a concentration of 14.75 g/m^2, a conductivity of 0.0269 S/m was achieved.

In another study, Liu *et al.* produced a CNC/TiO_2 nanocomposite to degrade MO dye [6]. TiO_2 nanoparticles were attached to the surface of CNCs in a manner similar to that used to produce CNC-organosilica composites. CNCs were mixed with titanium(IV) ethoxide in ethanol to promote the hydrolysis of the titanium precursor and subsequent condensation of Ti with the hydroxyl groups on the CNC surface. This resulted in TiO_2 with a highly anatase structure. The nanocomposite could effectively decompose MO under UV light and showed better stability against photo-corrosion in contrast to pure TiO_2 anatase nanoparticles. ZnO/CNC nanocomposites

have also been produced for MB dye degradation [135]. In one study, Yu *et al.* mixed citric acid modified CNCs with $Zn(NO_3)_2$ and allowed Zn^{2+} to coordinate with surface carboxylic acid groups. NaOH was then added to precipitate the Zn^{2+} as $Zn(OH)_2$, which was converted to ZnO through drying at 120°C. In addition to showing antimicrobial properties, the CNC-ZnO was able to degrade 93% of a 16 mg/L MB solution within 100 minutes. The authors were able to tune the size of ZnO nanoparticles on CNC surface by changing the ratio of $Zn(NO_3)_2$ used in the synthesis (**Figure 2.26**). A mass ratio of $Zn(NO_3)_2 \cdot 6H_2O$:CNC of 1:2 showed the best results for photocatalysis and antimicrobial tests. Finally, Yang *et al*. used bacterial cellulose as a template for CdS to degrade MO dye [137]. BCs were suspended in ethanol, mixed with $CdCl_2$ and thiourea and autoclaved at 180°C to allow CdS crystals to grow on the BC surface. The BC/CdS nanocomposite showed markedly improved photocatalytic activity for MO degradation compared to pure CdS prepared via a hydrothermal method and could be reused up to 5 cycles with only a 5 % decrease in effectiveness.

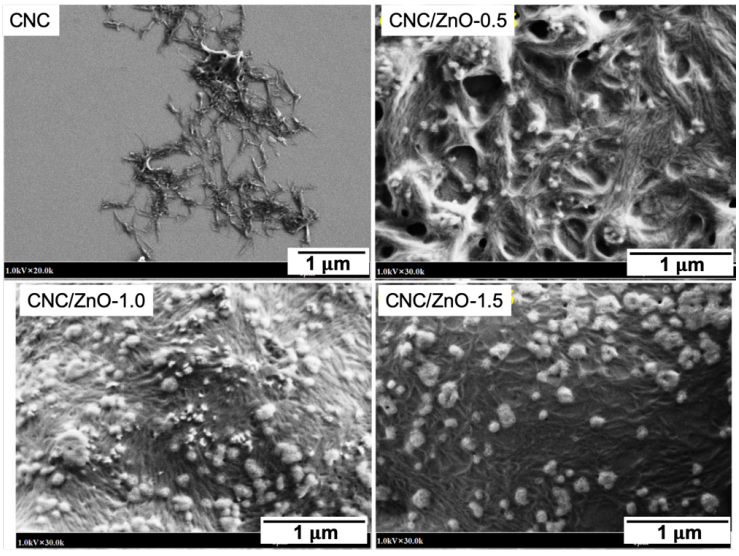

Figure 2.26: SEM images of unmodified CNCs and CNCs/ZnO hybrids prepared with CNC:ZnO mass ratios of 1:0.5, 1:1, and 1:1.5 [135]

2.3.10 Cellulose nanomaterial membrane nanocomposites

As discussed previously, nanomaterials may be used in membranes to enhance mechanical properties and to improve selectivity to the membrane via size exclusion and other approaches. CNs have been used in membranes as well, as the active top layer in thin film nanocomposites and applied on top of a substrate by simple dip coating [138] or by casting a suspension onto the substrate [58],[61],[139],[140]. Karim *et al.* dip-coated a CNF membrane into a CNC suspension for application in the treatment of mirror industry effluent [138]. The addition of CNCs increased the tensile strength of the membrane compared to that of an unmodified CNF membrane. The membrane also was able to effectively reject Ag^{+}, Cu^{2+}, and Fe^{2+}/Fe^{3+} ions from the incoming solution via adsorption and micro-precipitation onto the CNCs. Hsiao and coworkers formed UF membranes by casting a CNF suspension on top of a polyacrylamide (PAN) mid-layer supported on a polyethylene terephthalate woven substrate [58]. The maximum pore size of this membrane was 55 nm, so that it could effectively reject 0.1 μm latex microspheres and achieve both higher rejection ratios and a 5-fold greater permeate flux compared to that of commercial PAN10 UF membranes while filtering the same feed solution.

CNs may also be used to form membranes via two approaches: (1) filtering CNs onto a porous substrate and using an additive to cross-link them [63],[141] and (2) physically entangling the nanofibres, analogous to a paper-making process [142],[143],[144]. However, these methods may require additional processing in order to increase the porosity of the obtained membrane to enable its use for effective water filtration. In one instance, Karim *et al.* embedded CNCs in chitosan membranes crosslinked with glutaraldehyde to remove the cationic dyes Victoria blue 2B, rhodamine 6G and methyl violet 2B [63]. The authors attributed the high dye removal (up to 98% of methyl violet) to the presence of negatively charged CNCs. However, it is worth noting that the membrane was only evaluated under batch adsorption conditions and would require further testing

in a dead-end or cross-flow filtration setup for proper assessment. Quellmalz *et al*. developed CNF membranes cross-linked with citric acid for nanofiltration applications [141]. This method drastically improved the wet strength of the membrane while only increasing the average pore size from 11 to 15 nm so that the cross-linked membrane was able to efficiently remove 20 nm AuNPs (**Figure 2.27**). For membranes prepared via a paper making processes, Mautner *et al.* used a 0.3 wt% CNF suspension with $AlCl_3$ to form a filter cake via vacuum filtration, followed by hot pressing to form a membrane [142]. The addition of 1 mM Al^{3+} effectively cross-linked the CNF in the filter cake. The resulting membrane could reject polystyrene and polyethylene glycol polymers with molecular weights of 3.2 and 6 kDa, respectively. The same group of researchers also produced CNFs from fibre sludge using phosphoric acid to form membranes capable of rejecting copper ions [144]. The CNFs were decorated with phosphate groups that allowed them to reject copper ions via adsorption. Furthermore, the filter suffered only a 6% reduction in adsorption performance when competing Ca^{2+} ions were added to the feed. In addition, the membrane could be effectively regenerated using phosphoric acid and lost only 1% of its adsorption capacity following regeneration. Orsolini *et al.* prepared porous membranes by mixing CNFs with various nanosized calcium compounds (such as calcium hydroxide and calcium carbonate) as spacers. A filter cake was formed via vacuum filtration and then washed with HCl to remove the calcium compounds [143]. The calcium-templated CNF filter was found to have 2-3 times the permeability of pure CNF membranes prepared via a paper-making process, and could reject small solid particles when used to concentrate orange juice. This material showed significant promise as a microfiltration membrane.

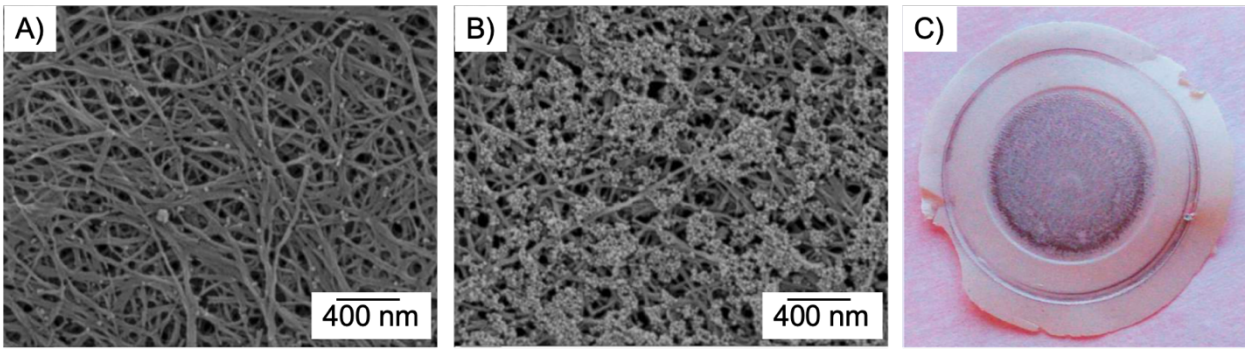

Figure 2.27: SEM images of A) unmodified CNF and B) cross-linked CNF following filtration of tracer nanoparticles C) Photograph of cross-linked CNF membrane following filtration of 26 nm AuNPs. Reprinted (adapted) with permission from [141]. Copyright 2015 American Chemical Society.

2.4 Summary

In closing, an overview of the use of CNs for wastewater treatment processes has been presented. These included a summary of the principles of adsorption, photocatalytic and membrane filtration operations, their operation in both batch and continuous modes as well as the introduction of nanomaterials to enhance their functions. This chapter also provides an in-depth review on cellulose nanomaterials, including their preparation, properties and their functionalization. It further investigated strategies where CNs can be utilized alone, in organosilane aerogels, metal oxide nanocomposites, polymeric hydrogels and membrane filters for wastewater treatment operations.

Cellulose nanomaterials have great potential to enhance wastewater treatment processes. Their nanosize dimensions make them suitable adsorbents, although they are difficult to recover from treated wastewater when used alone. Therefore, new adsorbents must be developed by embedding CNs in porous nanomaterials (CNC-ALG hydrogel beads) or by utilizing them in conjunction with other molecules to form porous scaffolds capable of functionalization (CNF-organosilica aerogels). Furthermore, they have only been used as adsorbents in batch processes

and not yet in fixed bed systems with continuous flow of wastewater, which is the main mode of remediating wastewater via adsorption. Thus, complete studies using fixed bed should be conducted with adsorbents consisting of CNC-ALG beads.

In addition, photocatalysts are promising materials for wastewater treatment processes, with new advancements into new metal oxides, such as BiOX. BiOX photocatalysts have great potential for wastewater treatment due to efficient charge separation and photocorrosion resistance [124]. However, as yet, no studies on the templating them on CNs to produce functional catalysts have been reported. Thus, we plan to use CNCs to prepare a CNC-BiOBr photocatalyst that is both nanosized and can be activated by visible light, with the added benefit of being immobilized within calcium alginate hydrogels for efficient recovery.

Finally, point of use membranes would be efficient in providing clean water in remote areas where electricity is not available. Their effectiveness can be enhanced by adding functionalized nanoparticles with surface charge to remove certain contaminants. Melamine formaldehyde CNCs have shown great promise as adsorbents for anionic contaminants and can reinforce the mechanical properties of cellulose fibre networks, similar to polycations in a paper-making processes. Thus, we will prepare cellulose fibre melamine-formaldehyde cellulose nanocrystals composite membranes to purify wastewater streams containing anionic dyes in a dead-end filtration setup.

Using these functionalization strategies, we will aim to develop CN-based materials that adsorb contaminants in batch and fixed bed column systems, degrade contaminants in batch photocatalytic experiments, and capture contaminants in dead-end filtration processes. The goal of this research will be to demonstrate the potential of CNs for the next generation of sustainable methods for the removal of contaminants in our water bodies.

Chapter 3: Thiol-ene Click Modified Cellulose Nanofibril Organosilica Aerogels for Anionic Dye Removal*

This chapter focuses on the use of cellulose nanofibrils (CNFs) and 3-mercaptoproyltrimethoxysilane (MPTMS) to prepare compressible aerogels, which are further functionalized with diallydimethylammonium chloride (DADMAC) and N,N'-methylenebis(acrylamide) (MBAA) via the thiol-ene click reaction to remove anionic dye methyl orange (MO) from wastewater. First, MPTMS undergoes controlled hydrolysis/condensation in the presence of CNF and then freeze dried to form a compressible aerogel. The aerogel was modified by polymerizing DADMAC and MBAA at varying initial ratios on the CNF fibres to maximize dye adsorption. The performance of the aerogel was evaluated using batch equilibrium experiments, with the maximum adsorption capacity for MO dye estimated to be 186.7 mg/g according to the Langmuir isotherm. Kinetic experiments reveal that mass transfer rate of MO dye into the aerogel could be described by the pore diffusion model, having a pore diffusion coefficient of 1.8×10^{-9} m^2/s. In addition, the effect of environmental conditions such as solution pH, ionic strength and temperature demonstrated that adsorption was influenced by electrostatic interactions between the MO and adsorbent surface, followed by physisorption. Finally, after regeneration of the aerogel using 2 M NaCl, the adsorbent retained 77 % of its initial adsorption capacity during a second use.

* This chapter is partially adapted from "Nathan Grishkewich, Yingzhan Li, Kimberly Liu, Kam Chui Tam, Thiol-ene click modified Cellulose Nanofibril Organosilica Aerogels for Anionic Dye Removal, *Manuscript under preparation*"

3.1 Introduction

Water is a valuable resource to sustain our existence and enable countless industrial activities. Thus, it is of great importance that this resource is treated effectively before it is discharged to the natural environment such as rivers and lakes. Many textile, cosmetics, leather and paper industries utilize dyes and dyestuff for their processes, which are then discharged as wastewater to water bodies [19]. Especially in countries with a large textile sector, such as China [145] and India [146], these factories can produce dye-laden wastewater that is not only unsightly but can be damaging to wildlife and human health when ingested. Fortunately, many physical and chemical treatment processes such as adsorption [147], membrane filtration [148], coagulation/flocculation [149] and photocatalysis [150] can effectively treat this wastewater. Adsorption processes are effective in treating this effluent as they are easy to implement due to their simple design and operation, require low initial investment and their surface chemistry can be tuned to remove a wide variety of contaminants [116]. Activated carbon is the most widely used adsorbent for water treatment due to its high surface area and high adsorption capacity for a variety of contaminants [33]. However, the large carbon footprint resulting from its production as well as the cost of regenerating the adsorbent are motivating researchers to develop low cost alternatives from sustainable sources [151],[152]. Cellulose, which is the most abundant biopolymer in the world[11] has been the subject of numerous studies, and shown in its unmodified and derivative forms to be effective adsorbents of dyes [153], heavy metal ions [154] and pharmaceuticals [155]. Cellulose nanofibrils (CNF) produced from the mechanical disintegration of cellulose fibres have great potential as adsorbents due to their high surface area due to their nano-dimensions (fibre diameter and lengths of 5 – 100 nm and 0.5 – 5 μm, respectively [81]) and abundant surface hydroxyl groups which can be utilized to graft compounds to alter their surface chemistry.

Furthermore, they can be combined with organosilicon precursors to form low density, flexible structures that facilitate their separation from treated wastewater [156].

The silanization of cellulose nanomaterials is a proven method to functionalize the surface of these materials. When added to a suspension of CNF, organosilicon compounds such as vinyltrimethyoxysilane (VTMOS) and 3-mercaptotrimethoxysilane (MPTMS) readily cross-link with their surface hydroxyl groups to form a network via controlled hydrolysis/condensation reactions [156],[110]. They can be converted into a porous solid via directional freezing that has excellent flexibility along the axis of freezing after the removal of the ice and subsequent curing [107]. Moreover, the type of organosilane precursor used can affect the functionality of the adsorbent, as shown by Wu *et al*. who developed a VTMOS/cellulose sponge for an oil/water separation process [110]. This was accomplished by performing a thiol-ene click reaction between the vinyl group of the material and a thiol-containing molecule. Thiol-ene click reactions are an effective tool functionalizing polymers and occurs between thiols and carbon-carbon double bonds in the presence of a radical initiator [157]. MPTMS has also been used with cellulose and CNFs to make sponges for complexing copper in catalytic reactions [12] as well as selectively removing mercury from wastewater [13]. This type of system can be modified to remove charged compounds, such as dyes through this thiol-ene click reaction, with a cationic monomer such as diallyldimethylammonium chloride (DADMAC). Poly(DADMAC) is a common flocculant, that imparts active sites on the adsorbent due to its permanent positive charge that is independent of solution pH.

In this study, CNF-organosilane aerogels were produced as effective adsorbents for methyl orange (MO) dye. First, the aerogels were prepared by mixing CNF with MPTMS to produce flexible structures using directional freezing, freeze drying and high temperature curing. Then, the aerogels were modified via thiol-ene click chemistry to anchor DADMAC onto the bound MPTMS

and free radical polymerization was performed simultaneously to graft additional N,N'-methylenebis(acrylamide) and DADMAC. The mechanical properties of the aerogels were evaluated using compression testing, while the adsorption properties were evaluated using batch equilibrium experiments with MO. The effect of various environmental parameters such as solution pH, ionic strength and temperature on the adsorption capacity were evaluated. Finally, the recyclability of the aerogel was investigated by desorbing the bound dye and using it for further adsorption experiments.

3.2 Materials and Methods

3.2.1 Materials

(3-Mercaptopropyl)trimethoxysilane (MPTMS, 95%), hydrochloric acid (HCl, 37%), diallyldimethylammonium chloride (DADMAC, 65% in water), 2,2′-azobis(2-methylpropionamidine) dihydrochloride (AIBA), N,N'-methylenebis(acrylamide) (MBAA), sodium chloride (NaCl), potassium bromide (KBr) and methyl orange (MO) were purchased from Sigma-Aldrich. The cellulose nanofibril (CNF) suspension was purchased from the University of Maine. MilliQ water was produced onsite using a MilliPore system (>18 MΩ/cm), and ethanol was purchased from Fisher Scientific.

3.2.2 Synthesis of CNF-Silica aerogels

In a typical synthesis, 240 mg of MPTMS was added to 20 g of a 1.2 wt% CNF dispersion in water (240 mg of CNF total) and mixed at 500 rpm. Then, 60 μL of 0.1 M HCl was added to the suspension to adjust the pH to 4.0 and the contents stirred for 2 hours. Following this, the mixture was poured into cylindrical molds and subject to directional freezing from the bottom and placed inside a Labconco freeze drier to remove water over a period of 48 hours. Following the

drying, the aerogels were placed inside an oven at 120°C for 30 minutes to cure the gels. The product was stored in a sealed vial at ambient conditions for further use and characterization.

3.2.3 Synthesis of DADMAC-MBAA modified CNF-Silica aerogels

DADMAC was grafted onto the CNF aerogel via the thiol groups on the MPTMS, and further cross-linked with MBAA. In a typical synthesis of DADMAC:MBAA 10:1 ratio, 1.27 mmol DADMAC and 0.127 mmol MBAA were added to 15 mL of ethanol and mixed in a round bottom flask to prepare the monomer solution. At the same time, 0.073 mmol of AIBA initiator was dispersed in 5 mL of deionized water to prepare the initiator solution. The initiator solution was then added to the flask containing monomer and mixed well under N_2 atmosphere to remove dissolved oxygen. Then, 50 mg CNF-MPTMS aerogel was added and gently agitated under further N_2 purging, allowing the components to diffuse into the pores of the aerogel. The temperature of the solution was increased to 60°C to initiate radical formation and allowed to continue for 4 hours to facilitate the thiol-ene reaction as well as polymerize the MBAA and DADMAC monomers. Following this, the aerogel was removed and washed 3 times with deionized water, followed by rinsing with acetone 3 times. The aerogel then underwent Soxhlet extraction with acetone for 6 hours to fully remove water and unreacted monomer from the aerogel. The aerogel was then placed in the oven at 80°C to dry and the modified aerogel was stored in a sealed vial at ambient conditions to be used for further adsorption experiments.

3.2.4 Mechanical Testing of Aerogels

Mechanical testing of the aerogels was performed using a CETR-UMT (Bruker). This was used to assess their compressive strength before and after modification with monomers. Aerogels were immersed in water and compressed between two plates at a rate of 20 mm/min and compressed to 50% of their original height while the force (mN) was measured, and relaxation occurred at the same rate, with this cycle performed a total of 10 times. The compressive strength was determined from the stress curves, with the stress calculated as follows:

$$\sigma = \frac{F}{A} \tag{3.1}$$

where σ is the computed stress (kPa), F is the measured force (N), and A is the cross-sectional area of the aerogel (m^2).

3.2.5 Adsorption Experiments

The adsorption ability of the aerogels was assessed by adsorbing MO dye in batch vessels. This was conducted by adding 25 mg aerogel to 15 mL of MO dye solution of varying concentrations and allowed to equilibrate. The amount of dye adsorbed at time t or at equilibrium can be calculated using Eq (3.2):

$$q = \frac{(C_0 - C)V}{m} \tag{3.2}$$

where C_0 is the initial bulk dye concentration (mg/L), C is the concentration of dye in the bulk (mg/L), V is the volume of solution treated (L), m is the mass of aerogel used (g), and q is the mass of dye adsorbed per gram of aerogel (mg/g). In addition to this, adsorption isotherms were fitted

to the equilibrium data using both the Langmuir isotherm and Freundlich isotherm. The Langmuir isotherm is described by Eq (3.3):

$$q_e = \frac{q_m K_L C_e}{(1+ K_L C_e)} \tag{3.3}$$

Where q_e is the mass of dye adsorbed per gram of aerogel at equilibrium (mg/g), C_e is the concentration of dye in bulk at equilibrium, K_L is the Langmuir constant (L/mg) and q_m is the theoretical maximum adsorption capacity of the adsorbent (mg/g). The Freundlich isotherm is described by Eq (3.4):

$$q_e = K_F (C_e)^{1/n} \tag{3.4}$$

K_F is a parameter describing the adsorbate loading on the adsorbent (i.e. Freundlich constant, units of (mg/g)(L/mg)$^{1/n}$), and *1/n* is related to the heterogeneity of the adsorbent surface. The sum of squared error (*SSE*) was used to assess the suitability of both isotherms in predicting the equilibrium adsorption behavior of the adsorbent as given by Eq (3.5):

$$SSE = \sum_{i=1}^{n} (q_{exp,i} - q_{pred,i})^2 \tag{3.5}$$

where q_{exp} and q_{pred} represent experimental and calculated values of the adsorbed dye at equilibrium, respectively. All adsorption experiments conducted were reproducible to within 10 % of their original value.

3.2.6 Mass transport modelling

Since the CNF aerogel has a cylindrical adsorbent, a model incorporating mass transport in both the radial and axial dimensions was established. The model would incorporate both diffusion from the bulk solution through the stagnant film boundary layer (film diffusion) to the adsorbent surface as well as diffusion into the pores of the adsorbent (pore diffusion). The

following boundary condition was used to account for film diffusion at the exterior surface of the adsorbent and relate the bulk dye concentration the concentration at the adsorbent exterior surface [158]:

$$\nabla C_b = -\frac{k_f}{D_p}\left[C_b - C_p\right] \tag{3.6}$$

This equation has the following initial condition:

$$C_b(0) = C_0 \tag{3.7}$$

where k_f is the external film diffusion coefficient (m/s) and D_p is the internal pore diffusion coefficient (m^2/s). To describe the transport of dye within the adsorbent, a general mass transfer model for porous media was used [29], described by:

$$\frac{\partial C_p}{\partial t} + \frac{\partial q}{\partial t} - D_p \nabla^2 C_p = 0 \tag{3.8}$$

$$\frac{\partial q}{\partial C_p} = \frac{\rho K_L q_m}{(1+K_L C_p)^2} \tag{3.9}$$

This equation had the following initial and boundary conditions:

$$C_p(0) = 0 \tag{3.10}$$

$$q(0) = 0 \tag{3.11}$$

At $0 < r < R_p$ for $z = 0,h$, and $r = R_p$ for $0 < z < h$, $t > 0$; $\quad \nabla C_p = \frac{k_f}{D_p}(C_b - C_p)$ (3.12)

where ρ is the density of the adsorbent (kg/m^3). Eqs (3.8) and (3.9) were solved using the finite element method with the COMSOL Multiphysics® software based on the boundary conditions described by equations (3.6) and (3.12). In total, the grid was divided into 4453 domain elements

and 218 boundary elements. The model was solved to yield C_0 versus i data that was compared to the experimental results. To evaluate the fit of the data, the SSE was calculated according to Eq (3.5).

3.2.7 Effect of solution pH

The effect of the solution pH on the adsorption of MO onto the CNF aerogels was studied by preparing 10 mL of 50 mg/L MO solution at pH of 3.13, 4.94, 6.78, 9.30, and 11.02, followed by adding approximately 11 mg aerogel to the solution and agitating the contents until equilibrium was reached.

3.2.8 Effect of solution ionic strength

The effect of the solution ionic strength on the adsorption of MO onto the CNF aerogels was studied by preparing 10 mL 50 mg/L MO solutions with NaCl concentrations of 0, 0.1, 0.25, 0.5 and 1 M. Approximately 11 mg aerogel was added to each solution and stirred until equilibrium was reached.

3.2.9 Effect of solution temperature

The effect of temperature and the associated thermodynamic parameters for adsorption were studied by preparing 10 mL of 50, 100, 250, 500 and 1000 mg/L MO solutions, adding approximately 11 mg of aerogel to each solution and allowing them to stir and reach equilibrium at 25, 35 and 45^{o}C while stirring at 150 rpm.

3.2.10 Regeneration of CNF-MPTMS-DADMAC-MBAA aerogel

The reusability of the modified CNF aerogels was investigated for one cycle. After one adsorption cycle, the CNF aerogel was immersed in 10 mL of 2 M NaCl, heated to 50^{o}C and stirred at 150 rpm for 1 hour to desorb MO. This was repeated two more times to achieve maximum desorption of MO, after which the aerogel was used for a second adsorption experiment.

3.2.11 Characterization

3.2.11.1 UV-Vis Spectrophotometry

A Cary 1E UV-Vis spectrophotometer was used to determine the concentration of MO in batch solutions. A calibration curve was prepared by measuring the absorbance of MO solutions as a function of concentration ranging from 0.1 mg/L to 15 mg/L to determine molar absorptivity according to the Beer-Lambert law:

$$A = \varepsilon l c \tag{3.13}$$

where A is the measured absorbance at λ = 454 nm, ε is molar absorptivity of MO (L/mg·cm), l is pathlength of the light (1 cm) and c is concentration of the MO (mg/L).

3.2.11.2 Fourier Transform Infrared Spectroscopy (FT-IR)

FT-IR spectroscopy was conducted using a PerkinElmer 1720 FT-IR spectrometer to validate the formation and modification of CNF aerogels. Measurements were conducted by grinding samples with potassium bromide and using a hydraulic press to form them into a transparent pellet, after which they were scanned in the instrument at a resolution of 4 cm^{-1} to obtain the spectra.

3.2.11.3 Conductometric Titration

Conductometric measurements were performed using a Metrohm Titrando potentiometric titrator to determine the amount of DADMAC grafted onto the CNF-Silica aerogels. A 0.01 M $AgNO_3$ solution was titrated to a solution containing 16.5 mg of the modified aerogel, which dissociated and formed an insoluble precipitate with the chloride counter ion of DADMAC. The titrant was added at a rate of 0.05 mL/min and the conductivity of the solution was measured. An inflection point in the conductivity curve occurred when all of the chloride counterion had

combined with the silver ion yielding the AgCl precipitates. The volume of titrant added at the inflection point corresponded to the amounts of DADMAC in the aerogel based on Eq. (3.14):

$$N = \frac{V \times C}{m} \tag{3.14}$$

where N is the moles of DADMAC per mass of aerogel (mmol/g), V is the volume of titrant required to complex with all of the chloride counterion (mL), C is the concentration of titrant use (mmol/mL), and m is the mass of aerogel sample used in the experiment (g).

3.3 Results and Discussion

3.3.1 Synthesis of CNF-Silica aerogels

The preparation of the cellulose nanofibril aerogel was based on the previous report by Wu *et al.* [110], whereby MPTMS was mixed with CNF in an acidic environment resulting in evenly coated cellulose nanofibrils (**Figure 3.1a**). The suspension was ice-templated via directional freezing to generate large ice crystals that induced the aggregation of the nanofibres into larger filaments yielding a robust network structure. After ice removal via sublimation, the sample was heated at 120ºC to condense the methoxysilane to silicate and cross-link the structure, resulting in a compressible aerogel sponge. The presence of thiol groups from the MPTMS permitted the use of thiol-ene click chemistry to form active adsorption sites by attaching cationic DADMAC monomers to its surface. By using a cross-linking agent such as MBAA, we could facilitate further grafting of DADMAC via free radical polymerization (**Figure 3.1b**). Four different modifications were carried out using the following compositions; MPTMS:DADMAC:MBAA ratios: 1:10:1, 1:10:2.5, 1:10:5, and 1:12.5:5.

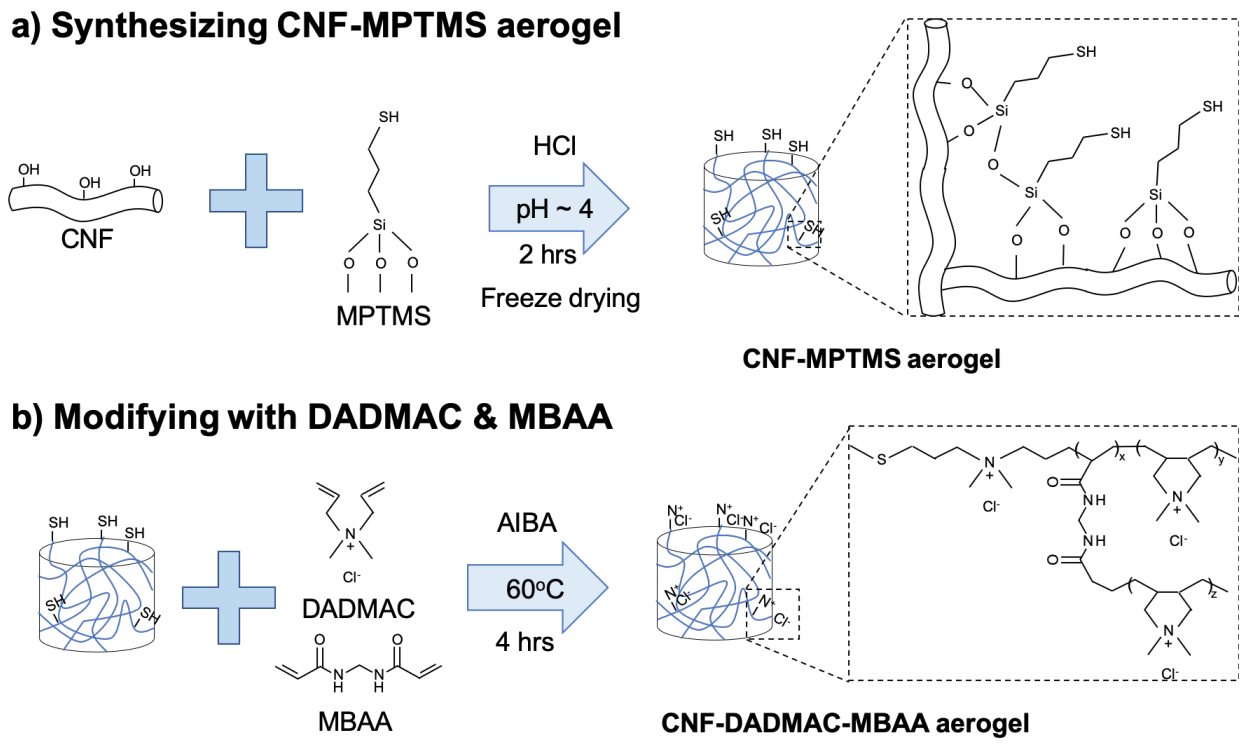

Figure 3.1: A) Condensation and cross-linking of MPTMS onto CNF to from aerogel skeleton, and B) thiol-ene click reaction and polymerization of DADMAC and MBAA onto CNF-organosilane aerogel

Following the formation of the aerogels, FT-IR was used to confirm the incorporation of MPTMS into the CNF structure as well as the presence of DADMAC and MBAA monomer (**Figure 3.2**). Although the main indicator of MPTMS incorporation within the aerogel is the marked increase in compressive strength, new peaks at 2550 cm^{-1}, 1260 cm^{-1} and 800 cm^{-1} confirmed the presence of thiol (-SH) groups from MPTMS, formation of Si-O-Si linkages, and formation of C-O-Si bonds, respectively [12]. Following the incorporation of DADMAC and MBAA monomers, the peak at 3060 cm^{-1} suggested the presence of DADMAC from residual C=C of the monomer structure [159], while the larger peaks at 1650, 1545 and 1380 cm^{-1} all corresponded to C=O, N-H bending and C-N bonds of the MBAA, respectively [160].

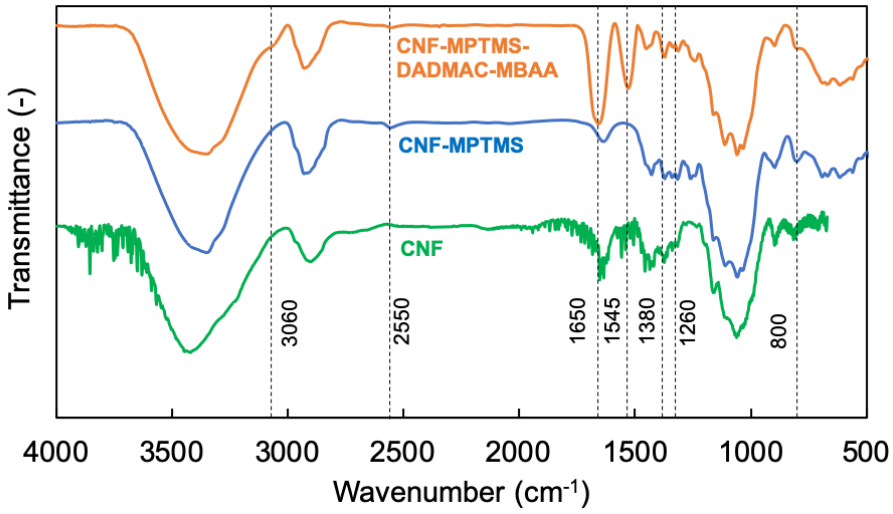

Figure 3.2: FTIR spectra for pure CNF (green), CNF-MPTMS (blue) and CNF-MPTMS-DADMAC-MBAA (orange)

Another technique that was used to validate the presence of DADMAC in the modified CNF aerogel was potentiometric titration. This technique was previously used to quantify the degree of cationic modification of CNCs, where Hasani *et al.* titrated $AgNO_3$ to determine the concentration of (2,3-Epoxypropyl)trimethylammonium chloride bound to their samples [161]. **Figure 3.3** shows the measured conductivity for the titration of $AgNO_3$ into a solution containing the CNF-MPTMS-DADMAC-MBAA (1:10:1) aerogel. The aerogel was cut into smaller pieces to ensure the titrant would be able to interact with bound DADMAC within the interior of the sample. Since $AgNO_3$ would dissociate when titrated to the sample, where Ag^+ combines with Cl^- ions on the DADMAC molecules to form an AgCl precipitate. Upon precipitation of all of the available Cl^- ions, the addition of $AgNO_3$ would contribute more to the total solution conductivity, culminating in a larger increase in solution conductivity with amount of titrant added. This point occurred at 0.988 mL of 0.01 M titrant, and after using Eq (3.14) this corresponded to 0.599 mmol DADMAC/g aerogel.

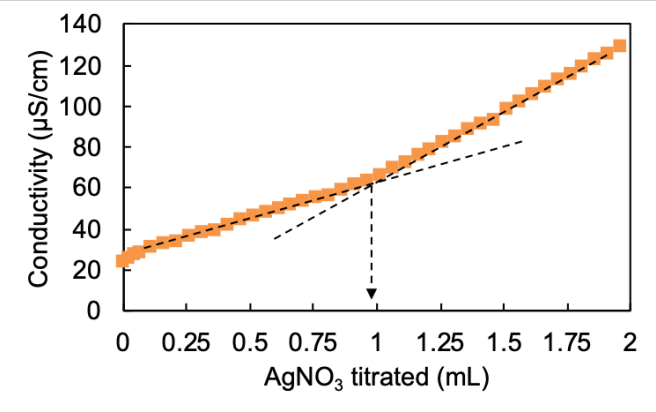

Figure 3.3: Titration of $AgNO_3$ into solution containing modified CNF aerogel to quantify content of DADMAC grafted to aerogel

3.3.2 Adsorption properties of CNF Aerogels

Following the successful formation of the CNF-MPTMS aerogel, the next step is to determine the optimal functionalization with DADMAC monomer and MBAA cross-linker. The hypothesis for using these two monomers to modify the aerogel involves the thiol-ene click chemistry to bind DADMAC monomer to the surface of the CNF-MPTMS aerogel, with the addition of MBAA to facilitate additional binding of DADMAC since it possesses two sites for radical polymerization. **Figure 3.4** shows the result of an adsorption experiment using 10 mL of 44 mg/L MO solution with the 4 aerogels produced using varying starting ratios of DADMAC to MBAA of 10:1, 10:2.5, 10:5, and 12.5:5. These express the molar ratios with respect to the moles of MPTMS present in the initial aerogel. Since DADMAC is difficult to polymerize at molar concentrations lower than 20 mol% due to strong columbic interactions of the monomer [162], the incorporation of MBAA would promote the formation of branched copolymers. Initially, the DADMAC should undergo thiol-ene reaction with the surface -SH groups of MPTMS, which would be followed by the addition of an MBAA molecule and then DADMAC monomer sequentially. The alternating polymerization was observed for DADMAC and vinylpyrrolidone

when working with monomer concentrations of 2 mol/L [163]. The ultimate goal is to maximize DADMAC incorporation that facilitated higher adsorption capacities for MO. As illustrated in **Figure 3.4,** all the aerogels showed good performance in removing at least 74% of the initial dye. The most effective aerogel is one with an DADMAC:MBAA ratio of 10:1, which removes 94 % of the dye. Further increase in the MBAA ratio results in a decrease adsorption to 74% at a 10:5 ratio. The addition of too much MBAA into the system was detrimental to its performance, as it might preferentially self-polymerize, rather than with DADMAC. Studies investigating the copolymerization of acrylamide and DADMAC indicated acrylamide possessed a higher reactivity ratio than DADMAC, implying that tenacious blends of copolymers would form when DADMAC concentrations were low in the case of solution polymerization [164]. Another explanation could be the strong electrostatic repulsion between DADMAC monomers at low concentration [164] that hindered their diffusion near the surface -SH sites, allowing the MBAA to preferentially polymerize by itself. From this result, the chosen initial monomer ratio to modify the CNF-MPTMS aerogel is 10:1 for DADMAC:MBAA.

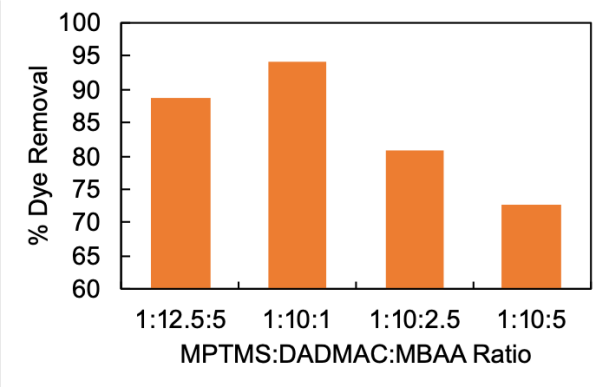

Figure 3.4: Comparison of dye removal of aerogels when using 15 mL of 10 mg/L MO dye solution with similar masses of adsorbent.

3.3.3 Mechanical Testing of Aerogels

It is important to determine if the modified aerogel still is compressible following the graft of DADMAC and MBAA. **Figure 3.5** shows the stress-strain curves for both unmodified CNF-MPTMS and CNF-MPTMS-DADMAC-MBAA (10:1) aerogels in water. Each sample is compressed a total of 10 times, with the first, second and tenth cycles shown in this figure. The unmodified aerogel exhibits a maximum stress of 11.2 kPa on the first cycle, which decreases to 10.14 kPa on the next cycle and finally to 8.79 kPa after the 10^{th} cycle (**Figure 3.5a**). This observed stress at 50 % compression is in agreement with that observed by Rong *et al.* for similar CNF-MPTMS aerogels [13]. Following the incorporation of DADMAC and MBAA, a marked reduction in the compressive strength is observed (**Figure 3.5b**), with the maximum stress of 3.5 kPa reported during the first cycle. However, the maximum stress observed after the 2^{nd} and 10^{th} compression cycles are 3.2 and 3.1 kPa, respectively, which shows a smaller decrease in stress compared to the unmodified aerogel after the 2^{nd} and 10^{th} cycles. The reduction in the strength may be the consequence of the additional atmospheric drying procedure performed after the modification with DADMAC, as a slight shrinkage was observed in the gel structure following modification and drying. Nonetheless, the aerogel still has the capability of recovering its shape following compression, as illustrated in **Figures 3.5c-e**. When compressed in air, the modified aerogel recovers its size very slowly; however after immersing in water, the aerogel immediately returned to its original shape. This is due to the presence of hydrophilic DADMAC and MBAA groups within the aerogel that have higher affinity for water allowing the aerogel to recover its original shape. In a typical CNF aerogel formed by directional freezing, the CNFs could aggregate into a sheet-like structure with large pore sizes of diameter 5 - 50μm [107]. These aligned pore channels along the length of the aerogel impart excellent compressibility along this axis, allowing the material to withstand external shear forces during the adsorption experiments.

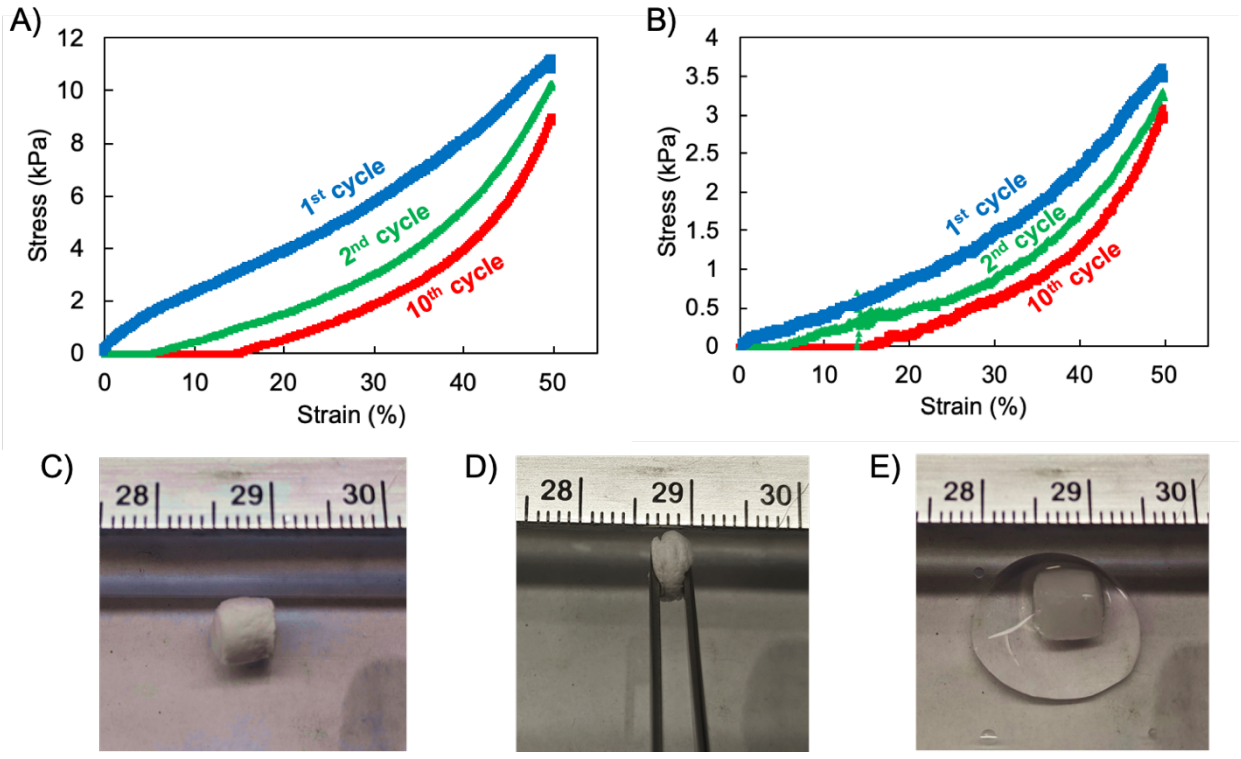

Figure 3.5: Compression test results of A) CNF-MPTMS aerogels in water, and B) CNF-MPTMS-DADMAC-MBAA (10:1), C) photograph of dry CNF-MPTMS-DADMAC-MBAA (10:1) aerogel before compression, D) photograph of aerogel compressed to 50 % strain, E) photograph of aerogel recovered to full size when immersed in water

3.3.4 Batch adsorption studies with optimized CNF aerogel

Following the optimization of the DADMAC-MBAA ratio inside the aerogel, the equilibrium adsorption properties of the aerogel were examined. **Figure 3.6** shows the results of equilibrium batch adsorption experiments (q_e vs. C_e) of MO onto the optimized aerogel with starting concentrations of 50, 100, 250, 500 and 1000 mg/L solutions, as well as the fitting of both the Langmuir and Freundlich isotherms. Using sum-of-squared error minimization, the isotherm parameters for the Langmuir isotherm (q_m and K_L) were determined to be 186.7 mg/g and 0.027 L/mg, respectively, with the SSE being 149. Similarly, the Freundlich isotherm parameters (K_F and n) parameters were found to be 34.4 mg/g and 3.88, respectively, with the SSE being 2376.

This analysis clearly showed that the adsorption of MO onto the aerogel obeyed the Langmuir isotherm much better, suggesting that the adsorption is restricted to monolayer and that all of the adsorption sites have homogeneous affinity to MO [165],[166]. The maximum adsorption capacity estimated by the Langmuir isotherm (186.7 mg MO/g aerogel) and the amount of DADMAC functionalized on the aerogel (0.599 mmol of DADMAC/g aerogel) appeared to be in agreement, as a 1:1 binding ratio of MO:DADMAC would imply a MO capacity of 196 mg/g using the latter value. This further validates the approach of potentiometric titration to estimate the concentration of DADMAC groups and the use of the Langmuir isotherm to predict the equilibrium behavior of the aerogel with MO.

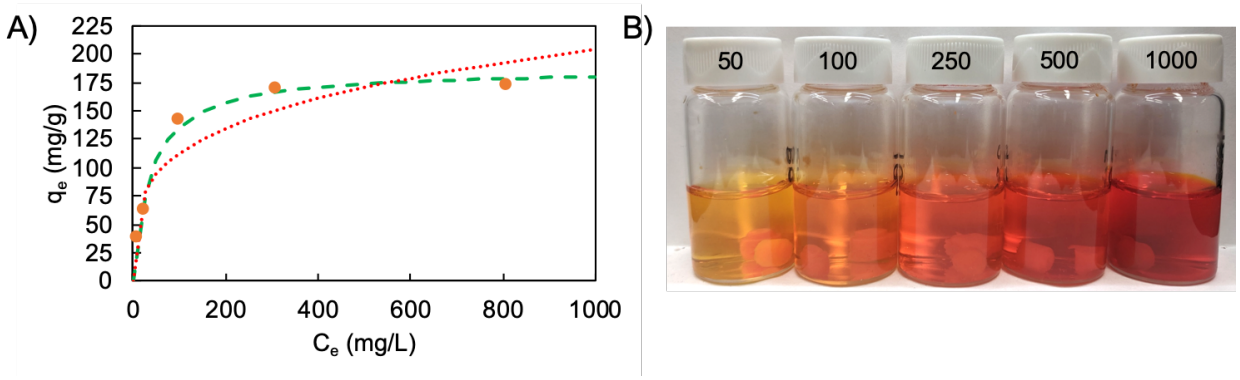

Figure 3.6: a) Isotherm of MO adsorption onto optimized CNF aerogel, with the orange points showing the raw data, the green dashed line showing the fitted Langmuir isotherm, and the red dotted line showing the fitted Freundlich isotherm b) Photographs of batch systems after reaching equilibrium showing varying levels of MO fixation, with labels indicating initial concentration of MO

Following the equilibrium studies, batch kinetic experiments were performed to elucidate the mass transfer and kinetic processes of adsorption. Given the porous nature of the CNF aerogel, the mass transfer into the interior of the aerogel is expected to be the rate limiting step for the dye uptake. **Figure 3.7a** shows the bulk dye concentration of MO measured during an adsorption experiment. The dashed blue line represents the fitted pore diffusion model incorporating external

film diffusion computed using COMSOL Multiphysics®. **Figure 3.7b** showing the geometry and coordinate system used to model the aerogel adsorbent, with **Figure 3.7c, d** and **e** showing the computed concentration profile of MO in the aerogel at t = 0 s, 7200 s and 14400 s, respectively. These results were obtained by optimizing the D_p and k_f parameters in the mass transfer model, which were determined to be 1.80×10^{-9} m^2/s and 4.05×10^{-5} m/s, respectively, resulting in a SSE of 7.1. The measured pore diffusion coefficient is much higher compared to that of other adsorbents having microporous structures. For example, Li *et al.* reported a pore diffusion coefficient of 4.12×10^{-10} m^2/s for the adsorption of phenol onto activated carbon [30]. This could be indicative of the macroporous structure of the aerogels due to the freezing templated process [107]. This should help facilitate the rapid adsorption of compounds from wastewater that would be expected for batch systems with a larger mass of adsorbent-to-water volume ratios.

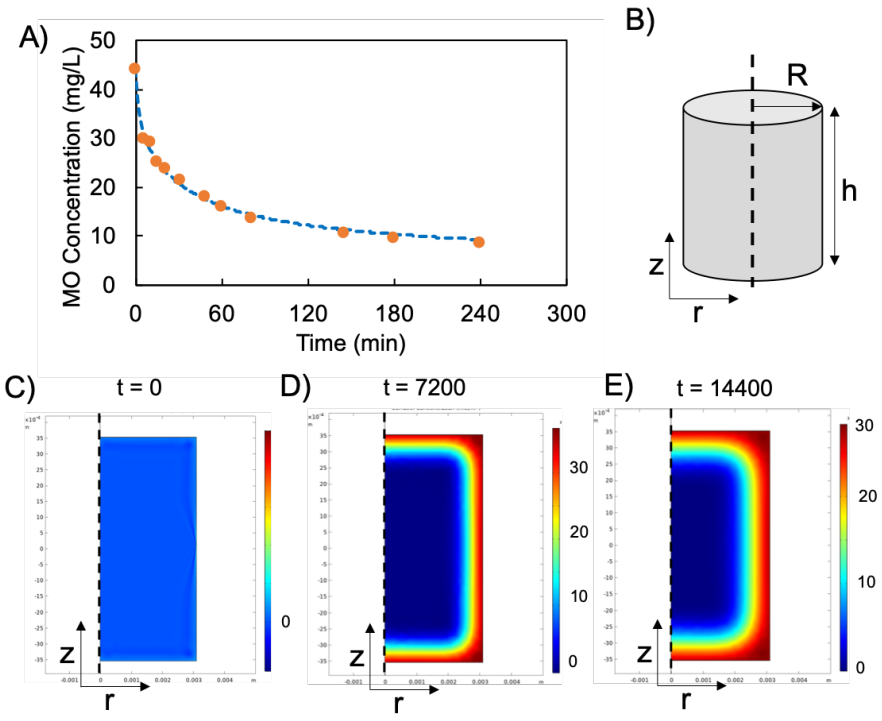

Figure 3.7: A) Adsorption kinetics of MO onto CNF aerogel with time, with the dashed blue line showing the fitting of the pore diffusion model incorporating external film diffusion. B) Geometry and coordinate system representing aerogel adsorbent, C) Concentration profile of MO in adsorbent at t = 0, D) t = 7200 s and E) t = 14400 s (color scale in mg/L).

3.3.4.1 Effect of solution pH and ionic strength

In order to predict the performance of the CNF aerogel in various environments, the interaction of MO with the surface of the CNF aerogel was investigated. Adsorption experiments were conducted at various solution pHs and salt concentrations. Since the CNF aerogel was designed to adsorb negatively charged compounds via electrostatic interaction, a high degree of DADMAC incorporation into its structure was necessary to achieve its intended function. **Figure 3.8a** shows the effect of pH on the dye removal. Dye removal remained constant at 67% at pH of 5 – 7, with a slight decrease at pH 9.3 but returned to 67% at pH 11. An increase to 79% removal was observed when the pH was decreased to 3.11, which was unexpected due to the aerogel containing no pH-responsive functional groups. No change in the performance was observed at

pH 11 since the quaternary ammonium groups on the DADMAC monomers cannot be deprotonated and so the adsorbent maintained a positive charge at all pHs, capable of binding anionic contaminants compared to other amine containing monomers, such as dimethylamino ethyl methacrylate [167]. **Figure 3.8b** shows the variation of % dye removal with ionic strength of the dye solutions. With MO dissolved in pure MilliQ water, the % dye removal is 66%. However, as the salt concentration increased, the % dye removal steadily decreased to 44% at NaCl concentrations of 1 M. This same trend was reported by Hu *et al.* for the adsorption of charged dyes onto various ion exchange resins that were primarily driven by long range electrostatic interactions [168]. The decrease observed in our studies validated the hypothesis that the adsorption process depends on long range electrostatic interaction to adsorb dye onto the CNF aerogel surface. Compared to our previous CNC-ALG hydrogel [14] which exhibited a 75% to 5% change in % dye removal when the salt concentration was increased to 1 M for methylene blue removal, this adsorbent showed greater resilience to charge screening by salt ions.

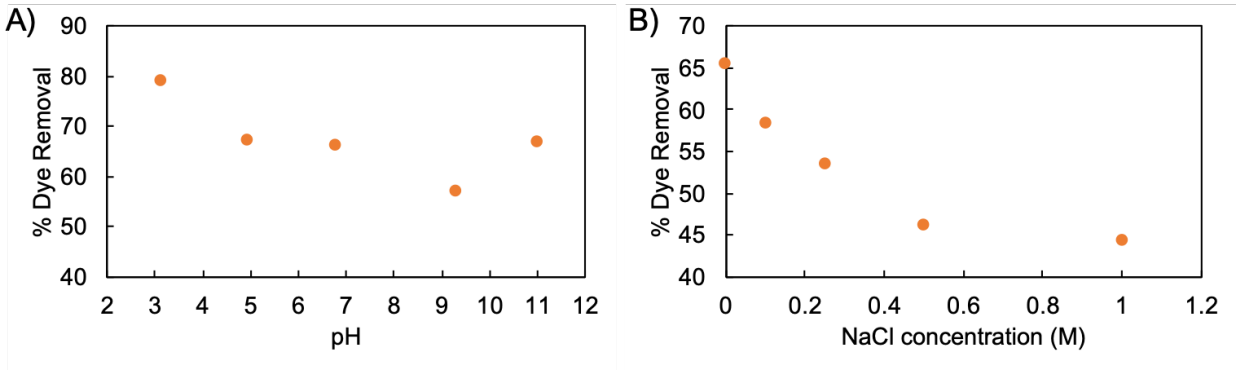

Figure 3.8: A) Effect of solution pH on MO removal, B) effect of ionic strength of NaCl solution on MO removal

3.3.4.2 Effect of Temperature

In addition to pH and ionic strength of the water to be treated, the temperature of the stream can have a large impact on the adsorption process. Equilibrium adsorption experiments conducted

at different temperatures can help determine if the process of MO uptake onto the CNF aerogel occurs by physisorption or chemisorption. **Figure 3.9a** shows the effect of temperature on the adsorption of MO onto the CNF aerogel, and fitted Langmuir isotherms through the data at temperatures of 25, 35 and 45°C. The figure shows that MO adsorbs onto the CNF aerogel in greater quantities at lower temperatures, implying that the adsorption process should be exothermic. However, in order to quantify the thermodynamics of the adsorption process, it is necessary to evaluate the adsorption equilibrium between the bulk and adsorbed phases by calculating the dimensionless equilibrium constant (K_c) via equation (3.15) [169]:

$$K_C = M_{wMO} \times 55.5 \times 1000 \times K_L \tag{3.15}$$

where K_L is the Langmuir constant (L/mg), M_{wMO} is the molecular weight of MO (327.37 g/mol), 55.5 is the number of moles of water per litre of water (mol/L), 1000 is a conversion factor from mg/g (mg/g). The purpose of incorporating these values into the calculation of K_C is to transform the isotherm constant (K_L) into a dimensionless number [169]. Following the calculation of K_C at all temperatures, the Gibbs free energy (ΔG^o), enthalpy (ΔH^o) and entropy (ΔS^o) were calculated using the following equations [169]:

$$\Delta G° = -RTlnK_c \tag{3.16}$$

$$\Delta G° = \Delta H° - T\Delta S° \tag{3.17}$$

Equations (3.16) and (3.17) can be combined to yield the van't Hoff equation:

$$lnK_c = -\left(\frac{\Delta H°}{RT}\right) + \left(\frac{\Delta S°}{R}\right) \tag{3.18}$$

where R is the gas constant (8.314 J/mol·K) and T is temperature (K). **Figure 3.9b** shows the van't Hoff plot described by Eq. (3.18) and the K_C values calculated from **Figure 3.9a**, allowing the

determination of the adsorption enthalpy and entropy from the slope and intercept, respectively. At the same time, the Gibbs free energy of adsorption for each temperature is estimated using Eq. (3.16). All of the thermodynamic parameters are summarized in **Table 3.1**. The large and negative ΔG^o values calculated at each temperature range from -32.47 to -33.09 kJ/mol indicating the spontaneous nature of the adsorption. However, the increasingly negative free energy with increasing temperature contradicts the hypothesis that the adsorption is favored at lower temperatures. In addition, the negative ΔH^o value extracted from the van't Hoff plot affirms that the adsorption is exothermic in nature, which is supported from the Langmuir isotherm data extracted at the different temperatures. Moreover, the magnitude of this value provided insights into whether the adsorption process is physisorption as characterized by ΔH^o ranging from 8 – 65 kJ/mol, or chemisorption, which is denoted by ΔH^o ranging from 84 – 420 kJ/mol [170]. The ΔH^o in this study was determined as -23.18 kJ/mol, suggesting that the adsorption of MO onto the CNF aerogel occurred by physisorption. This is consistent with the observation that the adsorbent could be readily regenerated to facilitate the recycling of the absorbents. The increase in entropy is indicative of the disruption of the highly ordered water cage surrounding the adsorption sites following the adsorption of MO, which reflects the high affinity of the MO to the DADMAC adsorption site.

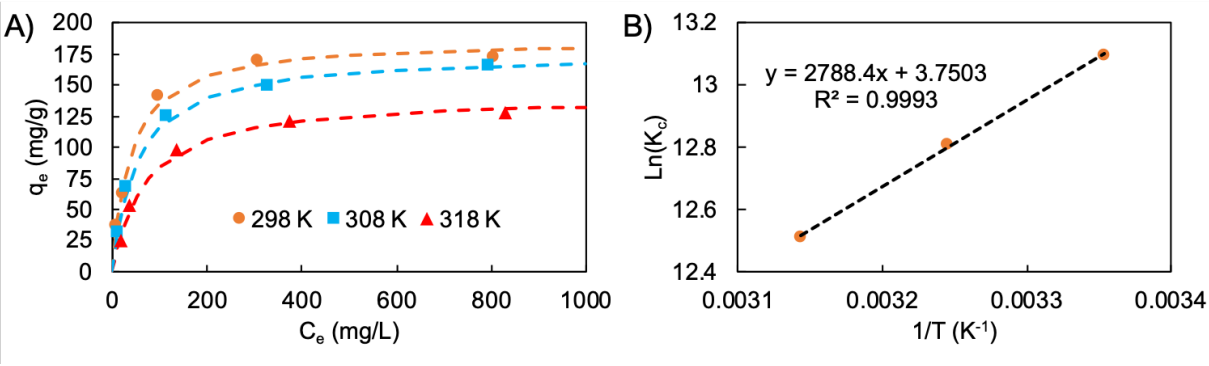

Figure 3.9: a) Effect of temperature on MO dye removal, and b) van't Hoff plot of the MO adsorption temperature study

Table 3.1: Thermodynamic parameters for adsorption of MO onto CNF aerogels

Temp. (K)	K_L (L/mg)	q_m (mg/g)	K_c (10^{-5})	ΔG^o (kJ/mol)	ΔH^o (kJ/mol)	ΔS^o (J/mol·K)
298.15	0.0269	186.7	4.881	-32.47		
308.15	0.0201	175.1	3.651	-32.81	-23.18	31.18
318.15	0.0149	141.1	2.711	-33.09		

3.3.5 Regeneration of CNF aerogel adsorbent

Since the adsorption process of MO onto the CNF aerogel occurs by physisorption, it can readily desorb and allow the recycling of the adsorbent. Traditional cationic adsorbents can be regenerated in basic conditions, although this will result in the breakdown of the silica shell of the CNF aerogel. Therefore, the saturated aerogel was regenerated in a highly saline solution (2 M NaCl) and held at 50°C for 1 hour to desorb the MO. **Figure 3.10a** shows the results of aerogel desorption over three consecutive washes (cycles), presented as % of the original amount of dye adsorbed. Following three washes, it was possible to remove 97.9 % of the bound dye, after which the adsorbent was washed with MilliQ water to remove salt within the aerogel pores. **Figure 3.10b** shows the % dye removal for both the initial and second adsorption cycle. The aerogel could remove 73% dye during the first cycle and 56% over the second cycle. This reduction in the performance is due to slight mass loss from the first cycle (using 9 mg of the original 11 mg of adsorbent) resulting from the repeated desorption and washing cycles, that corresponds to a 23%

reduction in the adsorption capacity. The reduced performance in the adsorbent could be easily resolved in practice by adding fresh adsorbent to the treatment system to make up for the loss in adsorption capacity to ensure the treatment objective was still achieved.

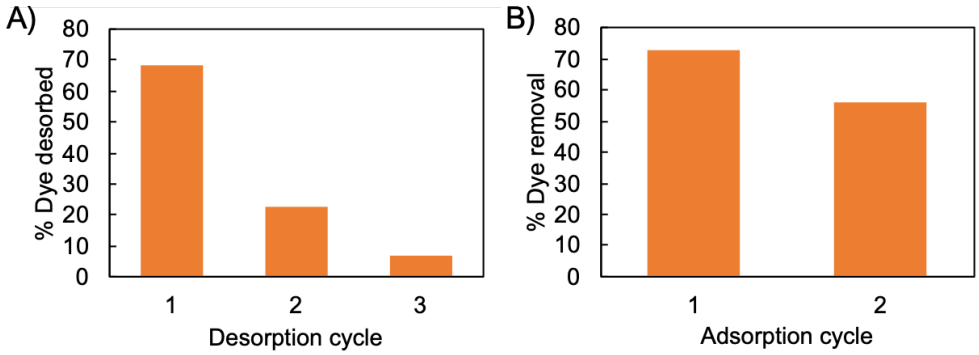

Figure 3.10: A) Amounts of dye desorbed with each desorption cycle with respect to amount of adsorbed dye, and B) % dye removal during first adsorption cycle and after desorption and regeneration of adsorbent

3.4 Conclusions

In this study, CNF-MPTMS aerogels were successfully prepared and modified via thiol-ene click chemistry with DADMAC and MBAA monomers. An initial monomer composition of 1:10:1 MPTMS:DADMAC:MBAA produced an adsorbent with the largest MO removal compared to aerogels modified with other monomer ratios, for a DADMAC grafting of 0.599 mmol/g aerogel. In addition, the modified aerogels retained the shape recovery properties of the unmodified CNF-MPTMS aerogel. The adsorption of MO onto the optimized aerogel obeyed the Langmuir isotherm, yielding a maximum adsorption capacity of 186 mg/g in agreement with potentiometric titration results. The adsorption of MO onto the aerogel was not influenced by pH between 4 – 11, with a moderate increase occurring at pH 3. The extent of adsorption decreased with increasing solution ionic strength confirming that the adsorption is influenced by electrostatic interaction. Experiments probing the thermodynamics of adsorption demonstrated that the uptake of MO occurred by physisorption, characterized by the exothermic process, where the adsorption capacity decreased

with increasing temperature. Finally, regeneration experiments demonstrated that the bound MO could be desorbed by exposing the adsorbent to 2 M NaCl at 50^{o}C for three successive wash cycles, and that the adsorbent could be reused with 77% of its original capacity.

Chapter 4: Cellulose Nanocrystals as Scaffolds for Bismuth-oxybromide Photocatalysts*

This chapter focuses on the preparation of nanosized bismuth oxybromide photocatalysts on cellulose nanocrystal templates. CNCs were modified with tannic acid (CNC-TA) to provide a platform for the growth of BiOBr nanocrystals via the addition of $Bi(NO_3)_3$ to a solution containing a stoichiometric amount of CNC-TA and hydrobromic acid (HBr). Transmission electron microscopy (TEM), scanning electron microscopy (SEM), powder X-ray diffraction and UV-Vis spectrophotometry confirmed the formation of BiOBr on CNCs (CNC-TA-BiOBr). The photocatalytic activity of the CNC-TA-BiOBr to degrade rhodamine B (RhB) dye under UV irradiation, and showed that the catalyst containing greater amounts of Bi^{3+} exhibited better performance. Quenching experiments revealed the photocatalyst could degrade RhB dye via the generation of superoxide (O_2^-) and direct oxidation from photogenerated holes (h^+) when the RhB was adsorbed on the photocatalyst surface. The CNC-TA-BiOBr photocatalyst was shown to effectively degrade RhB dye faster than BiOBr prepared on pure tannic acid. The photocatalyst was entrapped within a calcium alginate hydrogel matrix (ALG) for easy recovery from the treated solution. The amount of ALG used to form the hydrogel had negligible effect on the performance of the photocatalyst. However, smaller diameter beads had larger external surface area and so exhibited better degradation capabilities. The results revealed that CNCs are effective templates for preparing the BiOBr nanocatalyst, providing new opportunities for the development of different $Bi_xO_yBr_z$ crystal phases and heterojunctions with other bismuth oxyhalides on CNCs.

* This chapter is partially adapted from "Nathan Grishkewich, Mackenzie Strong, Kimberly Liu, Eli Bulger, Kam Chiu Tam, Cellulose Nanocrystals as Scaffolds for Bismuth-oxybromide Photocatalysts, *Manuscript under preparation*"

4.1 Introduction

Water treatment mainly focuses on two routes to purify water: (1) contaminant removal from a stream by partitioning them onto another phase (i.e adsorbents, flocculants) or (2) contaminant degradation to a less harmful form (i.e. advanced oxidation processes) [2]. The second approach is of interest as it avoids the creation of a secondary waste stream, i.e. spent activated carbon that must be disposed in a landfill. Advanced oxidation processes (AOPs) aim at mineralizing organic contaminants (converting them to carbon dioxide and water) by generating reactive oxygen species such as hydroxyl radicals (•OH). This is particularly important for decolorizing textile, paper and leather industry effluent containing organic dye compounds that may make their wastewater appear unsightly [39]. Some of these AOPs include ozonation, Fenton processes and photocatalysis. The latter process is beneficial since it requires only light (artificial or natural) to degrade organic compounds [40]. Photocatalysts are versatile compounds capable of catalyzing water splitting reactions in energy applications [127] as well as degrading contaminants in air and water [41],[42]. In the case of metal oxide semiconductors, such as titanium dioxide (TiO_2) [43] and zinc oxide (ZnO) [171], photocatalysts break down organic contaminants via two simultaneous reactions at their surfaces under radiation: (1) reduction processes from photo-generated electrons (e^-), and (2) oxidation processes from photo-generated holes (h^+) [44]. The generation of an electron/hole pair (exciton) can only occur when these metal oxides are excited by a photon with equal or greater energy than its band gap (E_g), which effectively promotes an electron into the conducting band (CB) while leaving a positively charged hole in the valence band (VB). While both these semiconductors have the ability to generate superoxide (O_2^-) and hydroxyl radicals, the latter can strongly oxidize organics, but is excited only by UV light due to their large band gap of 3.0-3.2 eV. This has prompted research into other metal oxides that have smaller band

gaps and can be excited by visible light. A promising system involves bismuth oxyhalide (BiOX, X = F, Cl, Br, I).

Bismuth oxyhalides are ternary compounds consisting of elements from the V-VI-VII families with a tetragonal matlockite crystal structure consisting of Bi_2O_2 layers interleaved with double halogen layers (i.e. X-Bi-O-Bi-X) [124],[125]. This structure is responsible for the presence of static electric fields perpendicular to these layers that facilitates the charge separation of electron-hole pairs, and extends their lifetime to participate in surface reactions [126]. Synthesis of BiOX using different halides will yield different electronic properties for the compound, where the band gap for BiOCl, BiOBr and BiOI are 3.3-3.22, 2.7-2.64 and 1.8-1.77 eV, respectively, where the latter two could be excited by visible light [127],[128]. These photocatalysts have been demonstrated for the treatment of a variety of water-borne contaminants such as toluene [132], rhodamine B (RhB) [125],[133] and methyl orange [48]. Obviously, the latter are relevant waste streams being considered in this study. One way to improve the effectiveness of photocatalyst is to reduce their size to nano-scale that will enhance their surface area as well as reduce the bulk recombination [40]. These can be achieved using reverse microemulsions [172] or nucleating them on a templating surface [135]. One such nanoparticle template that could be used for supporting this compound are cellulose nanocrystals (CNCs).

CNCs are rod-like nanoparticles having lengths of 100 – 300 nm and diameters of 5 – 15 nm, that are produced by acid hydrolysis of cellulosic biomass such as cotton, tunicate and wood [11]. The acid hydrolysis of CNCs yields nanoparticles with excellent colloidal stability due to high negative surface charge as well as large surface area (near 250 m^2/g). Hence, CNCs are selected for use as templates for various nanosized metal oxides, such as Fe_3O_4 [173] for magnetic properties or TiO_2 and ZnO for photocatalytic applications [135],[6]. Currently no attempts have been made to produce BiOX semiconductors on the surface of CNCs.

In this study, we used tannic acid coated CNCs to prepare nanosized BiOBr on their surface. Tannic acid itself has been shown to successfully produce nanosized BiOCl as it stabilizes the particles in an acid environment although their photocatalytic capabilities have never been evaluated [174]. Following the formation of CNC-TA-BiOBr, the nanocomposite was characterized for its ability to degrade RhB dye in solution as well as the mechanism of degradation. We also explored incorporation of the photocatalyst within calcium alginate hydrogel beads to facilitate their separation from treated water.

4.2 Materials and Methods

4.2.1 Materials

Tannic acid (TA), 4-(2-hydroxyethyl)piperazine-1-ethanesulfonic acid (HEPES), sodium hydroxide (NaOH), bismuth nitrate pentahydrate ($Bi(NO_3)_3 \cdot 5H_2O$), hydrobromic acid (HBr), rhodamine B (tetraethylrhodamine, RhB), p-benzoquinone (BQ), triethanolamine (TEOA), isopropyl alcohol (IPA), and calcium chloride ($CaCl_2$) were purchased from Millipore-Sigma. Sodium alginate (ALG, PROTANOL GP 3350) was purchased from FMC Corporation. MilliQ water was produced onsite using a MilliPore system (>18 MΩ/cm), while cellulose nanocrystals (CNCs) were provided by CelluForce Inc..

4.2.2 Preparation of CNC-TA

Tannic acid-coated cellulose nanocrystals (CNC-TA) were prepared according to a procedure reported by Hu *et al.*[87]. Cellulose nanocrystals (2 g) were dispersed in 150 mL MilliQ water using a homogenizer, HEPES (700 mg) was added to the mixture and then 3 mL 1 M NaOH was added to adjust the pH of the solution to 8. Following this, 50 mg TA was added to the solution which was stirred at 500 rpm for 6 hrs times at room temperature. The resulting product was

dialyzed against DI water for 3 days to remove free tannic acid and HEPES buffer. The CNC-TA was stored in a sealed container at ambient conditions and used immediately.

4.2.3 Preparation of CNC-TA-BiOBr and TA-BiOBr

The growth of BiOBr nanoparticles on the surface of CNC-TA was adapted from a procedure reported by Ascencio-Aguirre *et al.* [174]. 109 mg of CNC-TA was dispersed in 7.5 mL of MilliQ water and subsequently acidified with 0.6 mL of 0.1 M HBr. A second solution containing 14.5 mg $Bi(NO_3)_3$ dissolved in 7.5 mL MilliQ was prepared and then added dropwise to the first solution while stirring at 1000 rpm and at room temperature for 3 h. The resulting product was dialyzed for 3 days against deionized water (14,000 M_w cutoff membrane), and then concentrated using ultrafiltration with a 0.1 μm membrane. The synthesis of TA-BiOBr followed the synthesis procedure in [174] by acidifying 7.5 mL 0.77 g/L TA solution with 0.6 mL 0.1 M HBr and adding in 7.5 mL 1.46 g/L $Bi(NO_3)_3$ solution under 1000 rpm stirring. This solution was allowed to react for 3 hr at room temperature before being dialyzed against deionized water for 3 days (14,000 M_w cutoff membrane) and concentrated using ultrafiltration with a 0.1μm membrane.

4.2.4 Preparation of CNC-TA-BiOBr-ALG hydrogel beads

CNC-TA-BiOBr-ALG beads were prepared using a similar method developed in our lab [14]. Solutions of 4 wt% sodium alginate, 0.8 wt% CNC-TA-BiOBr and water were mixed in varying ratios to obtain the desired concentrations that were extruded through a hypodermic needle (either 22G or 30G) into 50 mL of 2 wt% $CaCl_2$ and cross-linked for 15 minutes. The resulting beads were collected and rinsed twice with deionized water to remove unbound calcium and then used immediately. For recycling studies, the beads were thoroughly rinsed with deionized water and soaked overnight to remove impurities and byproducts from the photocatalysis reaction for subsequent reuse.

4.2.5 Photocatalysis experiments

Photocatalytic experiments were conducted batchwise, with both pure photocatalyst suspensions as well as photocatalyst embedded within alginate hydrogel beads. Experiments were conducted at 25°C and at pH 6.2. Photocatalyst and RhB dye were mixed in a 20 mL vial under vigorous stirring for 30 minutes in the dark to reach adsorption/desorption equilibrium. Following this, a 100 W UV lamp (λ = 365 nm, Blak-Ray® B-100AP/R) was placed 10 cm from the vial to irradiate the sample under constant stirring. Samples were taken and loaded into a UV-Vis spectrophotometer to determine the RhB concentration by measuring the absorbance of the characteristic peak at λ = 554 nm. The Beer-Lambert law relates the absorbance to the RhB concentration, i.e.,

$$A = \varepsilon l c \tag{4.1}$$

where A is absorbance, ε is molar absorptivity of RhB (L/mg·cm), l is pathlength of the light (cm) and c is concentration of the RhB (mg/L). The kinetic rate data were analyzed using the Langmuir-Hinshelwood model as described by Eq. (4.2) [48]:

$$-\ln\left(\frac{C}{C_0}\right) = k_{app} t \tag{4.2}$$

where C_0 is the dye concentration at t = 0 (mg/L), C is the concentration of dye at time t (mg/L), and k_{app} is the apparent rate constant (min^{-1}), which accounts for both the adsorption equilibrium on the photocatalyst surface and the reaction rate constant of the photocatalytic reaction [175]. All photocatalytic experiments conducted were reproducible to within 10 % of their original value.

4.2.6 Quenching experiments

Various compounds were used to quench the active species produced during photocatalysis for example, p-benzoquinone (BQ) was used to quench superoxide radicals (O_2^-), triethanolamine

(TEOA) for holes (h^+), and isopropyl alcohol (IPA) for hydroxyl radicals (•OH). Each experiment consisted of adding 1 mM of one type of quenching agent to a photocatalyst/RhB mixture, allowing the photocatalysis to proceed under UV light and measuring the final RhB concentration after 90 minutes.

4.2.7 Characterization

UV-vis spectrophotometry (UV-vis) was used to detect and measure the concentration of RhB in solution to assess the photocatalytic degradation capability of the photocatalyst as well as measure the optical absorbance of photocatalysts. Scans were conducted to study the degradation of the dye using a visible lamp at wavelengths from 650 – 450 nm at a scan rate of 1 pt/nm in a Cary 1E UV-vis spectrophotometer. Scans were conducted from 750 – 250 nm using a visible and UV lamp at a scan rate of 1 pt/nm for optical absorbance measurements. Zeta potential measurements were carried out using a Malvern ZetaPLUS 90. X-ray powder diffraction (XRD) using a PANalytical Empyrean instrument Cu Kα radiation source (λ=1.5418 Å) equipped with a PIXcel bi-dimensional detector with a Ni Kβ filter was conducted to confirm the presence of BiOBr nanoparticles. SEM EDX was performed using a Zeiss FESEM Leo 1530, operated at an acceleration voltage of 10 kV to confirm the elemental ratios on the final CNC-TA-BiOBr composite. Transmission electron microscopy (TEM) images were obtained using a Philips CM10 unit with an acceleration voltage of 60 kV to investigate the size and morphology of the modified nanoparticles.

4.3 Results and Discussion

4.3.1 Synthesis of CNC-TA and CNC-TA-BiOBr

The scheme for coating tannic acid onto CNC and subsequent nucleation of bismuth oxybromide onto CNC is shown in **Figure 4.1**. This work is based on a previous study, where TA was oxidized in the presence of oxygen and basic media, causing it to oligomerize and deposit on

the surface of CNCs (**Figure 4.1a**) [87]. Next, BiOBr crystals were formed on the surface by adding $Bi(NO_3)_3$ into a solution containing HBr and CNC-TA. Many polyphenols, such as tannic acid are known to stabilize metal oxide formation in solution [174],[176]. A tannic acid coating on the CNC surface provides a site for the Bi^{3+} to complex and initiate crystal growth from the CNC-TA surface (**Figure 4.1b**).

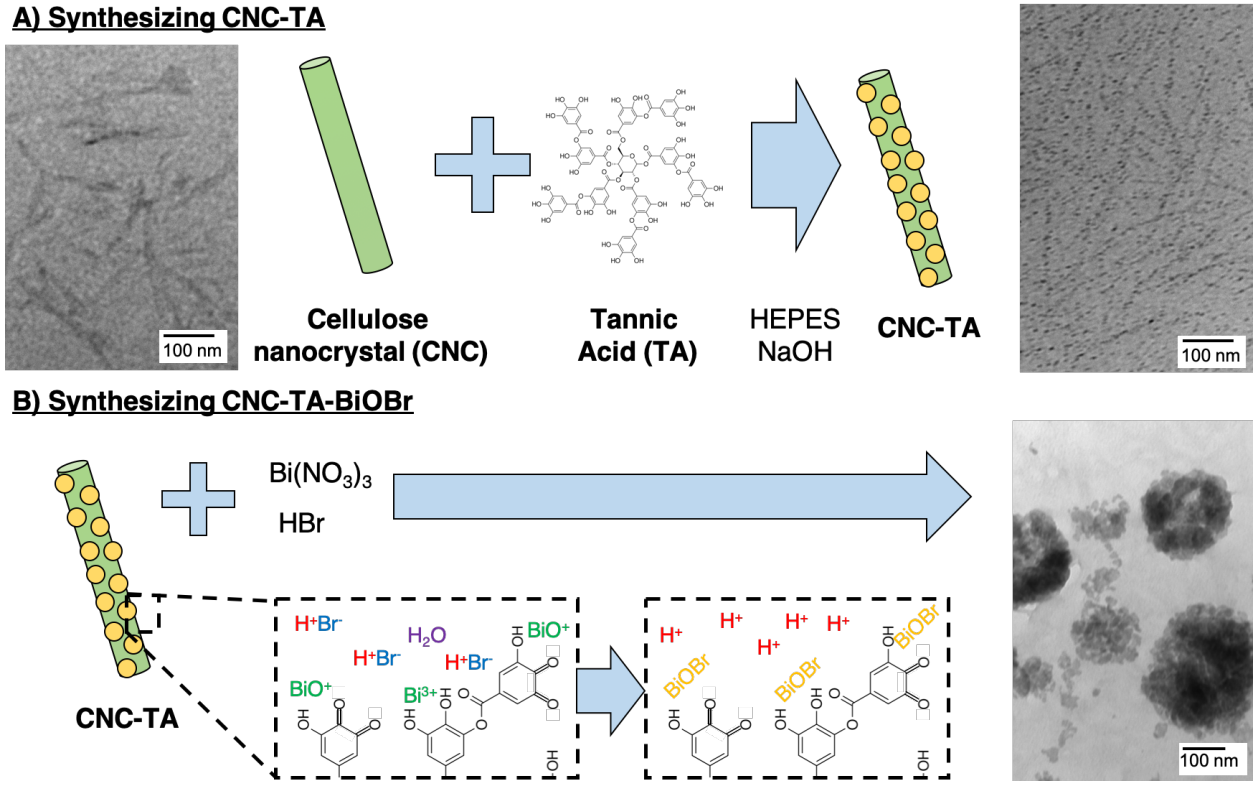

Figure 4.1: Schematic of A) modification of CNC with tannic acid, and B) chelation and growth of BiOBr on surface of CNC-TA

Zeta potential measurements and TEM examination were used to verify the coating of tannic acid on the CNC and subsequent modification with BiOBr. **Figure 4.2a** shows the zeta potential of CNCs, CNC-TA and CNC-TA-BiOBr at varying pHs. Sulfated CNCs typically have a high negative zeta potential that enhances their dispersibility water, and this value was between -45.8 to -53.9 mV. Coating tannic acid onto the surface of the CNCs resulted in a slightly smaller zeta

potential, as some of the sulfate ester groups of the CNCs were shielded with only the hydroxyl groups of tannic acid exposed [87]. After the formation of BiOBr on the surface of CNC-TA, the zeta potential became more negative at neutral pH and increased when the pH of the solution was lowered. A similar result was observed by Chang *et al.* with pure BiOBr nanoparticles where the isoelectric point occurred at a pH of 2.2 [177]. However, the CNC-TA-BiOBr retained a zeta potential of -30 mV at pH 3 due to the presence partial exposed sulfate ester groups on the CNCs.

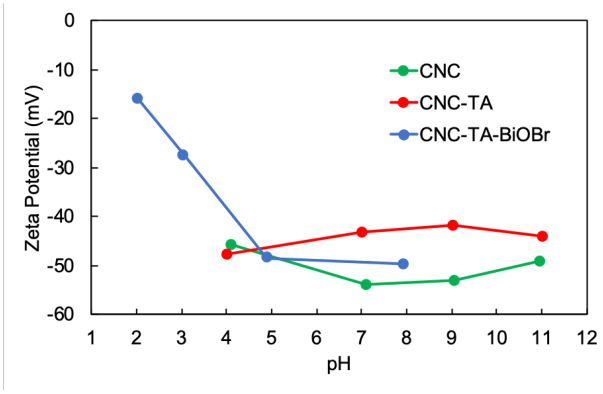

Figure 4.2: Zeta potential of CNCs, CNC-TA and CNC-TA-BiOBr at varying pH

Figure 4.3 shows TEM micrographs obtained for CNC, CNC-TA and CNC-TA-BiOBr samples. The CNCs in these micrograph (**Figure 4.3a**) have average lengths and diameters of 200 nm and 15 nm, respectively, and remain well-dispersed in the medium. Following the coating of tannic acid on the CNCs (**Figure 4.3b**), little size change in the CNCs was observed, although the surface became decorated with many nano-meter sized dark dots. A similar morphology was observed for tannic acid polymerized in bulk at pH 10 [176], likely due to tannic acid polymerization on the surface of CNCs. **Figure 4.3c** shows CNC-TA following the growth of BiOBr crystals on its surface. The metallic nature of this coating improves the contrast of the nanoparticles, allowing them to appear darker. The majority of morphologies generated during the synthesis of BiOBr by other groups include nanoparticles, nanoplates, nanoflowers and microspheres [125]. Based on observations reported in the literature, these structures appears to

resemble nanoplates, as reported by Chen *et al.* [42]. Based on previous studies [42][178], the reaction mechanism for the preparation of BiOBr on CNC-TA can be described below:

$Bi(NO_3)_3 \rightarrow Bi^{3+} + 3\ NO_3^-$ (1)

$Bi(NO_3)_3 + H_2O \rightarrow BiONO_3 + 2\ HNO_3$ (2)

$Bi^{3+} + HBr + H_2O + 3\ NO_3^- \rightarrow BiOBr + 3\ HNO_3$ (3)

$BiONO_3 + HBr \rightarrow BiOBr + HNO_3$ (4)

Steps 1 and 2 of the above reaction occur when the $Bi(NO_3)_3$ is sonicated in water. When it was added to the solution containing CNC-TA and HBr, Bi^{3+} and BiO^+ ions complex with pyrogallol and quinone groups of the CNC-TA according to steps 3 and 4 to form BiOBr crystals on their surfaces. This is supported by the observation that the addition of $Bi(NO_3)_3$ solution to 1.45 wt% CNC-TA solution yielded a gel due to the coordination of Bi^{3+} ions with pyrogallol and quinone groups of tannic acid on CNCs. The phenomenon was also confirmed by Fan *et al.* using Fe^{3+} trivalent ions to prepare supramolecular tannic acid hydrogels[85].

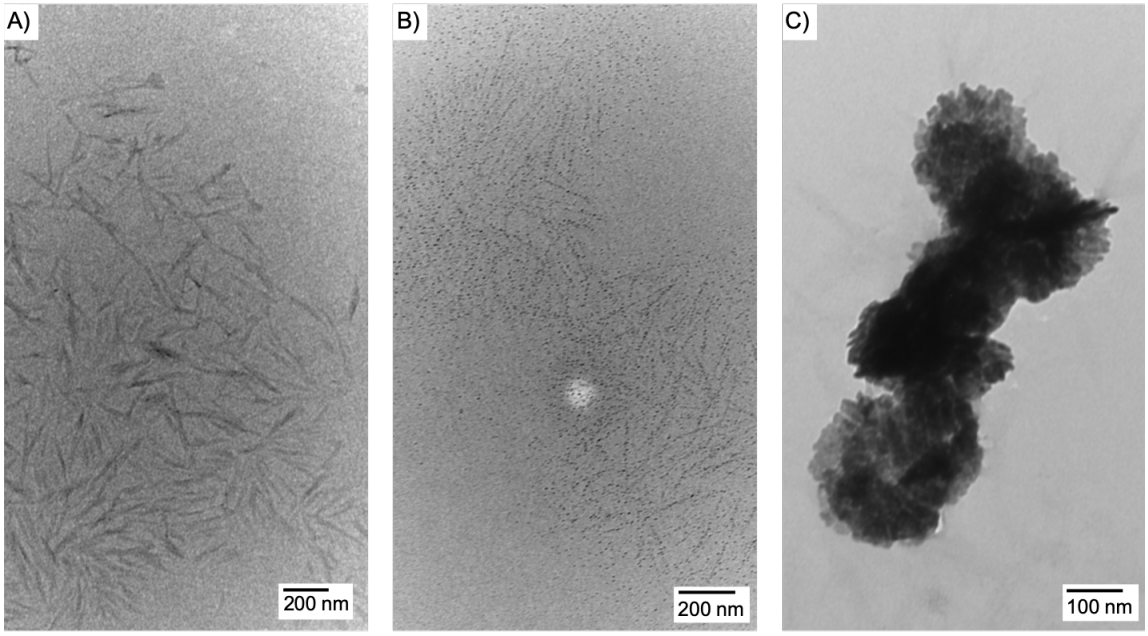

Figure 4.3: TEM of A) CNC, B) CNC-TA, C) CNC-TA-BiOBr

XRD analysis was used to confirm the presence of BiOBr on the CNC-TA, as shown in **Figure 4.4a**. The peaks at 15.9º and 23º are assigned to (110) and (200) typical of cellulose nanocrystals as reported by Chen *et al.* [179]. The peaks from BiOBr are assigned to (001), (011), (012), (110), (112), (020), and (122), as these are present in the BiOBr indexing card (ICSD 24609). These peaks were also observed in nanosheets and microspheres produced by Zhang *et al.* [124]. The existence of the peaks confirms the successful synthesis of BiOBr in the presence of CNC-TA.

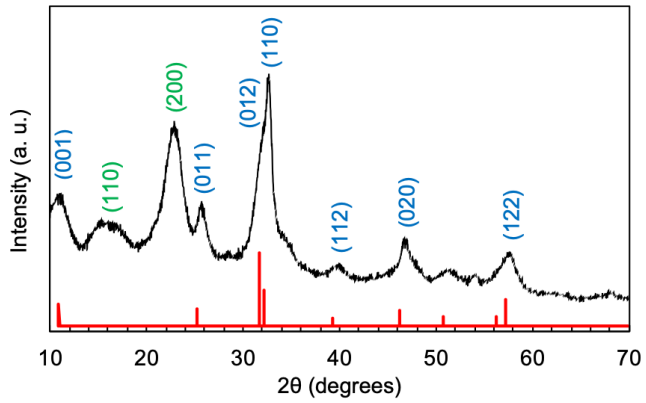

Figure 4.4: XRD pattern of CNC-TA-BiOBr sample (Green peaks are attributed to pure CNC, Blue peaks are attributed to BiOBr, red peak pattern is ICSD 24609 of BiOBr).

In addition, the electronic states of the BiOBr photocatalyst was investigated using UV-Vis spectrophotometry. **Figure 4.5a** compares the absorbance spectra of the CNC-TA-BiOBr and CNC-TA at the same concentrations. A new absorbance peak emerged at 313 nm due to the presence of BiOBr, although the absorbance edge preceding this peak was not as steep as those observed for pure BiOBr samples [127]. This optical absorption corresponded to the bandgap energy of the semiconductor and was determined by Eq. (4.3):

$$\alpha h\nu = A(h\nu - E_g)^{n/2} \tag{4.3}$$

where $h\nu$ corresponds to the photon energy (eV), A is the measured absorbance of a given photon, E_g is the bandgap energy (eV) and α is a constant [132]. The value n is dependent on the properties of the semiconductor and has a value of 1 and 4 for direct and indirect band gap semiconductors respectively [48]. As BiOBr possesses an indirect band gap, **Figure 4.5b** shows a tauc plot of $(\alpha h\nu)^{0.5}$ versus $h\nu$. Extrapolation to the x-axis along the tangent of this absorbance edge which yielded an approximate E_g of 2.4 eV, which is much lower than the 2.7 – 2.64 eV range reported previously [127]. This could be due to the fact that the photocatalyst was immobilized on the surface of CNCs. Similarly, the band gap for nano-sized TiO_2 decorated on CNCs was reported by

Liu *et al*. to be much smaller than bulk TiO_2 which the authors ascribed this to the quantum size effect [6].

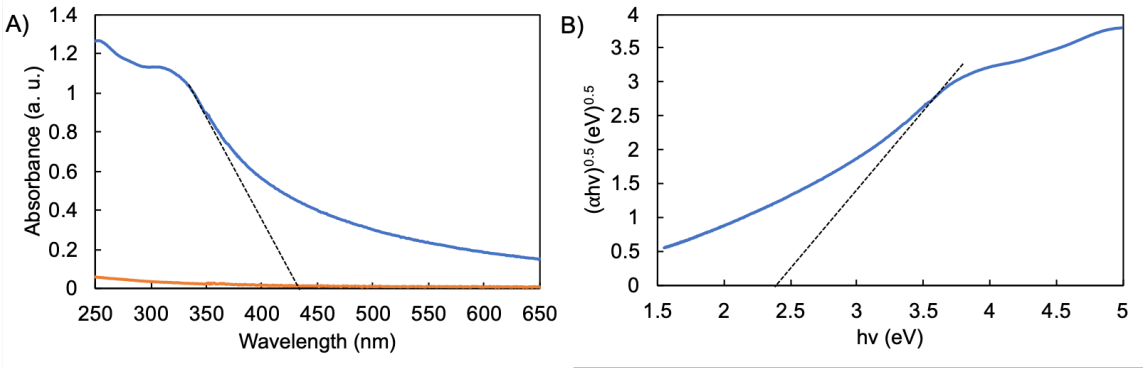

Figure 4.5: A) UV-Vis absorbance of CNC-TA (orange) and CNC-TA-BiOBr (blue), and B) $(\alpha hv)^{0.5}$ vs. hv for determination of bandgap energy E_g of CNC-TA-BiOBr

4.3.2 Photocatalytic activity of CNC-TA-BiOBr photocatalyst

In an attempt to modulate the photocatalytic activity and morphology of the CNC-TA-BiOBr, three different samples were produced using varying amounts of $Bi(NO_3)_3$. These are referred to as CTB0.5, CTB1, and CTB2, corresponding to mass ratios of Bi^{3+} to CNC-TA of 0.03, 0.057 and 0.11, respectively. **Figure 4.6** shows the morphologies of these as-prepared samples. All appear to bear some resemblance to **Figure 4.3c** with dark nanoplates of BiOBr decorating the CNC-TA particles. Visually, the main difference is the density of the BiOBr present in the samples. The large dark circular structures in **Figure 4.6c** appear due to the greater initial amount of Bi^{3+} present in forming BiOBr. These structures were less evident in the CTB1 and CTB0.5 samples produced using lower amounts of Bi^{3+}.

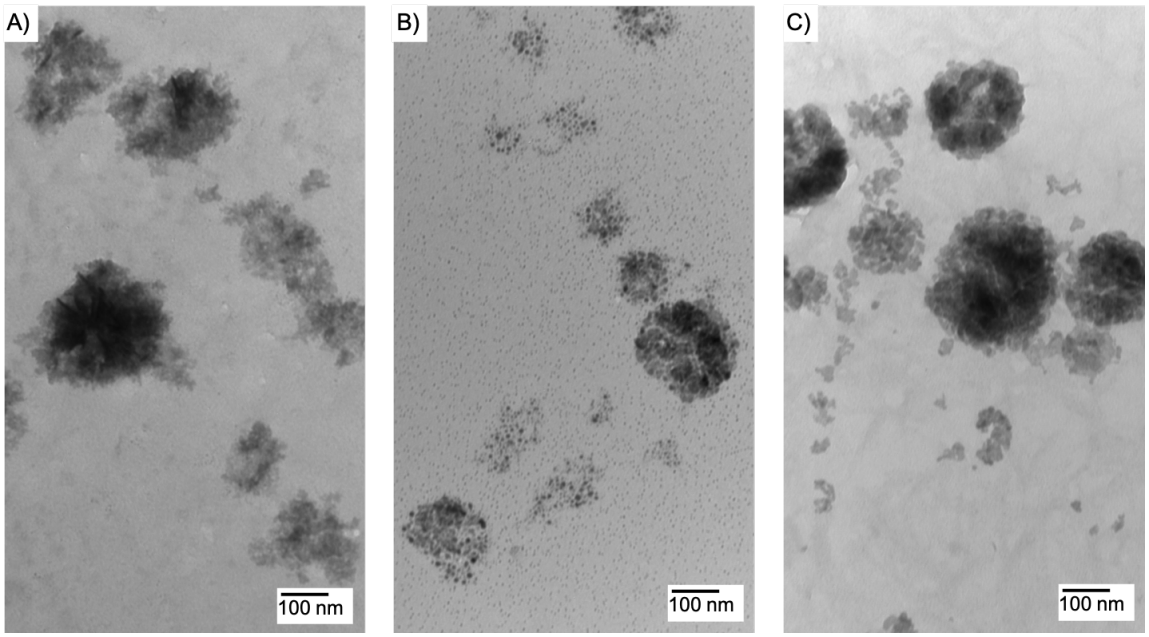

Figure 4.6: TEM of CNC-TA-BiOBr microstructures formed with different amounts of $Bi(NO_3)_3$ (a) 0.5 (CTB0.5) (b) 1 (CTB1) (c) 2 (CTB2)

In order to elucidate the proportion of BiOBr on the modified CNCs, SEM EDX measurements were performed on the CTB2 sample to verify the amount of BiOBr on the CNC-TA surface (**Figure 4.7**). **Figure 4.7a** shows an SEM image of the bulk sample and **Figure 4.7b-e** presents the elemental mapping of C, O, Br and Bi in the sample. The images indicate an even distribution of Br and Bi atoms, confirming that the photocatalyst is distributed homogeneously on the CNC-TA. **Figure 4.7f** shows the distribution of C, O, Br, and Bi elements by atomic mass. After averaging the values obtained in several images taken over different regions of the CTB2 sample, the atomic weights of the 4 elements were determined to be 47.7, 29.6, 5.9 and 16.8 wt%, respectively. This indicated a Bi/Br atomic ratio of 1.11, very close to the BiOBr target designed during the synthesis, which also confirmed that BiOBr comprised 23.9 wt% of the entire CTB2 sample.

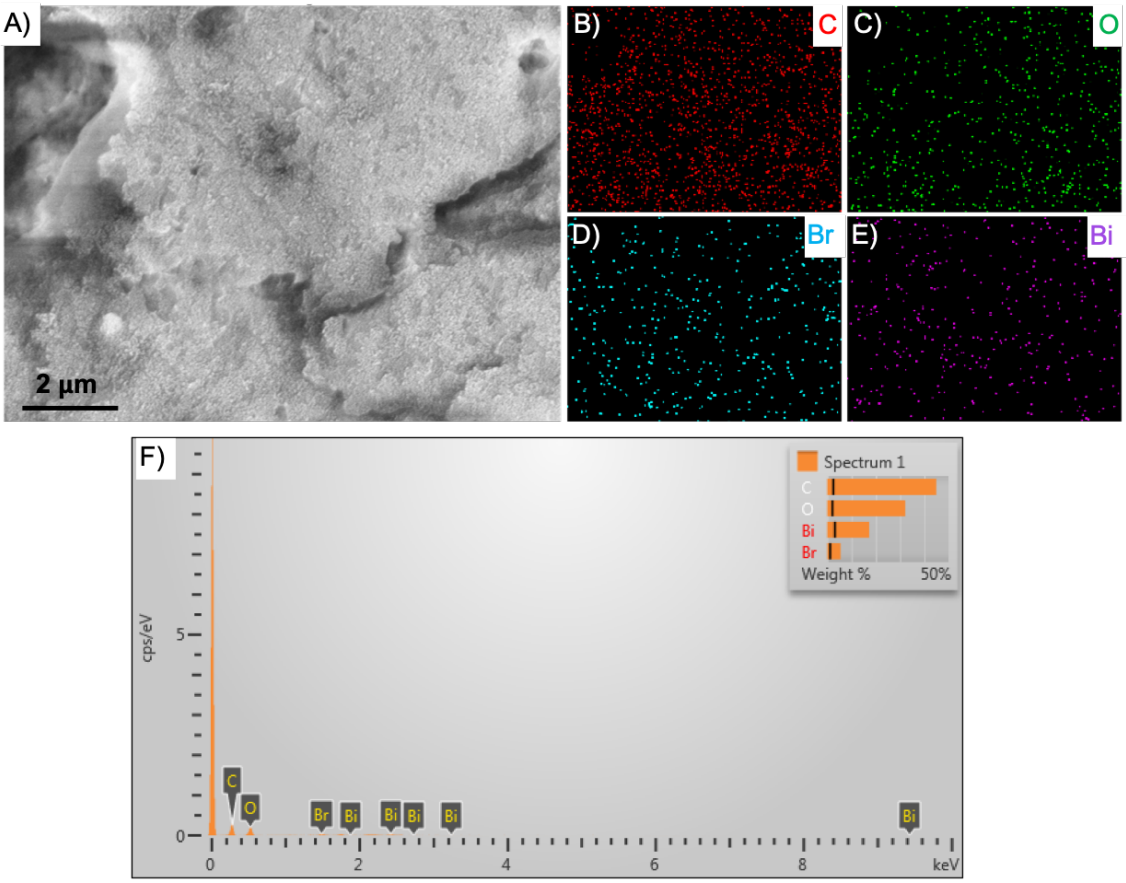

Figure 4.7: A) SEM of CTB2 sample with elemental mapping of B) C, C) O, D) Br, E) Bi, and F) shows the EDS spectrum of CTB2 sample, with inset showing wt% of the C, O, Br, and Bi atoms in the sample.

To further support this hypothesis, photocatalytic experiments using these three samples to degrade RhB under UV light were conducted, at similar photocatalyst concentrations of 0.723 mg/mL (**Figure 4.8a**). CTB2 exhibited the best catalytic performance, degrading the entire 8.8 mg/L dye solution within 105 minutes, while CTB1 and CTB0.5 achieved 61 % and 31% degradation, respectively, after 240 minutes. As the amount of sample used in each system was similar, the greater photocatalytic performance of the CTB2 could be due to more BiOBr present on the CNC-TA. This would support the observation made in **Figure 4.6** regarding the density of BiOBr on the CNC-TA in each sample prepared with different amounts of Bi^{3+}. **Figure 4.8b** presents the kinetic

data plotted in the form of the Langmuir-Hinshelwood model. It appeared that the kinetic profiles of CTB 2 and CTB 1 were not linear in the short time region. It is possible that they obeyed the pseudo-zero order reaction kinetics (which would be reflected as a linear decrease in concentration with time in **Figure 4.8a**), which may be related to the catalyst surface being fully saturated with the reactant. The CTB0.5 sample would be expected to show the same trend if the experiment were conducted at longer times, although the aim is to compare the reaction rates of the 3 samples. To further investigate the kinetics of the photocatalysts, experiments were conducted with CTB2 at different initial dye concentrations of 7.3, 5.7 and 3.9 mg/L (**Figure 4.8c**). A reduction in the initial dye concentration results in its more rapid degradation. This effect was further examined using the Langmuir-Hinshelwood kinetic model as shown in **Figure 4.8d**. The Langmuir-Hinshelwood model appeared to fit the data at C_0 of 3.9 mg/L with an apparent rate constant of 0.0904 min^{-1}. At concentrations of 5.7 and 7.3 mg/L, the model did not fit well as revealed by the two linear regions. This could be due to saturation of RhB on the catalyst surface at the start of the experiment when the bulk concentration of RhB was high. Once the RhB concentration decreased sufficiently, the rate of reaction was no longer governed by the amount of available adsorption sites but by the kinetics of decomposition so that the Langmuir-Hinshelwood model yielded a better fit.

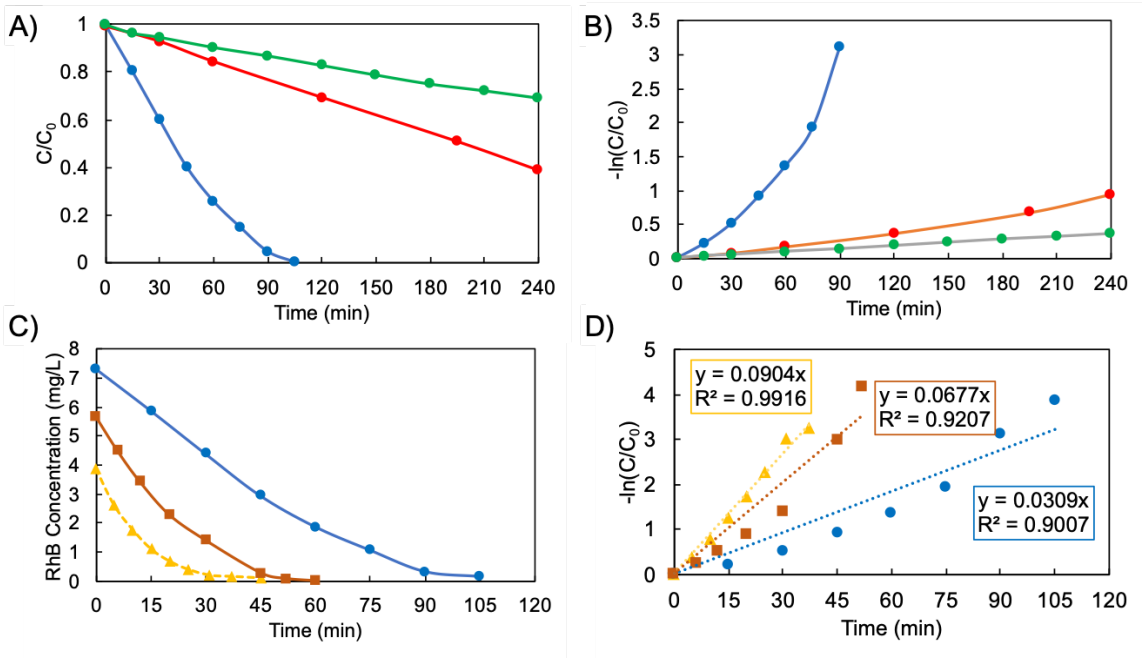

Figure 4.8: A) Photocatalysis of RhB under UV light with different CNC-TA-BiOBr samples, B) Data plotted to the Langmuir-Hinshelwood model, with CTB0.5 (green), CTB1 (red) and CTB2 (blue), C) Experiments conducted with CTB2 with initial RhB concentrations of 7.3 (blue), 5.7 (brown) and 3.9 ppm (yellow), D) Data from C) plotted in Langmuir-Hinshelwood model, with initial RhB concentrations of 7.3 (blue), 5.7 (brown), and 3.9 ppm (yellow)

4.3.3 Mechanism of CNC-TA-BiOBr photocatalysis of RhB dye

In order to investigate the mechanism of the degradation of RhB dye by the CNC-TA-BiOBr photocatalyst, various quenching agents were used (**Figure 4.9a**). P-benzoquinone (BQ) was used as a O_2^- quencher, triethanolamine (TEOA) as a h^+ quencher and isopropyl alcohol (IPA) as a •OH quencher, as previously reported by Ye *et al.* [122] and Li *et al.* [133]. We observed that the degradation of RhB was not affected by the addition of IPA, whereas the degradation was suppressed with the addition of BQ and TEOA. This indicates that both O_2^- and h^+ play an active role in degrading RhB under UV light, whereas •OH has no influence. A common reaction pathway for O_2^- is to combine with another electron and 2 protons to form hydrogen peroxide, which can undergo further reduction to produce hydroxyl radicals. At the valence band of some photocatalysts such as TiO_2 and ZnO, photogenerated holes can interact with adsorbed water or

hydroxide ions to form hydroxyl radicals. Both proposed reaction pathways could be neglected in this system since hydroxyl radicals are not formed as evident from the quenching experiments. Therefore, the following reactions are proposed for the degradation of RhB by the CTB photocatalyst:

$O_2 + e^- \rightarrow O_2^-$ (1)

$O_2^- + RhB \rightarrow$ Degradation Products (2)

$h^+ + RhB_{ads} \rightarrow$ Degradation Products (3)

These reaction pathways were postulated by Li *et al.* who prepared a $BiOBr/Bi_{24}O_{31}Br_{10}$ heterojunction system, and observed similar results when h^+ and O_2^- quenchers were added to their system [133]. The adsorption of RhB onto the photocatalyst is of paramount importance in order for the photogenerated holes to effectively oxidize the dye molecule. With regard to the degradation pathway of RhB dye, **Figure 4.9b** shows the UV-Vis spectra of the degradation of RhB in the presence of CTB2 under UV light. RhB displays a characteristic peak at λ = 554 nm. Over the course of the degradation, the absorbance of this peak decreased and shifted to a lower wavelength. This peak shift was observed previously [39],[177],[180],[181] and was attributed to the de-ethylation of the N-ethyl groups of the RhB structure. As RhB contains 4 ethyl groups, this de-ethylation process can occur successively until the molecule is degraded to rhodamine, which has a characteristic peak at λ = 498 nm [180]. This process occurs simultaneously with the oxidation of the main chromophore structure resulting in the observed reduction in the absorbance. The de-ethylation process which occurs under both visible and UV light was found to occur primarily near the surface of the photocatalyst due to the proximity of active species [180]. Wu *et al.* found that rhodamine itself exhibited an ε value 70% of RhB. The fact that the measured peak

at t = 75 at λ = 498 nm was much less than 70% and only 8% the magnitude of the original peak supported the simultaneous de-ethylation and cleavage of the chromophore structure [180].

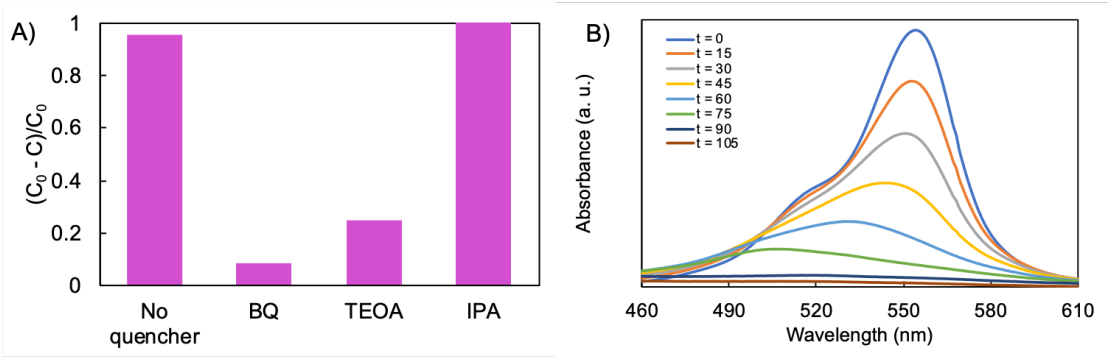

Figure 4.9: A) Effects of various quenching agents on the degradation of RhB by CNC-TA-BiOBr under UV light irradiation. B) Peak shift of RhB during UV-light degradation

4.3.4 Recyclability of CNC-TA-BiOBr photocatalyst

Another measure of the effectiveness of the CNC-TA-BiOBr photocatalyst is to examine its reusability over many cycles. **Figure 4.10** shows the degradation of RhB over 3 cycles. The RhB solution was fully decolorized when exposed to UV light for 105 minutes over the first cycle. The photocatalyst was still capable of degrading the same amount of RhB within 120 minutes over the following 2 cycles. Thus, the photocatalyst did not lose any of its activity during repeated use, indicating its excellent stability under UV light.

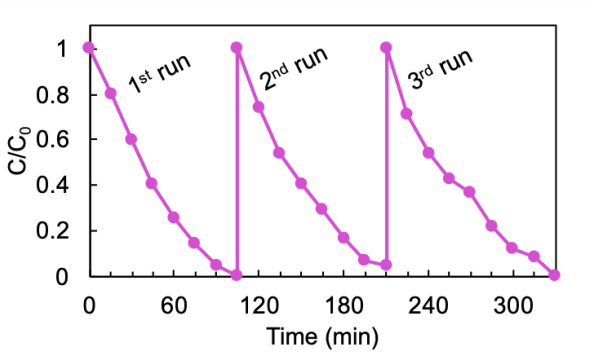

Figure 4.10: Recycling of CNC-TA-BiOBr photocatalyst for degrading RhB.

4.3.5 Comparison of TA-BiOBr and CNC-TA-BiOBr

In order to evaluate the effectiveness of the CNC scaffold to support BiOBr nanoparticles, the CTB2 photocatalyst was compared with TA-BiOBr. **Figure 4.11** shows the degradation of 8.3 mg/L RhB using 0.2 g/L CTB2 and TA-BiOBr. **Figure 4.11a** shows that the CTB2 photocatalyst could degrade the dye more rapidly than TA-BiOBr. Using the Langmuir-Hinshelwood model as shown in **Figure 4.11b**, the apparent rate constant for CTB2 was 12 times larger than TA-BiOBr, which confirms the benefits offered by CNC as a template for TA in nucleating the growth of BiOBr on its surface.

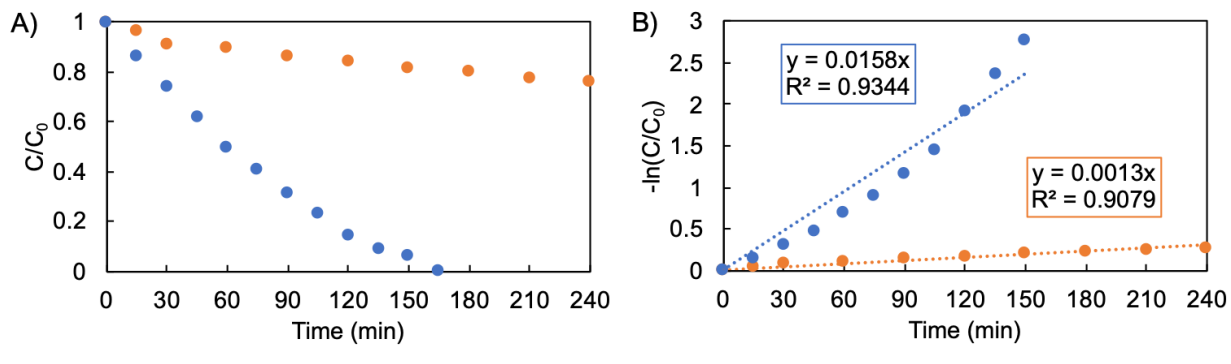

Figure 4.11: A) Comparison of RhB degradation performance of CTB2 (blue) to TA-BiOBr (orange), and B) Langmuir-Hinshelwood model of RhB degradation by CTB2 (blue) and TA-BiOBr (orange)

4.3.6 Incorporation of CNC-TA-BiOBr within calcium alginate hydrogels

In order to facilitate the easy recovery and immobilization of the CTB photocatalyst, the nanoparticle was mixed with sodium alginate solution and a hydrogel bead was formed via ionotropic gelation. Our previous study confirmed that CNC could be used as an active agent for the adsorption of cationic contaminants as well as a reinforcing agent [14]. Hence, we prepared hydrogels of different sizes using various ratios of alginate and CTB2. Photocatalytic hydrogel beads of 1 – 2 mm diameter were prepared using 0.5 – 2 wt% alginate via ionotropic gelation. **Figure 4.12a** shows RhB degradation by the CTB2 photocatalyst embedded in 2, 1 and 0.5 wt%

ALG beads as well as a control comprising 2 wt% ALG with no CTB2. The control shows that ALG exhibited little affinity towards RhB since equilibrium is reached after only 30 minutes and only about 8% dye absorbs. Thus, the ALG matrix is not able to remove RhB from the solution, confirming that the reduction in the concentration of RhB is due to the photocatalysis by CTB2. The beads containing CTB2 all appear to degrade RhB at similar rates between 0 to 60 minutes. Beyond this point, they deviated, with 0.5 wt% ALG beads showing a slower degradation, while the 2 wt% ALG sample exhibited the fastest. We hypothesize that a larger alginate content led to a tighter and narrower polymer cage surrounding the photocatalyst and assisted in directing the RhB molecules to the catalytic sites via Brownian motion. However, from the analysis of the data using Langmuir-Hinshelwood kinetic model (**Figure 4.12b**), the three sets of beads exhibited an identical k_{app} (between 0.0057 – 0.0059 min^{-1}), which seems reasonable since this value depended upon photocatalytic activity and surface area of the photocatalyst. This does infer that mass transfer barrier resulting from a tighter alginate network did not inhibit the photocatalytic performance of CTB amongst the other ALG-CTB samples, but perhaps only the CTB on the outer surface of the bead was degrading the dye based on the low degradation rate compared to the free CTB (**Figure 4.12a**). Moreover, the lower degradation rate of the ALG-CTB beads could be attributed to a slower mass transfer process as the RhB must diffuse into the bead to access internal CTB particles, of which these limitations are much less pronounced for free CTB particles. Since the ALG content of the hydrogel has a negligible effect on the photocatalytic performance of the hydrogel, additional experiments were conducted with 1 wt% ALG hydrogels since this offered an excellent balance between hydrogel strength (0.5 wt% ALG beads were weakest) and processability (2 wt% ALG formulations were too viscous to extrude through smaller hypodermic needles).

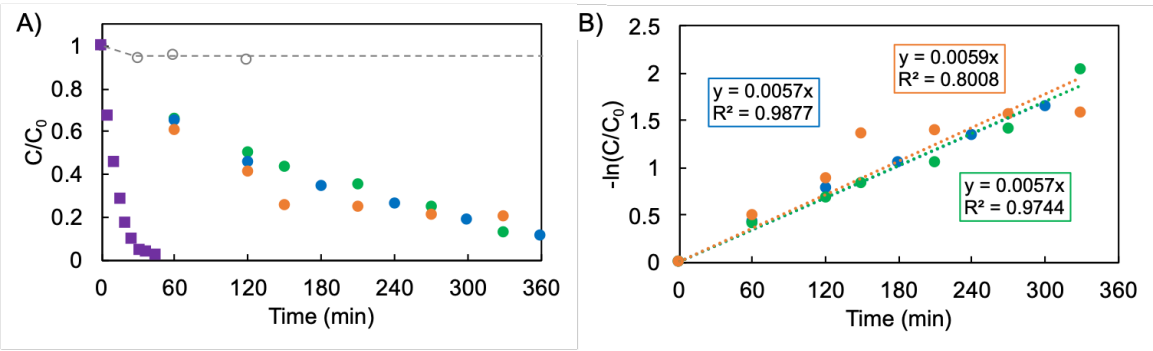

Figure 4.12: Degradation of RhB by CNC-TA-BiOBr/Alginate beads, A) Varying ALG content, 2 wt% ALG (orange circles), 1 wt% ALG (blue circles), 0.5 wt% ALG (green circles), 2 wt% ALG with no CTB (grey hollow circles), and free CTB2 (purple squares) B) Langmuir-Hinshelwood kinetics of dye degradation using beads, 0.5 wt% ALG (green), 1 wt% ALG (blue), and 2 wt% ALG (orange)

Figure 4.13a shows the results obtained when the same mass of smaller 1 mm beads was used. The 2 wt% ALG formulation was not used since the precursor solution was too viscous to be extruded through the 30G hypodermic needle to form beads with 1 mm diameter. The effect of hydrogel size reduction was very pronounced since the 1 mm beads degrades twice the amount of dye within the first 60 minutes compared to the 2 mm beads. This enhancement could be attributed to both an increase in the external surface area of the beads, where the 1 mm beads have twice the surface area to volume ratio as the 2 mm beads, as well as reduced mass transfer resistance due to smaller size. However, after 60 minutes, the reaction rate slowed and little difference was observed in the reaction rates of the two beads. **Figure 4.13b** presents the data using the Langmuir-Hinshelwood kinetic model, which incorporates the adsorption step of RhB onto the surface of the catalyst. The reaction rate with the 2 mm beads is determined to be 0.0057 min^{-1}, while the reaction rate of the 1 mm beads was 0.0088 min^{-1}, achieving a maximum at 0.0164 min^{-1} within the first 60 minutes. In order to understand this reduction in the reaction rate for the 1 mm beads, we analyzed and compared the UV-Vis spectra of the degraded RhB when contacted with pure CTB (**Figure 4.13c**), 2 mm (**Figure 4.13d**) and 1 mm (**Figure 4.13e)** beads. With the pure CTB photocatalyst,

a simultaneous reduction in the peak height as well as a gradual shift in the peak were observed, indicating simultaneous de-ethylation and chromophore cleavage. On the other hand, with the 2 mm beads, full de-ethylation to rhodamine (peak shift to 498 nm) occurs before the chromophore was fully degraded. This process was also observed for the 1 mm beads, where full de-ethylation occurred much more rapidly but the chromophore degradation appeared to proceed at the same rate as the 2 mm beads. These two competing reactions appeared to occur at different rates. The kinetic rates with the 1 mm beads was higher due to the larger surface area and so provided better performance for photocatalysis. The effect of reusing of the photocatalyst is also shown in **Figure 4.13a**. The 2 mm beads maintain their performance over the entire second cycle of reuse, whereas the 1 mm beads display no change up to 180 minutes but then deviate from the original cycle thereafter. Before being reused, the CTB2 beads were washed 3 times with MilliQ to remove bound degradation products. This step could have affected the integrity of the 1 mm beads resulting in some breakage. The 2 mm beads were likely more robust, capable of withstanding the mechanical shear experienced during washing. Therefore, an additional cross-linking step using $CaCl_2$ may be required for the 1 mm beads in order to improve their robustness in future photocatalytic applications.

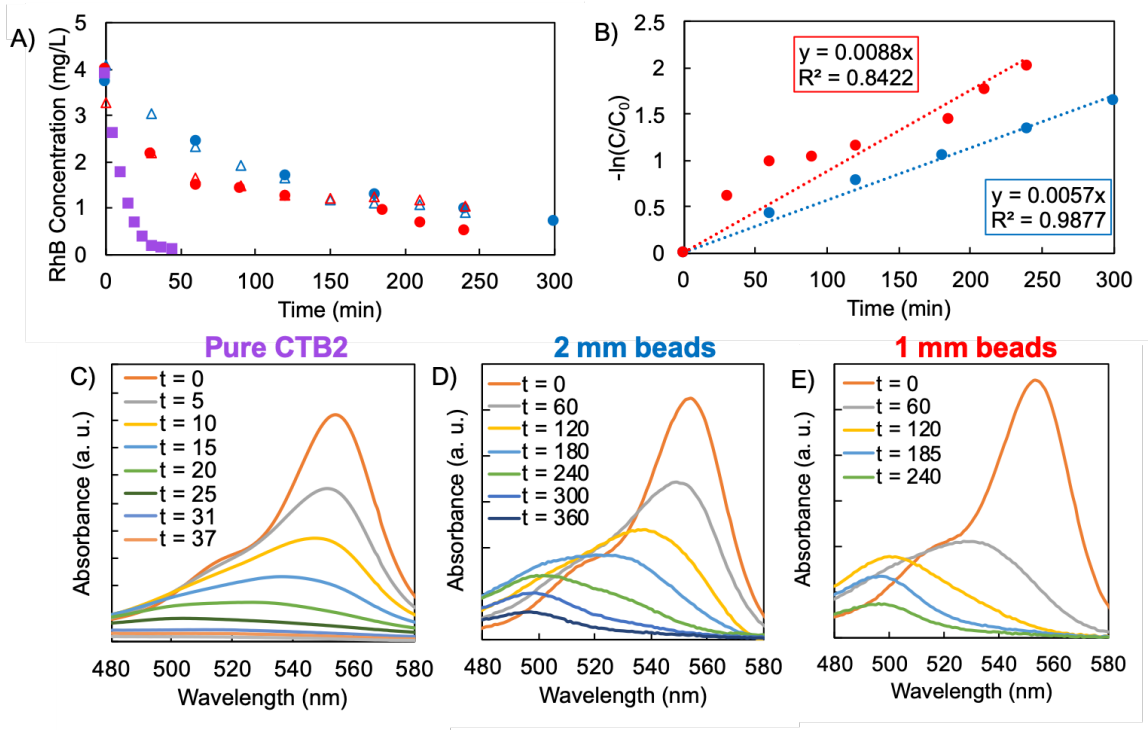

Figure 4.13: Degradation of RhB by CNC-TA-BiOBr/Alginate beads, A) Varying hydrogel diameter, 2 mm diameter (blue circles and triangles, C_0: 3.74 mg/L and 4.01 mg/L respectively), 1 mm diameter (red circles and triangles, C_0: 4.01 mg/L and 3.3 mg/L respectively), reusability also shown with circles and hollow triangles representing first use and washed/recycled beads, respectively, and free CTB2 (purple squares, C_0: 3.9 mg/L) B) Reaction rate using Langmuir-Hinshelwood model, 2 mm diameter beads (blue circles) and 1 mm diameter beads (red circles), and UV-Vis spectra of RhB during degradation using C) pure CTB2, D) 2 mm diameter beads, E) 1 mm diameter beads

4.4 Conclusions

In this study, a BiOBr photocatalyst was prepared using CNC-TA as a templating material. The photocatalytic activity of the nanocomposite could be tuned by modifying the amount of Bi^{3+} precursor. The photocatalyst degrades RhB dye under UV light. Quenching experiments revealed that O_2^- and h^+ are the main active species responsible for the degradation of RhB. CTB degraded the RhB via two simultaneous reaction steps: (1) successive de-ethylation of the molecule and (2) cleavage of the chromophore structure. The CTB2 photocatalyst was more effective than TA-BiOBr. Furthermore, it retained its ability to degrade RhB when incorporated into calcium alginate

beads in order to greatly facilitate recovery and separation from the treated media. The amount of alginate used to prepare the hydrogel matrix has little effect on its photocatalytic activity, although the beads with smaller diameter showed a more rapid degradation of the RhB due to the larger surface area to volume ratio. The promising photocatalytic performance of these BiOBr/CNCs nanocomposites suggests the feasibility of developing sustainable photocatalyst. Other $Bi_xO_yBr_z$ phases could be prepared as heterojunctions with other BiOX crystals to further improve the photocatalytic activity of the nanocomposite.

Chapter 5: Removal of Methylene Blue using Cellulose Nanocrystal-Alginate hydrogel beads in Self-loading Packed Columns*

In this chapter, we investigated the use of sodium alginate/cellulose nanocrystal (ALG-CNC) composite hydrogels to remove methylene blue (MB) from an aqueous solution in a fixed bed column. A self-contained unit to produce the ALG-CNC beads in-situ was developed. Batch adsorption studies using 0.5 wt% ALG and 2 wt% CNC beads were conducted and the Langmuir isotherm analysis yielded a maximum adsorption capacity of 410.5 mg MB/g adsorbent. Fixed bed column experiments were conducted at various initial dye concentrations, flow rates and adsorbent contents (bed height). The results were evaluated with a model accounting for fluid and particle phase continuity incorporating axial dispersion, film and pore diffusion. Good agreement between the fitted model and experimental data were observed. The effect of residual Ca^{2+} ions in the adsorbent during batch and column adsorption studies was elucidated, and found that it dye adsorption in the batch process more than in the column process. An initial shrinkage of the adsorbent in the column was associated with the loss of Ca^{2+} ions. On the other hand, the presence of Ca^{2+} interfered with the initial adsorption resulting in the observed overshoot in MB concentration profiles.

* This chapter is partially adapted from "Nathan Grishkewich, Kathryn Toffolo, Kam Chiu Tam, Removal of Methylene Blue using Cellulose Nanocrystal-Alginate hydrogel beads in Self-loading Packed Columns, *Manuscript under preparation*"

5.1 Introduction

Water is essential for life and a vital component needed for our daily activities, as well as maintaining all life forms on this planet. As water resources are shared, it is essential that we remove all traces of human activity from our water before it is discharged to the environment. This is especially important for industrial activities that may discharge pollutants that interfere with the life cycles of organisms. Industries involved in the production or processing of leather, paper and textiles often use dyes and pigments to color their products, resulting in large quantities of contaminated wastewater. Some of these dyes such as methylene blue (MB) are visible in water at concentrations below 1 ppm, and may also cause undesirable effects upon ingestion, such as nausea, diarrhea, and burning sensations [182],[183]. Thus, effective processes must be used to remove these contaminants from the water before discharge to rivers and lakes.

Sophisticated treatment processes such as adsorption [184], coagulation/flocculation [185], membrane separation [186], biological processes [187], and photocatalysis [188] have been developed to treat dyes found in effluent streams. Adsorption processes are attractive as they are easy to implement (typically with a low initial investment cost) and operate and are capable of removing a variety of contaminants [116],[189]. For small operations, batch adsorption processes are feasible due to the low volumes of waste generated. However, larger-scale industrial processes which require high throughput treatment operations commonly use adsorbents in fixed bed columns [35].

Activated carbon is a popular and widely used adsorbent due to its ability to remove a wide range of contaminants as well as its availability to consumers. However, the large carbon footprint associated with its production via high temperature activation processes make adsorbents from bio-renewable and sustainable sources more appealing [182],[190],[151]. Many bio-renewable materials, such as sodium alginate [25],[115], chitosan [191], starch [192],[193] and cellulose [8]

have been used to remove this dye among many others. A promising bio-renewable material for this application are cellulose nanocrystals (CNC), which have high surface area, excellent colloidal stability and has proven to adsorb MB [8],[10]. Various strategies have been used to facilitate the separation of CNCs from treated water, including immobilizing them within polymer matrices [119],[194] or functionalizing them with magnetic nanoparticles for separation via a magnetic field [195],[81]. We have previously used a method of embedding CNCs in a sodium alginate hydrogel matrix to produce hydrogel beads [14],[116]. The previous study only focused on the adsorbent behavior and column performance at short times, whereas the current study will examine the full column behavior as well as the mass transfer dynamics of the system.

In order to understand the dynamic mass transfer between bulk fluid and adsorbent in a fixed bed column, a mathematical mass transfer model will be considered. The model consists of equations describing the concentration of contaminant in the fixed bed, mass transport inside the adsorbent and equilibrium isotherm between the contaminant and the adsorbent [35]. This model is suitable to describe the flow dynamics for non-ideal cases that account for axial dispersion in the bulk fluid, external film diffusion and pore diffusion mass transfer within the adsorbent [196]. The advection-diffusion equation, pore diffusion model and the Langmuir isotherm were used to describe the mass transport within the bulk fluid, mass transport in the adsorbent and the adsorption equilibrium, respectively.

In this study, a composite hydrogel consisting of sodium alginate and cellulose nanocrystals was used to remove MB, from water. The performance and benefit of this adsorbent is demonstrated using a self-contained system that produces the adsorbent in-situ and loaded into a fixed bed vessel to remove MB from the wastewater. The effects of operating parameters such as initial dye concentration, flow rate and adsorbent content (fixed bed height) on the performance of the column were examined by monitoring the effluent concentrations. The results were then

used to validate the mathematical model describing the mass transfer processes occurring inside the fixed bed, such as axial dispersion, external film mass transfer and pore diffusion. In addition, the effects of calcium ion concentration on the uptake of dye as well as the bed height were evaluated to obtain a better understanding on bead expansion/shrinkage observed previously.

5.2 Materials and Methods

5.2.1 Materials

Cellulose nanocrystals (CNCs, spray dried) were supplied by CelluForce Inc. Sodium alginate (ALG, PROTANOL GP 3350) and methylene blue hydrate (MB) were purchased from FMC Corporation and Sigma Aldrich, respectively. Calcium chloride ($CaCl_2$) was purchased from Fisher Scientific, while MilliQ water was produced onsite using a MilliPore system (>18 MΩ/cm). Hydrochloric acid (37 wt%) was purchased from Sigma Aldrich and ethanol (99.9%) from onsite chemistry store. Perspex tubing of 1" (2.54 cm) outer diameter and 7/8" (2.22 cm) inner diameter were purchased from P&A Plastics Inc, Hamilton, Ontario.

5.2.2 Preparation of Adsorbent

The procedure for preparing the adsorbent was reported previously [14]. CNC-ALG beads were prepared by mixing CNC and ALG solutions and dispensing them through a hypodermic needle into an aqueous $CaCl_2$ gelation bath. In this study, the CNC-ALG composite solution was prepared by mixing equal volumes of 1 wt% ALG and 4 wt% CNC solutions, which was homogenized using a IKA-WERK Ultra-turrax homogenizer at 20,000 rpm for 5 minutes yielding hydrogel beads with a composition of 0.5 wt% ALG and 2 wt% CNC. For batch experiments, the ALG-CNC solution was extruded through a 22 G needle tip via a peristaltic pump at a flowrate of 5 mL/min into a 2 wt% $CaCl_2$ gelation bath, where the hydrogels were allowed to cross-link for 15 minutes. Following this, the beads were rinsed with MilliQ water, placed in a 14,000 MW cutoff dialysis bag and kept in deionized water for 3 days before subsequent adsorption experiments. For

column experiments, the CNC-ALG solution was dispensed through an array of 22 G needles via a peristaltic pump at a flow rate of 12.5 mL/min into a 2 wt% $CaCl_2$ solution that was cycled through the fixed bed vessel to randomly pack the beads. The hydrogel beads were formed upon contact with the gelation bath and allowed to crosslink for 15 minutes at neutral pH and 25°C. The beads were rinsed with 500 mL deionized water to remove residual $CaCl_2$ from their surface by pumping deionized water through the fixed bed column.

5.2.3 Characterization of adsorbent

The porosity of the beads was determined using a gravimetric method similar to that reported by Zhao *et al.* [197]. It was obtained using the following expression:

$$\varepsilon_p = \frac{(W_w - W_d)/\rho_w}{W_d/\rho_m + (W_w - W_d)/\rho_w} \tag{5.1}$$

where ε_p is the bead porosity, W_w (kg) and W_d (kg) are the weight of the hydrogel in the wet and dry state, respectively, ρ_w is the density of water (1000 kg/m^3) and ρ_m is the density of the dry hydrogel matrix (1600 kg/m^3). The radius of the adsorbent particles (R_p) was determined to be 1.00 ± 0.07 mm using a caliper.

5.2.4 Batch adsorption experiments

Experiments were conducted as described previously [14] to determine the equilibrium batch adsorption properties. Approximately 375 mg of dry adsorbent was immersed in 25 mL of dye solutions having concentrations of 345.2, 2078, 3066, and 4292 mg/L MB, for 180 minutes to allow equilibrium to be reached. The amount of dye uptake by the adsorbent is described by Eq. (5.2):

$$q = \frac{(C_0 - C_b)V_L}{m} \tag{5.2}$$

Measurement of the bulk dye concentration C_b at first allows q to be determined. Similarly, the equilibrium dye concentration (C_e) was used to obtain q_e. The Langmuir isotherm as given in Eq. (5.3) is known to describe the adsorption process:

$$q_e = \frac{q_m K_L C_e}{1+K_L C_e} \tag{5.3}$$

where K_L is the Langmuir constant (L/mg) and q_m is the theoretical maximum loading (adsorption capacity) of the adsorbent (mg/g). K_L and q_m will be determined using a non-linear regression analysis embedded in Microsoft Excel's SOLVER function. All adsorption experiments conducted were reproducible to within 10 % of their original value.

5.2.5 Fixed bed column adsorption experiments

Adsorption experiments were conducted in a 2.22 cm inner diameter Perspex column that can accommodate approximately 11 adsorbent particles along its diameter. Fitting at least 10 adsorbent particles along the diameter of the column has been known to limit channeling of fluid along the bed walls [35]. Water was introduced to the bottom of the column using a Watson-Marlow peristaltic pump 101U/R, and a stainless-steel mesh was placed 2.54 cm above the fluid inlet to support the adsorbent particles and ensure proper flow distribution at the column inlet. The adsorbents were produced by extruding the alginate-CNC solution through 32 22G needles (ID: 0.413 mm) and these spherical droplets formed robust beads in 2 wt% $CaCl_2$ after undergoing the ionotropic gelation process. The beads were then conveyed to the bottom of the column using a recycling stream that permitted the adsorbent to randomly pack in the column. Then, 500 mL of MilliQ water was pumped through the column to remove residual calcium ions for 1 hour to prepare the column for subsequent adsorption experiments. The peristaltic pump was adjusted to the correct flowrate by measuring the volume of eluted water over a known time interval. During the experiment, the column effluent would pass through a UV-Vis spectrophotometer fitted with

a flow-cell that provided real-time measurements of the MB concentration in the effluent. All the experiments were conducted at room temperature (25 ± 2 ºC) and neutral pH. Breakthrough curves were obtained by plotting C_b (mg/L) versus t (min). To calculate the equilibrium MB loading in the column after the bed became saturated, the following equation was used:

$$q_e = \frac{Q}{m}\int_0^{t_s}(C_0 - C_b(t))dt \tag{5.4}$$

where C_0 is the inflow MB concentration, Q is the flow rate (L/hr), m is the mass of adsorbent used (g) and t_s is the time when the effluent concentration is equal to C_0 (saturation time).

5.2.6 Effect of various operating parameters

The effluent concentration over time was used to assess the performance of the column for various operating parameters such as initial dye concentration, flow rate and adsorbent mass loading (bed height). The experiments were allowed to proceed to the saturation condition of the adsorbent ($C_b = C_0$).

5.2.6.1 Effect of initial dye concentration

The effect of initial dye concentration was examined at MB concentrations of 57, 111 and 158 mg/L. These experiments were performed at a flow rate near 0.497 L/hr and an adsorbent content of 6.25 g.

5.2.6.2 Effect of flow rate

The effect of flow rate on the column adsorption was evaluated at levels of 0.342, 0.497 and 0.60 L/hr with an initial dye concentration of 111 mg/L and 6.25 g adsorbent.

5.2.6.3 Effect of adsorbent mass

The effect of adsorbent amount (packing height) was assessed by using adsorbent mass of 3.13, 4.69, 6.25 and 7.81 g. These experiments were conducted at an initial dye concentration of 111 mg/L and at flow rate of 0.497 L/hr.

5.2.7 Regeneration of Adsorbent/Adsorbent Recycling

The eluent solution (1M HCl:ethanol (1:1 V:V)) was pumped through the column to desorb bound MB from the saturated adsorbent at a rate of 0.497 L/hr. Samples were removed from the column outlet and diluted in water in triplicate for further analysis by the UV-Vis spectrometer. Following elution, the adsorbent was washed with MilliQ water and soaked in 2 wt% $CaCl_2$ for 12 hours before the next adsorption experiment.

5.2.8 Mass transport modeling

Both batch and fixed bed systems were modeled using the mass transfer models described in references [35] and [29].

5.2.8.1 Modeling of mass transfer in batch system

As the CNC-ALG adsorbent is spherical, a model incorporating 1-D transport in the radial axis (r) was used. To form the basis of this model, the final step of adsorption will be assumed to occur more quickly in comparison to the transport of dye from the bulk solution to the adsorption site on the adsorbent [29]. As described earlier, the mass transport model used would incorporate both diffusion of MB from the bulk solution through the stagnant film boundary layer (film diffusion) to the adsorbent surface as well as diffusion into the pores of the adsorbent (pore diffusion). The boundary condition relating the bulk solution MB concentration to the concentration in the adsorbent pores at the exterior surface is as follows:

$$\frac{\partial C_b}{\partial t} = -\frac{3mk_f}{V_L \rho_p R_p}\left[C_b - C_{p,r=R_p}\right] \tag{5.5}$$

where C_b and C_p are the concentration of MB in the bulk solution and pore fluid respectively, m is the mass of adsorbent, k_f is the film diffusion coefficient (m/s), V_L is the volume of the liquid medium, ρ_p is the density of the adsorbent (kg/m^3), R_p is the radius of the adsorbent particle. This equation has the following initial conditions:

$$C_b = C_b(0) = C_0 \tag{5.6}$$

In describing the transport of dye within the adsorbent, the pore diffusion model for spherical adsorbents was used:

$$\rho_p \frac{\partial q}{\partial t} + \varepsilon_p \frac{\partial C_p}{\partial t} = D_p\left[\frac{1}{r^2}\frac{\partial}{\partial r}\left(r^2 \frac{\partial C_p}{\partial r}\right)\right] \tag{5.7}$$

where q is the concentration of MB on the adsorbent in the adsorbed phase, D_p is the pore diffusion coefficient (m^2/s), and ρ_p and ε_p were determined experimentally. This equation has the following initial and boundary conditions:

$$C_p = C_p(0,r) = 0 \tag{5.8}$$

$$q = q(0,r) = 0 \tag{5.9}$$

Boundary conditions:

$$r = 0,\ t > 0; \quad \frac{\partial C_p}{\partial r} = 0 \tag{5.10}$$

$$r = R_p,\ t > 0; \quad \frac{\partial C_p}{\partial r} = \frac{k_f}{D_p}(C_b - C_{p,r=R_p}) \tag{5.11}$$

To relate the concentration of MB in the pore fluid and on the adsorbent surface (pseudo-equilibrium) Eq (5.12) was used:

$$\frac{\partial q}{\partial C_p} = \frac{K_L q_m}{(1+ C_p K_L)^2} \tag{5.12}$$

Equations (5.5) and (5.7) were solved numerically using a finite difference method, and the resulting algebraic equations along with Eq (5.12) were solved simultaneously using MATLAB®, using 41 nodes for the radial coordinate with a timestep of 1 s.

Both k_f and D_p were adjusted in the model as these controlled in impact of the film diffusion and pore diffusion processes during batch adsorption, and the model was fitted to the experimental data. To evaluate the model in describing the experimental data, the root-mean-square error (RMSE) for the bulk dye concentration was evaluated, Eq. (5.13):

$$RMSE = \frac{1}{C_0}\sqrt{\frac{1}{N}\sum_{i=1}^{N}\left(C_{b,exp}(t_i) - C_{b,calc}(t_i)\right)^2} \tag{5.13}$$

where $C_{b,exp}$ and $C_{b,calc}$ are the experimental and calculated bulk dye concentrations respectively.

5.2.8.2 Modeling of mass transfer within fixed bed

The advection-diffusion equation (continuity equation in the bulk-fluid phase) with dispersed flow and film diffusion was used to model the concentration of dye in the bulk [198].

$$\frac{\partial C_b}{\partial t} = D_b \frac{\partial^2 C_b}{\partial z^2} - v\frac{\partial C_b}{\partial z} - \frac{3k_f(1-\varepsilon_b)}{R_p \varepsilon_b}[C_b - C_{p,r=R_p}] \tag{5.14}$$

The model assumes 1-D transport in the z-direction, where D_b is the axial dispersion coefficient of the fluid flow (m^2/s), v is the interstitial flow velocity (m/s), and ε_b is the bed void fraction. k_f is determined by the correlation of Wilson and Geankoplis [37]:

$$k_f = \frac{1.09 D_m}{2\varepsilon_b R_p}\left(\frac{\mu_w}{\rho_w D_m}\right)^{1/3} Re^{1/3} \tag{5.15}$$

where D_m is the molecular diffusivity of MB in water (m^2/s), μ_w is the viscosity of water (Pa.s), and Re is the Reynolds number. The axial dispersion coefficient (D_b) was determined by [38]:

$$D_b = \frac{\mu_w}{\rho_w} \frac{Re}{0.2+0.011Re^{0.48}} \tag{5.16}$$

With Reynolds number (Re) defined as:

$$Re = \frac{2\rho_w v R_p}{\mu_w} \tag{5.17}$$

The Biot number (Bi) was used to determine whether external mass transfer (film diffusion) or intraparticle diffusion (pore diffusion) were the controlling mass transfer step, which is given by:

$$Bi = \frac{k_f R_p}{\epsilon_p D_p} = \frac{film\ mass\ transfer}{intraparticle\ mass\ transfer} \tag{5.18}$$

The following initial and boundary conditions were used in Eq (5.14):

$$C_{b0} = C_b\,(0,z) = 0 \tag{5.19}$$

$$\text{At inlet: } z = 0,\ t > 0;\quad \frac{\partial C_b}{\partial z} = \frac{v}{D_b}(C_b - C_0) \tag{5.20}$$

$$\text{At outlet: } z = L,\ t > 0;\ \frac{\partial C_b}{\partial z} = 0 \tag{5.21}$$

where C_0 is the feed dye concentration. Similar to the batch system, Eq. (5.12) was used to relate the amount of dye adsorbed on the surface to the concentration of dye in the pores. Eqs. (5.7) and (5.14) were solved numerically using the finite difference method. The resulting algebraic equations along with Eq (5.12) were solved simultaneously using MATLAB® using 41 z nodes, 21 r nodes and a timestep of 1 s. To evaluate the ability of the model to fit the experimental data, the root-mean-squared error for the breakthrough curve was evaluated, using Eq. (5.13) in a similar manner. **Table 5.1** lists the parameters and their values used in the mass transfer model.

Table 5.1: Parameters used for modelling

Parameter	Description	Value
ε_b	Bed void fraction	0.41
ε_p	Bead porosity	0.962
μ_w	Viscosity of water (Pa*s)	8.9×10^{-4}
ρ_p	Density of adsorbent (kg/m^3)	35
ρ_w	Density of water (kg/m^3)	1000
D_m	Molecular diffusivity of methylene blue (m^2/s)	8.31×10^{-10} [199]
R_p	Radius of adsorbent particle (m)	0.001

5.2.9 Calcium Elution experiments

The concentration of $CaCl_2$ leaving the beads was monitored in batch and column experiments using an ion selective electrode (ISE). For batch experiments, Ca^{2+} was measured by immersing the ISE into the batch vessel for the duration of the experiment. For column experiments, Ca^{2+} was measured by immersing the electrodes in a beaker serving as a continuous stirred vessel fed by the effluent from the column, while an outflow emptied the vessel at the same flowrate to maintain a constant volume. To calculate the true concentration of Ca^{2+} leaving the column (i.e. the input to the measurement vessel), the following equation was used:

$$C_0 = \frac{dC}{dt}\frac{V}{Q} + C \tag{5.22}$$

where C is the concentration of Ca^{2+} measured by the ISE in the measuring vessel, V is the volume of the measuring vessel (mL), Q is the flowrate through the vessel (and conversely the column), and C_0 is the concentration of Ca^{2+} leaving the column and entering the measuring vessel. dC/dt was determined by central difference approximation:

$$\frac{dC_i}{dt} = \frac{C_{i+1} - C_{i-1}}{2\Delta t} + O(\Delta t)^2 \tag{5.23}$$

Where C_{i+1} and C_{i-1} represent the measured concentrations measured after and before C_i, respectively (mg/L), Δt is the time measurement interval (s), and $O(\Delta t)^2$ represents the associated residual error.

5.2.10 Instrumentation

5.2.10.1 UV-Vis Spectrophotometry

The concentration of MB was determined using a Cary 100 UV-Vis spectrophotometer for the batch adsorption experiments, and a calibration curve was obtained by measuring the absorbance at λ = 664 nm to determine the initial and final concentrations of the batch system using the Beer-Lambert law. This was used for samples diluted in the range of 0.1 – 5 mg/L. Similarly, a Cary 300 UV-Vis spectrophotometer was used for the continuous experiments, where the effluent from the column was pumped to a quartz flow-cell with a path length of 500 μm. The calibration curve was determined by measuring absorbance at λ = 610 nm as this was found to vary linearly with concentration within the range of 0.1 – 200 ppm MB.

5.2.10.2 Ion selective electrode

The concentration of $CaCl_2$ diffusing from the beads was monitored in both the batch and column experiments. An ORION calcium ion selective electrode and Metrohm AgCl reference electrode were immersed in the solution and the Ca^{2+} concentration was monitored via a Metrohm Potentiometric Titrator. A calibration curve was used to convert the measured signal to Ca^{2+} concentration.

5.3 Results and Discussion

5.3.1 Preparation of Adsorbent

The preparation and characterization of the adsorbent was outlined in our previous publication [14]. The amount incorporated into the hydrogels was increased from 1 wt% in our

previous work to 2 wt% to increase the adsorption capacity of the adsorbent. The internal porosity of the gel (ε_p) was determined by gravimetric methods by measuring both the wet and dry mass of a sample of 30 hydrogels and using Eq (5.1) to calculate a porosity of 0.962. This value is in agreement with the solid content of the beads, which was 3.71 wt% after ionotropic gelation.

5.3.2 Batch Adsorption Experiments

The equilibrium properties of the adsorbent were determined from the batch experiments and then used to analyze the results from the column tests. **Figure 5.1** shows the equilibrium isotherm obtained in this way. The dashed line represents the fit of the Langmuir isotherm to the experimental data [14]. In this study, the model parameters were determined using a non-linear regression as opposed to linearizing the isotherm expression since the latter process alters the error structure of the expression and leads to parameters with larger uncertainty [189]. The maximum adsorption capacity (q_m) and Langmuir constant (K_L) were determined to be 401.8 mg/g and 7.9 m^3/kg, respectively. The maximum adsorption capacity of this adsorbent was 60% higher than our previous study, due to the higher mass of CNC present.

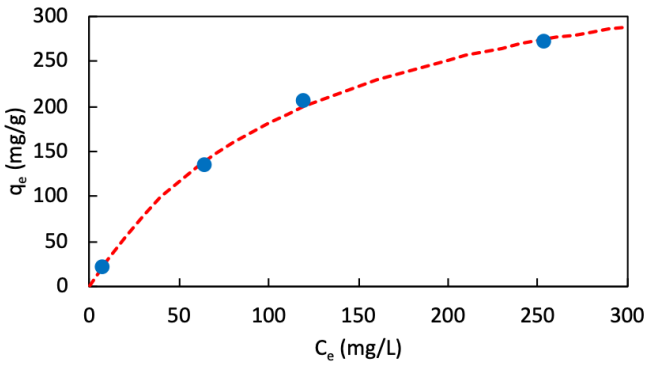

Figure 5.1: Equilibrium adsorption data of 0.5 wt% ALG – 2 wt% CNC adsorbent from various initial concentrations of MB.

5.3.3 Batch Kinetic Experiments

To ensure that equilibrium was achieved within 180 minutes, the concentration of the bulk MB dye was measured as a function time during the batch experiments. **Figure 5.2** shows the variation of the concentration of bulk dye in solution with time at various initial MB dye concentrations. The adsorption of MB on alginate-CNC was previously found to obey pseudo-second order behavior [14]. In this study, we examined the mass transfer process using the pore transport model with film diffusion. This approach is necessary to determine the film mass transfer (k_f) and pore diffusion (D_p) coefficients, which are required to model the mass transport processes in column studies [29],[30]. The fitted curves are denoted by the red dashed line in **Figure 5.2**.

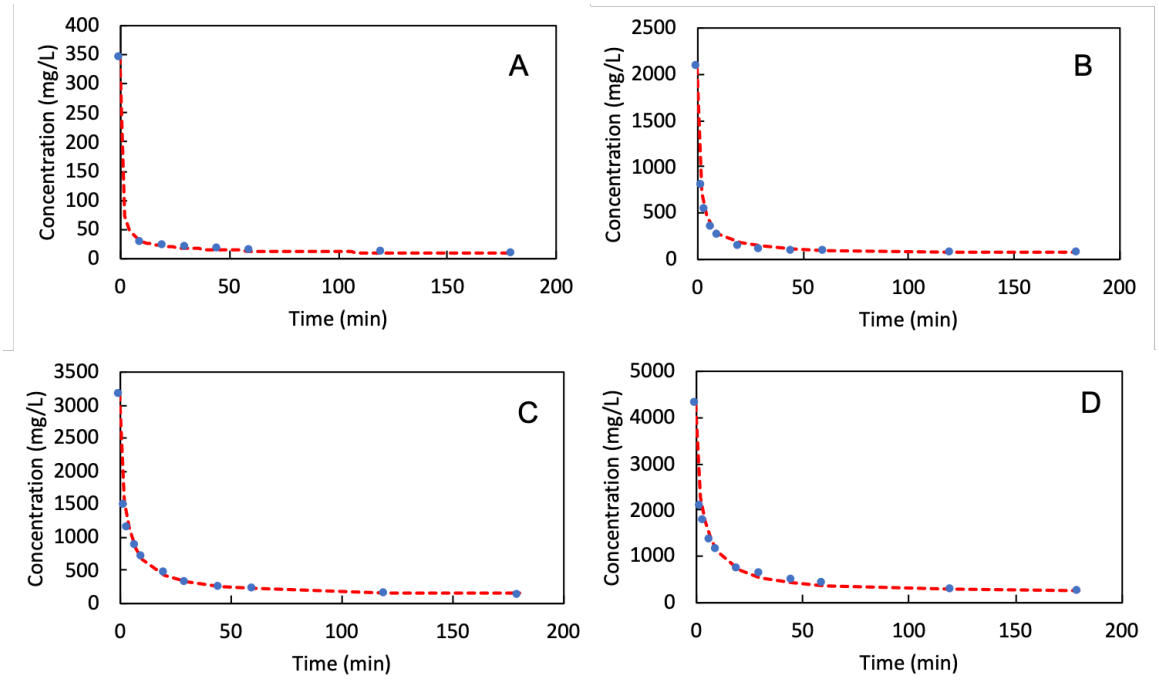

Figure 5.2: Batch kinetic experiments showing the uptake of dye by the 0.5 wt% ALG 2 wt% CNC adsorbent with time (blue circles) for C_0 of 345.2 mg/L (A), 2055 mg/L (B), 3165.9 mg/L (C), and 4291.9 mg/L (D). The mass transport model incorporating film diffusion and pore diffusion was used to model each data set (red dashed line)

When dealing with a new adsorbate/adsorbent mixture, the k_f and D_p are unknown. The value of k_f could be estimated from the slope at t = 0 of $\ln(C/C_0)$ vs. time, which was obtained by integrating Eq (5.5) and assuming C_p to be 0 at t = 0 as described by [29]:

$$k_f = -\frac{V_L R_p \rho_p}{3m} \frac{d\left(\ln\left(\frac{C}{C_0}\right)\right)}{dt}_{t=0} \tag{5.24}$$

This value was then used in the model (Eqs 5.5 – 5.12) to determine D_p by optimizing the fitting of the data by minimizing the RMSE. However, the minimal RMSE appeared large (**Table 5.2**), which was largely due to the poor fitting of the rapid adsorption region within the first 10 minutes. The bulk dye concentrations predicted were much higher than the experimental values, implying that the predicted k_f from Eq (5.24) was too small. Hence, k_f values were varied instead to minimize RMSE over the entire time range. This yielded k_f values that were an order of magnitude larger than that obtained using Eq. (5.24) and a smaller RMSE (**Table 5.2**).

The k_f values obtained at the 4 MB concentrations ranged from 5.16 to 6.53 x 10^{-5} m/s, with only minor variation since this mass transfer coefficient is related to the agitation speed of the batch vessel and the molecular diffusion of the adsorbate in solution, which is a function of temperature. Likewise the D_p values ranged from 3.5 x 10^{-10} m^2/s to 5.6 x 10^{-10} m^2/s, which is dependent on the inner pore geometry of the adsorbent, as well as the molecular diffusion of the adsorbent that is dependent on temperature [29].

The calculated D_p values were in agreement with the values reported by other research groups for the adsorption of large molecules on aromatic structures. Li *et al.* reported a D_p value of 4.12 x 10^{-10} m^2/s for phenol adsorption on activated carbon [30], while Saraydin *et. al* reported a value of 2.12 x 10^{-10} m^2/s for the adsorption of brilliant cresyl blue (a dye with a similar structure to MB) on acrylamide/maleic acid hydrogels [200]. In addition, Mohammed *et al.* obtained a

diffusion coefficient of 1.01 x 10^{-10} m^2/s for adsorption of heavy metal ions onto alginate hydrogel beads [201]. Thus, a D_p of 5.6 x 10^{-10} m^2/s was used since this corresponded to the smallest RMSE for the fitting of the data with the mass transport model and was also obtained with a C_0 that was within the range the column experiments would be conducted.

Table 5.2: Fitting parameters for batch kinetic experiments

C_0 (mg/L)	C_e (mg/L)	q_e (mg/g)	k_f est (m/s)	**RMSE**	D_p (m^2/s)[b]	k_f (m/s)[b]	**RMSE**
345.2	7.9	21.6	$6.53*10^{-6}$ [a]	0.0123	$5.6*10^{-10}$	$6.53*10^{-5}$	0.0028
2078.0	64.7	136.1	$6.53*10^{-6}$	0.0374	$5.3*10^{-10}$	$6.53*10^{-5}$	0.0152
3165.9	119.2	206.7	$5.22*10^{-6}$	0.0432	$3.5*10^{-10}$	$5.22*10^{-5}$	0.0091
4291.9	253.6	271.5	$5.16*10^{-6}$	0.0537	$3.6*10^{-10}$	$5.16*10^{-5}$	0.0156

[a]Could not directly predict k_f from data

[b]These were the values used to produce the red dashed line in **Figure 5.2**

5.3.4 Development of self-contained system

The following sections describe the design considerations for a unit capable of forming CNC-ALG beads and conveying them into a fixed bed vessel for dye removal.

5.3.4.1 Development of adsorbent producing unit

One key feature in the design and construction of the self-contained system is the capability of the system to produce adsorbents and transport them to the column. The beads were produced by extruding the adsorbent solution through a hypodermic needle into a gelation bath of calcium chloride and beads of 2 mm diameter was produced via ionotropic gelation. A syringe pump and a single syringe was used in batch experiments to extrude the solution into a beaker to produce the beads (**Figure 5.3a**). A scalable adsorbent producing unit (APU) consisting of a perforated plate with 32 hypodermic needles was designed as shown in **Figure 5.3b**. The APU enabled for the continuous production of beads using a peristaltic pump to convey the absorbent solution via 32 hypodermic needles.

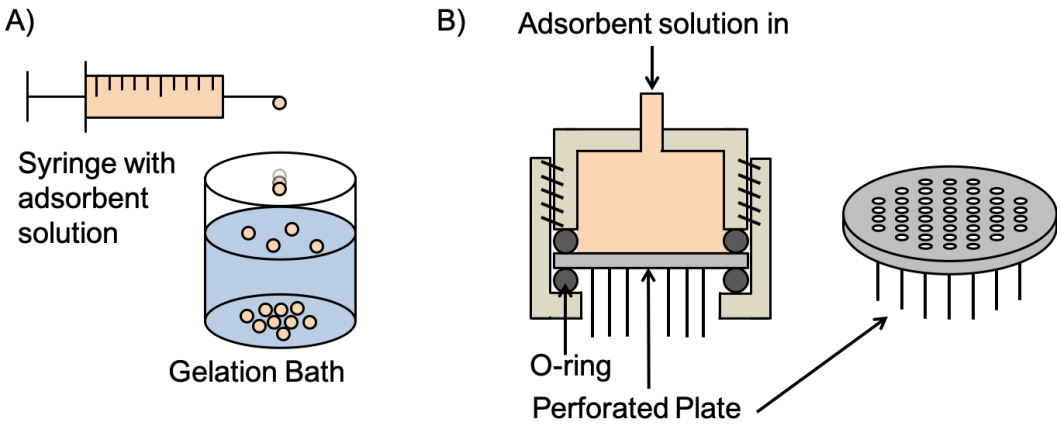

Figure 5.3: A) Diagram of batch production of CNC-ALG beads using a syringe and gelation bath, B) Diagram of APU showing adsorbent solution comprising of a vessel with perforated plate through which the hypodermic needles extrude the beads

5.3.4.2 Operation of self-loading column

Once the adsorbent particles were produced, they were conveyed to the adsorption column to form a uniform packing that preserved the integrity of the hydrogel. Since the beads comprised of 96% water, they tended to remain near the air/water interface on entry to the gelation bath and subsequently migrate to the bottom of the column as the beads were cross-linked by the calcium ions. The APU was installed above the fixed bed vessel so that gravity could be used to convey the beads to the column. Additionally, a recycling stream was introduced to the top of the column that forced the beads to flow to the bottom of the column. **Figure 5.4a** shows the experimental set-up of the continuous bead formation and adsorption system for dye removal, while **Figure 5.4b** shows a schematic diagram of the processing unit preparing the adsorbent.

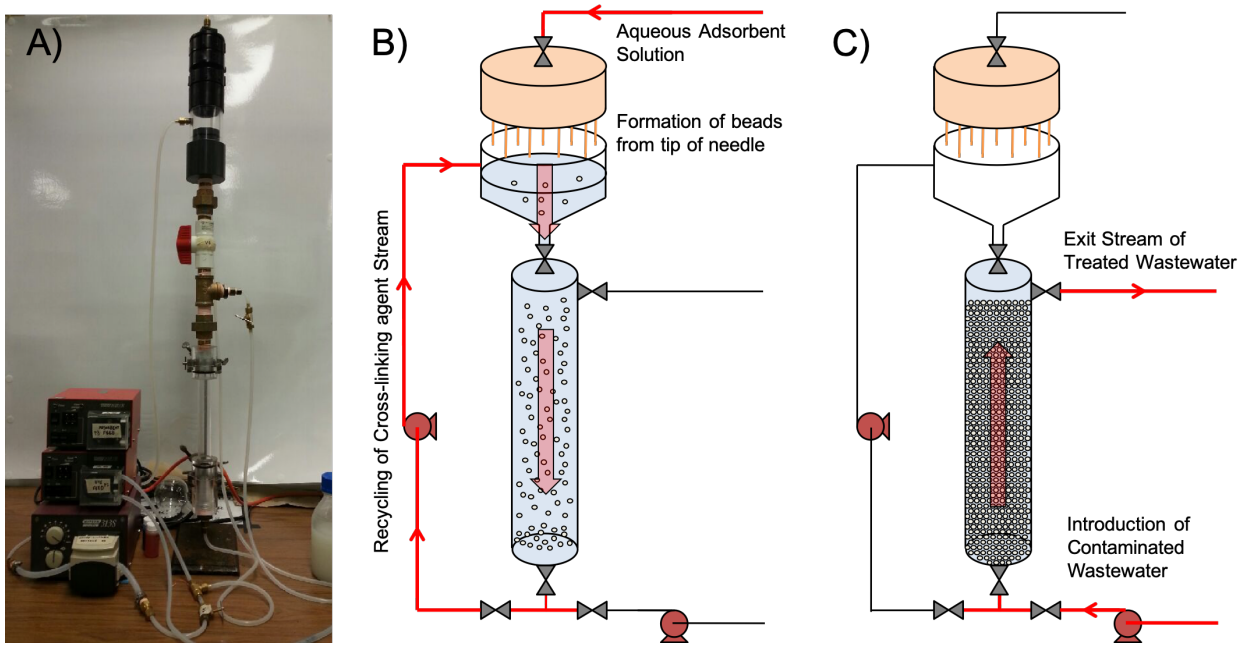

Figure 5.4: A) Photograph of self-loading column with adsorbent producing unit located on top and the fixed bed vessel below, B) Process flow diagram of self-contained system operating in adsorbent production mode, C) Process flow diagram of self-contained system operating in wastewater treatment mode

The self-loading of fresh adsorbent into the fixed bed vessel operated efficiently and the adsorbent was conveyed into the column when the cycling flow of cross-linker was kept at 179.4 mL/min. This generated a superficial velocity of 46.2 cm/min through the 2.22 cm column, allowing the beads to pack in a random fashion that gave rise to a desirable flow distribution during the wastewater treatment phase. The adsorbent was conveyed from the APU to the fixed bed column using a PVC tube with a reducing diameter from an ID of 5.72 to 2.22 cm (being the ID of the fixed bed vessel) over a length of 7.5 cm. After demonstrating the self-loading capabilities using the APU, it was necessary to optimize the operation of the APU. For the 5.72 cm diameter APU, 32 hypodermic needles could be installed giving an upper limit on the number of beads produced per second while considering the time it would take for beads to migrate from the air/water interface into the column. This constrained the flowrate of adsorbent solution into the APU, which was determined to be a maximum of 12.5 mL/min for a 2.22 cm diameter bed. Once the beads

were packed into the column, it was then switched to the wastewater treatment mode, as shown in **Figure 5.4c**. During this mode, the wastewater flowed from the bottom of the column through the adsorbent with minimal channeling and the column operated until the adsorbent became saturated. Thereafter, it was regenerated by flowing a solution of 1 M HCl:ethanol (1:1 V:V) through the bed until the most of the bound MB was removed from the beads (by measuring the effluent concentration), and the bed could be reused for subsequent adsorption tests.

5.3.5 Column Adsorption experiments

When operating a water treatment system, key operating parameters, such as initial dye concentration, flow rate, and adsorbent amount will have a large impact on the column performance. 8 runs were conducted, and these 3 parameters were varied while the effluent concentration was monitored, and the resulting adsorption capacity (Q_e), as well as model parameters D_p, k_f, D_b, and RMSE are summarized in **Table 5.3**.

Table 5.3: Parameters determined from column experiments and mass transport model

Run #	1	2	3	4	5	6	7	8
C_0 (mg/L)	56.6	111.1	158.2	115.4	117	115	108.3	110.2
Q (L/hr)	0.492	0.492	0.492	0.342	0.6	0.453	0.462	0.48
m (g)	6.25	6.25	5.63	6.44	6.25	3.13	4.69	7.81
$Q_{e\ exp}$ (mg/g)	367.9	377.9	392.2	379.9	374	368.9	380.5	382.2
$Q_{e\ calc}$ (mg/g)	362.4	381.2	388.7	380.2	388.2	384.3	379.5	381
D_p (m^2/s) ($\times 10^{10}$)	5.60	5.60	5.60	5.60	5.60	5.60	5.60	5.60
k_f (m/s) ($\times 10^5$)	1.42	1.42	1.40	1.25	1.51	1.38	1.39	1.40
D_b (m^2/s) ($\times 10^6$)	8.03	8.01	7.74	5.63	9.70	7.40	7.54	7.82
Re	1.940	1.936	1.869	1.346	2.361	1.783	1.818	1.889
Bi	26.28	26.27	25.96	23.27	28.06	25.55	25.72	26.05
RMSE	**0.044**	**0.043**	**0.023**	**0.032**	**0.038**	**0.040**	**0.023**	**0.037**

Figure 5.5a shows the breakthrough curves for runs 1, 2 and 3 for initial dye concentration of 56, 111, to 158 mg/L respectively. A reduction of the initial dye concentration prolonged the breakthrough time. When the adsorbent was exposed to less dye per unit volume of treated wastewater, thus it took a larger throughput of dye at low concentration to reach the breakthrough compared to a more concentrated influent. This lower dye concentration also resulted in a smaller slope in the breakthrough profile since the driving force for dye adsorption was lower at smaller inlet concentrations [202]. Similarly, increasing the dye concentration will result in earlier breakthrough times, although in run 3 this effect was also compounded by the lower amount of

adsorbent used. **Figure 5.5b** shows the breakthrough curves for runs 4, 2 and 5 at flow rates of 0.342, 0.49 to 0.60 L/hr respectively. When the flowrate was increased, the breakthrough point occurred sooner, which was also observed in other studies [30],[202],[203], since the earlier breakthrough at higher flowrates is due to the adsorbent being exposed to more dye, which became saturated in shorter times. Additionally, there will be a competitive effect between the rate of uptake on the adsorbent in the column as well as rate of convection through the bed that will cause dye to proceed farther down the bed before being adsorbed, which will result in shorter breakthrough times at high flow rates. Plotting this same set of data as C/C_0 vs. bed volumes treated (**Figure 5.5d**) reveals that the same volume of wastewater was treated prior to saturation for each experiment, which is expected because the amount of adsorbent used and initial concentration of dye solution were kept near constant. This further validates that the fixed bed operated properly within the range of flow rates studied for these experiments. **Figure 5.5c** shows the breakthrough curves for runs 6, 7, 2 and 8 in which the mass of adsorbent was varied from of 3.13, 4.69, 6.25 to 7.81 g respectively. Not surprisingly, the breakthrough curve shifted to longer times with increasing adsorbent content. Since the amount of adsorbent in the bed increased, this would increase the capacity of the bed to remove dye and thus increase the breakthrough time [204]. Varying each of the operating parameters in these runs produced the anticipated result in accordance with proper fixed bed operation, which verifies the ability of CNC-ALG beads to be used in a fixed bed vessel for continuous water treatment.

5.3.6 Column experiment Modeling

To design a fixed bed column to operate at a desired flowrate and initial dye concentration, a comprehensive understanding of the mass transfer phenomena during operation is necessary. Furthermore, to ensure any given model provides an adequate prediction of the adsorption process, validation to experimental data is needed. Thus, the breakthrough curves were modeled using the

advection-diffusion equation incorporating dispersed flow, film diffusion and pore diffusion (Eqs. (5.14) – (5.21)) to determine the influence of film diffusion and pore diffusion on the fixed bed operation, and the RMSE (Eq. (5.13)) was calculated to determine their capability to predict the breakthrough profile.

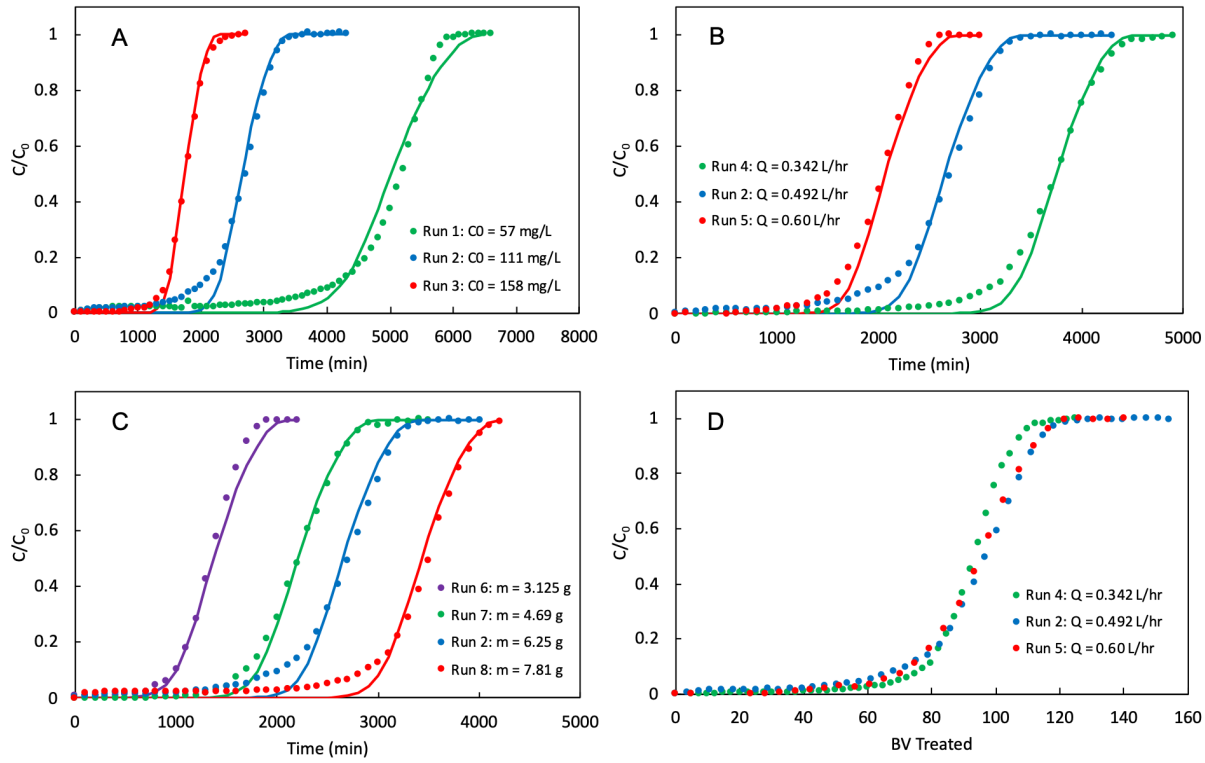

Figure 5.5: (A) Breakthrough curves of Runs 1, 2 and 3 at the initial dye concentration of 56, 111 and 158 mg/L, with the flow rate kept constant at 0.497 L/hr and adsorbent amount of 6 g, (B) Breakthrough curves of Runs 4, 2, and 5 at flow rates of 0.342, 0.492 and 0.60 L/hr, with the initial dye concentration kept constant near 114 mg/L and adsorbent amount of 6.3 g, (C) Breakthrough curves of Runs 6, 7, 2, and 8 at adsorbent content of 3.13, 4.69, 6.25 and 7.81 g respectively, with the initial dye concentration kept constant at 111 mg/L and a flow rate of 0.48 L/hr, (D) Breakthrough curves of concentration vs. volume treated at varying flow rates. Note that each experiment appears to have a similar breakthrough profile. All solid lines were predicted result from mass transfer equations using parameters in **Table 5.3**

Although the model was formulated to determine the concentration of MB at any point in the column, the mass of adsorbent used (m) in each experiment was readily converted to bed height

by taking into account the cross-sectional area of the column (3.878×10^{-4} m^2) as well as the density of the adsorbent in the column (21.61 kg/m^3). Under normal circumstances, the equilibrium parameters of the adsorbent with MB determined from batch experiments would be used when modelling the adsorption in a fixed bed column. However, some discrepancy was noted in the column experiments when the equilibrium loading Q_e was calculated. **Table 5.3** summarizes the equilibrium loading of the adsorbent for each column experiment, which could be used to estimate equilibrium parameters using the Langmuir Isotherm [35]. **Figure 5.6** shows the equilibrium curve obtained from the column and batch experiments. The most noticeable difference between the two data sets is the calculated Langmuir constant, where the column K_L was 23 times larger than the batch K_L (183.7 m^3/kg vs. 7.9 m^3/kg). This implies that the MB had a higher affinity to the CNC-ALG adsorbent during column operation, as evident from the slope of the equilibrium curve at low C_e values. The q_m values determined from the column and batch equilibrium data were 410.5 mg/g and 401.8 mg/g respectively, which is reasonable since the number of adsorption sites would be similar for the two operations.

Thus, one possible explanation for the differing K_L values could be associated with the calcium ions present in the adsorbent. Since the batch system is a closed system, any Ca^{2+} ions that leach from the beads during adsorption would migrate to the bulk solution, resulting in a higher ionic strength that would reduce the binding of MB onto the adsorbent. This behavior was observed when using different concentrations of NaCl when performing batch adsorption experiments [14]. In the case of the column studies, the constant flow of MB solution removed Ca^{2+} ions from the column due to the flow of dye solution, which reduced this interference and improved the partitioning of MB onto the adsorbent. Section 5.3.7 will investigate this effect in greater detail, and for the following modelling operations, the equilibrium parameters used were those calculated from the column adsorption experiments.

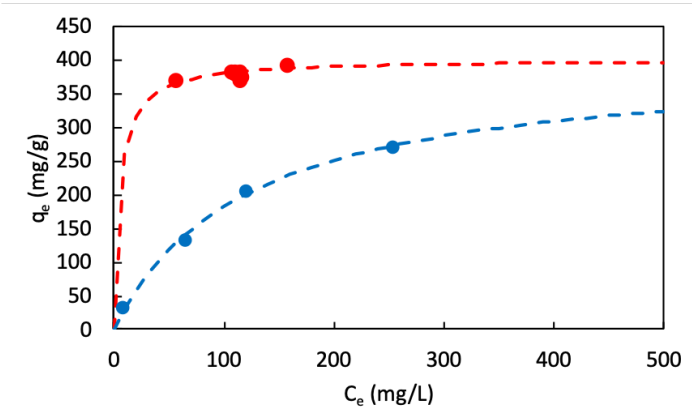

Figure 5.6: Langmuir Isotherm estimated from batch (blue points) and column equilibrium data (red points)

Figures 5.5a-c shows the fit of the mass transport model to the column data (denoted by the solid line) with the corresponding modelling parameters, such as the pore diffusion coefficient (D_p), film diffusion coefficient (k_f), axial dispersion coefficient (D_b), as well as Reynolds number and Biot number listed in **Table 5.3**. In **Figure 5.5a**, the fit for run 3 (C_0 of 158 mg/L) run was excellent. In addition, the model could accurately predict breakthrough for the other experiments (runs 1 and 2) although it cannot accurately predict the behavior prior to breakthrough. In **Figure 5.5b**, the model shows an adequate fit for run 5 (0.60 L/hr) and accurately predicts the time of breakthrough for run 4 (0.342 L/hr), but again it is not able to predict the behavior before breakthrough. From **Figure 5.5c**, it is evident that the model accurately predicts the breakthrough profiles for runs 6 and 7 (m = 3.13 g and m = 4.69 g runs), whereas it predicts breakthrough at a slightly earlier time for run 8 (m = 7.81 g) and again it fails to predict the behavior prior to breakthrough for runs 6 and 8. For the majority of the runs, the mass transport model cannot predict the behavior observed before breakthrough, as reflected by the residual MB leaving the column.

This phenomenon may have been due to the presence of residual Ca^{2+} ions that inhibit the uptake of cationic contaminants into the alginate beads. This behavior was observed by An *et al.* for the adsorption of Cu^{2+} ions onto calcium alginate beads [205], which will be discussed in

greater detail in section 5.3.7. Beside the initial residual flow of MB through the column, we could assess the model prediction of the breakthrough for the CNC-ALG system by calculating the Q_e for both the experimental and model data, as well as the RMSE as summarized in **Table 5.3**. The model appears to provide good estimates of the equilibrium adsorption capacity, with the RMSE lower than 0.045 for all the tests. Using this model, we could see the effect of the operating parameters of the mass transfer occurring within the column. When the flowrate was increased between runs 4 and 5, k_f and D_b increased, which also resulted in an increase in *Re* and *Bi* values. In comparison, these numbers remained constant for runs 1, 2, 3, 6, 7 and 8 when the initial dye concentration and adsorbent mass were varied and the flowrate was constant. k_f and D_b depend on the hydrodynamic conditions inside the column, such as flow velocity, where an increasing flowrate would improve the film mass transfer due to a reduced film thickness, but it would induce greater axial dispersion [202]. Another important parameter that provides insight into the mass transport within the column is the Biot (*Bi*) number. By definition, the Biot number is a measure of the influence of both external and intraparticle mass transfer on the overall mass transfer rate in the column [206]. When the Biot number is high (>50), film diffusion is fast and intraparticle diffusion controls the overall mass transport, and vice versa for low Biot numbers (<0.5). In all the experimental runs, the *Bi* number ranges between 23.27 to 28.06, indicating neither film diffusion or intraparticle diffusion are rate limiting processes. It is important to note the increase in the *Bi* number from 23.27 to 28.06 corresponding to the flowrate increase from 0.342 to 0.600 L/hr is related to the reduction in mass transfer resistance from film diffusion due to a shrinking film barrier around the adsorbent. An additional analysis was conducted to study the influence of D_b, k_f, and D_p in the mass transfer model on the resulting breakthrough curves as shown in **Figure 5.7**.

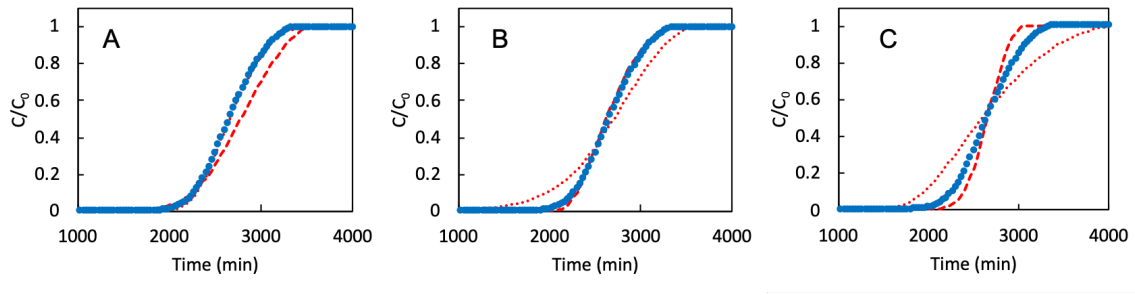

Figure 5.7: Variation of key mass transfer parameters and their impact on calculated breakthrough curve from Run 2. (A) Varying D_b (Dashed: D_b: 4.01×10^{-5} m^2/s, dotted: D_b: 1.6×10^{-6} m^2/s), (B) Varying k_f ((Dashed: k_f: 7.08×10^{-5} m/s, dotted: k_f: 2.83×10^{-6} m/s), (C) Varying D_p (Dashed: D_p: 1.12×10^{-9} m^2/s, dotted: D_p: 2.8×10^{-10} m^2/s)

The parameters were either increased or decreased by a factor of 2 in order to observe their impact on the simulated breakthrough curve (BTC), although this factor was increased further if this did not produce a visible change. In all cases, the base case of the BTC is denoted by the blue symbols, while the dashed and dotted lines correspond to larger and smaller mass transfer parameter, respectively. In the case of D_b, reducing the axial dispersion coefficient by a factor of 5 did not change the shape of the breakthrough profile, whereas increasing it by a factor of 5 broadened the profile. Since decreasing D_b from its present value would have little effect on the shape of the breakthrough curve, it could be deduced that the fixed bed was operating in the desirable flow regime where axial dispersion did not affect the performance of the column.

In the case of k_f, an increase by a factor of 5 did not change the original breakthrough profile, whereas decreasing it by a factor of 5 resulted in earlier breakthrough and a broader breakthrough curve. The effect was related to a larger stagnant film barrier surrounding the adsorbent particles, which would inhibit the uptake of MB, resulting in early breakthrough. Since the shape of the curve did not change greatly when increasing this value, the external film diffusion did not likely hinder the mass transfer of dye from the bulk fluid to the adsorbent during operation.

On the other hand, an increase in D_p by a factor of 2 made the breakthrough curve steeper and sharper, where a decrease by a factor of 2 resulted in an earlier onset of the breakthrough and loss of it symmetrical S shape. The increase in D_p corresponded to a lower mass transfer resistance to intraparticle diffusion, permitting the breakthrough curve to achieve its ideal S shape, whereas decreasing D_p results in greater intraparticle mass transfer resistance, producing a tailing effect due to the slow and steady saturation of the adsorbent after $C/C_0 = 0.5$. Using an adsorbent with a high D_p would be desirable although this may mean using an adsorbent with large pore dimensions, which would reduce the internal surface area and ultimately adsorption capacity.

5.3.7 Influence of $CaCl_2$ on MB uptake: Batch studies

The effect of solution ionic strength on the electrostatic interaction is a well-documented phenomenon, especially in adsorbate/adsorbent systems that rely on such attractive forces for adsorption [207]. Although calcium chloride plays an important role as cross-linkers for preparing the beads, free calcium ions could influence the binding of MB to the adsorbent by increasing solution ionic strength. An *et al.* investigated the adsorption of Cu^{2+} ions onto calcium alginate beads, where the calcium ions could screen the electrostatic interaction [205]. The presence of residual calcium chloride on the adsorbent during fixed bed operation was believed to be responsible for the overshoot observed in the concentration profile in the early stages of column adsorption [116]. We further investigated this phenomenon by focusing on whether MB displaced Ca^{2+} ions in a form of ion exchange during adsorption. The initial experiment involved monitoring the release of Ca^{2+} from CNC-ALG beads in both pure water and a MB solution. **Figure 5.8** shows the results of Ca^{2+} release when rinsed adsorbent was placed into 50 mL of MilliQ water and 250 mg/L MB respectively. In both cases, an identical trend was observed, where the Ca^{2+} diffused from the adsorbent to the bulk solution, approaching an equilibrium after 1600 seconds. This is likely a combination of unbound and bound calcium ions diffusing into the bulk solution along

with chloride counterions, and in both cases, the concentration plateaued at approximately the same value. Thus, we could conclude that MB did not directly displace Ca^{2+} in the CNC-ALG adsorbent, rather that Ca^{2+} and Cl^- counterions diffused into the bulk solution driven by the concentration gradient.

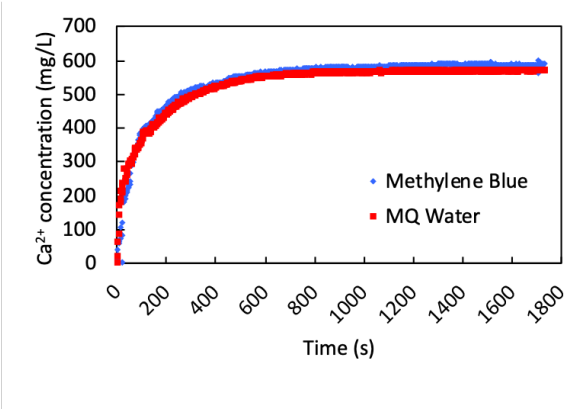

Figure 5.8: Release of Ca^{2+} ions in batch mode in 50 mL of MilliQ water (red) and 250 mg/L MB solution (blue)

The presence of Ca^{2+} ions leaching into the bulk solution affected the uptake of MB on the beads. **Figure 5.9** shows the effect of two different adsorbent pretreatments: dialyzing the beads against deionized water for 2 days (blue dots) or rinsing the beads with 10 mL of deionized water twice (orange dots) and draining the wash water prior to the adsorption experiments. The equilibrium parameters determined for the latter case are q_m = 298 mg/g and K_L = 1.7 m^3/kg. The lower dye adsorption resulting from this pretreatment was due to calcium leaching from the beads during the adsorption experiment that subsequently participated in charge screening inhibiting the diffusion and adsorption of the MB onto the adsorbent. The free Ca^{2+} ions in the adsorbent could have a detrimental effect in a closed adsorption system, which could explain the discrepancy between the equilibrium parameters obtained for the batch and column adsorption studies. Therefore, it is necessary to investigate the effect of Ca^{2+} ions on MB during column adsorption in order to confirm this explanation.

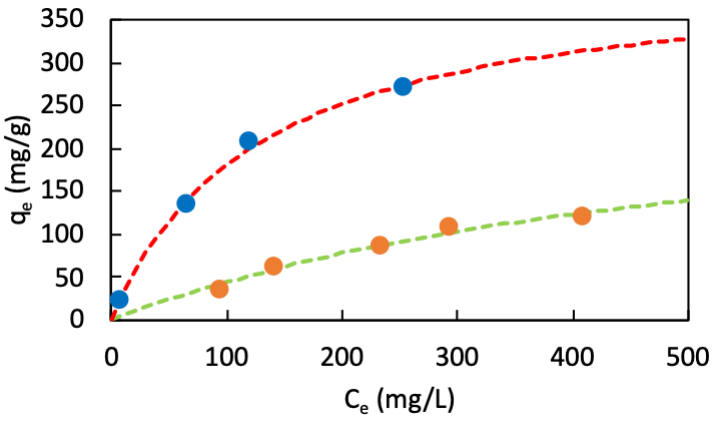

Figure 5.9: Batch experiments showing the effect of Ca^{2+} removal via dialysis (Blue dots) vs. rapid wash (Orange dots) on MB uptake

5.3.8 Influence of $CaCl_2$ on MB uptake: Column studies

Two studies were designed to investigate the effect of Ca^{2+} ions on the uptake of MB on the adsorbent during the column experiments: (i) use of adsorbent without pre-wash, and (ii) use of absorbent washed with 250 mL MilliQ water for 1200 seconds (20 min wash). **Figure 5.10** shows the discharge concentration of Ca^{2+} ions and MB as a function of time for both adsorbents (i) and (ii), using a short column containing only 1.25 g adsorbent. In case (i) (hollow blue and hollow red curves), a 20 mg/L solution of MB was pumped through the column, and unbound Ca^{2+} ions were liberated from the adsorbent/column resulting in steady decrease in the concentration, with a corresponding overshoot in the MB concentration profile (similar to previous results [116]). In case (ii) (solid blue and solid red curves), MilliQ water was pumped through the column for 1200 seconds to remove excess/unbound Ca^{2+} from the adsorbent, after which a solution of 20 mg/L MB was pumped through the column. The trend observed for Ca^{2+} concentration was nearly identical to case (i); however, the MB concentration profile was markedly different. No overshoot was observed, instead the MB concentration dud not breakthrough until 1500 sec and then increased to 4 mg/L. Due to the small amount of adsorbent used in these two cases, the mass transfer zone did not fully form within the column and caused an early breakthrough. In case (i),

the MB concentration appeared to also plateau at 4 mg/L, occurring after the concentration of Ca^{2+} ion leaving the column became negligible. Thus, we concluded that the presence of unbound Ca^{2+} ions in the column have a dramatic impact on MB removal at short time due to charge screening. Based on case (ii), it appeared that 250 mL of MilliQ water (equivalent to 4.6 bed volumes for the 1.25 g of adsorbent) was sufficient to remove unbound Ca^{2+} that would have interfered in MB uptake once the solution was pumped through the column. In addition to these findings, comparing studies (i) and (ii) indicated that the presence of MB in the incoming solution did not displace the Ca^{2+} ions, which is in agreement with the batch studies described in section 5.3.7.

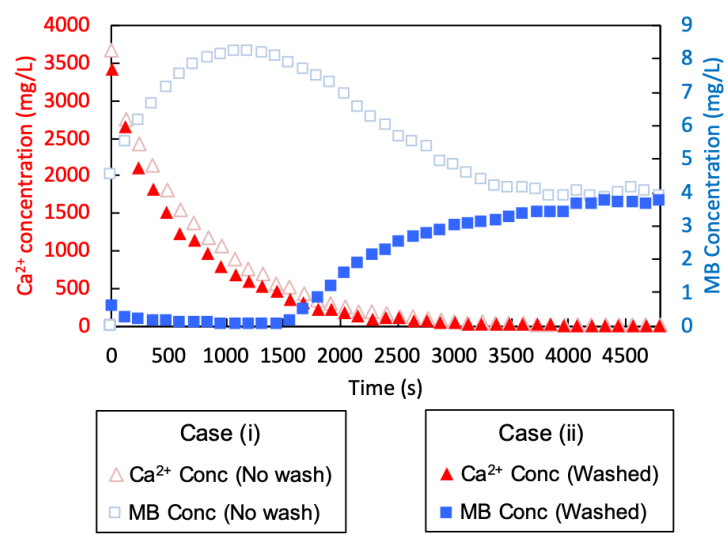

Figure 5.10: Ca^{2+} and MB concentration in effluent from column after different adsorbent pre-treatments, operating at an initial MB concentration of 20 mg/L and 1.25 g of adsorbent

5.3.9 Influence of $CaCl_2$ on bed height

Another property that was investigated was the swelling and shrinkage of the hydrogel adsorbent during MB adsorption. **Figure 5.11** shows the breakthrough curve for Run 2 (C_0 = 111 mg/L, Q = 0.492 L/hr, and m = 6.25 g), as well as the height of the packing during the operation. During the initial 500 minutes, the packing height increased by almost 10% due to expansion of the adsorbent

beads and subsequently decreased until 2750 minutes corresponding to 50% breakthrough before leveling off thereafter. Since the changes in the bed height could be influenced by MB adsorption, we investigated the role of Ca^{2+} on adsorbent swelling/shrinkage.

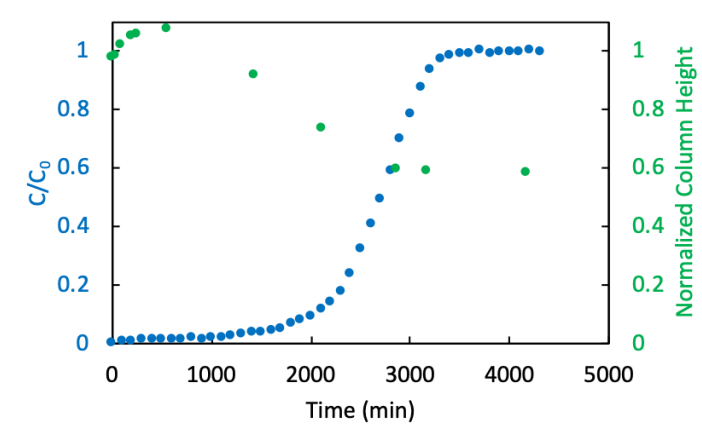

Figure 5.11: Breakthrough curve and variations of height of packing material with time during run 2 (C_0 = 111 mg/L, Q = 0.492 L/hr, m = 6.25 g)

For this investigation, three scenarios were postulated to investigate the effect of adsorbent pretreatment on the packing height and MB concentration leaving the column during the initial stages of adsorption. The following three pretreatments prior to contact with MB were carried out: (1) Soaking the adsorbent in 2 wt% $CaCl_2$ solution for 30 minutes, (2) cycling a 2 wt% solution of $CaCl_2$ solution through the adsorbent for 30 minutes to expand the bed, and (3) washing the adsorbent with 250 mL MilliQ water for 30 minutes. **Figure 5.12** shows the breakthrough curve and bed height for cases (1) & (2). In case (1), the soaking of the adsorbent in stagnant $CaCl_2$ did not affect the bed height and the size of the adsorbent gel particles. This indicates that the adsorbent achieved a fast equilibrium with the $CaCl_2$ cross-linking solution when initially prepared and did not uptake anymore Ca^{2+} when left to soak in the solution beyond 15 minutes. In Case (2), pumping 2 wt% $CaCl_2$ through the adsorbent at 0.492 L/hr for 30 minutes prior to adsorption did not change the bed height, suggesting no change in the adsorbent size and packing density. This

further shows that the flow rate of 0.492 L/hr used did not cause the adsorbent packing to expand, and that any changes in size could be attributed to exposure to MB solution or MilliQ water. However, a visible change in packing height was observed only after pumping of the MB solution through the column began. In case (1), an overshoot in the MB concentration and a corresponding reduction in the Ca^{2+} ions leaving the column were observed (this trend was identical to case (i) **Figure 5.10**). The packing height also increased, suggesting that the adsorbent beads expanded in size. Since the flowrate (0.492 L/hr) was below the fluidization velocity, the bed expansion was not caused by fluid dynamics but by changes in adsorbent size. The behaviour observed in Case (2) was similar to that of Case (1), where a larger overshoot in MB concentration was observed in Case (2). This larger overshoot is due to a higher screening of the adsorbent by the higher $CaCl_2$ concentration in the column resulting from the pretreatment step, as shown before. As in Case (1), the bed height increased and followed an identical trend in terms of rate of height increase and final height. The bed height appeared to plateau after 5500 seconds, which coincided with the Ca^{2+} and MB concentrations reaching a steady state. It can be concluded that exposing the adsorbent to either stagnant or flowing $CaCl_2$ did not influence its initial packing.

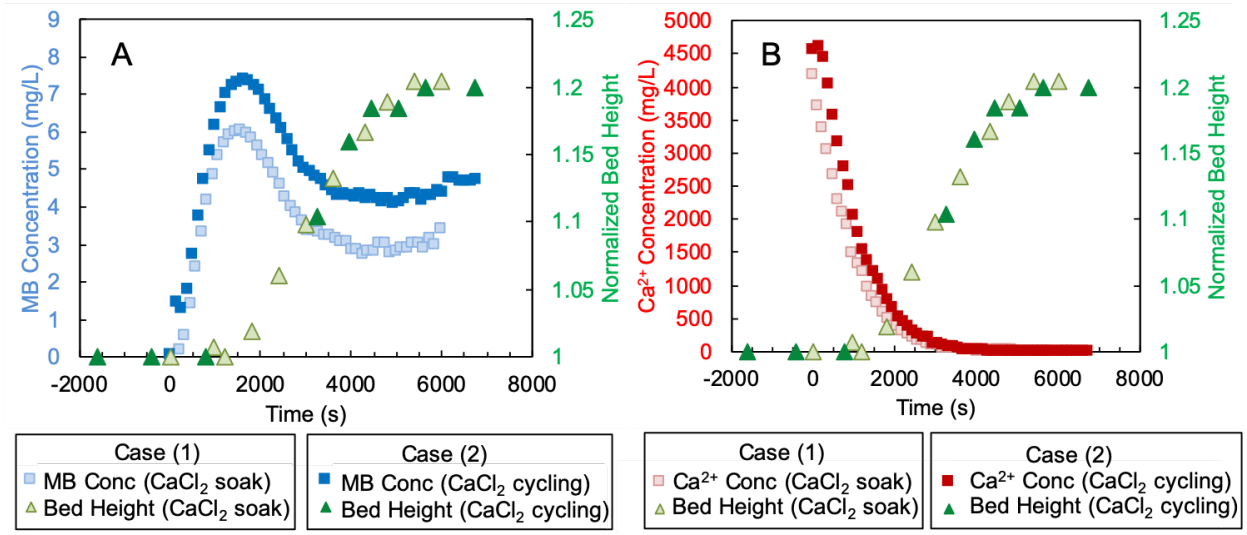

Figure 5.12: MB concentration and bed height (left) and Ca^{2+} concentration and bed height (right) for pretreatments involving 30 minutes of $CaCl_2$ cycling through the adsorbent and 30 minutes of adsorbent soaking in $CaCl_2$ with C_0 = 20 mg/L and m = 1.25 g

Figure 5.13 shows the trends in bed height, MB and calcium concentration for Case (2) and (3). The effect of pre-washing with water for 30 minutes (Case (3)) was very noticeable. Over the first 30 minutes of Case (3) (prior to introduction of MB), the bed height decreased due to the shrinkage of the adsorbent. Davidovich-Pinhas *et al.* investigated the swelling and shrinkage (syneresis) of alginate tablets prepared with differing concentrations of calcium and found that alginate cross-linked with 25 mM Ca^{2+} or higher led to a reduction in the mass when placed in water. This was attributed to water exudation, resulting in a reduction of volume of the cross-linked alginate [208]. The bed appeared to stop shrinking after 1200 seconds, at which point it remained at a constant level of 95% of its starting height. With the introduction of MB into the column (at 1800 s), the adsorbent began to swell, but it did not reach same bed height observed in Cases (1) and (2) (+ 20%). It however achieved 112% of the initial height, which is very close to the bed height expansion observed in run 2 (**Figure 5.11)**, which experienced a 9% increase when exposed to the incoming MB solution and shrank 2% initially from the same water pretreatment.

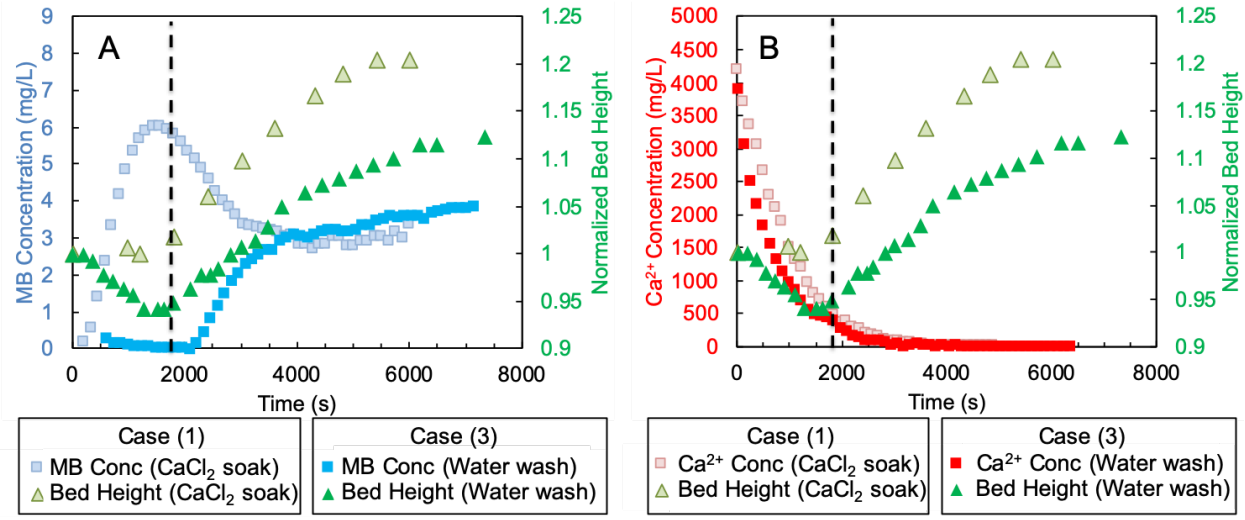

Figure 5.13: MB concentration and bed height (left) and Ca^{2+} concentration and bed height (right) for pretreatment involving 30 minutes of adsorbent soaking in $CaCl_2$ and 30 minutes of washing adsorbent with water with C_0 = 20 mg/L and m = 1.25 g (the dashed line indicates the 30 minutes mark when MB solution was introduced in water washing case).

We could use the results observed in case (3) (**Figure 5.13**) to infer what occurred in run 2 (**Figure 5.11**) since they underwent the same pretreatment process and similar operating conditions. **Figure 5.14** shows the proposed mechanism for the role of washing pretreatment and MB exposure on the size of the adsorbent. In stage (1), water washing the adsorbent caused unbound Ca^{2+} and Cl^- ions to leave the adsorbent, reducing the net repulsion inside the hydrogels and causing them to shrink. In stage (2), the hydrogel has an abundance of unshielded negatively charged sulfate ester and carboxylic acid groups which facilitated the transport of MB molecules into the hydrogel, causing it to swell due to osmotic pressure [116]. After stage (1) in Case (3) (**Figure 5.13b**), the Ca^{2+} concentration in solution decreased to a negligible concentration once the bed had expanded to the maximum. Therefore, this same trend should be expected in columns with more packing, such as the experiment in **Figure 5.11**. Since the adsorbent had already lost most of its calcium in the initial stages of operation, the bed shrinkage observed during later times must be caused by the high concentrations of adsorbed MB and not the loss of Ca^{2+} ions. After the adsorbent has swelled

to its maximum, stage (3) occurred and the hydrogel interior experienced charge shielding from the adsorbed dye, resulting in the expulsion of water and the gradual shrinkage of the hydrogel matrix. Stage (4) occurred when the adsorbent has reached its maximum capacity and cannot adsorb more dye, so that its size remained constant. Hence, it appears that both the external Ca^{2+} concentrations and the amount of MB adsorbed influenced the size of the adsorbent beads, with the MB having a larger effect over the course of the adsorbent usage.

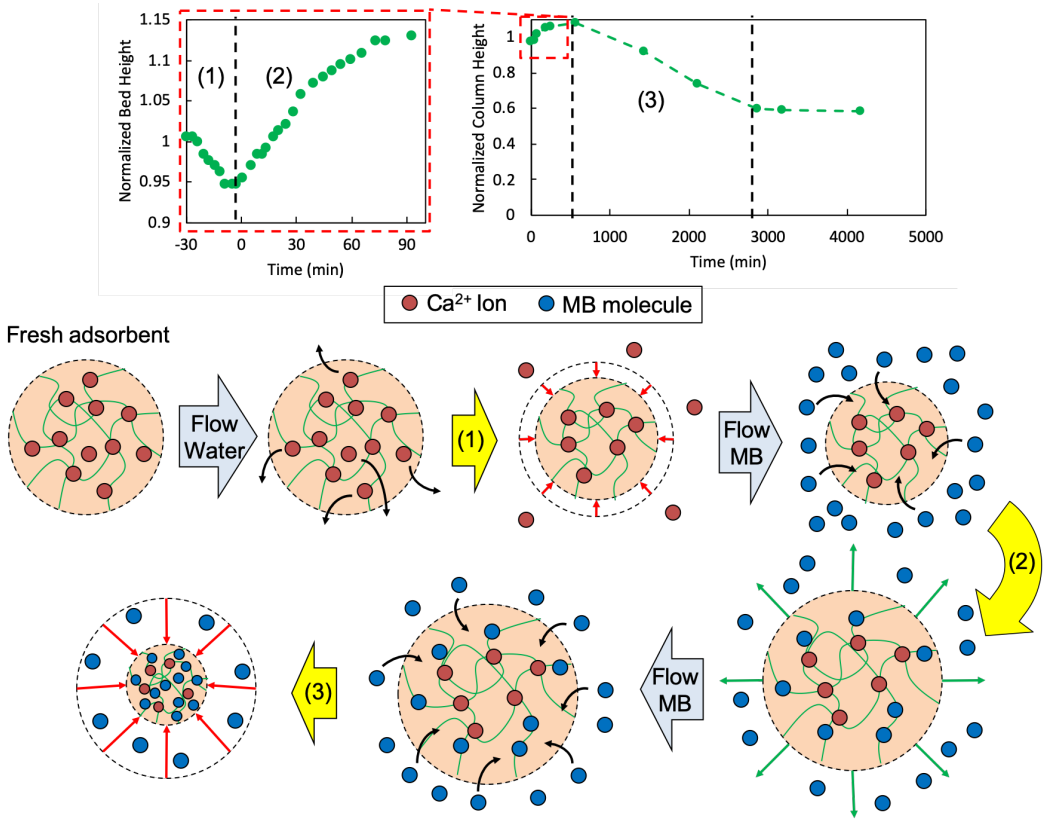

Figure 5.14: Mechanism of bead swelling/shrinkage corresponding to bed height changes during column operation

5.3.10 Column Desorption Study

The regeneration of the CNC-ALG adsorbent was conducted using a 1:1 (V:V) solution of 1 M HCl and ethanol to desorb the MB. **Figure 5.15** shows the result of the desorption test from the experiment conducted after run 2. The concentration profile of MB leaving the column

decreased exponentially, with a very high initial desorption of MB, suggesting that the majority of the MB was desorbed from the adsorbent after passing 2 L of eluent through the column (corresponding to 10 times the bed volume (10 BV)). This is a favourable trend for regenerating the adsorbent, considering nearly 100 BV of 111 mg/L MB was required to saturate the adsorbent (**Figure 5.5d run 2**). By integrating the area under the desorption curve, the total mass of dye desorbed was 1.945 g, amounting to 81% recovery of the dye. Even after treating the adsorbent with 4 L of eluent solution, the adsorbent retained a deep blue color, indicating a portion of the dye had irreversibly adsorbed onto the CNC-ALG.

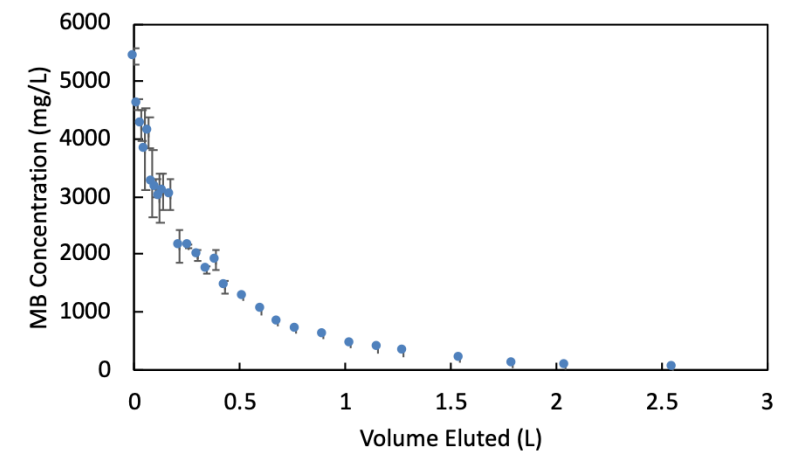

Figure 5.15: Desorption of MB from spent adsorbent from run 2 (C_0 = 111 mg/L, Q = 0.492 L/hr, with a total mass of 6.25 g)

Following the desorption step, the adsorbent was soaked in 2 wt% $CaCl_2$ for 12 hours to reintroduce divalent Ca^{2+} ions into the alginate matrix, and it was then loaded into the column for subsequent runs. **Figure 5.16** shows the second adsorption run using the regenerated adsorbent, which was compared to the first run. This test (run 9) had a C_0 of 104 mg/L MB, flowrate of 0.552 L/hr with 6.25 g of adsorbent recovered from the previous run. The breakthrough trend is similar to the previous run, depicting a slow increase in effluent concentration before the breakthrough occurred. The breakthrough occurred much earlier than expected, further confirming that the

adsorbent did not regain its original adsorption capacity following the regeneration step. Using this data with Eq (5.4) revealed that 1.932 g of MB was adsorbed, which is very close to the amount of dye desorbed in the previous step (1.945 g). Also, the simulation of this adsorption experiment using the operating parameters listed above (solid line in **Figure 5.16**) did not fit well with the observed results. However, if the mass of usable adsorbent was set to 81% of its original value (corresponding to the 81% of bound dye that was removed after the first run), the simulation could accurately predict the breakthrough profile (dashed line in **Figure 5.16**). This further validates the use of the model to predict the adsorption behavior of the CNC-ALG adsorbent in a fixed bed column. To check if the adsorption capacity of the adsorbent would decrease further after multiple uses, a second desorption experiment was conducted (**Figure 5.17**).

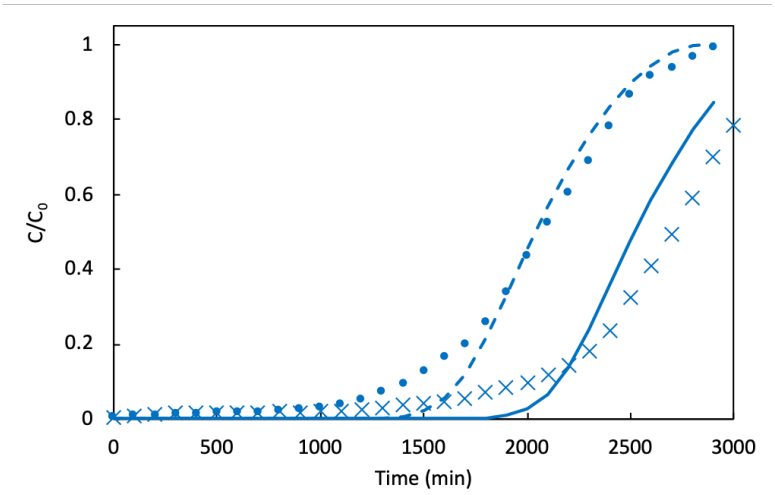

Figure 5.16: Adsorption of MB onto regenerated adsorbent during run 9 (circle), C_0 = 104 mg/L, Q = 0.552 L/hr, m = 6.25 g. Solid line represents simulated adsorption with 100% usable adsorbent (with x markings depicting original adsorbent run), Dashed line represents adsorption with 81% usable adsorbent

This desorption curve follows the same trend as the first desorption, with the majority of the bound MB removed after flowing 2 L of eluent solution through the adsorbent. From the integration of the area under this curve, the mass of MB desorbed from the adsorbent was 1.862 g, constituting 96% removal of the bound MB from the previous adsorption experiment. Despite the loss of 19%

of the adsorption capacity of the adsorbent during the first adsorption cycle, the remaining 81% of the sites could be regenerated for multiple MB adsorption cycles, confirming the reusability of this adsorbent.

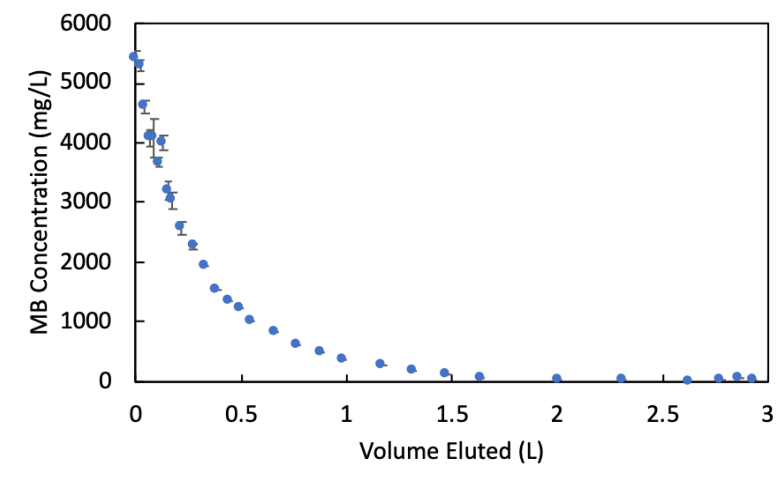

Figure 5.17: Desorption of MB from spent adsorbent from run 9 (C_0 = 104 mg/L, Q = 0.552 L/hr, with a total mass of 6.25g) using 1 M HCl:Ethanol (1:1 v:v) solution

5.4 Conclusions

The adsorption of MB onto CNC-ALG in packed columns was investigated under varying operating conditions. The K_L values for the column and batch adsorption experiments, were found to be 183 m^3/kg and 7.9 m^3/kg, respectively. This discrepancy is attributed to the presence of Ca^{2+} ions in the batch systems, resulting in high ionic strength which reduced the MB fixation on the adsorbent. On the contrary, this was not observed in the column experiments as the Ca^{2+} was eluted from the column by the incoming flow. The advection-diffusion equation coupled with the pore diffusion model including axial dispersion and film diffusion provided excellent predictions for the column operation, and correlated well with experimental results yielding RMSE values less than 0.045. The uptake of MB by the adsorbent during batch and column studies did not displace Ca^{2+} bound directly to the adsorbent, and that the overshoot in the column adsorption experiments observed at short times was due to charge screening by Ca^{2+} ions leached from the adsorbent.

Furthermore, the expansion of the adsorbent during the initial stages was not caused by Ca^{2+} ions, but rather by the bound MB that induced an osmotic swelling of the beads [116]. Finally, regeneration experiments with a 1 M HCl:ethanol (1:1 v:v) solution confirmed that 81% of the adsorbed dye was removed from the adsorbent after a single pass resulting in a 19% reduction in the absorption capacity. Regeneration of the adsorbent following the second adsorption cycle revealed that 96% of the adsorbed dye was removed, confirming that the adsorbent could be reused for several cycles without a noticeable reduction in the performance.

Chapter 6: Melamine Formaldehyde Functionalized Cellulose Nanocrystals Incorporated Paper Based Membrane Filters in Point-of-Use Water Treatment*

This chapter reports on the development and use of melamine formaldehyde (MF)-functionalized cellulose nanocrystals (CNC) incorporated into hardwood pulp (HWP) membranes for the removal of anionic contaminants in water. MF was first coated onto CNCs using an *in situ* polycondensation reaction, which was followed by batch experiments to examine its capability to remove methyl orange (MO). MF-CNCs could be easily incorporated into HWP membranes via a simple paper-making process. The adsorption of MO onto MF-CNC obeyed the Freundlich isotherm and reached a capacity greater than 80 mg/g at 25ºC. This level rose with increasing temperature. The MF-CNCs could be regenerated by washing with 1 M HCl. The incorporation of 14 wt% MF-CNCs in HWP membranes improved the wet strength and dye removal performance of the membranes. However, the inclusion of MF-CNCs decreased the flux through the membranes due to the reduction of their pore size. Up to 20 layers of MF-CNC HWP could be prepared and operated at flow pressures up to 30 psi. MF-CNCs readily bind MO inside the HWP matrix, making them effective filtration media. Functionalized CNC-incorporated HWP membranes hold great promise for the removal of a wide variety of contaminants. The simplicity and low cost of preparing and using these membranes for the removal of contaminants make this system a suitable in point-of-use water treatment method.

* This chapter is partially adapted from "Nathan Grishkewich, Nishil Mohammed, Stephen Wei, Madhav Vasudev, Zengqian Shi, Richard M Berry, Kam Chiu Tam, Melamine Formaldehyde Functionalized Cellulose Nanocrystals Incorporated Paper Based Membrane Filters in Point-of-Use Water Treatment, *Manuscript under preparation*"

6.1 Introduction

Water is an essential ingredient necessary for life. In many parts of the world that do not have access to centralized water treatment facilities, the need exists for small scale low energy clean water production [64]. This can take the form of bio-sand and ceramic filters, chlorination processes [66] or membrane filtration. Membrane filtration is a technique whereby contaminants are rejected based on their size relative to the pore size of the membrane. The various types of membrane filtration are: microfiltration (pore sizes ranging from 50 – 500 nm), ultrafiltration (2 – 50 nm), nanofiltration (< 2 nm) and reverse osmosis (0.3 – 0.6 nm). Microfiltration removes bacteria and yeast cells, while reverse osmosis removes ions [3]. The reduction in the pore size of these membranes increases the energy consumption since the incoming stream has to be pressurized to drive flow across the membrane. With the advances in nanotechnology solutions for membrane filtration, the above separations can now be achieved with increased permeability, fouling resistance as well as self-cleaning capabilities through catalytic activity [3].

The use of nanomaterials in membranes serves two main purposes: adding reinforcement to the membrane structure [57] and providing enhanced rejection/retention of contaminants by acting as a barrier layer [58]. These nanomaterials include porous zeolites [59], carbon nanotubes [59] and more recently cellulose nanomaterials (CNs) [61], the last of which have many desirable properties. CNs can be derived from cellulosic biomasses and can take the form of cellulose nanocrystals (CNCs) or cellulose nanofibrils (CNFs). CNC particles are rod-like with lengths of 100 – 300 nm and diameters of 5 – 15 nm [11]. Their high stiffness, hydrophilicity and surface area make them valuable additions to membranes to enhance their strength and functionality [81].

CNs have been incorporated into membranes either by deposition onto the surface to form a thin film nanocomposite (TFN) membrane or incorporating them within the membrane matrix itself. These membranes treat wastewater by either size exclusion or other active modes such as

adsorption. In the case of an active layer, membranes are dip-coated in CNC suspensions [138] or CNC films are cast onto woven membrane substrates [61],[58],[139],[140]. The bulk of the membrane containing CNs may be prepared on a porous substrate and cross-linked with an additive [141],[63] or physically entangled as in paper making [142],[143],[144]. However, in these cases an added step may be necessary to increase the porosity of the membrane when used for water filtration. Karim *et al.* used CNCs in chitosan membranes crosslinked with glutaraldehyde for the purpose of removing cationic dyes, such as Victoria blue 2B, rhodamine 6G and methyl violet 2B [63]. They reported that the high dye removal (up to 98% of methyl violet) was due to the negatively charged CNC in batch adsorption. In a similar study, Mautner *et al.* synthesized CNFs via phosphoric acid to decorate them with phosphate groups to prepare membranes capable of rejecting copper ions [144]. These membranes could reject copper ions and still perform well with a feed solution contaminated with calcium ions and retain its adsorption capacity after various regeneration cycles.

One way to produce low cost membranes is to produce them using cellulose pulp fibres via traditional paper making [64]. However, pulp fibre mats have low wet strength and require additives to enhance their mechanical strength for use in water filtration applications. Many researchers have explored the use of cationic polymers such as chitosan [209], cationic starch, precipitated calcium carbonate [210] and cationic polyacrylamide [211] to improve the wet strength or functionality of cellulose sheets. We believe this could also be achieved using modified CNCs. A melamine formaldehyde (MF) resin can be used by itself or condensed onto polymers and has proven to adsorb contaminants from water [212],[213],[90],[214]. It was recently polymerized onto CNC [92] although its ability to remove contaminants from water has not yet been explored.

In this work, CNCs were coated with MF (MF-CNCs) and their capacity to remove an anionic dye such as methyl orange (MO) was examined. MF-CNCs were incorporated into hardwood pulp (HWP) membrane filters at amounts between 2 – 18 wt% of the total solid content via traditional paper making. The membranes were evaluated based on their wet tensile index and dye removal capabilities to determine the optimal loading of MF-CNCs. The membrane containing 14 wt% MF-CNC exhibited the best performance and were used in a dead-end filtration apparatus to investigate dye removal from wastewater under varying operating pressures and flow rates. The use of 20 14 wt% MF-CNC HWP membranes gave excellent results for dye removal. Further steps to improve their capability to screen contaminants as well as the incorporation of other functionalities for self-cleaning and bactericidal functions will be examined in the future.

6.2 Materials and Methods

6.2.1 Materials

CNCs (spray-dried) were supplied by CelluForce Inc., while hardwood pulp (HWP) was supplied by Suzano, Brazil. Melamine, formaldehyde (37 wt%), methyl orange (MO), hydrochloric acid (HCl 37 wt%), sodium hydroxide (NaOH, 95 wt% pellets) and potassium bromide (KBr) were purchased from Sigma-Aldrich. MilliQ water was produced in the laboratory using a MilliPore system (>18 MΩ/cm). Whatman™ filter papers (110 mm diameter, GE Healthcare) were purchased from VWR Canada.

6.2.2 Synthesis of MF-CNC

The synthesis of MF-CNC was adapted from that described in previous studies [92],[91],[215]. 2.2 g of melamine and 4.0 g of formaldehyde (37% in water) were combined with 10 mL of MilliQ water in a 50 mL flask while being stirred. The pH of the solution was adjusted to 9 using 1 M NaOH and the temperature was increased to 80ºC. This solution became turbid after 5 minutes and then added to 100 mL of a 1 wt% CNC solution after 30 minutes. The pH of

the solution mixture was then adjusted to 4 using 1 M HCl and mixed at 80ºC for 2 hours. After the solution was cooled to room temperature, the product was repeatedly washed with Milli Q water through a Whatman™ filter paper until the filtrate was clear.

6.2.3 Preparation of control and MF-CNC loaded membrane filter papers

The preparation of the membrane filter papers proceeded as follows: first, dry HWP sheets were shredded and dispersed in deionized water to produce a 0.3 wt% suspension. Hand sheet membranes were prepared from this suspension by adding an appropriate amount of MF-CNC dispersion to yield a MF-CNC/HWP suspension. In a typical preparation, a suspension containing 750 mg HWP and MF-CNC were added to a 4 inch (101.6 mm) cylindrical column containing a 200 stainless steel mesh (75 μm pore size) at the bottom. A vacuum was applied below the mesh to draw the HWP/MF-CNC suspension over the mesh to produce the hand sheet. The resulting hand sheet was removed and dried with Whatman™ filter paper. Once the hand sheet was sufficiently dried, it was peeled from the support mesh and compressed in a hydraulic press under 2 tonne force for 5 minutes to expel the trapped water and then placed between 2 glass plates and left to dry at 75ºC for 24 hrs. This produced hand sheets with a mass density of 92.6 $g*m^{-2}$ (determined by dividing the mass of the handsheet by its area). Smaller circular membranes (diameter of 26 mm) were prepared for dye adsorption experiments using a puncher or cut into strips for tensile testing.

6.2.4 Batch dye adsorption experiments

Adsorption experiments were conducted using a model anionic dye methyl orange (MO). MO dye solutions of volume (V) with initial concentration C_0 was mixed with a known mass (m) of adsorbent. When the equilibrium condition was reached, the final concentration (C_e) was

determined using UV-Vis spectrophotometry. The adsorption capacity (q_e) of the MF-CNC was then calculated using Eq. (6.1):

$$q_e = \frac{(C_0 - C_e)V}{m} \tag{6.1}$$

For kinetic experiments, samples of the filtrate were removed after each time period to calculate the dye concentration C and then calculate q. For comparison, the % dye removal was calculated (Eq.(6.2)) by keeping the initial dye concentration constant and varying other parameters, such as pH and ionic strength:

$$\%\ Dye\ removal = \frac{C_0 - C_e}{C_0} \tag{6.2}$$

To determine the adsorption isotherm, experiments were conducted with initial MO concentrations of 200, 600, 1200, 1600 and 2000 mg/L with 50 mg MF-CNC adsorbent (added to solution) in a total batch volume of 10 mL. The mixture containing adsorbent (MF-CNCs) and adsorbate (MO) was stirred for 120 minutes. MF-CNCs were then separated via centrifugation and the supernatant was removed and the residual MO concentration C_e was measured. Then, q_e was calculated using Eq. (6.1), and plotted and fitted according to the Langmuir isotherm described by Eq. (6.3).

$$q_e = \frac{q_m K_L C_e}{1 + K_L C_e} \tag{6.3}$$

where K_L is the Langmuir constant (L/mg) and q_m is the theoretical maximum adsorption capacity (mg/g). The Freundlich isotherm represents another isotherm used for liquid-solid systems as described by Eq. (6.4):

$$q_e = K_F (C_e)^{1/n} \tag{6.4}$$

where q_e and C_e are the same parameters described in Eq. (6.3), the Freundlich constant K_F is related to the adsorbate loading on the adsorbent (units of $(mg/g)(L/mg)^{1/n}$) and *1/n* is another constant that is sensitive to the heterogeneity of the adsorbent surface [216]. The sum-of-squared error (SSE) (Eq. (6.5)) was calculated to determine the fit of the respective models to the experimental adsorption data, i.e.,

$$SSE = \sum_{i=1}^{n}(q_{exp,i} - q_{pred,i})^2 \quad (6.5)$$

6.2.5 Effect of various parameters on dye adsorption

MO adsorption onto MF-CNCs may be influenced by several parameters such as pH, solution ionic strength and temperature.

6.2.5.1 Effect of solution pH

The effect of solution pH on the uptake of MO onto MF-CNC was studied by contacting 10 mL of 100 mg/L MO solutions at pHs of 2.18, 2.42, 4.15, 4.42, 6.92, 9.35 and 11.4, with 100 mg of MF-CNC until the system reached equilibrium while continuously stirring at 500 rpm and 25^{o}C.

6.2.5.2 Effect of solution ionic strength

The effect of ionic strength on the uptake of MO onto MF-CNC was examined by mixing 10 mL of 100 mg/L MO solutions in 0, 0.05, 0.1, 0.25, 0.5 and 1 M NaCl with 100 mg MF-CNC until the system approached the equilibrium while stirring at 500 rpm, pH 7 and 25^{o}C.

6.2.5.3 Effect of temperature

The effect of temperature and associated thermodynamic parameters were studied by adding 50 mg MF-CNC to 10 mL of 200, 600, 1200, and 1600 mg/L MO solutions (pH 7) and allowing the system to reach equilibrium at 25, 35, 45 or 55^{o}C while stirring at 500 rpm.

6.2.6 Regeneration of MF-CNC

The reusability of the MF-CNC was investigated for one cycle. Following a normal adsorption cycle, the MF-CNC was washed with 10 mL of 1M HCl at 45^{o}C for 1 hour followed by centrifugation. A sample of the supernatant was then removed to determine the amount of MO desorbed. The process was repeated several times to achieve maximum desorption.

6.2.7 Wet strength testing of HWP and MF-CNC HWP membranes

Wet tensile testing was carried out on the membranes by cutting them into strips 60 mm long and 14 mm wide. Then, 30 μL of MilliQ water was placed on the strip until it was fully absorbed before being loaded on the tester and extended until fracture. Five replicate tests were performed for each membrane type produced.

6.2.8 Gravity filtration of MO solution from MF-CNC HWP membranes

In these experiments, HWP and MF-CNC HWP membranes (92.55 gm^{-2}) were cut into 26 mm round sheet (380 mm^2 active area, 35.2 mg) and loaded in a 10 mL Amicon™ dead-end ultrafiltration cell. 5 mL of a 50 mg/L MO solution was added to the vessel and the filtrate was

allowed to permeate through at atmospheric pressure. The time taken for full elution was recorded and the final concentration of the permeate solution measured to determine the % dye removal.

6.2.9 Pressure-driven flow through HWP and MF-CNC HWP membranes

In these experiments, an apparatus was constructed consisting of a 300 mL MO feed tank connected to a pressurized air supply that would feed the dye solution into a membrane module containing 1 to 20 HWP membranes stacked in series in a dead-end filtration configuration. Membranes were cut into 35 mm diameter circles (755 mm^2 active area, 69.9 mg) and placed in the membrane module. Then, 100 mL of 25 mg/L MO solution was loaded into the feed tank and air pressures of 5 – 30 psi were applied to drive the solution through the membranes. The total time to elute the solution and the final concentration of the permeate solution were recorded.

6.2.10 Time-dependent study of pressure driven flow through MF-CNC HWP membranes

Experiments were conducted with MF-CNC HWP membranes using the same apparatus as described in section 6.2.9. Samples of the permeate at specific times were removed and analyzed to assess the performance of the membrane in removing MO as a function of time.

6.2.11 Instrumentation

6.2.11.1 UV-Vis Spectrophotometry

A Cary 1E UV-Vis spectrophotometer was used to determine the concentration of methyl orange solutions. A calibration curve for MO was determined using the Beer-Lambert law and measuring the peak absorbance at λ = 554 nm. This technique was used to measure the initial and final MO concentration during batch adsorption experiments.

6.2.11.2 Tensile testing

Tensile tests of membranes were conducted using a CETR-UMT (Bruker) instrument. Wet tensile tests were conducted on 60 x 14 mm membrane strips which were wetted with 30 µL water

and secured between two clamps 40 mm apart. With the elongation rate set at 18 mm/min the textile index (TI) (units of N·m/g) was calculated according to the TAPPI method T494 om-01 using the following equation [217] :

$$TI = \frac{Tensile\ Strength}{Grammage} = \frac{\frac{F \cdot g}{W}}{\frac{m}{L \cdot W}} \quad (6.6)$$

where F is the maximum force measured by the instrument (reported in kg), g is the gravitational acceleration constant (9.81 m/s^2), W and L are the width and length of the membrane strip tested, respectively (m), and m is the mass of the membrane strip tested (g).

6.2.11.3 Fourier transform infrared spectroscopy

FT-IR spectroscopy was carried out using a PerkinElmer 1720 FT-IR spectrometer to confirm the presence of MF coating on the CNC. Samples for measurement were prepared by mixing the samples with KBr and then pressed into a transparent pellet. These pellets were then scanned at a resolution of 4 cm^{-1} to obtain the spectra.

6.2.11.4 Thermogravimetric analysis

The composition of MF on the MF-CNCs was estimated using TGA (TA instruments - TGA Q500 V20.10 Build 36), while assuming that the thermal degradation of the composite nanoparticle proceeded exactly the same as in the CNC and MF resins. Samples of MF, CNC and MF-CNCs were weighed onto platinum dishes and heated from 25 to 800ºC at rate of 10ºC/min with an N_2 flow of 20 mL/min.

6.2.11.5 Zeta potential analysis

The zeta potentials of samples were measured using a zetasizer (Malvern, Nano ZS90). MF-CNC samples were diluted to an approximate concentration of 0.1 wt% prior to the measurements.

6.2.11.6 Scanning electron microscopy (SEM)

SEM images were obtained using a Zeiss FESEM Leo 1530, operated at an acceleration voltage of 10 kV. Cross-sectional samples were obtained by wetting samples and fracturing them in a liquid N_2 bath. The samples were sputtered with Ag to obtain conductive surfaces.

6.3 Results and Discussion

6.3.1 Synthesis and characterization of MF-CNC

As mentioned earlier, melamine formaldehyde was coated onto the surface of CNCs to impart positive charge functional groups to the CNCs. An illustration of the coating mechanism is shown in **Figure 6.1a**.

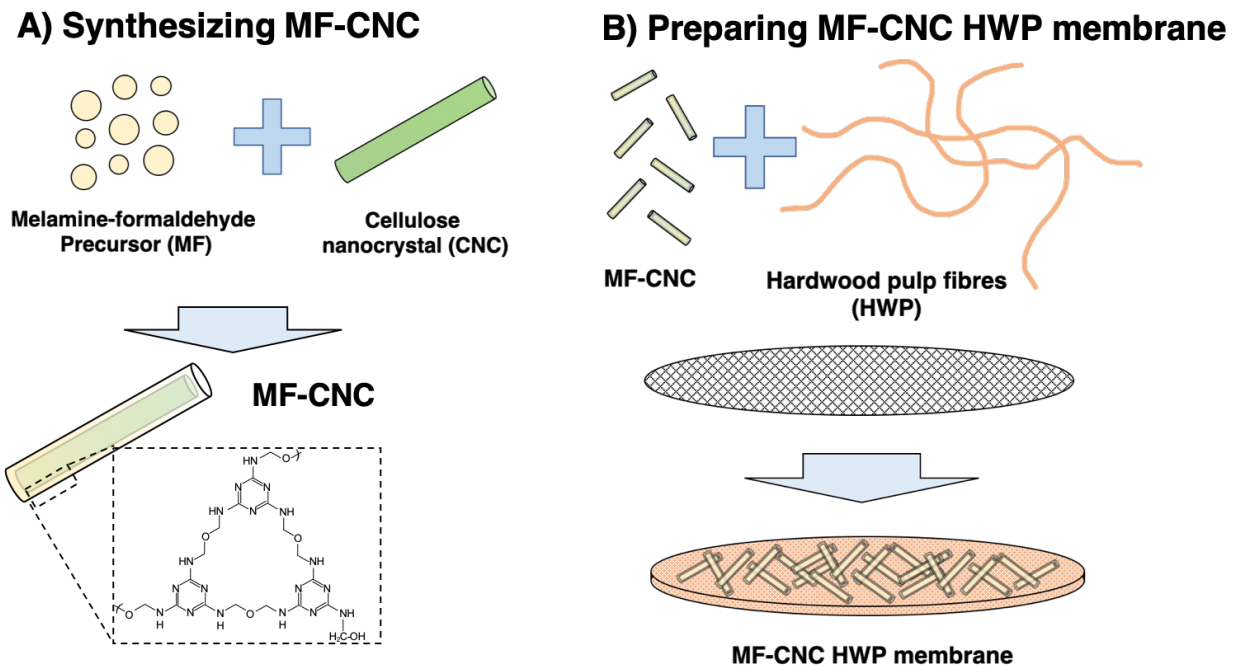

Figure 6.1: Schematic of A) MF-CNC synthesis and B) preparation of MF-CNC-loaded HWP membrane

FTIR analysis was used to confirm the presence of MF in the MF-CNC samples. **Figure 6.2a** shows the FTIR spectra of pure CNC (green) and MF-CNC (orange). Several new peaks are

visible in the MF-CNC spectrum, most notably at 812 cm^{-1} corresponding to the triazine ring in the melamine group, 1330 cm^{-1} corresponding to the -CH bending of MF, and 1556 cm^{-1} corresponding to the C=N ring vibration from the melamine group [93],[92]. To deduce the degree of MF coating on the surface of CNCs, thermogravimetric analysis (TGA) was conducted (**Figure 6.2b**). The residual mass of MF resin, CNC, and MF-CNC samples at 600°C were found to be 36.7, 11.5 and 26.9%, respectively. Based on the mass balances shown in Eq. (6.7) and (6.8), the amount of MF coated on CNC is determined to be 61.1%, in close agreement with previous results [92].

$$m_{CNC} + m_{MF} = 1 \tag{6.7}$$

$$0.115m_{CNC} + 0.367m_{MF} = 0.269 \tag{6.8}$$

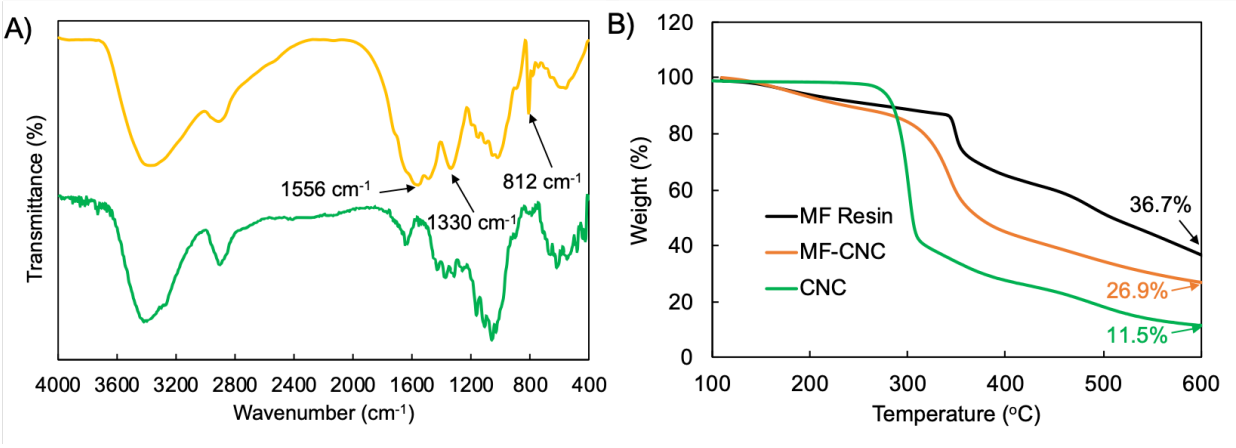

Figure 6.2: A) FTIR spectra of Pure CNC (green) and MF-CNC (orange), B) TGA data of Pure CNC (green), MF-CNC (orange), and MF resin (black) samples

6.3.2 MF-CNC batch adsorption experiments

Following the characterization of the MF-CNC, we evaluated the capacity of MF-CNC to adsorb anionic contaminants such as MO. **Figure 6.3** shows the results from batch adsorption experiments to compare dye removal by pure CNC and MF-CNC. After determining the equilibrium conditions for each batch experiment (C_e and q_e) respectively, an isotherm was fitted to the data and the equilibrium parameters were determined by minimizing the sum-of-squared

errors. Both the Langmuir and Freundlich isotherms were used to model the data (**Figure 6.3a**). Based on the Langmuir isotherm, the q_m and K_L values were determined to be 74.77 mg/g and 0.297 L/mg, respectively, with an SSE of 82. Similarly, the Freundlich parameters K_F and n were determined to be 33.53 mg/g and 8.34 respectively, with an SSE of 30. The squared error was observed to be consistently lower for all data points using the Freundlich isotherm, whereas two points contributed most of the squared error for the Langmuir isotherm. Therefore, the Freundlich isotherm was chosen to model the equilibrium adsorption of MO on MF-CNC. A comparison was made between pure CNC and MF-CNC to confirm the performance enhancement using the MF coating (**Figure 6.3b**). When both samples were added to a 100 mg/L MO solution, pristine CNCs could remove only 28% of the dye (q_e of 2.89 mg/g) whereas the MF-CNCs adsorbed 98.7% (q_e of 10.13 mg/g), corresponding to a 250% increase in adsorption capacity. This demonstrates the capability of the MF coating to improve the affinity of CNCs toward anionic compounds.

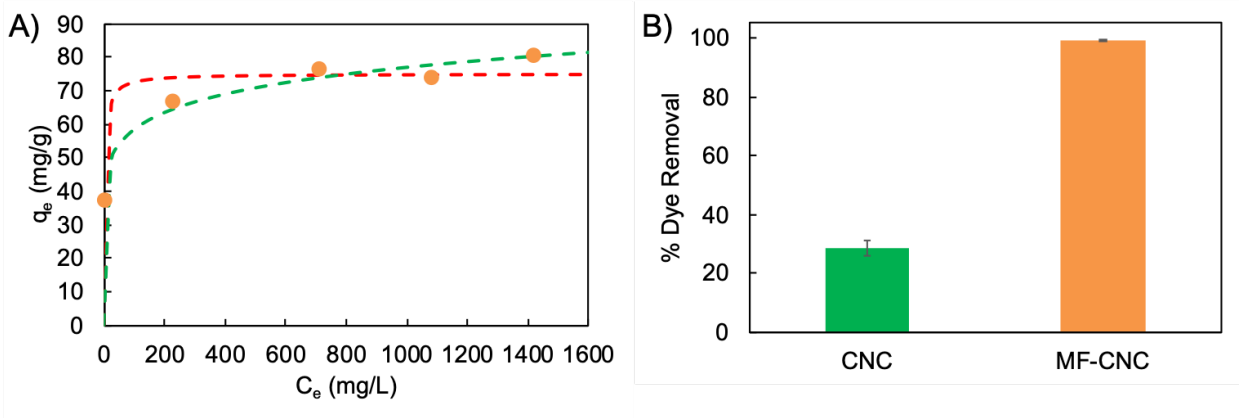

Figure 6.3: (A) Isotherm plots of MO adsorption onto MF-CNC, with orange symbols representing experimental data, red dashed line corresponding to the Langmuir isotherm and the green dashed line to the Freundlich isotherm, and (B) comparison of MO adsorption onto 100 mg CNC and MF-CNC at an initial MO concentration of 200 mg/L.

In addition to the equilibrium experiments, batch kinetic experiments were performed to determine the rate at which the dye binds to the surface of the MF-CNC. In contrast to our previous study using CNC-alginate hydrogels [14] we expect faster adsorption since a mass transfer barrier

for the MO no longer exists. **Figure 6.4a** shows the variation of bulk dye concentrations with time, while **Figure 6.4b** shows the adsorbed concentration versus time. It is evident that the system achieved equilibrium after 30 seconds. The pseudo-first and pseudo-second order models were applied to determine the kinetics of adsorption, with the pseudo-first order described by Eq. (6.9) [31]:

$$\frac{dq_t}{dt} = k_1(q_e - q_t) \tag{6.9}$$

With its integrated form:

$$\frac{q_e - q_t}{q_e} = e^{-k_1 t} \tag{6.10}$$

where q_e is the amount of dye adsorbed at equilibrium (mg/g), q_t is the amount of dye adsorbed at time t (mg/g), and k_1 is the pseudo-first order rate constant (1/min). Similarly, the pseudo-second order is described by Eq. (6.11) [32]:

$$\frac{dq_t}{dt} = k_2(q_e - q_t)^2 \tag{6.11}$$

with its integrated form being:

$$q_t = \frac{q_e^2 k_2 t}{q_e k_2 t + 1} \tag{6.12}$$

where q_e and q_t have the same definitions as the pseudo-first order model, and k_2 is the pseudo-second order rate constant (g/mg·min). One requirement in using these models is to ensure that either the amount of adsorption sites (adsorbent) or adsorbate is in excess, thus the experiments were conducted with an initial MO concentration of 2000 mg/L. After fitting Eq. (6.10) to the experimental data using non-linear regression the parameters q_e and k_1 were determined to be 74.97 mg/g and 36.46 min^{-1}, respectively, with an SSE of 153.98. Using the same procedure for Eq.

(6.12), the parameters q_e and k_2 were determined as 74.97 mg/g and 7.46×10^4 g/ mg·min, with an SSE of 153.98. The q_t estimated using Eq (6.10) was plotted as a blue dashed line in **Figure 6.4b** and corresponds to rapid equilibrium reached between the MF-CNC and the solution. As a result, the kinetic parameters k_1 and k_2 were abnormally high to reflect this behavior. From the data, it is impossible to discern whether the adsorption kinetics follows pseudo-first or pseudo-second order since the system appeared to reach equilibrium after the first 30 seconds, which was compounded by the challenges of sampling at such short times due to the necessity of centrifugation and filtering the sample before taking a measurement for concentration. On the other hand, since the adsorption of MO is extremely fast the hardwood pulp-MF-CNC membrane will be a suitable medium to remove the dye.

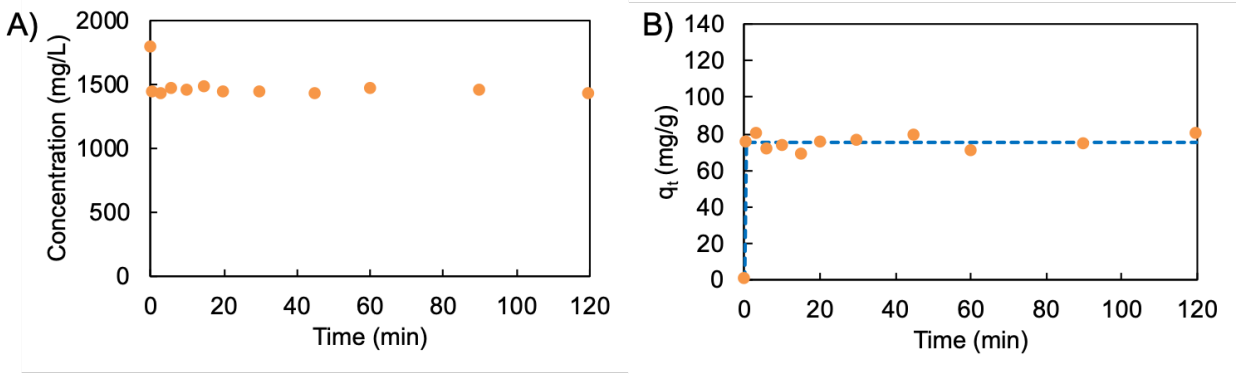

Figure 6.4: Batch kinetic experiment for MO adsorption onto MF-CNC (A) Bulk concentration over time (orange dots) and B) MO adsorbed over time (orange dots) with fit of pseudo-first order model (blue dashed line)

6.3.2.1 Effect of solution pH and ionic strength

To further examine the interaction of MO with the surface of MF-CNCs, experiments were conducted at various solution pHs and ionic strengths. These tests are also important to elucidate the performance of the adsorbent in waste streams containing other chemical species. **Figure 6.5a and 6.5b** shows the performance of MF-CNCs in removing MO and the corresponding zeta potential of MF-CNCs at various pHs, respectively. The trend in **Figure 6.5a** showing a decrease

of % dye removal with increasing pH could be understood by analyzing the trend with respect to zeta potential (**Figure 6.5b**). The zeta potential of the MF-CNC is positive (>+30 mV) between pH 2 and 9, but decreased sharply to -9.67 mV at pH 11. The high positive charge at low pH also reported by other researchers [214],[88],[218],[89] is associated with the protonation of primary and secondary amines present on the MF-CNC surface. Consequently the deprotonation of these functional groups at higher pH yielded an increasingly negative surface charge [214],[88],[89], and the % dye removal followed this trend by decreasing with increasing pH. Since MO contains a negatively charged sulfonate group, this correlation reflects that electrostatic interactions play a crucial role in the adsorption onto MF-CNC. A reduction in the % dye removal at a high pH when the surface of the MF-CNC is no longer positively charged supports this hypothesis. To further support the hypothesis of electrostatic driven adsorption, it is necessary to study the effect of solution ionic strength on dye removal.

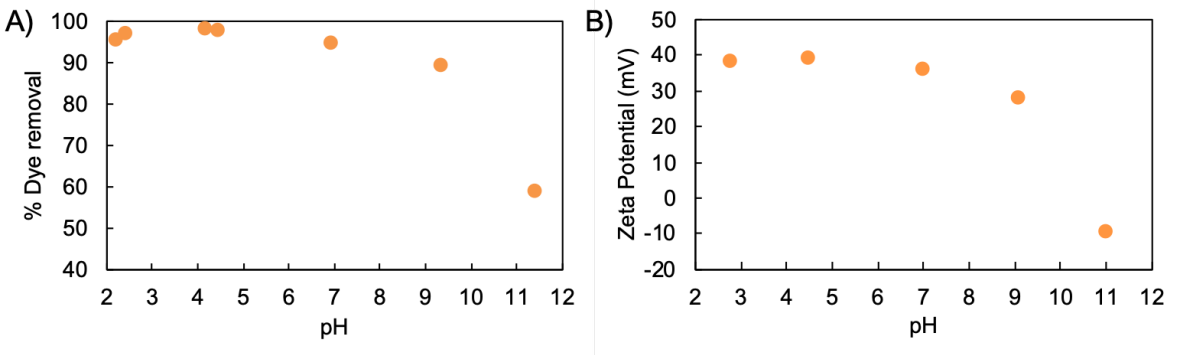

Figure 6.5: Effect of solution pH on (A) MO dye removal and (B) zeta potential of MF-CNC

Figure 6.6 shows the effect of ionic strength on dye removal by using varying concentrations of NaCl. The addition of NaCl to the MO solution tends to screen the long-range electrostatic interactions between the adsorbate molecules (MO) and adsorbent. The % dye removal decreased from 99 to 73% when the NaCl concentration was increased from 0 to 1 M, suggesting that electrostatic interaction promotes the adsorption of MO on the MF-CNC [14]. This

is in contrast to the methylene blue adsorption on the cellulose nanocrystal-alginate beads, where the % dye removal was reduced from 75 to 5% when the NaCl was increased from 0 to 1 M. This suggests that the adsorption of MO on MF-CNC is influenced by other factors besides electrostatic interaction. Chen *et al.* determined that hydrogen bonding between adsorbed protons on palygorskite clays and oxygen groups of the SO_3^- on MO occurred at low pH. Thus, the interactions between primary and secondary amines of the MF-CNC and MO aid in the MO adsorption [219].

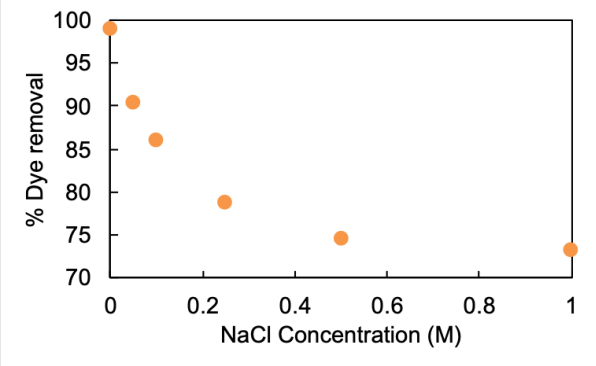

Figure 6.6: Effect of solution ionic strength on MO dye removal

6.3.2.2 Effect of Temperature

It is also necessary to understand the effect of temperature on adsorption, which will provide information on whether this process is endothermic or exothermic. **Figure 6.7a** shows the effect of temperature on the adsorption isotherm for a temperature range of 25 to 55°C, which revealed that higher temperatures favour greater adsorption. However, to probe the thermodynamics of the adsorption process the equilibrium constant (K_c) between the bulk and adsorbed phase must be evaluated Eq. (6.13) [169]:

$$K_c = K_F \rho \left(\frac{10^6}{\rho}\right)^{(1-1/n)} \tag{6.13}$$

where K_c is the dimensionless equilibrium constant, K_F is the Freundlich constant ((mg/g)(L/mg)$^{1/n}$), and ρ is the density of the water medium (1 g/mL approximately). From the

known values, thermodynamic properties such as Gibbs free energy (ΔG^o), enthalpy (ΔH^o) and entropy (ΔS^o) can be determined using the following equations [169]:

$$\Delta G° = \Delta H° - T\Delta S° \tag{6.14}$$

$$\Delta G° = -RTlnK_c \tag{6.15}$$

where Eqs. (6.14) and (6.15) can be combined to yield Eq. (6.16)

$$lnK_c = -\left(\frac{\Delta H°}{RT}\right) + \left(\frac{\Delta S°}{R}\right) \tag{6.16}$$

where R is the gas constant (8.314 J/mol·K) and T is temperature (K). **Figure 6.7b** shows the van't Hoff plot obtained using Eq. (6.16). The results of this analysis are summarized in **Table 6.1.** The large negative ΔG^o values ranged from -38.85 to -40.42 kJ/mol confirming the spontaneous nature of this process and reinforced the observation that the adsorption is favoured at higher temperatures with larger negative ΔG^o values. Furthermore, the negative value for ΔH^o extracted from the van't Hoff plot confirmed that the adsorption process is exothermic. The positive increase in the entropy indicates that despite the loss of freedom of the MO after binding to the surface of the adsorbent, the MF-CNC adsorbent and solvent had undergone changes that resulted in a net increase in the entropy [170]. The magnitude of ΔH^o could further elucidate whether the adsorption process is physisorption (ΔH^o between 8 to 65 kJ/mol), or chemisorption (ΔH^o between 84 to 420 kJ/mol) [220]. The magnitude of ΔH^o observed from this study further confirmed that the adsorption is physisorption. Although one would expect the adsorption process to be endothermic given the increase in the adsorption with temperature, the sign and magnitude of ΔH^o supported physisorption, which is an exothermic process [169]. The increase in the adsorption capacity could also be aided by higher temperatures by increasing the mobility of MO in solution [152].

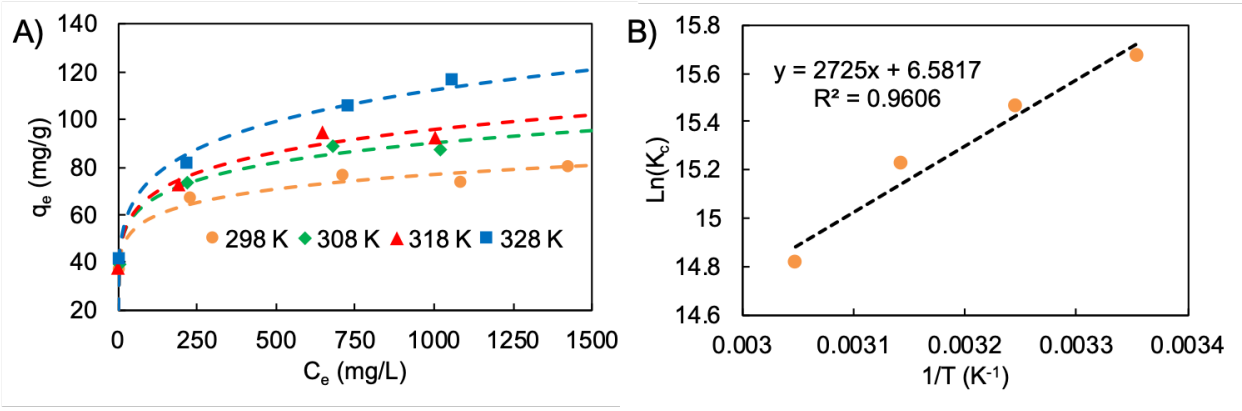

Figure 6.7: (A) Effect of temperature on MO dye removal, and (B) van't Hoff plot of MO adsorption temperature study

Table 6.1: Thermodynamic parameters for adsorption of MO onto MF-CNC

Temp. (K)	K_F (mg/g)* $(L/mg)^{1/n}$	n	K_c (10^{-6})	ΔG^o (kJ/mol)	ΔH^o (kJ/mol)	ΔS^o (J/mol·K)
298	33.53	8.34	6.397	-38.85	-22.66	54.72
308	34.84	7.25	5.187	-39.61		
318	33.57	6.58	4.118	-40.29		
328	32.53	5.56	2.717	-40.42		

6.3.3 Regeneration of the adsorbent

Lastly, the regeneration of MF-CNCs was investigated to determine if they can be reused. **Figure 6.8** shows the results after using a 1 M HCl eluent to desorb MO from MF-CNCs in successive cycles. Although the results from **Figure 6.5b** would indicate a high pH environment would more readily desorb MO, 1 M NaOH was found to only remove a maximum of 24% of adsorbed dye after one cycle (data not shown). Following the first round, only 52 % of the adsorbed MO was desorbed from the MF-CNC. To enhance this, the MF-CNC was separated from the eluent mixture by centrifugation and fresh eluent was added at the start of each desorption cycle, with the % of original MO desorbed shown in **Figure 6.8**, where 92 % of the initially adsorbed MO was desorbed following 6 desorption cycles, demonstrating that the MF-CNC can be regenerated and used for further adsorption operations.

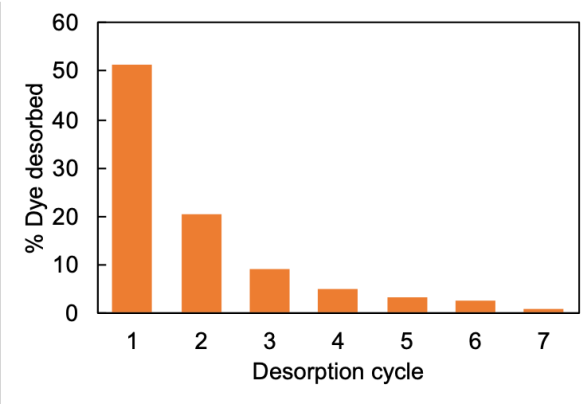

Figure 6.8: Results of using 1 M HCl to desorb MO from MF-CNC. % Dye desorbed corresponded to percentage of initially adsorbed dye desorbed in that stage

6.3.4 Pure HWP and MF-CNC incorporated HWP membranes

As described earlier, the incorporation of MF-CNCs into hardwood pulp membranes offers two major benefits: (1) selective removal of anionic contaminants (2) and enhancement of the wet strength of the membrane. Both of these characteristics should be influenced by the mass of MF-CNC incorporated into the membrane. The selective removal is likely to be proportional to the mass of MF-CNC incorporated, whereas the wet strength may deteriorate if too much MF-CNC displaced the HWP in the membrane structure. Thus, the performance of the membranes would be evaluated by their capability to remove MO dye from a continuous stream as well as their tensile index.

During the membrane formation process, the 101.6 mm diameter membrane dry mass was kept constant at 750 mg (corresponding to 92.6 gsm) while the designed ratio of hardwood pulp to MF-CNC was varied from 0 to 18 wt%. **Figure 6.9** shows the zeta potential of the filtrate recovered during the membrane formation process with varying MF-CNC loadings. In the case of 0 wt% MF-CNC, the filtrate contained only hardwood pulp fibres, having a negative surface charge due to surface carboxylic acid groups. As the content of MF-CNC increased, the zeta potential of the filtrate became less negative as the MF-CNC were bound to the pulp fibres, increasing their surface

charge until they became positive at high MF-CNC loadings. Since the HWP fibres and MF-CNC were mixed for 30 minutes prior to the membrane formation, a homogenous distribution of MF-CNC onto the HWP fibres was achieved, hence the material in the resulting membrane and the filtrate should be reproducible. Therefore, loadings above 10 wt% should yield the desired positive surface charge for the removal of anionic contaminants.

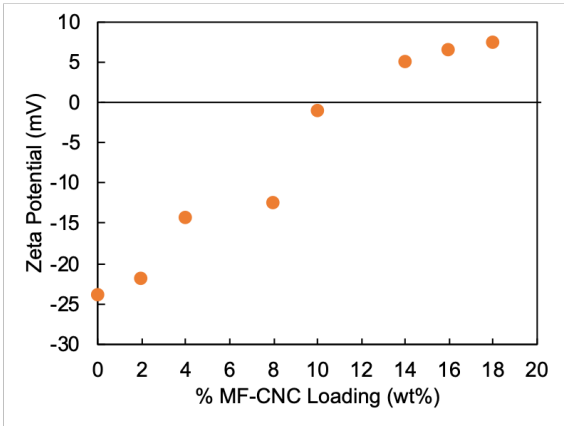

Figure 6.9: Zeta potential of filtrate sample removed during membrane formation process

6.3.5 Wet tensile index of HWP and MF-CNC HWP membranes

Following the preparation of the MF-CNC hardwood pulp membranes, the mechanical strength and MO adsorption capacity were investigated. **Figure 6.10** shows the wet tensile index of MF-CNC HWP membranes at varying degrees of MF-CNC incorporation. The incorporation of MF-CNC increased the wet tensile index of these membranes from 1.9 Nm/g to 12.2 Nm/g at 14 wt% MF-CNC. This value is similar to that reported by Saito *et al.* for the incorporation of poly(amideamine-epichlorohydrin) into hardwood kraft pulp handsheets that possessed a wet strength of 11.5 Nm/g [211]. Sarwar *et al.* also observed the same enhancement by adding chitosan as a wet strength additive to bamboo and acacia pulp [221], where larger loadings of chitosan improved the surface coverage on the pulp fibres necessary for inter-fibre bonding. From the analysis of **Figure 6.10**, a threshold occurred at 14 wt%, where further addition of MF-CNC to the

HWP matrix did not further increase the wet strength of the membrane. On the contrary, the wet tensile index decreased to 10.5 nm/g when the MF-CNC content approached 18 wt%. This reduction may be caused by the presence of less HWP in the membrane and/or the MF-CNCs approaching an optimum, where no further cross-linking or inter-fibre interactions of the pulp fibres occurred. This is evident from **Figure 6.9**, where further addition of MF-CNC beyond 14 wt% did not increase the surface charge of the fibres, suggesting that a maximum coverage of the pulp fibres by MF-CNCs was reached. Since no further enhancement in the tensile index beyond 14 wt% MF-CNC was observed, subsequent formulations to improve the functionality of the membranes were prepared up to 14 wt% MF-CNC.

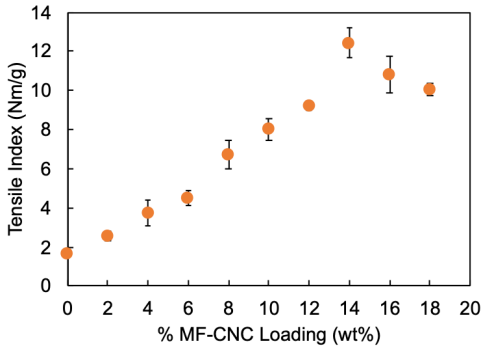

Figure 6.10: Wet tensile index as a function of MF-CNC loading for HWP membranes

6.3.6 Gravity-assisted MO removal using HWP and MF-CNC HWP membranes

The HWP membranes with varying amounts of MF-CNC were used to remove MO. **Figure 6.11a** shows the % dye removal from 5 mL of a 50 mg/L stock MO solution passing through a 380 mm^2 membrane in a dead-end filtration setup at atmospheric pressure. The dead-end filtration setup was chosen as the anticipated flows for purification would have a low total dissolved solids and total suspended solids content so that little filter cake build-up on the membrane was expected. Also, this would allow the system to operate at atmospheric pressure. As expected, the % dye

removal increased proportionally with MF-CNC content, whereas the pure HWP membrane retained only an insignificant amount of dye. The elution time increased proportionally with MF-CNC loading, enhancing the contact time of the dye and membrane that facilitate the adsorption of MO. The increase in the elution time was due to the reduction in the pore size of the membranes resulting from the increased interfibre bonding of MF-CNC and HWP in the membrane. This same behavior was observed with cellulose membranes loaded with varying amounts of chitosan, which blocked the pore structure formed by the cellulose [209]. The elution time observed at 14 wt% loading of MF-CNC was nearly 3 times longer than at 12 wt% MF-CNC loading with only a marginal increase of 2 % dye removal. The large increase in the elution time is caused by the further reduction in pore size resulting from the bonding of MF-CNC and pulp fibres. However, the % dye removal at the highest MF-CNC loadings was lower than that observed in the batch studies. Hence, multiple membranes arranged in series should be used in order to achieve the desired % dye removal. **Figure 6.11b** shows the results of % dye removal and elution time of varying MF-CNC content in two MF-CNC HWP membranes arranged in series. As expected, the % dye removal increased by more than two times over the single membrane system. This improvement is due to the longer contact time between the embedded MF-CNC and dye solution, where the elution time increased a factor of 4 in many of the MF-CNC ratios studied. In the double membrane system, the same behavior was again observed, where a large increase in the elution time was observed for MF-CNC loadings of 12 to 14 wt% with only a marginal increase in % dye removal. From these studies, we concluded that the optimal loading of MF-CNC to achieve an optimal wet strength and dye removal is 14 wt% MF-CNC.

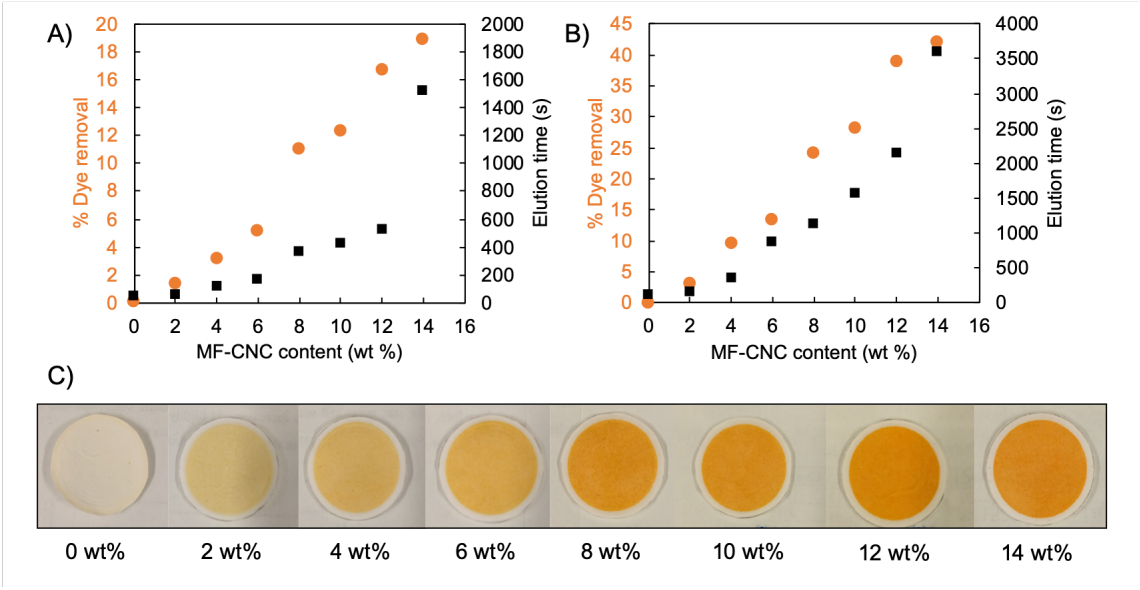

Figure 6.11: Performance of HWP membranes in removing MO dye as a function of MF-CNC content (A) one membrane, (B) two membranes in series, (C) MO fixation onto membranes with varying amounts of MF-CNC

6.3.7 Surface and cross-sectional morphology of MF-CNC HWP membranes

To further investigate the impact of incorporating MF-CNCs into HWP membranes, SEM images of a 14 wt% MF-CNC membrane were taken. **Figure 6.12a** shows the surface morphology of the membrane containing long HWP fibres of approximately 8 µm in diameter covering the membrane surface with MF-CNCs located in some regions across the membrane instead of evenly dispersed on the pulp fibres. In **Figure 6.12b** aggregates of MF-CNCs were observed to protrude between two HWP fibres, while **Figure 6.12c** shows an MF-CNC aggregate on a HWP fibre. Since MF-CNCs were mixed with a suspension of HWP fibres to yield a homogenous mixture before filtering onto a mesh, MF-CNC may aggregate and adsorb onto the surface of HWP fibres. Thus, the MF-CNC will tend to agglomerate between the pulp fibres, acting as an adhesive between the pulp fibres due to their opposite surface charges. To further probe whether the MF-CNC became embedded within the membrane interior, cross-sectional images were taken (**Figure 6.12d**). Entangled HWP fibres were observed, giving rise to an ill-defined pore structure compared to

conventional membranes prepared by casting or polymer coagulation [3]. **Figure 6.12e** shows a magnified image of **Figure 6.12d**, while **Figure 6.12f** is an expanded magnification of **Figure 6.12e** of an aggregate of MF-CNC adsorbed onto an interior fibre. These images confirmed that MF-CNC was distributed throughout the HWP matrix.

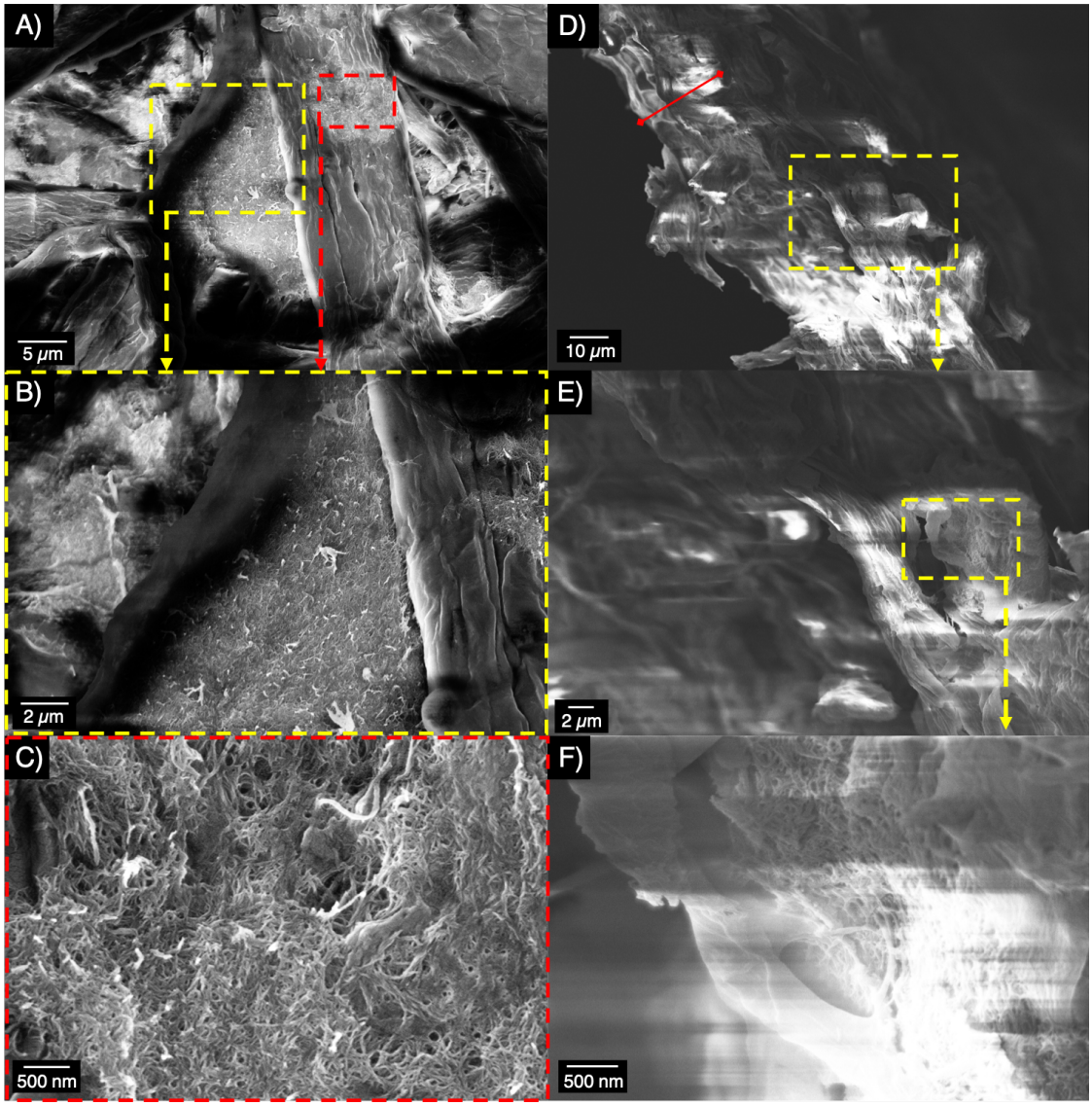

Figure 6.12: SEM images of 14 wt% MF-CNC HWP membrane A) Surface morphology of the membrane, B) Yellow region of A) zoomed in, C) Red region of A) zoomed in showing individual MF-CNCs, D) Cross-section image of membrane, red line measures 24 µm, E) Yellow region of D) zoomed in, F) yellow region of E) zoomed in showing MF-CNC in interior of membrane

Water contact angle measurements were conducted to investigate the effect of MF-CNC on the wettability of the membrane (**Figure 6.13**). When a drop of water was placed on the surface of pure HWP and those containing 2, 6 and 10 wt% MF-CNC, it immediately wicked into the membrane, registering a contact angle from 26.8° to 28.7°. At 14 wt% MF-CNC loading the water droplet remained on the surface for several seconds before wicking into the membrane, with a corresponding contact angle of 40.3°. This observation is consistent with the longer elution times reported for MO solution flowing through the 14 wt% MF-CNC membranes at atmospheric pressure (**Figure 6.11**). Thus, the incorporation of 14 wt% MF-CNC significantly hinders the transport of water through the membrane, likely a result of a smaller pores within the HWP structure.

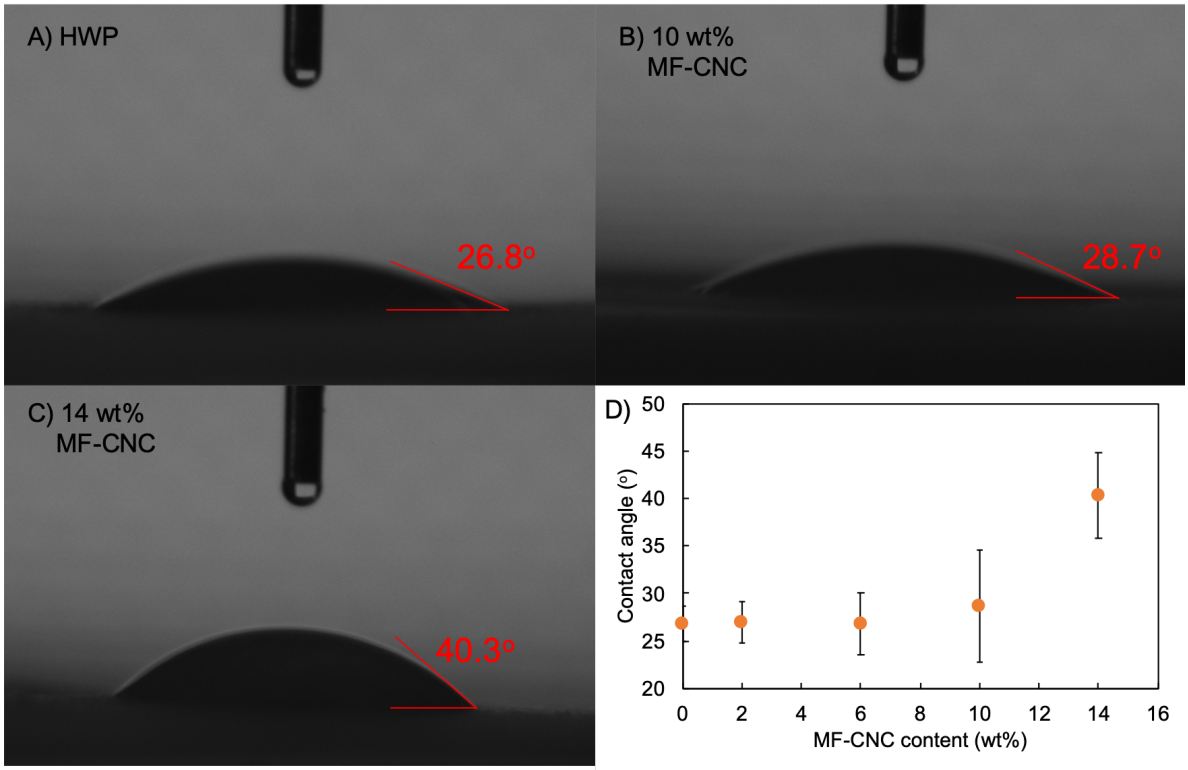

Figure 6.13: Contact angle measurements of water on (A) pure HWP membrane, (B) 10 wt% MF-CNC HWP membrane, (C) 14 wt% MF-CNC HWP membrane and (D) contact angle of water on membranes as a function of MF-CNC content

6.3.8 Pressure-driven filtration of HWP and MF-CNC HWP Membranes

Following the characterization of the membranes using gravity-driven filtration, we developed another experimental setup (**Figure 6.14**) that could accommodate more membranes and produce higher feed fluxes via pressurized flow. With more membranes (with active area of 755 mm^2) the performance of the system in treating higher volumes of water could be enhanced. **Figure 6.15a** and **6.15b** shows the dye removal using ten HWP and 14 wt% MF-CNC/HWP membranes in series for the treatment of 100 mL of a 25 mg/L MO solution, respectively. In **Figure 6.15a**, a negligible amount of dye was bound to the pure HWP membranes, similar to the observation from the small-scale experiments. Even at low pressure (5 psi), the flux across the membrane was 3965 L/m^2h, which increased to 8795 L/m^2h when the applied pressure was increased to 30 psi. On the other hand, % dye removal was significantly higher when the HWP contained 14 wt% MF-CNCs, which decreased from 36.9 to 31.2 % when the applied pressure was increased from 5 to 30 psi. Since % dye removal is influenced by the contact time, an increase in the applied pressure produced a higher flux across the membrane, resulting in lower contact times. By comparing the fluxes obtained in the pure HWP and MF-CNC HWP membrane systems at different pressures, the MF-CNC membranes required higher applied pressures to achieve the same flux. For example, an applied pressure of 20 psi was needed to achieve a flux of 3869 L/m^2h whereas a similar flux was achieved at 5 psi for the pure HWP membrane. This difference may be attributed to the smaller pores in the MF-CNC HWP membranes since the MF-CNC enhanced inter-fibre bonding and aggregated clusters of MF-CNC in the membrane interior reduced the pore size.

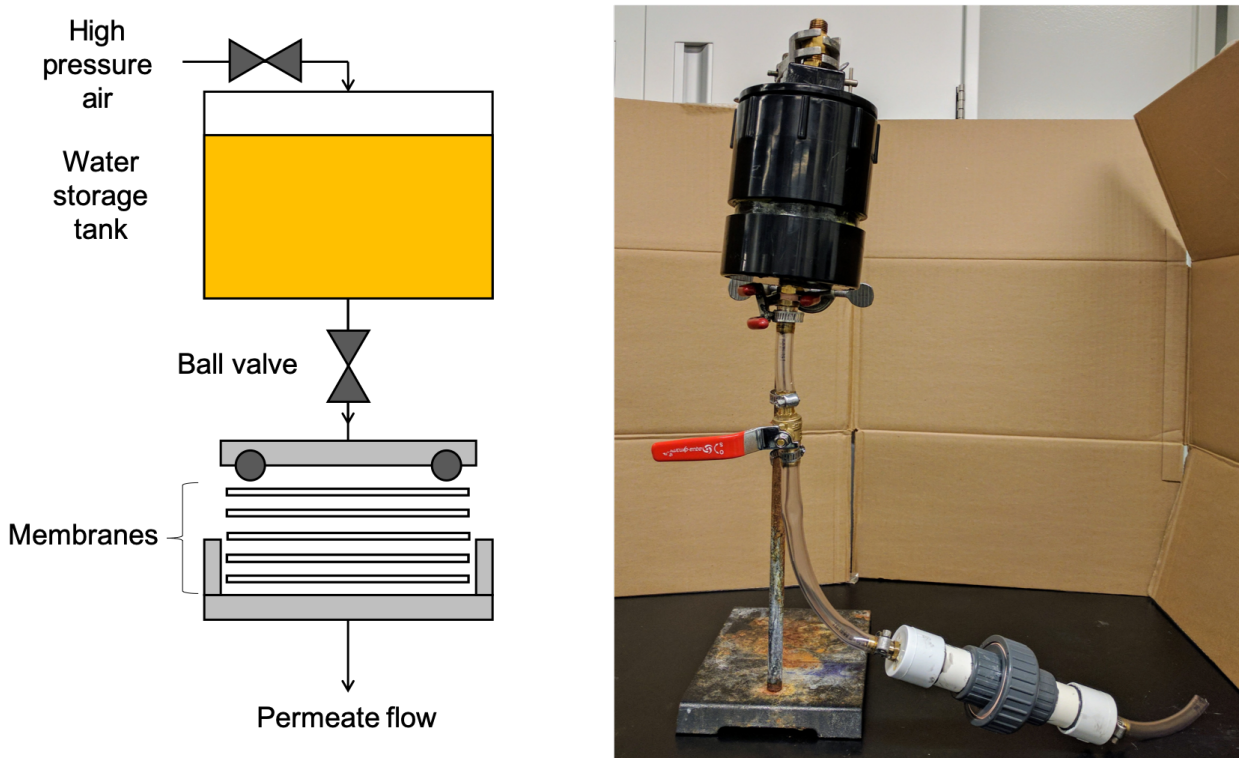

Figure 6.14: Schematic and photograph of setup used for large volume and pressure driven flow

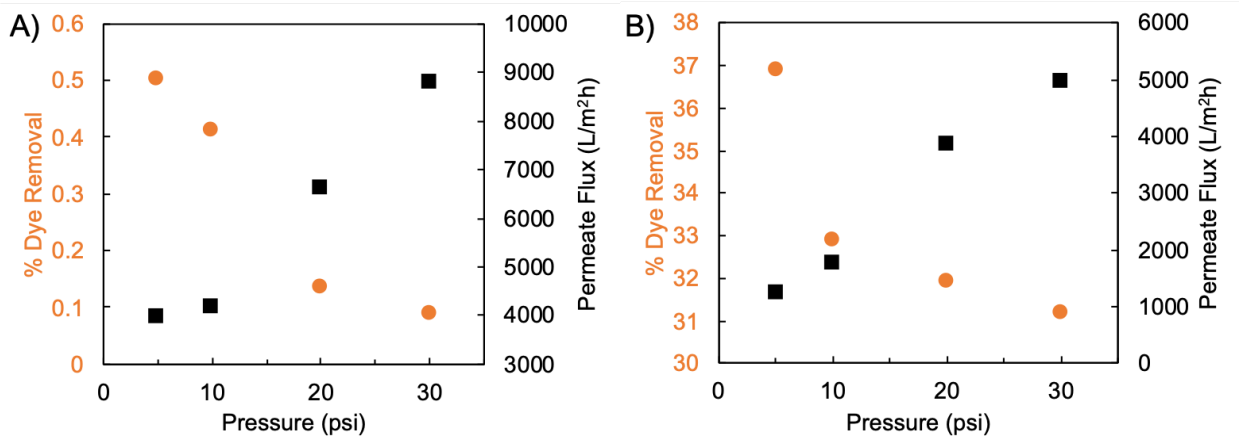

Figure 6.15: MO dye removal using 10 layers of membranes for (a) pure HWP membranes and (b) 14 wt% MF-CNC HWP membranes

6.3.9 Varying number of MF-CNC HWP membranes in series

Figure 6.16a shows that an increase in the number of 14 wt% MF-CNC HWP membranes in series enhanced % dye removal. It is important to understand the effect of the number of layers

on the permeate flux. The % dye removal increased with the number of membranes from 22.4 % with 5 membranes (49.0 mg MF-CNC) to 61.0 % with 20 membranes (196.0 mg MF-CNC). On the other hand, the flux across the membrane decreased sharply from 3869 L/m^{2}h (5 membranes) to 1340 L/m^{2}h (10 membranes) and further to 820 L/m^{2}h for 20 membranes. The lower flux aided in the removal of MO since the contact time was increased, as evident in **Figure 6.16b**. This figure describes the performance of the membrane system (orange points) compared to the tests performed at the equilibrium condition (black points). As the number of membranes in series increased, the operating line (dashed green line) became less steep and the final dye binding conditions shifted closer to their maximum performance at equilibrium.

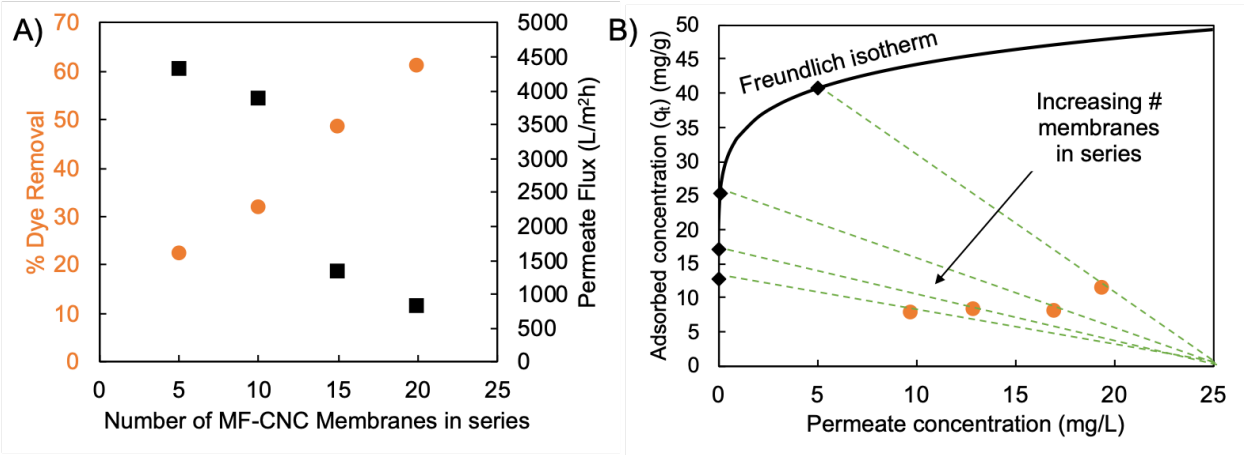

Figure 6.16: % Dye removal from 100 mL of a 25 mg/L MO solution with varying number of 14 wt% MF-CNC HWP membranes in series. Experiments were conducted at feed pressure of 20 psi

6.3.10 Time-dependent performance of MF-CNC HWP membrane

Another approach to evaluate membrane capability to remove dye is to measure the dye concentration in the permeate as a function of time. **Figure 6.17** shows the permeate concentration as a function of time for the ten 14 wt% MF-CNC HWP membranes in series. The average membrane flux was 3869 L/m^{2}h, and the MO removal progressively decreased as the adsorption sites on the MF-CNC became saturated. During the initial operation, MF-CNC (trapped within the

HWP matrix) rapidly adsorbed MO dye. However, the surface sites quickly became saturated, resulting in high MO concentration in the permeate stream at the end of the filtration. Our findings suggest that larger membranes or more membranes in series should be used to achieve optimal dye removal.

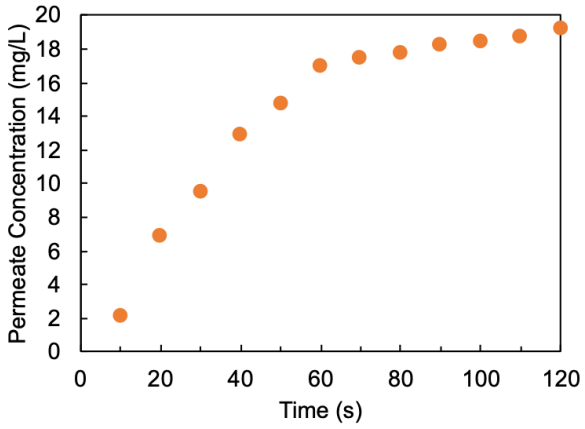

Figure 6.17: Removal of MO dye over time using ten 14 wt% MF-CNC membranes at a pressure of 20 psi. Total volume is 100 mL from a 25 mg/L MO solution

6.4 Conclusions

The use of melamine formaldehyde coated CNCs (MF-CNC) to remove anionic dyes by incorporating them within hardwood pulp membranes was investigated. Melamine formaldehyde was coated onto CNCs using an *in situ* polycondensation method that constituted 61.1 % of the mass of the final product. Batch experiments showed that the adsorption of methyl orange onto MF-CNCs followed the Freundlich isotherm capable of adsorbing this dye up to 80 mg/g, with higher dye adsorption at elevated temperatures. Kinetic experiments revealed that MO was rapidly bound to the MF-CNC within 30 seconds of contact. The MF-CNC membrane was capable of removing 70 % dye in solutions containing 1 M NaCl. MF-CNCs could be regenerated using both concentrated NaOH and HCl, and 92 % of adsorbed dye could be removed with 6 consecutive wash cycles using 1 M HCl. When incorporated into HWP membranes, the MF-CNC enhanced

the maximum tensile index at a loading of 14 wt%. The % MO removal in gravity-driven filtration steps was proportional to MF-CNC loading in the membrane. The incorporation of MF-CNC reduced the pore size of the HWP membranes, with longer elution times at higher MF-CNC loadings in the membranes. The MF-CNC membranes could be stacked in series to enhance the removal of MO in larger treatment systems operated at pressures up to 30 psi. Further modifications to these membranes include the incorporation of silver nanoparticles on MF-CNCs to impart antibacterial properties to the membrane. In regions where no electricity is available to operate mechanical pumps, suction produced by hand pumps could be used, producing large amounts of drinking water with up to 20 membranes in series.

Chapter 7: Original Contributions and Recommendations

7.1 Original Contributions to Research

Water treatment solutions require the use of materials that will have minimal impact on the environment during their extraction, production and end-of-life disposal. Cellulose nanomaterials (CNs) have undergone extensive study from a material science perspective to enhance their potential for water treatment operations. However, researchers rarely continue the evaluation of their materials in continuous treatment processes, which has impeded their implementation in large-scale treatment operations. This thesis seeks to produce novel CN nanocomposites for use in advanced treatment processes as well as evaluate CN nanocomposites in continuous treatment processes. The main objectives of this thesis include:

(a) development of CNF-organosilica flexible aerogels for adsorption of methyl orange in batch studies,

(b) development of CNC-TA-BiOBr nanocomposites to degrade rhodamine B in batch photocatalytic processes as well as examine their effectiveness in encapsulated ALG hydrogel beads,

(c) development of a process to simultaneously produce and transport CNC-ALG beads into a fixed bed column to continuously remove methylene blue from wastewater. The column performance and the applicability of standard mass transfer models to predict the process performance at various operating parameters were evaluated as well as the influence of Ca^{2+} on adsorption of methylene blue, and

(d) evaluation of the capability of MF-CNC nanocomposites to remove methyl orange dye in batch adsorption experiments and their ability to strengthen cellulose fibres to remove methyl orange in a continuous dead-end membrane filtration process.

My research examined both the material synthesis of new CN-based nanocomposites for water treatment as well as their implementation in specific water treatment processes. The following sections will summarize the major findings of this doctoral research.

7.1.1 Development of thiol-ene click modified CNF-MPTMS aerogels for removal of anionic contaminants

In this study, CNF-MPTMS aerogels were successfully prepared using directional freezing followed by freeze-drying and high temperature curing. The aerogels were further functionalized via thiol-ene click chemistry using DADMAC and MBAA monomers to generate adsorption sites for anionic compounds. Preliminary experiments suggested that an initial monomer composition of 1:10:1 of MPTMS:DADMAC:MBAA yielded the highest MO removal compared to aerogels modified at other monomer ratios, with a DADMAC grafting of 0.599 mmol/g aerogel. The modified aerogel also possessed similar shape recovery properties as the unmodified system. The adsorption of MO onto the modified aerogel was evaluated using batch experiments and shown to the Langmuir equilibrium isotherm which predicted maximum adsorption capacity of 186 mg/g, in agreement with potentiometric titration results. Kinetic experiments confirmed that the pore diffusion model could describe the mass transport of MO into the aerogel. Experiments aimed at investigating the effect of solution ionic strength suggested that electrostatic interaction influenced the adsorption process. Experiments confirmed that the adsorption proceeded by physisorption and the adsorption capacity decreased with increasing temperatures. Finally, the modified aerogel could be regenerated by washing with 2 M NaCl at 50^{o}C for three successive cycles and maintain 77 % of its adsorption capacity for MO after the second cycle. These experiments suggest that the modified CNF aerogel holds promise for use in continuous treatment operations.

7.1.2 Cellulose nanocrystals as scaffolds for bismuth-oxybromide photocatalytic nanoparticles

CNC-TA templates were used to nucleate BiOBr nanoparticles for photocatalytic degradation of rhodamine B dye. The photocatalytic performance of the CTB nanocomposite was influenced by the amount of Bi^{3+} precursor used in the synthesis. The CTB photocatalyst could effectively degrade RhB dye under UV light, while quenching experiments revealed that O_2^- and h^+ were the main active species that facilitated the degradation. UV-Vis measurements indicated that CTB degraded the RhB via two simultaneous reactions: (1) successive de-ethylation of the molecule and (2) cleavage of the chromophore structure. Direct comparisons showed that CTB photocatalyst outperformed TA-BiOBr in degrading RhB. The CTB was formulated into ALG hydrogel beads via ionotropic gelation and was shown to effectively degrade RhB. Moreover, the photocatalytic activity of the beads was not influenced by the alginate content of the hydrogel. Smaller beads displayed faster degradation of RhB due to their larger surface area-to-volume ratio. Thus, CTB-ALG nanocomposite is a viable material to degrade RhB and could be recovered from batch systems and incorporated in continuous flow columns to degrade organic contaminants.

7.1.3 Removal of methylene blue using cellulose nanocrystal-alginate hydrogel beads in self-loading packed columns

A self-loading fixed bed vessel was designed and fabricated to generate and load CNC-ALG beads to adsorb and remove methylene blue dye from the wastewater. The effect of Ca^{2+} ions on the adsorption of MB during batch and fixed bed adsorption was elucidated. The K_L values obtained from batch and column experiments were 7.9 and 183 m^3/kg, respectively. The significantly greater MB removal in the column was attributed to the absence of interference from Ca^{2+} during column operation as the majority of these ions were eluted from the adsorbent shortly after column experiments began. On the other hand, Ca^{2+} remained in the closed batch vessel for the duration of the experiment. In addition, batch and column adsorption experiments showed that

the Ca^{2+} ions were not displaced by the binding of MB to the adsorbent. An overshoot in MB concentration was observed during the column experiments and attributed to charge screening by unbound Ca^{2+} from the adsorbent. The swelling of the adsorbent during the initial stages was not caused by Ca^{2+} ions, but rather by osmotic swelling due to counterions associated with the bound MB. Additionally, the advection-diffusion equation coupled with the pore diffusion model including axial dispersion and film diffusion provided excellent prediction of the MB adsorption onto the CNC-ALG beads. Finally, the adsorbent could be regenerated to 81 % of its adsorption capacity after washing with 1 M HCl:ethanol (1:1 v:v). A second adsorption/desorption cycle indicated that the adsorbent could be regenerated to 96 % of this value. These experiments validated the potential of the CNC-ALG beads to purify water in a continuous process. The experiments and models used in this study could be potentially applied to other materials including CNF aerogels.

7.1.4 Melamine formaldehyde functionalized cellulose nanocrystals incorporated paper based membrane filters in point-of-use water treatment

Melamine formaldehyde was condensed onto the surface of CNCs for the purpose of removing methyl orange dye and strengthening the hardwood pulp membranes. The ability of the MF-CNCs to remove MO was evaluated using batch adsorption experiments. The system was found to obey the Freundlich equilibrium isotherm with a capacity to adsorb MO dye up to 80 mg/g. Kinetic experiments showed that MO rapidly bound to the MF-CNC nanocomposite and could remove up to 70 % MO dye in solutions containing 1 M NaCl. Regeneration experiments showed that the MO could be desorbed from MF-CNCs using both concentrated NaOH and HCl. The application of 6 successive cycles of elution with 1 M HCl could recover 92 % of the adsorbed dye from the nanocomposite. The incorporation of 14 wt% MF-CNC to the HWP membranes led to an 6-fold increase in wet strength. In addition, MF-CNC HWP membranes exhibited higher MO removal compared to pure HWP membranes, while an increase in the MF-CNC content resulted

in higher elution times of feed solution due to the reduced pore size of the membrane. Furthermore, the MF-CNC membranes could be stacked in series to enhance the removal of MO with feed pressures up to 30 psi confirming their potential for use in larger POU treatment systems.

7.2 Recommendations for Future Studies

Based on the scope of the study conducted in this doctoral research, the following next steps could be considered to further expand on the research to address related topics not covered. In Chapter 3, a compressible CNF-organosilane nanocomposite aerogel was produced to adsorb MO dye. The next steps could include investigating its capability to remove other anionic contaminants from wastewater, such as phosphate ions or perfluorooctanesulfonic acid. Following this, the aerogels could be loaded into fixed bed columns and their performance evaluated at various operating conditions, similar to the evaluation of the CNC-ALG hydrogels described in Chapter 5.

In Chapter 4, the synthesis and photocatalytic properties of a CNC-TA-BiOBr nanocomposite was reported. The study mainly explored the feasibility of templating this metallic oxide onto CNCs. Changes to the synthesis procedure could be introduced to improve the yield and size of the photocatalysts. It has been shown that heterojunctions formed between various BiOX metal oxide types lead to superior photocatalytic performance compared to pure BiOBr. Thus, a heterojunction of this metal oxide could be templated onto the CNCs. Following this, the new photocatalyst could be used to degrade contaminants other than RhB, such as emerging pharmaceutical compounds that are difficult to remove using current processes in municipal water treatment operations. Finally, the photocatalyst could be embedded within alginate hydrogels and used in a continuous stirred tank system fitted with high powered lamps to degrade incoming streams of dye.

In Chapter 5, the demonstration of CNCs in hydrogel beads to operate in a continuous column was comprehensively studied. Mass transport models for both bulk and transport within the adsorbent pores were able to predict the performance of the CNC-ALG adsorbent in a continuous flow process. The next steps will be to assess the validity of these models in the removal of other cationic contaminants, such as Cu^{2+} and Pb^{2+} ions. Additionally, the results obtained for the CNC-ALG hydrogel system for MB removal could be scaled up, with the potential of realizing the construction of fixed bed columns comprising 10 to 100 times the mass of adsorbent used in this study to treat discharge streams from textile mills containing MB dye.

In Chapter 6, we demonstrated that CNCs could be coated with MF resin to effectively remove MO dye as well as strengthen the HWP membrane filters. Several routes can be explored to further expand on the research in this field. The first would be to continue with point of use treatment, where an antibacterial function could be added to the membrane by depositing AgNPs or CuNPs *in situ* on the membrane to inactivate bacteria present in the feed stream. Another route would be to produce a membrane for a pressure-driven filtration process. This could be accomplished by switching HWP with CNF and using MF-CNC to cross-link CNFs to prepare a tighter network capable of rejecting both anionic compounds as well as medium weight polymeric compounds via smaller pore sizes. This membrane could then be evaluated in a cross-flow filtration setup for the continuous treatment of anionic dye-laden wastewater.

The research conducted in this thesis has mainly focused on treating single component artificial waste streams consisting of small molecules. The nanocomposites and processes developed in this thesis could be tested in the treatment train to treat multicomponent waste streams, eg., mixtures of MB, MO and RhB dyes. The first step of this treatment train could include a membrane filtration step using the MF-CNC membrane, to remove large colloids and MO dye simultaneously. Next, a fixed bed column consisting of CNC-ALG beads followed by one

consisting of CNF-MPTMS-DADMAC-MBAA aerogel could selectively remove the MB and residual MO dyes from the waste stream, respectively. This final stream could then pass through a photocatalytic reactor containing CNC-TA-BiOBr/ALG beads to degrade the RhB dyes not removed by the CNC-ALG adsorbent. This process integration would demonstrate the capability of CN nanocomposite systems for the treatment of wastewater and bring us one step closer to fully utilizing sustainable solutions to remediate our environment.

References

[1] Z. Carmen, S. Daniela, Textile Organic Dyes – Characteristics , Polluting Effects and Separation / Elimination Procedures from Industrial Effluents – A Critical Overview, in: T. Puzyn (Ed.), Org. Pollut. Ten Years After Stock. Conv. - Environ. Anal. Updat., InTech, 2012. http://www.intechopen.com/books/organic-pollutants-ten-years- after-the-stockholm-convention-environmental-and-analytical-update/textile-organic-dyes-characteristics- polluting-effects-and-separation-elimination-procedures-from-in.

[2] R. Andreozzi, V. Caprio, A. Insola, R. Marotta, Advanced oxidation processes (AOP) for water purification and recovery, Catal. Today. 53 (1999) 51–59. doi:10.1016/S0920-5861(99)00102-9.

[3] M.M. Pendergast, E.M.V. Hoek, A review of water treatment membrane nanotechnologies, Energy Environ. Sci. 4 (2011) 1946–1971. doi:10.1039/c0ee00541j.

[4] F.L. Slejko, Adsorption technology. A step-by-step approach to process evaluation and application, Dekker, New York; Basel, 1985.

[5] R. Batmaz, N. Mohammed, M. Zaman, G. Minhas, R.M. Berry, K.C. Tam, Cellulose nanocrystals as promising adsorbents for the removal of cationic dyes, Cellulose. 21 (2014) 1655–1665. doi:10.1007/s10570-014-0168-8.

[6] S. Liu, D. Tao, H. Bai, X. Liu, Cellulose-nanowhisker-templated synthesis of titanium dioxide/cellulose nanomaterials with promising photocatalytic abilities, J. Appl. Polym. Sci. 126 (2012) E282–E290. doi:10.1002/app.36637.

[7] Y.L. Ji, Q.F. An, Y.S. Guo, W.S. Hung, K.R. Lee, C.J. Gao, Bio-inspired fabrication of high perm-selectivity and anti-fouling membranes based on zwitterionic polyelectrolyte nanoparticles, J. Mater. Chem. A. 4 (2016) 4224–4231. doi:10.1039/c6ta00005c.

[8] X. He, K.B. Male, P.N. Nesterenko, D. Brabazon, B. Paull, J.H.T. Luong, Adsorption and desorption of methylene blue on porous carbon monoliths and nanocrystalline cellulose, ACS Appl. Mater. Interfaces. 5 (2013) 8796–8804. doi:10.1021/am403222u.

[9] R.J. Moon, A. Martini, J. Nairn, J. Simonsen, J. Youngblood, Cellulose nanomaterials review: structure, properties and nanocomposites, 2011. doi:10.1039/c0cs00108b.

[10] R. Batmaz, N. Mohammed, M. Zaman, G. Minhas, R.M. Berry, K.C. Tam, Cellulose nanocrystals as promising adsorbents for the removal of cationic dyes, Cellulose. 21 (2014) 1655–1665. doi:10.1007/s10570-014-0168-8.

[11] N. Grishkewich, N. Mohammed, J. Tang, K.C. Tam, Recent advances in the application of cellulose nanocrystals, Curr. Opin. Colloid Interface Sci. 29 (2017) 32–45. doi:10.1016/j.cocis.2017.01.005.

[12] C. Zhang, M. Zhou, S. Liu, B. Wang, Z. Mao, H. Xu, Y. Zhong, L. Zhang, B. Xu, X. Sui, Copper-loaded nanocellulose sponge as a sustainable catalyst for regioselective hydroboration of alkynes, Carbohydr. Polym. 191 (2018) 17–24. doi:10.1016/j.carbpol.2018.03.002.

[13] L. Rong, Z. Zhu, B. Wang, Z. Mao, H. Xu, L. Zhang, Y. Zhong, X. Sui, Facile fabrication of thiol-modified cellulose sponges for adsorption of Hg2+ from aqueous solutions, Cellulose. 25 (2018) 3025–3035. doi:10.1007/s10570-018-1758-7.

[14] N. Mohammed, N. Grishkewich, R.M. Berry, K.C. Tam, Cellulose nanocrystal–alginate hydrogel beads as novel adsorbents for organic dyes in aqueous solutions, Cellulose. 22 (2015) 3725–3738. doi:10.1007/s10570-015-0747-3.

[15] D. Hendricks, Fundamentals of Water Treatment Unit Processes: Physical, Chemical, and Biological, CRC Press, 2010.

[16] M. Pei, B. Zhang, Y. He, J. Su, K. Gin, O. Lev, G. Shen, S. Hu, State of the art of tertiary treatment technologies for controlling antibiotic resistance in wastewater treatment plants, Environ. Int. 131 (2019) 105026. doi:10.1016/j.envint.2019.105026.

[17] P.B. Tchounwou, C.G. Yedjou, A.K. Patlolla, D.J. Sutton, Heavy Metal Toxicity and the Environment, in: A. Luch (Ed.), Nih, Birkhäuser Basel, Basel, 2012: pp. 133–164. doi:10.1007/978-3-7643-8340-4_6.

[18] M. Brown, B. Barley, H. Wood, Minewater treatment: technology, application and policy, IWA Publishing, 2002.

[19] P. Sharma, H. Kaur, M. Sharma, V. Sahore, A review on applicability of naturally available adsorbents for the removal of hazardous dyes from aqueous waste., Environ. Monit. Assess. 183 (2011) 151–95. doi:10.1007/s10661-011-1914-0.

[20] Priority substances list assessment report - Textile Mill effulents, Environment Canada, 2001.

[21] D.O. Cooney, the Importance of Axial Dispersion in Liquid-Phase Fixed-Bed Adsorption Operations, Chem. Eng. Commun. 110 (1991) 217–231. doi:10.1080/00986449108939951.

[22] K.E. Noll, Adsorption technology for air and water pollution control, CRC Press, 1991.

[23] H.S. Fogler, Elements of Chemical Reaction Engineering (4th Edition), Pearson Prentice Hall, Upper Saddle River, NJ, 2005.

[24] I. Langmuir, the Constitution and Fundamental Properties of Solids and Liquids. Part I. Solids., J. Am. Chem. Soc. 252 (1916) 2221–2295. doi:10.1021/ja02268a002.

[25] R. Aravindhan, N.N. Fathima, J.R. Rao, B.U. Nair, Equilibrium and thermodynamic studies on the removal of basic black dye using calcium alginate beads, Colloids Surfaces A Physicochem. Eng. Asp. 299 (2007) 232–238. doi:10.1016/j.colsurfa.2006.11.045.

[26] H. Freundlich, Of the adsorption of gases. Section II. Kinetics and energetics of gas adsorption. Introductory paper to section II, Trans. Faraday Soc. 28 (1932) 195. doi:10.1039/tf9322800195.

[27] L. Liu, Y. Wan, Y. Xie, R. Zhai, B. Zhang, J. Liu, The removal of dye from aqueous solution using alginate-halloysite nanotube beads, Chem. Eng. J. 187 (2012) 210–216. doi:10.1016/j.cej.2012.01.136.

[28] S. Hokkanen, E. Repo, S. Lou, M. Sillanpää, Removal of arsenic(V) by magnetic nanoparticle activated microfibrillated cellulose, Chem. Eng. J. 260 (2015) 886–894. doi:10.1016/j.cej.2014.08.093.

[29] E. Worch, Chapter 5: Adsorption kinetics, in: Adsorpt. Technol. Water Treat. - Fundam. Process. Model., 2012.

[30] P. Li, G. Xiu, L. Jiang, ADSORPTION AND DESORPTION OF PHENOL ON ACTIVATED CARBON FIBERS IN A FIXED BED, Sep. Sci. Technol. 36 (2001) 2147–2163. doi:10.1081/SS-100105910.

[31] S. Lagergren, About the theory of so-called adsorption of soluble substances, K. Sven. Vetenskapsakademiens Handl. 24 (1898) 1–39.

[32] Y.S. Ho, G. McKay, Pseudo-second order model for sorption processes, Process Biochem. 34 (1999) 451–465. doi:10.1016/S0032-9592(98)00112-5.

[33] N. Kannan, M.M. Sundaram, Kinetics and mechanism of removal of methylene blue by adsorption on various carbons—a comparative study, Dye. Pigment. 51 (2001) 25–40. doi:10.1016/S0143-7208(01)00056-0.

[34] I. Ali, V.K. Gupta, Advances in water treatment by adsorption technology., Nat. Protoc. 1 (2006) 2661–2667. doi:10.1038/nprot.2006.370.

[35] E. Worch, Chapter 6: Adsorption dynamics in fixed-bed adsorbers, Walter de Gruyter, Berlin, 2012.

[36] a a Ahmad, B.H. Hameed, Fixed-bed adsorption of reactive azo dye onto granular activated carbon prepared from waste., J. Hazard. Mater. 175 (2010) 298–303. doi:10.1016/j.jhazmat.2009.10.003.

[37] E.J. Wilson, C.J. Geankoplis, Liquid mass transfer at very low reynolds numbers in packed beds, Ind. Eng. Chem. Fundam. 5 (1966) 9–14. doi:10.1021/i160017a002.

[38] S.F. Chung, C.Y. Wen, Longitudinal dispersion of liquid flowing through fixed and fluidized beds, AIChE J. 14 (1968) 857–866. doi:10.1002/aic.690140608.

[39] T.S. Natarajan, M. Thomas, K. Natarajan, H.C. Bajaj, R.J. Tayade, Study on UV-LED/TiO2 process for degradation of Rhodamine B dye, Chem. Eng. J. 169 (2011) 126–134. doi:10.1016/j.cej.2011.02.066.

[40] S. Zhu, D. Wang, Photocatalysis: Basic principles, diverse forms of implementations and emerging scientific opportunities, Adv. Energy Mater. 7 (2017) 1–24. doi:10.1002/aenm.201700841.

[41] W. Zhang, Q. Zhang, F. Dong, Visible-light photocatalytic removal of NO in air over BiOX (X = Cl, Br, I) single-crystal nanoplates prepared at room temperature, Ind. Eng. Chem. Res. 52 (2013) 6740–6746. doi:10.1021/ie400615f.

[42] L. Chen, R. Huang, M. Xiong, Q. Yuan, J. He, J. Jia, M.Y. Yao, S.L. Luo, C.T. Au, S.F. Yin, Room-temperature synthesis of flower-like BiOX (X=Cl, Br, I) hierarchical structures and their visible-light photocatalytic activity, Inorg. Chem. 52 (2013) 11118–

11125. doi:10.1021/ic401349j.

[43] M. Humayun, F. Raziq, A. Khan, W. Luo, Modification strategies of TiO 2 for potential applications in photocatalysis: A critical review, Green Chem. Lett. Rev. 11 (2018) 86–102. doi:10.1080/17518253.2018.1440324.

[44] A. Fujishima, X. Zhang, D.A. Tryk, TiO2 photocatalysis and related surface phenomena, Surf. Sci. Rep. 63 (2008) 515–582. doi:10.1016/j.surfrep.2008.10.001.

[45] K. Mondal, A. Sharma, Recent advances in the synthesis and application of photocatalytic metal–metal oxide core–shell nanoparticles for environmental remediation and their recycling process, RSC Adv. 6 (2016) 83589–83612. doi:10.1039/C6RA18102C.

[46] W. Wu, C. Jiang, V.A.L. Roy, Recent progress in magnetic iron oxide-semiconductor composite nanomaterials as promising photocatalysts, Nanoscale. 7 (2015) 38–58. doi:10.1039/c4nr04244a.

[47] J. Kaur, S. Singhal, Facile synthesis of ZnO and transition metal doped ZnO nanoparticles for the photocatalytic degradation of Methyl Orange, Ceram. Int. 40 (2014) 7417–7424. doi:10.1016/j.ceramint.2013.12.088.

[48] H. Lin, H. Ye, X. Li, J. Cao, S. Chen, Facile anion-exchange synthesis of BiOI/BiOBr composite with enhanced photoelectrochemical and photocatalytic properties, Ceram. Int. 40 (2014) 9743–9750. doi:10.1016/j.ceramint.2014.02.060.

[49] C. Mondal, J. Pal, M. Ganguly, A.K. Sinha, J. Jana, T. Pal, A one pot synthesis of Au–ZnO nanocomposites for plasmon-enhanced sunlight driven photocatalytic activity, New J. Chem. 38 (2014) 2999. doi:10.1039/c4nj00227j.

[50] V.C. Sarasidis, K. V. Plakas, S.I. Patsios, A.J. Karabelas, Investigation of diclofenac degradation in a continuous photo-catalytic membrane reactor. Influence of operating parameters, Chem. Eng. J. 239 (2014) 299–311. doi:10.1016/j.cej.2013.11.026.

[51] Y. Lin, Z. Geng, H. Cai, L. Ma, J. Chen, J. Zeng, N. Pan, X. Wang, Ternary graphene-TiO2-Fe3O4nanocomposite as a recollectable photocatalyst with enhanced durability, Eur. J. Inorg. Chem. (2012) 4439–4444. doi:10.1002/ejic.201200454.

[52] A. Fernández-Pérez, V. Rodríguez-Casado, T. Valdés-Solís, G. Marbán, A new continuous flow-through structured reactor for the photodegradation of aqueous contaminants, J. Environ. Chem. Eng. 6 (2018) 4070–4077. doi:10.1016/j.jece.2018.06.018.

[53] S. Mosleh, M.R. Rahimi, M. Ghaedi, K. Dashtian, S. Hajati, Sonochemical-assisted synthesis of CuO/Cu2O/Cu nanoparticles as efficient photocatalyst for simultaneous degradation of pollutant dyes in rotating packed bed reactor: LED illumination and central composite design optimization, Ultrason. Sonochem. 40 (2018) 601–610. doi:10.1016/j.ultsonch.2017.08.007.

[54] S. Sarkar, S. Chakraborty, C. Bhattacharjee, Photocatalytic degradation of pharmaceutical wastes by alginate supported TiO<inf>2</inf> nanoparticles in packed bed photo reactor (PBPR), Ecotoxicol. Environ. Saf. 121 (2015) 263–270.

doi:10.1016/j.ecoenv.2015.02.035.

[55] N.H.H. Hairom, A.W. Mohammad, A.A.H. Kadhum, Effect of various zinc oxide nanoparticles in membrane photocatalytic reactor for Congo red dye treatment, Sep. Purif. Technol. 137 (2014) 74–81. doi:10.1016/j.seppur.2014.09.027.

[56] M. Rezakazemi, A. Khajeh, M. Mesbah, Membrane filtration of wastewater from gas and oil production, Environ. Chem. Lett. 16 (2018) 367–388. doi:10.1007/s10311-017-0693-4.

[57] B.S. Lalia, E. Guillen, H.A. Arafat, R. Hashaikeh, Nanocrystalline cellulose reinforced PVDF-HFP membranes for membrane distillation application, Desalination. 332 (2014) 134–141. doi:10.1016/j.desal.2013.10.030.

[58] H. Ma, C. Burger, B.S. Hsiao, B. Chu, Fabrication and characterization of cellulose nanofiber based thin-film nanofibrous composite membranes, J. Memb. Sci. 454 (2014) 272–282. doi:10.1016/j.memsci.2013.11.055.

[59] A.S. Brady-Estévez, S. Kang, M. Elimelech, A Single-Walled-Carbon-Nanotube Filter for Removal of Viral and Bacterial Pathogens, Small. 4 (2008) 481–484. doi:10.1002/smll.200700863.

[60] Y. Huang, X. Feng, Polymer-enhanced ultrafiltration: Fundamentals, applications and recent developments, J. Memb. Sci. 586 (2019) 53–83. doi:10.1016/j.memsci.2019.05.037.

[61] H. Ma, C. Burger, B.S. Hsiao, B. Chu, Ultrafine Polysaccharide Nanofibrous Membranes for Water Purification, Biomacromolecules. 12 (2011) 970–976. doi:10.1021/bm1013316.

[62] R. Xiong, H.S. Kim, S. Zhang, S. Kim, V.F. Korolovych, R. Ma, Y.G. Yingling, C. Lu, V. V. Tsukruk, Template-Guided Assembly of Silk Fibroin on Cellulose Nanofibers for Robust Nanostructures with Ultrafast Water Transport, ACS Nano. 11 (2017) 12008–12019. doi:10.1021/acsnano.7b04235.

[63] Z. Karim, A.P. Mathew, M. Grahn, J. Mouzon, K. Oksman, Nanoporous membranes with cellulose nanocrystals as functional entity in chitosan: Removal of dyes from water, Carbohydr. Polym. 112 (2014) 668–676. doi:10.1016/j.carbpol.2014.06.048.

[64] T.A. Dankovich, D.G. Gray, Bactericidal paper impregnated with silver nanoparticles for point-of-use water treatment, Environ. Sci. Technol. 45 (2011) 1992–1998. doi:10.1021/es103302t.

[65] S.M. Praveena, L.S. Han, L.T.L. Than, A.Z. Aris, Preparation and characterisation of silver nanoparticle coated on cellulose paper: evaluation of their potential as antibacterial water filter, J. Exp. Nanosci. 11 (2016) 1307–1319. doi:10.1080/17458080.2016.1209790.

[66] M.D. Sobsey, C.E. Stauber, L.M. Casanova, J.M. Brown, M.A. Elliott, Point of Use Household Drinking Water Filtration: A Practical, Effective Solution for Providing Sustained Access to Safe Drinking Water in the Developing World, Environ. Sci. Technol. 42 (2008) 4261–4267. doi:10.1021/es702746n.

[67] L. Kong, D. Zhang, Z. Shao, B. Han, Y. Lv, K. Gao, X. Peng, Superior effect of TEMPO-

oxidized cellulose nanofibrils (TOCNs) on the performance of cellulose triacetate (CTA) ultrafiltration membrane, Desalination. 332 (2014) 117–125. doi:10.1016/j.desal.2013.11.005.

[68] Z. Wang, H. Ma, B.S. Hsiao, B. Chu, Nanofibrous ultrafiltration membranes containing cross-linked poly(ethylene glycol) and cellulose nanofiber composite barrier layer, Polymer (Guildf). 55 (2014) 366–372. doi:10.1016/j.polymer.2013.10.049.

[69] I.H. Tsibranska, B. Tylkowski, Concentration of ethanolic extracts from Sideritis ssp. L. by nanofiltration: Comparison of dead-end and cross-flow modes, Food Bioprod. Process. 91 (2013) 169–174. doi:10.1016/j.fbp.2012.09.004.

[70] Z. Karim, A.P. Mathew, V. Kokol, J. Wei, M. Grahn, High-flux affinity membranes based on cellulose nanocomposites for removal of heavy metal ions from industrial effluents, RSC Adv. 6 (2016) 20644–20653. doi:10.1039/c5ra27059f.

[71] M. Mota, J.A. Teixeira, A. Yelshin, Influence of cell-shape on the cake resistance in dead-end and cross-flow filtrations, Sep. Purif. Technol. 27 (2002) 137–144. doi:10.1016/S1383-5866(01)00202-7.

[72] S. Ebrahim, Cleaning and regeneration of membranes in desalination and wastewater applications: State-of-the-art, Desalination. 96 (1994) 225–238. doi:10.1016/0011-9164(94)85174-3.

[73] E. Lam, K.B. Male, J.H. Chong, A.C.W. Leung, J.H.T. Luong, Applications of functionalized and nanoparticle-modified nanocrystalline cellulose, Trends Biotechnol. 30 (2012) 283–290. doi:10.1016/j.tibtech.2012.02.001.

[74] A. Šturcová, G.R. Davies, S.J. Eichhorn, Elastic modulus and stress-transfer properties of tunicate cellulose whiskers, Biomacromolecules. 6 (2005) 1055–1061. doi:10.1021/bm049291k.

[75] Y. Habibi, L.A. Lucia, O.J. Rojas, Cellulose nanocrystals: Chemistry, self-assembly, and applications, Chem. Rev. 110 (2010) 3479–3500. doi:10.1021/cr900339w.

[76] M.M. de S. Lima, J.T. Wong, M. Paillet, R. Borsali, R. Pecora, Translational and rotational dynamics of rodlike cellulose whiskers, Langmuir. 19 (2003) 24–29. doi:10.1021/la020475z.

[77] O. Nechyporchuk, M.N. Belgacem, J. Bras, Production of cellulose nanofibrils: A review of recent advances, Ind. Crops Prod. 93 (2016) 2–25. doi:10.1016/j.indcrop.2016.02.016.

[78] B.L. Peng, N. Dhar, H.L. Liu, K.C. Tam, Chemistry and applications of nanocrystalline cellulose and its derivatives: A nanotechnology perspective, Can. J. Chem. Eng. 89 (2011) 1191–1206. doi:10.1002/cjce.20554.

[79] J. Araki, M. Wada, S. Kuga, T. Okano, Flow properties of microcrystalline cellulose suspension prepared by acid treatment of native cellulose, Colloids Surfaces A Physicochem. Eng. Asp. 142 (1998) 75–82. doi:10.1016/S0927-7757(98)00404-X.

[80] O. Nechyporchuk, M.N. Belgacem, F. Pignon, Current Progress in Rheology of Cellulose

Nanofibril Suspensions, Biomacromolecules. (2016) acs.biomac.6b00668. doi:10.1021/acs.biomac.6b00668.

[81] N. Mohammed, N. Grishkewich, K.C. Tam, Cellulose nanomaterials: promising sustainable nanomaterials for application in water/wastewater treatment processes, Environ. Sci. Nano. 5 (2018) 623–658. doi:10.1039/C7EN01029J.

[82] A. Pei, N. Butchosa, L. a. Berglund, Q. Zhou, Surface quaternized cellulose nanofibrils with high water absorbency and adsorption capacity for anionic dyes, Soft Matter. 9 (2013) 2047. doi:10.1039/c2sm27344f.

[83] H. Ma, B.S. Hsiao, B. Chu, Ultrafine cellulose nanofibers as efficient adsorbents for removal of UO 2 2+ in water, ACS Macro Lett. 1 (2012) 213–216. doi:10.1021/mz200047q.

[84] J. Tang, R.M. Berry, K.C. Tam, Stimuli-Responsive Cellulose Nanocrystals for Surfactant-Free Oil Harvesting, Biomacromolecules. 17 (2016) 1748–1756. doi:10.1021/acs.biomac.6b00144.

[85] H. Fan, J. Wang, Q. Zhang, Z. Jin, Tannic Acid-Based Multifunctional Hydrogels with Facile Adjustable Adhesion and Cohesion Contributed by Polyphenol Supramolecular Chemistry, ACS Omega. 2 (2017) 6668–6676. doi:10.1021/acsomega.7b01067.

[86] M. Shibata, K. Nakai, Preparation and properties of biocomposites composed of bio-based epoxy resin, tannic acid, and microfibrillated cellulose, J. Polym. Sci. Part B Polym. Phys. 48 (2010) 425–433. doi:10.1002/polb.21903.

[87] Z. Hu, R.M. Berry, R. Pelton, E.D. Cranston, One-Pot Water-Based Hydrophobic Surface Modification of Cellulose Nanocrystals Using Plant Polyphenols, ACS Sustain. Chem. Eng. 5 (2017) 5018–5026. doi:10.1021/acssuschemeng.7b00415.

[88] Z. Lv, C. Liang, J. Cui, Y. Zhang, S. Xu, A facile route for the synthesis of mesoporous melamine-formaldehyde resins for hexavalent chromium removal, RSC Adv. 5 (2015) 18213–18217. doi:10.1039/c4ra16866f.

[89] G. Ming, H. Duan, X. Meng, G. Sun, W. Sun, Y. Liu, L. Lucia, A novel fabrication of monodisperse melamine-formaldehyde resin microspheres to adsorb lead (II), Chem. Eng. J. 288 (2016) 745–757. doi:10.1016/j.cej.2015.12.007.

[90] Y. Wang, Y. Xie, Y. Zhang, S. Tang, C. Guo, J. Wu, R. Lau, Anionic and cationic dyes adsorption on porous poly-melamine-formaldehyde polymer, Chem. Eng. Res. Des. 114 (2016) 258–267. doi:10.1016/j.cherd.2016.08.027.

[91] Z. Shi, X. Wu, K.C. Tam, R. Berry, Processes for preparing amine-functionalized cellulose nanocrystals and nitrogen doped carbon nanofibers, US 2018 / 0216256 A1, 2018.

[92] X. Wu, Z. Shi, R. Tjandra, A.J. Cousins, S. Sy, A. Yu, R.M. Berry, K.C. Tam, Nitrogen-enriched porous carbon nanorods templated by cellulose nanocrystals as high performance supercapacitor electrodes, J. Mater. Chem. A. 3 (2015) 23768–23777. doi:10.1039/c5ta07252b.

[93] D.J. Merline, S. Vukusic, A.A. Abdala, Melamine formaldehyde: Curing studies and reaction mechanism, Polym. J. 45 (2013) 413–419. doi:10.1038/pj.2012.162.

[94] H. Qiao, Y. Zhou, F. Yu, E. Wang, Y. Min, Q. Huang, L. Pang, T. Ma, Effective removal of cationic dyes using carboxylate-functionalized cellulose nanocrystals, Chemosphere. 141 (2015) 297–303. doi:10.1016/j.chemosphere.2015.07.078.

[95] S. Eyley, W. Thielemans, Imidazolium grafted cellulose nanocrystals for ion exchange applications., Chem. Commun. 47 (2011) 4177–9. doi:10.1039/c0cc05359g.

[96] C.H. Chan, C.H. Chia, S. Zakaria, M.S. Sajab, S.X. Chin, Cellulose nanofibrils: a rapid adsorbent for the removal of methylene blue, RSC Adv. 5 (2015) 18204–18212. doi:10.1039/C4RA15754K.

[97] X. Yu, S. Tong, M. Ge, L. Wu, J. Zuo, C. Cao, W. Song, Adsorption of heavy metal ions from aqueous solution by carboxylated cellulose nanocrystals, J. Environ. Sci. 25 (2013) 933–943. doi:10.1016/S1001-0742(12)60145-4.

[98] H. Sehaqui, U.P. de Larraya, P. Liu, N. Pfenninger, A.P. Mathew, T. Zimmermann, P. Tingaut, Enhancing adsorption of heavy metal ions onto biobased nanofibers from waste pulp residues for application in wastewater treatment, Cellulose. 21 (2014) 2831–2844. doi:10.1007/s10570-014-0310-7.

[99] P. Liu, P.F. Borrell, M. Božič, V. Kokol, K. Oksman, A.P. Mathew, Nanocelluloses and their phosphorylated derivatives for selective adsorption of Ag(+), Cu(2+) and Fe(3+) from industrial effluents., J. Hazard. Mater. 294 (2015) 177–85. doi:10.1016/j.jhazmat.2015.04.001.

[100] A. Soleimani Dorcheh, M.H. Abbasi, Silica aerogel; synthesis, properties and characterization, J. Mater. Process. Technol. 199 (2008) 10–26. doi:10.1016/j.jmatprotec.2007.10.060.

[101] C.J. Brinker, G.W. Scherer, Sol-gel science: the physics and chemistry of sol-gel processing, Academic Press, 2013.

[102] H. Maleki, L. Durães, A. Portugal, An overview on silica aerogels synthesis and different mechanical reinforcing strategies, J. Non. Cryst. Solids. 385 (2014) 55–74. doi:10.1016/j.jnoncrysol.2013.10.017.

[103] R.A. Strøm, Y. Masmoudi, A. Rigacci, G. Petermann, L. Gullberg, B. Chevalier, M.A. Einarsrud, Strengthening and aging of wet silica gels for up-scaling of aerogel preparation, J. Sol-Gel Sci. Technol. 41 (2007) 291–298. doi:10.1007/s10971-006-1505-7.

[104] S. Zong, W. Wei, Z. Jiang, Z. Yan, J. Zhu, J. Xie, Characterization and comparison of uniform hydrophilic/hydrophobic transparent silica aerogel beads: skeleton strength and surface modification, RSC Adv. 5 (2015) 55579–55587. doi:10.1039/C5RA08714G.

[105] G. Zu, K. Kanamori, A. Maeno, H. Kaji, K. Nakanishi, Superflexible Multifunctional Polyvinylpolydimethylsiloxane-Based Aerogels as Efficient Absorbents, Thermal Superinsulators, and Strain Sensors, Angew. Chemie - Int. Ed. 57 (2018) 9722–9727. doi:10.1002/anie.201804559.

[106] S. Zhao, Z. Zhang, G. Sèbe, R. Wu, R. V. Rivera Virtudazo, P. Tingaut, M.M. Koebel, Multiscale assembly of superinsulating silica aerogels within silylated nanocellulosic scaffolds: Improved mechanical properties promoted by nanoscale chemical compatibilization, Adv. Funct. Mater. 25 (2015) 2326–2334. doi:10.1002/adfm.201404368.

[107] Y. Li, N. Grishkewich, L. Liu, C. Wang, K.C. Tam, S. Liu, Z. Mao, X. Sui, Construction of functional cellulose aerogels via atmospheric drying chemically cross-linked and solvent exchanged cellulose nanofibrils, Chem. Eng. J. 366 (2019) 531–538. doi:10.1016/j.cej.2019.02.111.

[108] Z. Zhang, G. Sèbe, D. Rentsch, T. Zimmermann, P. Tingaut, Ultralightweight and flexible silylated nanocellulose sponges for the selective removal of oil from water, Chem. Mater. 26 (2014) 2659–2668. doi:10.1021/cm5004164.

[109] Y. Li, L. Xu, B. Xu, Z. Mao, H. Xu, Y. Zhong, L. Zhang, B. Wang, X. Sui, Cellulose Sponge Supported Palladium Nanoparticles as Recyclable Cross-Coupling Catalysts, ACS Appl. Mater. Interfaces. 9 (2017) 17155–17162. doi:10.1021/acsami.7b03600.

[110] Z. Wu, Y. Li, L. Zhang, Y. Zhong, H. Xu, Z. Mao, B. Wang, X. Sui, Thiol-ene click reaction on cellulose sponge and its application for oil/water separation, RSC Adv. 7 (2017) 20147–20151. doi:10.1039/C7RA00847C.

[111] Y. Li, L. Zhu, N. Grishkewich, K.C. Tam, J. Yuan, Z. Mao, X. Sui, CO2-Responsive Cellulose Nanofibers Aerogels for Switchable Oil-Water Separation, ACS Appl. Mater. Interfaces. 11 (2019) 9367–9373. doi:10.1021/acsami.8b22159.

[112] J.P. Gong, Why are double network hydrogels so tough?, Soft Matter. 6 (2010) 2583. doi:10.1039/b924290b.

[113] M. Bruchet, A. Melman, Fabrication of patterned calcium cross-linked alginate hydrogel films and coatings through reductive cation exchange, Carbohydr. Polym. 131 (2015) 57–64. doi:10.1016/j.carbpol.2015.05.021.

[114] G.T. Grant, E.R. Morris, D.A. Rees, P.J.C. Smith, D. Thom, Biological interactions between polysaccharides and divalent cations: The egg-box model, FEBS Lett. 32 (1973) 195–198. doi:10.1016/0014-5793(73)80770-7.

[115] S.K. Papageorgiou, F.K. Katsaros, E.P. Kouvelos, J.W. Nolan, H. Le Deit, N.K. Kanellopoulos, Heavy metal sorption by calcium alginate beads from Laminaria digitata, J. Hazard. Mater. 137 (2006) 1765–1772. doi:10.1016/j.jhazmat.2006.05.017.

[116] N. Mohammed, N. Grishkewich, H.A. Waeijen, R.M. Berry, K.C. Tam, Continuous flow adsorption of methylene blue by cellulose nanocrystal-alginate hydrogel beads in fixed bed columns, Carbohydr. Polym. 136 (2016) 1194–1202. doi:10.1016/j.carbpol.2015.09.099.

[117] Z.H. Hu, A.M. Omer, X.K. Ouyang, D. Yu, Fabrication of carboxylated cellulose nanocrystal/sodium alginate hydrogel beads for adsorption of Pb(II) from aqueous solution, Int. J. Biol. Macromol. 108 (2018) 149–157. doi:10.1016/j.ijbiomac.2017.11.171.

[118] H. Yang, A. Sheikhi, T.G.M. Van De Ven, Reusable Green Aerogels from Cross-Linked Hairy Nanocrystalline Cellulose and Modified Chitosan for Dye Removal, Langmuir. 32 (2016) 11771–11779. doi:10.1021/acs.langmuir.6b03084.

[119] C. Zhou, Q. Wu, T. Lei, I.I. Negulescu, Adsorption kinetic and equilibrium studies for methylene blue dye by partially hydrolyzed polyacrylamide/cellulose nanocrystal nanocomposite hydrogels, Chem. Eng. J. 251 (2014) 17–24. doi:10.1016/j.cej.2014.04.034.

[120] F. Zhao, E. Repo, Y. Song, D. Yin, S. Ben Hammouda, L. Chen, S. Kalliola, J. Tang, K.C. Tam, M. Sillanpää, Polyethylenimine-cross-linked cellulose nanocrystals for highly efficient recovery of rare earth elements from water and a mechanism study, Green Chem. 19 (2017) 4816–4828. doi:10.1039/c7gc01770g.

[121] C. Wang, X. Zhang, B. Yuan, Y. Wang, P. Sun, D. Wang, Y. Wei, Y. Liu, Multi-heterojunction photocatalysts based on WO3 nanorods: Structural design and optimization for enhanced photocatalytic activity under visible light, Chem. Eng. J. 237 (2014) 29–37. doi:10.1016/j.cej.2013.10.003.

[122] L. Ye, J. Liu, C. Gong, L. Tian, T. Peng, L. Zan, Two different roles of metallic Ag on Ag/AgX/BiOX (X = Cl, Br) visible light photocatalysts: Surface plasmon resonance and Z-Scheme bridge, ACS Catal. 2 (2012) 1677–1683. doi:10.1021/cs300213m.

[123] Y. Tian, T. Tatsuma, Mechanisms and applications of plasmon-induced charge separation at TiO2 films loaded with gold nanoparticles, J. Am. Chem. Soc. 127 (2005) 7632–7637. doi:10.1021/ja042192u.

[124] D. Zhang, M. Wen, B. Jiang, G. Li, J.C. Yu, Ionothermal synthesis of hierarchical BiOBr microspheres for water treatment, J. Hazard. Mater. 211–212 (2012) 104–111. doi:10.1016/j.jhazmat.2011.10.064.

[125] K. Zhang, J. Liang, S. Wang, J. Liu, K. Ren, X. Zheng, H. Luo, Y. Peng, X. Zou, X. Bo, J. Li, X. Yu, BiOCl Sub-Microcrystals Induced by Citric Acid and Their High Photocatalytic Activities, Cryst. Growth Des. 12 (2012) 793–803. doi:10.1021/cg201112j.

[126] Q.C. Liu, D.K. Ma, Y.Y. Hu, Y.W. Zeng, S.M. Huang, Various bismuth oxyiodide hierarchical architectures: Alcohothermal- controlled synthesis, photocatalytic activities, and adsorption capabilities for phosphate in water, ACS Appl. Mater. Interfaces. 5 (2013) 11927–11934. doi:10.1021/am4036702.

[127] D.S. Bhachu, S.J.A. Moniz, S. Sathasivam, D.O. Scanlon, A. Walsh, S.M. Bawaked, M. Mokhtar, A.Y. Obaid, I.P. Parkin, J. Tang, C.J. Carmalt, Bismuth oxyhalides: Synthesis, structure and photoelectrochemical activity, Chem. Sci. 7 (2016) 4832–4841. doi:10.1039/c6sc00389c.

[128] X. Zhang, Z. Ai, F. Jia, L. Zhang, Generalized one-pot synthesis, characterization, and photocatalytic activity of hierarchical BiOX (X = Cl, Br, I) nanoplate microspheres, J. Phys. Chem. C. 112 (2008) 747–753. doi:10.1021/jp077471t.

[129] S. Shenawi-Khalil, V. Uvarov, S. Fronton, I. Popov, Y. Sasson, A novel heterojunction BiOBr/bismuth oxyhydrate photocatalyst with highly enhanced visible light photocatalytic

properties, J. Phys. Chem. C. 116 (2012) 11004–11012. doi:10.1021/jp3009964.

[130] M. Gao, D. Zhang, X. Pu, H. Li, D. Lv, B. Zhang, X. Shao, Facile hydrothermal synthesis of Bi/BiOBr composites with enhanced visible-light photocatalytic activities for the degradation of rhodamine B, Sep. Purif. Technol. 154 (2015) 211–216. doi:10.1016/j.seppur.2015.09.063.

[131] J. Zhang, J. Lv, K. Dai, C. Liang, Q. Liu, One-step growth of nanosheet-assembled BiOCl/BiOBr microspheres for highly efficient visible photocatalytic performance, Appl. Surf. Sci. 430 (2018) 639–646. doi:10.1016/j.apsusc.2017.02.101.

[132] Y. Feng, L. Li, J. Li, J. Wang, L. Liu, Synthesis of mesoporous BiOBr 3D microspheres and their photodecomposition for toluene, J. Hazard. Mater. 192 (2011) 538–544. doi:10.1016/j.jhazmat.2011.05.048.

[133] F. Li, Q. Wang, J. Ran, Y. Hao, X. Wang, D. Zhao, S.Z. Qiao, Ionic liquid self-combustion synthesis of BiOBr/$Bi_{24}O_{31}Br_{10}$ heterojunctions with exceptional visible-light photocatalytic performances, Nanoscale. 7 (2015) 1116–1126. doi:10.1039/C4NR05451B.

[134] L. Chen, S.F. Yin, R. Huang, Y. Zhou, S.L. Luo, C.T. Au, Facile synthesis of BiOCl nano-flowers of narrow band gap and their visible-light-induced photocatalytic property, Catal. Commun. 23 (2012) 54–57. doi:10.1016/j.catcom.2012.03.001.

[135] H.Y. Yu, G.Y. Chen, Y.B. Wang, J.M. Yao, A facile one-pot route for preparing cellulose nanocrystal/zinc oxide nanohybrids with high antibacterial and photocatalytic activity, Cellulose. 22 (2015) 261–273. doi:10.1007/s10570-014-0491-0.

[136] K. Liu, J. Nasrallah, L. Chen, L. Huang, Y. Ni, Preparation of CNC-dispersed Fe3O4 nanoparticles and their application in conductive paper, Carbohydr. Polym. 126 (2015) 175–178. doi:10.1016/j.carbpol.2015.03.009.

[137] J. Yang, J. Yu, J. Fan, D. Sun, W. Tang, X. Yang, Biotemplated preparation of CdS nanoparticles/bacterial cellulose hybrid nanofibers for photocatalysis application, J. Hazard. Mater. 189 (2011) 377–383. doi:10.1016/j.jhazmat.2011.02.048.

[138] Z. Karim, S. Claudpierre, M. Grahn, K. Oksman, A.P. Mathew, Nanocellulose based functional membranes for water cleaning: Tailoring of mechanical properties, porosity and metal ion capture, J. Memb. Sci. 514 (2016) 418–428. doi:10.1016/j.memsci.2016.05.018.

[139] X. Wang, T.M. Yeh, Z. Wang, R. Yang, R. Wang, H. Ma, B.S. Hsiao, B. Chu, Nanofiltration membranes prepared by interfacial polymerization on thin-film nanofibrous composite scaffold, Polymer (Guildf). 55 (2014) 1358–1366. doi:10.1016/j.polymer.2013.12.007.

[140] X. Cao, M. Huang, B. Ding, J. Yu, G. Sun, Robust polyacrylonitrile nanofibrous membrane reinforced with jute cellulose nanowhiskers for water purification, Desalination. 316 (2013) 120–126. doi:10.1016/j.desal.2013.01.031.

[141] A. Quellmalz, A. Mihranyan, Citric Acid Cross-Linked Nanocellulose-Based Paper for Size-Exclusion Nanofiltration, ACS Biomater. Sci. Eng. 1 (2015) 271–276.

doi:10.1021/ab500161x.

[142] A. Mautner, K.Y. Lee, P. Lahtinen, M. Hakalahti, T. Tammelin, K. Li, A. Bismarck, Nanopapers for organic solvent nanofiltration, Chem. Commun. 50 (2014) 5778–5781. doi:10.1039/c4cc00467a.

[143] P. Orsolini, T. Marchesi D'Alvise, C. Boi, T. Geiger, W.R. Caseri, T. Zimmermann, Nanofibrillated Cellulose Templated Membranes with High Permeance, ACS Appl. Mater. Interfaces. 8 (2016) 33943–33954. doi:10.1021/acsami.6b12107.

[144] A. Mautner, H.A. Maples, T. Kobkeatthawin, V. Kokol, Z. Karim, K. Li, A. Bismarck, Phosphorylated nanocellulose papers for copper adsorption from aqueous solutions, Int. J. Environ. Sci. Technol. 13 (2016) 1861–1872. doi:10.1007/s13762-016-1026-z.

[145] S. You, S. Cheng, H. Yan, The impact of textile industry on China's environment, Int. J. Fash. Des. Technol. Educ. 2 (2009) 33–43. doi:10.1080/17543260903055141.

[146] R. Chavan, Indian textile industry-environmental issues, Indian J. Fibre Text. Res. 26 (2001) 11–21. http://nopr.niscair.res.in/handle/123456789/24908.

[147] A. Mittal, A. Malviya, D. Kaur, J. Mittal, L. Kurup, Studies on the adsorption kinetics and isotherms for the removal and recovery of Methyl Orange from wastewaters using waste materials, J. Hazard. Mater. 148 (2007) 229–240. doi:10.1016/j.jhazmat.2007.02.028.

[148] H. Ma, C. Burger, B.S. Hsiao, B. Chu, Nanofibrous microfiltration membrane based on cellulose nanowhiskers, Biomacromolecules. 13 (2012) 180–186. doi:10.1021/bm201421g.

[149] P.J. Quinlan, A. Tanvir, K.C. Tam, Application of the central composite design to study the flocculation of an anionic azo dye using quaternized cellulose nanofibrils, Carbohydr. Polym. 133 (2015) 80–89. doi:10.1016/j.carbpol.2015.06.095.

[150] Y. Huang, H. Li, M.S. Balogun, W. Liu, Y. Tong, X. Lu, H. Ji, Oxygen vacancy induced bismuth oxyiodide with remarkably increased visible-light absorption and superior photocatalytic performance, ACS Appl. Mater. Interfaces. 6 (2014) 22920–22927. doi:10.1021/am507641k.

[151] N. Arena, J. Lee, R. Clift, Life Cycle Assessment of activated carbon production from coconut shells, J. Clean. Prod. 125 (2016) 68–77. doi:10.1016/j.jclepro.2016.03.073.

[152] A.A.A. Darwish, M. Rashad, H.A. AL-Aoh, Methyl orange adsorption comparison on nanoparticles: Isotherm, kinetics, and thermodynamic studies, Dye. Pigment. 160 (2019) 563–571. doi:10.1016/j.dyepig.2018.08.045.

[153] C.H. Chan, C.H. Chia, S. Zakaria, M.S. Sajab, S.X. Chin, Cellulose nanofibrils: a rapid adsorbent for the removal of methylene blue, RSC Adv. 5 (2015) 18204–18212. doi:10.1039/C4RA15754K.

[154] Z.H. Hu, A.M. Omer, X.K. Ouyang, D. Yu, Fabrication of carboxylated cellulose nanocrystal/sodium alginate hydrogel beads for adsorption of Pb(II) from aqueous solution, Int. J. Biol. Macromol. 108 (2018) 149–157.

doi:10.1016/j.ijbiomac.2017.11.171.

[155] L. Chen, R.M. Berry, K.C. Tam, Synthesis of β-Cyclodextrin-Modified Cellulose Nanocrystals (CNCs)@Fe 3 O 4 @SiO 2 Superparamagnetic Nanorods, ACS Sustain. Chem. Eng. 2 (2014) 951–958. doi:10.1021/sc400540f.

[156] Y. Li, L. Zhu, B. Wang, Z. Mao, H. Xu, Y. Zhong, L. Zhang, X. Sui, Fabrication of Thermoresponsive Polymer-Functionalized Cellulose Sponges: Flexible Porous Materials for Stimuli-Responsive Catalytic Systems, ACS Appl. Mater. Interfaces. 10 (2018) 27831–27839. doi:10.1021/acsami.8b12060.

[157] A.H. Soeriyadi, G.-Z. Li, S. Slavin, M.W. Jones, C.M. Amos, C.R. Becer, M.R. Whittaker, D.M. Haddleton, C. Boyer, T.P. Davis, Synthesis and modification of thermoresponsive poly(oligo(ethylene glycol) methacrylate) via catalytic chain transfer polymerization and thiol–ene Michael addition, Polym. Chem. 2 (2011) 815. doi:10.1039/c0py00372g.

[158] E. Sabio, F. Zamora, C.M. González-García, B. Ledesma, A. Álvarez-Murillo, S. Román, Homogeneous Diffusion Solid Model as a Realistic Approach to Describe Adsorption onto Materials with Different Geometries, Nanoscale Res. Lett. 11 (2016). doi:10.1186/s11671-016-1746-5.

[159] A.C. Tibbits, L.E. Mumper, C.J. Kloxin, Y.S. Yan, A Single-Step Monomeric Photo-Polymerization and Crosslinking via Thiol-Ene Reaction for Hydroxide Exchange Membrane Fabrication, J. Electrochem. Soc. 162 (2015) F1206–F1211. doi:10.1149/2.0321510jes.

[160] A.R. Fajardo, S.L. Fávaro, A.F. Rubira, E.C. Muniz, Reactive & Functional Polymers Dual-network hydrogels based on chemically and physically crosslinked chitosan / chondroitin sulfate, 73 (2013) 1662–1671. doi:10.1016/j.reactfunctpolym.2013.10.003.

[161] M. Hasani, E.D. Cranston, G. Westman, D.G. Gray, Cationic surface functionalization of cellulose nanocrystals, Soft Matter. 4 (2008) 2238–2244. doi:10.1039/B806789A.

[162] A. Hebeish, S. Sharaf, Novel nanocomposite hydrogel for wound dressing and other medical applications, RSC Adv. 5 (2015) 103036–103046. doi:10.1039/c5ra07076g.

[163] D.A. Topchiev, A.I. Martynenko, E.Y. Kabanova, V.D. Oppengeim, Y.□. Kirsh, T.M. Karaputadze, Copolymerization of N-vinylpyrrolidone with N,N-dimethyl-N,N-diallylammonium chloride, Bull. Acad. Sci. USSR Div. Chem. Sci. 39 (1990) 1788–1791. doi:10.1007/BF00958238.

[164] C. Wandrey, J. Hernández-Barajas, D. Hunkeler, Diallyldimethylammonium Chloride and its Polymers, in: Radic. Polym. Polyelectrolytes, Springer Berlin Heidelberg, Berlin, Heidelberg, 1999: pp. 123–183. doi:10.1007/3-540-70733-6_3.

[165] M.V. Subbaiah, D.-S. Kim, Adsorption of methyl orange from aqueous solution by aminated pumpkin seed powder: Kinetics, isotherms, and thermodynamic studies., Ecotoxicol. Environ. Saf. 128 (2016) 109–17. doi:10.1016/j.ecoenv.2016.02.016.

[166] G.F. Malash, M.I. El-Khaiary, Methylene blue adsorption by the waste of Abu-Tartour

phosphate rock, J. Colloid Interface Sci. 348 (2010) 537–545. doi:10.1016/j.jcis.2010.05.005.

[167] A. Salama, N. Shukry, M. El-Sakhawy, Carboxymethyl cellulose-g-poly(2-(dimethylamino) ethyl methacrylate) hydrogel as adsorbent for dye removal, Int. J. Biol. Macromol. 73 (2015) 72–75. doi:10.1016/j.ijbiomac.2014.11.002.

[168] Y. Hu, T. Guo, X. Ye, Q. Li, M. Guo, H. Liu, Z. Wu, Dye adsorption by resins: Effect of ionic strength on hydrophobic and electrostatic interactions, Chem. Eng. J. 228 (2013) 392–397. doi:10.1016/j.cej.2013.04.116.

[169] H.N. Tran, S.J. You, H.P. Chao, Thermodynamic parameters of cadmium adsorption onto orange peel calculated from various methods: A comparison study, J. Environ. Chem. Eng. 4 (2016) 2671–2682. doi:10.1016/j.jece.2016.05.009.

[170] J.M. Thomas, The existence of endothermic adsorption, J. Chem. Educ. 38 (1961) 138. doi:10.1021/ed038p138.

[171] K.M. Lee, C.W. Lai, K.S. Ngai, J.C. Juan, Recent developments of zinc oxide based photocatalyst in water treatment technology: A review, Water Res. 88 (2016) 428–448. doi:10.1016/j.watres.2015.09.045.

[172] J. Henle, P. Simon, A. Frenzel, S. Scholz, S. Kaskel, Nanosized BiOX (X = Cl, Br, I) particles synthesized in reverse microemulsions, Chem. Mater. 19 (2007) 366–373. doi:10.1021/cm061671k.

[173] L. Chen, R.M. Berry, K.C. Tam, Synthesis of β-Cyclodextrin-modified cellulose nanocrystals (CNCs)@Fe3O4@SiO2 superparamagnetic nanorods, ACS Sustain. Chem. Eng. 2 (2014) 951–958. doi:10.1021/sc400540f.

[174] F.M. Ascencio-Aguirre, L. Bazán-Díaz, R. Mendoza-Cruz, M. Santana-Vázquez, O. Ovalle-Encinia, A. Gómez-Rodríguez, R. Herrera-Becerra, Chemical synthesis and characterization of bismuth oxychloride BiOCl nanoparticles, Appl. Phys. A Mater. Sci. Process. 123 (2017) 1–6. doi:10.1007/s00339-017-0797-5.

[175] A. Idris, N. Hassan, R. Rashid, A. Ngomsik, Kinetic and regeneration studies of photocatalytic magnetic separable beads for chromium (VI) reduction under sunlight, J. Hazard. Mater. 186 (2011) 629–635. doi:10.1016/j.jhazmat.2010.11.101.

[176] R. Herrera-Becerra, J.L. Rius, C. Zorrilla, Tannin biosynthesis of iron oxide nanoparticles, Appl. Phys. A Mater. Sci. Process. 100 (2010) 453–459. doi:10.1007/s00339-010-5903-x.

[177] X. Chang, M.A. Gondal, A.A. Al-Saadi, M.A. Ali, H. Shen, Q. Zhou, J. Zhang, M. Du, Y. Liu, G. Ji, Photodegradation of Rhodamine B over unexcited semiconductor compounds of BiOCl and BiOBr, J. Colloid Interface Sci. 377 (2012) 291–298. doi:10.1016/j.jcis.2012.03.021.

[178] M. Shang, W. Wang, L. Zhang, Preparation of BiOBr lamellar structure with high photocatalytic activity by CTAB as Br source and template, J. Hazard. Mater. 167 (2009) 803–809. doi:10.1016/j.jhazmat.2009.01.053.

[179] J. Chen, D. Wu, K.C. Tam, K. Pan, Z. Zheng, Effect of surface modification of cellulose nanocrystal on nonisothermal crystallization of poly(β-hydroxybutyrate) composites, Carbohydr. Polym. 157 (2017) 1821–1829. doi:10.1016/j.carbpol.2016.11.071.

[180] T. Wu, G. Liu, J. Zhao, H. Hidaka, N. Serpone, Photoassisted Degradation of Dye Pollutants. V. Self-Photosensitized Oxidative Transformation of Rhodamine B under Visible Light Irradiation in Aqueous TiO 2 Dispersions, J. Phys. Chem. B. 102 (1998) 5845–5851. doi:10.1021/jp980922c.

[181] T. Watanabe, T. Takizawa, K. Honda, Photocatalysis through excitation of adsorbates. 1. Highly efficient N-deethylation of rhodamine B adsorbed to CdS, J. Phys. Chem. 81 (1977) 1845–1851. doi:10.1021/j100534a012.

[182] M. Rafatullah, O. Sulaiman, R. Hashim, A. Ahmad, Adsorption of methylene blue on low-cost adsorbents: A review, J. Hazard. Mater. 177 (2010) 70–80. doi:10.1016/j.jhazmat.2009.12.047.

[183] D. Ghosh, K.G. Bhattacharyya, Adsorption of methylene blue on kaolinite, Appl. Clay Sci. 20 (2002) 295–300. doi:10.1016/S0169-1317(01)00081-3.

[184] A. Hethnawi, N.N. Nassar, A.D. Manasrah, G. Vitale, Polyethylenimine-functionalized pyroxene nanoparticles embedded on Diatomite for adsorptive removal of dye from textile wastewater in a fixed-bed column, Chem. Eng. J. 320 (2017) 389–404. doi:10.1016/j.cej.2017.03.057.

[185] D.J. Joo, W.S. Shin, J.H. Choi, S.J. Choi, M.C. Kim, M.H. Han, T.W. Ha, Y.H. Kim, Decolorization of reactive dyes using inorganic coagulants and synthetic polymer, Dye. Pigment. 73 (2007) 59–64. doi:10.1016/j.dyepig.2005.10.011.

[186] Y.-Y. Fu, L.-J. Zhu, F. Liu, D. Zhou, L. Xue, B. Ma, Positively charged loose nanofiltration membrane grafted by diallyl dimethyl ammonium chloride (DADMAC) via UV for salt and dye removal, React. Funct. Polym. 86 (2014) 191–198. doi:10.1016/j.reactfunctpolym.2014.09.003.

[187] C.R. Holkar, A.J. Jadhav, D. V Pinjari, N.M. Mahamuni, A.B. Pandit, A critical review on textile wastewater treatments : Possible approaches, J. Environ. Manage. 182 (2016) 351–366. doi:10.1016/j.jenvman.2016.07.090.

[188] F. Kazemi, Z. Mohamadnia, B. Kaboudin, Z. Karimi, Photodegradation of methylene blue with a titanium dioxide/polyacrylamide photocatalyst under sunlight, J. Appl. Polym. Sci. 133 (2016). doi:10.1002/app.43386.

[189] K.Y. Foo, B.H. Hameed, Insights into the modeling of adsorption isotherm systems, Chem. Eng. J. 156 (2010) 2–10. doi:10.1016/j.cej.2009.09.013.

[190] M.R. Khan, S.I. Mozumder, A. Islam, D.M.R. Prasad, M.M. Alam, Methylene Blue Adsorption onto Water Hyacinth: Batch and Column Study, Water, Air, Soil Pollut. 223 (2012) 2943–2953. doi:10.1007/s11270-012-1078-8.

[191] S. Olivera, H.B. Muralidhara, K. Venkatesh, V.K. Guna, K. Gopalakrishna, Y. Kumar K., Potential applications of cellulose and chitosan nanoparticles/composites in wastewater

treatment: A review, Carbohydr. Polym. 153 (2016) 600–618. doi:10.1016/j.carbpol.2016.08.017.

[192] E.S. Dragan, D.F. Apopei Loghin, Enhanced sorption of methylene blue from aqueous solutions by semi-IPN composite cryogels with anionically modified potato starch entrapped in PAAm matrix, Chem. Eng. J. 234 (2013) 211–222. doi:10.1016/j.cej.2013.08.081.

[193] F. Delval, G. Crini, J. Vebrel, M. Knorr, G. Sauvin, E. Conte, Starch-Modified Filters Used for the Removal of Dyes from Waste Water, Macromol. Symp. 203 (2003) 165–171. doi:10.1002/masy.200351315.

[194] L. Jin, Q. Sun, Q. Xu, Y. Xu, Adsorptive removal of anionic dyes from aqueous solutions using microgel based on nanocellulose and polyvinylamine, Bioresour. Technol. 197 (2015) 348–355. doi:10.1016/j.biortech.2015.08.093.

[195] L. Chen, R.M. Berry, K.C. Tam, Synthesis of β-Cyclodextrin-modified cellulose nanocrystals (CNCs)@Fe3O4@SiO2 superparamagnetic nanorods, ACS Sustain. Chem. Eng. 2 (2014) 951–958. doi:10.1021/sc400540f.

[196] K.H. Chu, Fixed bed sorption: Setting the record straight on the Bohart–Adams and Thomas models, J. Hazard. Mater. 177 (2010) 1006–1012. doi:10.1016/j.jhazmat.2010.01.019.

[197] F. Zhao, B. Yu, Z. Yue, T. Wang, X. Wen, Z. Liu, C. Zhao, Preparation of porous chitosan gel beads for copper(II) ion adsorption, J. Hazard. Mater. 147 (2007) 67–73. doi:10.1016/j.jhazmat.2006.12.045.

[198] A.H. Sulaymon, K.W. Ahmed, Competitive Adsorption of Furfural and Phenolic Compounds onto Activated Carbon in Fixed Bed Column, Environ. Sci. Technol. 42 (2008) 392–397. doi:10.1021/es070516j.

[199] D.G. Leaist, The effects of aggregation, counterion binding, and added sodium chloride on diffusion of aqueous methylene blue, Can. J. Chem. 66 (1988) 2452–2457. doi:10.1139/v88-386.

[200] D. Saraydin, E. Karadağ, O. Güven, Use of superswelling acrylamide/maleic acid hydrogels for monovalent cationic dye adsorption, J. Appl. Polym. Sci. 79 (2001) 1809–1815. doi:10.1002/1097-4628(20010307)79:10<1809::AID-APP90>3.0.CO;2-L.

[201] N. Mohammed, A. Baidya, V. Murugesan, A.A. Kumar, M.A. Ganayee, J.S. Mohanty, K.C. Tam, T. Pradeep, Diffusion-Controlled Simultaneous Sensing and Scavenging of Heavy Metal Ions in Water Using Atomically Precise Cluster–Cellulose Nanocrystal Composites, ACS Sustain. Chem. Eng. 4 (2016) 6167–6176. doi:10.1021/acssuschemeng.6b01674.

[202] X. Lin, Q. Huang, G. Qi, S. Shi, L. Xiong, C. Huang, X. Chen, H. Li, X. Chen, Estimation of fixed-bed column parameters and mathematical modeling of breakthrough behaviors for adsorption of levulinic acid from aqueous solution using SY-01 resin, Sep. Purif. Technol. 174 (2017) 222–231. doi:10.1016/j.seppur.2016.10.016.

[203] N.E. Davila-Guzman, F.J. Cerino-Córdova, E. Soto-Regalado, M. Loredo-Cancino, J.A. Loredo-Medrano, R.B. García-Reyes, A mass transfer model for the fixed-bed adsorption of ferulic acid onto a polymeric resin: axial dispersion and intraparticle diffusion., Environ. Technol. 3330 (2016) 1–9. doi:10.1080/09593330.2015.1135993.

[204] M. Tamez Uddin, M. Rukanuzzaman, M. Maksudur Rahman Khan, M. Akhtarul Islam, Adsorption of methylene blue from aqueous solution by jackfruit (Artocarpus heteropyllus) leaf powder: A fixed-bed column study, J. Environ. Manage. 90 (2009) 3443–3450. doi:10.1016/j.jenvman.2009.05.030.

[205] S.H. Lee, H. Son, S.W. Hong, J. Chung, B. An, J.W. Choi, Calcium and hydrogen effects during sorption of copper onto an alginate-based ion exchanger: Batch and fixed-bed column studies, Chem. Eng. J. 232 (2013) 51–58. doi:10.1016/j.cej.2013.07.079.

[206] E. Worch, Chapter 7: Fixed-bed adsorber design, in: Adsorpt. Technol. Water Treat. - Fundam. Process. Model., 2012.

[207] G. Newcombe, M. Drikas, Adsorption of NOM onto activated carbon: Electrostatic and non-electrostatic effects, Carbon N. Y. 35 (1997) 1239–1250. doi:10.1016/S0008-6223(97)00078-X.

[208] M. Davidovich-Pinhas, H. Bianco-Peled, A quantitative analysis of alginate swelling, Carbohydr. Polym. 79 (2010) 1020–1027. doi:10.1016/j.carbpol.2009.10.036.

[209] L. Yang, W.W. Hsiao, P. Chen, Chitosan-cellulose composite membrane for affinity purification of biopolymers and immunoadsorption, J. Memb. Sci. 197 (2002) 185–197. doi:10.1016/S0376-7388(01)00632-9.

[210] M. He, B.U. Cho, J.M. Won, Effect of precipitated calcium carbonate - Cellulose nanofibrils composite filler on paper properties, Carbohydr. Polym. 136 (2016) 820–825. doi:10.1016/j.carbpol.2015.09.069.

[211] T. Saito, A. Isogai, Wet strength improvement of TEMPO-oxidized cellulose sheets prepared with cationic polymers, Ind. Eng. Chem. Res. 46 (2007) 773–780. doi:10.1021/ie0611608.

[212] A. Baraka, P.J. Hall, M.J. Heslop, Melamine-formaldehyde-NTA chelating gel resin: Synthesis, characterization and application for copper(II) ion removal from synthetic wastewater., J. Hazard. Mater. 140 (2007) 86–94. doi:10.1016/j.jhazmat.2006.06.051.

[213] A. Baraka, P.J. Hall, M.J. Heslop, Preparation and characterization of melamine-formaldehyde-DTPA chelating resin and its use as an adsorbent for heavy metals removal from wastewater, React. Funct. Polym. 67 (2007) 585–600. doi:10.1016/j.reactfunctpolym.2007.01.015.

[214] M.X. Tan, Y.N. Sum, J.Y. Ying, Y. Zhang, A mesoporous poly-melamine-formaldehyde polymer as a solid sorbent for toxic metal removal, Energy Environ. Sci. 6 (2013) 3254–3259. doi:10.1039/c3ee42216j.

[215] N. Mohammed, Cellulose Nanocrystals Incorporated Nanocomposites for Water Treatment Applications by, 2016.

[216] E. Worch, Chapter 3: Adsorption equilibrium I : General aspects and single-solute adsorption, in: Adsorpt. Technol. Water Treat. - Fundam. Process. Model., 2012.

[217] D. Muchorski, Tensile properties of paper and paperboard (using constant rate of elongation apparatus), 2006.

[218] Y.H. Jang, S. Hwang, S.B. Chang, J. Ku, D.S. Chung, Acid Dissociation Constants of Melamine Derivatives from Density Functional Theory Calculations, J. Phys. Chem. A. 113 (2009) 13036–13040. doi:10.1021/jp9053583.

[219] H. Chen, A. Zhong, J. Wu, J. Zhao, H. Yan, Adsorption behaviors and mechanisms of methyl orange on heat-treated palygorskite clays, Ind. Eng. Chem. Res. 51 (2012) 14026–14036. doi:10.1021/ie300702j.

[220] R. Ahmad, R. Kumar, Adsorptive removal of congo red dye from aqueous solution using bael shell carbon, Appl. Surf. Sci. 257 (2010) 1628–1633. doi:10.1016/j.apsusc.2010.08.111.

[221] J.M. Sarwar, A. Noori, L. Ahsan, D.A.N. Chowdhury, M.A. Quaiyyum, Effects of Chitosan as Dry and Wet strength additive in Bamboo and Acacia Pulp, IPPTA J. 20 (2009) 85–88.